NOTICE

The quality of this microform is heavily dependent upon the quality of the original thesis submitted for microfilming. Every effort has been made to ensure the highest quality of reproduction possible.

If pages are missing, contact the university which granted the degree.

Some pages may have indistinct print especially if the original pages were typed with a poor typewriter ribbon or if the university sent us an inferior photocopy.

Reproduction in full or in part of this microform is governed by the Canadian Copyright Act, R.S.C. 1970, c. C-30, and subsequent amendments.

AVIS

La qualité de cette microforme dépend grandement de la qualité de la thèse soumise au microfilmage. Nous avons tout fait pour assurer une qualité supérieure de reproduction.

S'il manque des pages, veuillez communiquer avec l'université qui a conféré le grade.

La qualité d'impression de certaines pages peut laisser à désirer, surtout si les pages originales ont été dactylographiées à l'aide d'un ruban usé ou si l'université nous a fait parvenir une photocopie de qualité inférieure.

La reproduction, même partielle, de cette microforme est soumise à la Loi canadienne sur le droit d'auteur, SRC 1970, c. C-30, et ses amendements subséquents.

A Measurement of Proton and Pion Induced P-wave Charmonium Hadroproduction

Marzia Rosati

Physics Department

McGill University, Montreal

January, 1992

A Thesis submitted to the Faculty of Graduate Studies and Research

in partial fulfillment of the requirements for the degree of

Doctor of Philosophy

ISBN 0-315-74783-8

Abstract

The production of charmonium states, χ_1 and χ_2, was measured at 300 GeV/c with π^+, π^-, and proton beams on a lithium target. The cross-sections were determined by analyzing the full data sample recorded, during the 1987-1988 running period, by experiment E705 at Fermilab. The χ mesons were detected through their radiative decay into J/ψ γ and the subsequent decay, $\psi \rightarrow \mu^+\mu^-$.

The measured cross-sections for the χ mesons and estimates of the cross section for direct production of J/ψ 's have been compared with measurements obtained in other experiments and with theoretical predictions within the framework of Quantum ChromoDynamics.

Sommaire

La production des états charmomium, χ_1 et χ_2, a été mesurée avec des faisceaux de π^+, π^-, et de protons de 300 GeV/c sur une cible de lithium. Les sections éfficaces ont été déterminées par l'analyse des événements enrégistrés par l'expérience E705 au Fermilab au cours des années 1987-1988. Les mésons χ ont été mesurés en utilisant leur désintégration en J/ψ γ et la transition subséquente $\psi \rightarrow \mu^+\mu^-$.

Les sections éfficaces mesurées pour les mésons χ et l'estimation de la section éfficace de production direct de J/ψ , ont été comparées aux valeurs obtenues par d'autres expériences et aux prédictions théoriques faites dans le cadre de la théorie Chromodinamique Quantique.

Original Material and Contributions of the Candidate

My principal contributions to the accomplishment of the E705 experiment, in chronological order, were:

- Responsibility for the debugging, testing, and timing of all the 560 scintillation counters of the experiment.
- Participating on shifts for the day-to-day operation of the experiment and maintaining the counter systems during the run (June 1987 - Feb 1988).
- Writing the online diagnostic and monitoring program for the beam proportional chambers, developing the beam tracking reconstruction program, and software aligning the beam stations and measuring their efficiencies throughout the run.
- Working on the charged particle tracking reconstruction on the ACP[1] multiprocessor system. This detailed study considerably improved the dimuon tracking efficiency. Also, I checked the consistency between the experimentally measured momentum resolution and the intrinsic resolution of the spectrometer, using a Monte Carlo simulation. I developed an algorithm to reconstruct the vertex which improved vertex resolution considerably. I studied the final sample of high mass dimuon pairs in order to extract the purest ψ signal.
- Working on the analysis of the electromagnetic detector in an effort to improve the energy resolution. I studied electrons from calibration runs and electrons in the dimuon triggers and this effort showed the necessity of improvements in the correction due to the shower longitudinal development and in the shower energy fitting package. These modifications improved our energy resolution. Also

using the electrons, the energy absolute scale was determined and was checked by reconstructing π^0 and η decays in two photons.

- Working on the extraction of the χ signals and evaluating the detector acceptance and the χ reconstruction efficiency (by a Monte Carlo program).

- Determining χ_1 and χ_2 cross-sections for pion and proton beams and the cross section for direct production of ψ.

Acknowledgements

Any high energy physics experiment is a collaborative effort. While this thesis bears my name, it is the work of a number of people: E705 collaborators, beam line physicists and many Fermilab personnel. They all deserve my gratitude; without their talents, experience and cooperation, the experiment would not have been possible.

First, I would like to thank my thesis advisor, Professor Sergio Conetti for his continued guidance, encouragement and understanding. I am particularly grateful for his patient and numerous readings of this document.

Alberto Marchionni's help was precious, through my early days at Fermilab and later as I struggled through the analysis of E705 data. Although he has moved back to Italy, he has always kept in touch, by making short trips back to Fermilab and by many conversations through electronic mail. His comments, suggestions, encouragement and friendship were invaluable.

I want to thank my fellow student George Zioulas. Throughout these years of graduate school we shared many "good" and some "tough" times. He and his wife Rachel are true friends; babysitting their son, Chris, gave me something to smile about while I was working on this thesis.

I am grateful I had the opportunity to work closely, throughout the years, with several E705 collaborators and, since many of them passed to greener pastures, I want the take this opportunity to thank all of them. Steve Delchamps, Merrill Jenkins, Takis Pramatiotis, Shen Qifeng, André Simard, Lenny Spiegel, Rick Tesarek, Tim Turkington, Spyros Tzamarias greatly contributed to the data collection and analysis. They were valuable sources of knowledge from whom I learned not only physics, hardware and computing techniques, but also English, literature, cooking, and some Greek. Their

companionship allowed me to get through night, owl shifts and long working hours while actually enjoying it.

None of my accomplishments would have been possible without the support of the people I love. My deep gratitude is to David, for his endless support and encouragement and his patience in putting up with many "vacations" at Fermilab. The support of my family always played an important role on the achievement of my goals. Throughout my life my parents, although they did not always agree with me, have always allowed me to make my own decisions, respected them and been very supportive. They deserve special recognition for their understanding and continued encouragement throughout my graduate work. My sister Fabia deserves a real "grazie", her friendship and her sense of humor helped smooth over the rough times, putting everything into perspective.

Table of Contents

List of Figures

List of Tables

Chapter 1

Introduction

The work presented in this thesis is based upon data collected at the Fermi National Accelerator Laboratory (Fermilab) in experiment E705 during the 1987-1988 run. E705 employed a large aperture, open geometry, fixed target spectrometer installed in the Proton West beam line at Fermilab, to study the following processes and decay sequence:

$$\begin{aligned} (p, \pi^+, \pi^-, \bar{p})\ N \rightarrow\ & \chi + \text{anything} \\ & \hookrightarrow \quad \psi\gamma \\ & \hookrightarrow \mu^+\mu^- \end{aligned} \tag{1.1}$$

where χ and J/ψ are charmonium states: bound states of a charm quark and anti-quark ($c\bar{c}$). These states are produced in high energy collisions between the elementary constituents of strongly interacting particles (hadrons). The framework to study the dynamics of strong interactions among particles is provided by the Quantum Chromodinamics (QCD) theory. The specific predictions, obtained when QCD is applied to χ production, can be compared to the experimental results to obtain valuable information on the dynamics of strong interactions. Furthermore, the comparison of reactions initiated by different incident particles, with different internal structure (like pions and protons) allows one to investigate the role of the hadronic constituents.

The E705 spectrometer consisted of a tracking system, an analysis magnet, an electromagnetic calorimeter and a muon detector. Beam particles were tagged with two gas Cherenkov counters; the negative beam was 98.5% π^- and 1.5% $\bar{p}$, the positive one was 40% π^+ and 60% p. The dimuon trigger consisted of two stages: two muons in different quadrants were required by the first level; at the second level a fast online processor

performed the computation of the invariant mass of the dimuon system, selecting events with apparent mass $\geq$2.4 GeV/c^2.

The analysis leading to the extraction of the χ signal and the first set of results for χ production, induced for both pion and proton beams, will be presented in this thesis.

1.1 Quark model

In the past 30 years, important progress in our understanding of particle physics has been achieved. In the early 1960's a large number of meson and baryon resonances had been discovered, and some regularities or patterns were noted among the observed states. In 1964 M. Gell-Mann [2] and G. Zweig [3] suggested that the observed regularities could be accounted for by postulating that all known particles were some sort of bound state of two or three elementary spin 1/2 particles, quarks, which can appear in three different types or "flavors" called "up", "down", "strange" (u,d,s). Within the model, the known strong interacting particles are interpreted as bound states of three quarks (baryons) or of a quark-antiquark pair (mesons). Further developments of the quark model suggested [4] that quarks must have an additional degree of freedom, which was given the name "color", and that the observed particles had net zero color. The introduction of the concept of color was able to provide, among other things, the correct rate for two well-known processes, which bear indirect evidence for the color degrees of freedom: the decay $\pi^0 \rightarrow \gamma\gamma$ and e^+e^- annihilation. In these processes the number of colors appear as an extra factor for the reaction rate and the experimentally measured rates are consistent with quarks appearing in three different colors. In 1970, Glashow, Iliopoulos, and Maiani [5] proposed the existence of a fourth quark, "charm" (c), to explain the absence of some flavor-changing reactions induced by the weak interaction. For example, the ratio of neutral to charged-current rates in kaon decay is [9]:

$$\frac{K^+ \rightarrow \pi^+ \nu\bar{\nu}}{K^+ \rightarrow \pi^0 \mu^+ \nu_\mu} < 10^{-5} \qquad (1.2)$$

At the time, no particle containing a charm quark had yet been observed. In November 1974 a narrow resonance with a mass of 3.1 GeV/c^2, the J/ψ , was simultaneously

discovered in experiments at the Brookhaven Alternating Gradient Synchotron[6] and at the Stanford Linear Accelerator[7]. This was the first direct evidence of the existence of charm, since the newly discovered particle was eventually interpreted as a 1^{--} $c\bar{c}$ bound state.

The discovery of the J/ψ was followed in 1977 by the observation of similar narrow resonances in the mass region 9.5-10.5 GeV/c^2, attributed to bound states of an even higher mass quark, the "bottom" or "b" quark [8]. The $1S^1$ bound state of a bottom quark antiquark, referred to as Υ, was first seen in p-nucleus interactions, but it was studied in detail at e^+e^- colliders. Also, experimental upper limits on $b \rightarrow d$ and $b \rightarrow s$ neutral current decays indicate that, if the current description of the quarks properties is correct, the b quark should belong to a doublet together with a sixth quark. This sixth quark, called "top", has not been directly established and is the subject of an ongoing search at the Fermilab $p\bar{p}$ Collider experiments.

The dynamics governing quark systems are described by a non-Abelian gauge field theory with color symmetry, called Quantum Chromodynamics (QCD). Just like the photon, which is the gauge field mediating electromagnetic interactions, the non-Abelian gauge field in QCD, the gluon, mediates color interactions between quarks. A major difference between QED and QCD is that, while photons have no electric charge, gluons carry color charges and therefore, in addition to interacting with quarks, they can interact with each other. This property of the gluons implies that the interaction between quarks becomes weaker at shorter distances. This characteristic of color interactions is called "asymptotic freedom". Accordingly, the property of asymptotic freedom of QCD allows perturbation theory to be used in describing short distance ($\leq$1 fm) interactions.

In conclusion, the fundamental hadronic (i.e. strongly interacting) entities are six quarks, whose properties are listed in Table 1.1[9] and the gluons which are the mediators of the color interaction between quarks. In the quark model with color symmetries, each quark appear in three possible colors, while baryons and mesons appear as colorless states. In the framework of this theory, it is assumed that only colorless states are physically realized and hence quarks cannot be observed as isolated states.

Table 1.1: Summary of the characteristics of quarks.

Flavor	Q/e	mass (GeV/c^2)
u	2/3	$\simeq 4 \cdot 10^{-3}$
d	-1/3	$\simeq 7 \cdot 10^{-3}$
s	-1/3	$\simeq 0.2$
c	2/3	$\simeq 1.5$
b	-1/3	$\simeq 5$
t	2/3	?

The discovery of the J/ψ, right after the foundation of QCD, presented an ideal testing ground for the Lagrangian formulation of the quark model. In analogy with the electromagnetic interaction, the Born term for the quark-quark or quark-antiquark interaction is of the familiar Coulomb (1/r) form, at least at short distances. The gluon self-coupling results in a slow decrease of the effective coupling strength with decreasing distance. By calculating the first quantum correction to the color Coulomb potential[11], the strong interaction analog of the fine-structure constant $\alpha_s = g_s^2/4\pi$ can be parametrised as:

$$\alpha_s(Q^2) = \frac{12\pi}{(33 - 2n_f)ln(Q^2/\Lambda^2)} \tag{1.3}$$

Here Q is the four-momentum transferred between the incoming and outgoing particles during the interaction, n_f is the number of participating quark flavors (in general a quark i of mass m_i is expected to contribute to the interaction only when $Q^2 > 4m_i^2$), and Λ is a fundamental constant of QCD which must be determined experimentally (values reported from various experiments are of the order of 200 MeV[9]). Perturbation theory is applicable only for $Q^2 >> \Lambda$, for which $\alpha_s << 1$.

1.2 Charmonium spectrum

Charmonium states are flavorless mesons which are bound states of charm and anticharm quarks ($c\bar{c}$). The level diagram for the observed charmonium states is shown

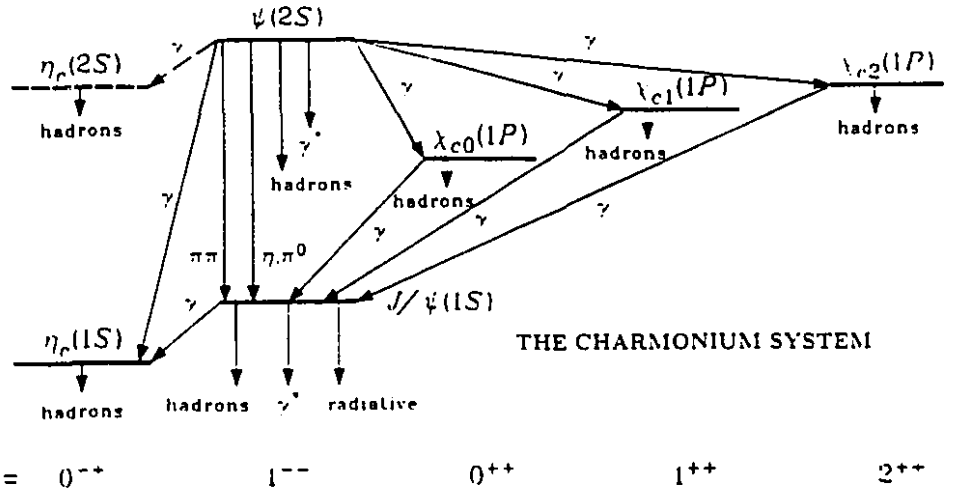

Figure 1.1: The current state of knowledge of the charmonium system and transitions as interpreted in the charmonium model

in Figure 1.1[9]. For each particle, the spectroscopic notation $^{2S+1}L_J$ is also listed. In a non-relativistic approximation, the total angular momentum of a quark-antiquark system is J=L+S with spin states S=0 (antisymmetric) and S=1 (symmetric). The parity and charge conjugation of the system are $P = (-1)^{L+1}$ and $C = (-1)^{L+S}$. Charmonium states above threshold for production of two charmed mesons (referred to as charm threshold, $2M_{D^0} = 3727$ MeV/c^2), decay strongly into the charmed mesons and therefore have large widths. One very interesting feature of the charmonium spectrum in Figure 1.1 is that the level spacings are very small compared to the overall mass scale of the system. Even before the J/ψ discovery, Appelquist and Politzer [12] suggested that, as a consequence of asymptotic freedom, a system of bound massive quarks could be described as a non-relativistic atomic system analogous to positronium (the bound state of e^+e^-). Since the charm quark is rather massive ($\simeq$ 1.5 GeV/c^2) and thus has small kinetic energy in a charmonium bound state, non-relativistic potential models are used to describe the bound states.

In this model, one can write the standard Schroedinger equation for the bound state:

$$-\frac{\hbar^2}{m_c}\nabla^2\Psi(\vec{r}) + V(\vec{r})\Psi(\vec{r}) = E\Psi(\vec{r}) \tag{1.4}$$

By solving this equation the energy levels, E_n, are obtained, and the bound state masses can be expressed as:

$$M_n(c\bar{c}) = 2m_c + E_n \tag{1.5}$$

Ignoring spin for the moment, central potential models may be divided into two categories. The first class consists of models which are directly motivated by QCD considerations. The second class is purely phenomenological.

For a pair of bound quarks in a color singlet state, the exchange of one gluon at short distances leads to a Coulomb-like interaction. For large distances ($\geq$ 1 Fermi), interactions are dominated by the confinement term which leads to potentials which rise with large inter-quark separation r. With these QCD premises, the "Cornell potential"[13] was proposed:

$$V(r) = -\frac{4\alpha_s}{3r} + kr \tag{1.6}$$

The two parameters of this model could be adjusted to predict the correct mass separation for the ψ' and J/ψ states.

Bhanot[14] improved upon the Cornell potential by interpolating logarithmically between the coulombic and the linear term; the potential can then be written as:

$$\begin{aligned} V(r) &= -\frac{4\alpha_s}{3r} \qquad R < R_1 \\ V(r) &= b\ln r/r_0 \qquad R_1 < r < R_2 \\ V(r) &= +ar \qquad R > R_2 \end{aligned} \tag{1.7}$$

Requiring V(r) to be continuous with continuous derivatives at R_1 and R_2, the six parameters reduce to two independent adjustable parameters.

In another approach, proposed by Richardson[15], the potential was written in momentum space using a minimal number of parameters. The Fourier transform of a $1/r$ potential at small r behaves as $1/Q^2$ for large momentum transfer Q while the linear

potential for large r behaves as $1/Q^4$ for small Q. An expression embodying both limits that reproduces the expected logarithmic variation of the strong coupling constant for large Q^2 is:

$$V(Q^2) = -\frac{16\pi}{(33 - 2N_f)Q^2 \ln(1 + Q^2/\Lambda^2)} \tag{1.8}$$

N_f is the number of flavors and Λ is the QCD cut-off parameter. The spin-independent features of quarkonium spectroscopy are well described by any of the above mentioned potentials.

An expansion of these models is needed to incorporate relativistic effects and spin dependences in the interquark interaction. McClary et al.[16] calculated the relativistic corrections mainly for the radiative decay $\psi' \rightarrow \chi\gamma$, where the non-relavistic model predicted twice the value of the experimentally determined width. When relativistic corrections were taken into account, the relativistic distortions of the 2S and 1P wave functions reduce the value of the predicted width. Although differences still remain among various relativistic treatments, the overall agreement is satisfactory. In the limit of vanishing spin-dependent forces, the P-wave states would be degenerate in mass. In order to calculate spin-orbit interactions (leading to fine structure, e.g. ^3P_J level spacings), spin-spin interactions (hyperfine structure: $^3S - ^1S$, $^3P - ^1P$ spacings) and tensor interactions, spin must be incorporated into the potential models. The spin-dependent potential can be written as the sum of the spin-spin, spin-orbit and tensor terms:

$$V_{spin}(r) = V_{SS} + V_{SO} + V_T \tag{1.9}$$

Many different parametrizations were proposed for the spin-dependent effects in quarkonium. A simple model based on a short-range vector interaction $V_V(r)$ and a long range scalar interaction $V_S(r)$ is compatible with present data[17]. The vector term is natural on the basis of single gluon exchange while an effective scalar term can arise from an exchange of many gluons. There is an encouraging agreement of the spectrum predicted by equation 1.9 spin interaction, with the ^3P_J measured masses, but more work is needed both experimentally and theoretically.

1.3 Hadroproduction mechanisms of Charmonium

Since the discovery of the J/ψ there has been a lot of theoretical work in the effort of understanding the production mechanisms of charmonium and, more generally, heavy-quark bound states. In the framework of QCD, the production of $c\bar{c}$ states can proceed through annihilation of quarks or gluon fusion.

The scattering of high energy, strongly interacting particles is described within the framework of the parton model, in terms of the lowest order subprocesses, which are two-body scatterings. In the parton model, hadrons are represented as a collection of free partons (i.e. pointlike constituents), each carrying a fraction x of the hadron momentum. Initial and final partons are assumed to be collinear with the corresponding initial and final hadrons, i.e. the transverse momenta of the partons are neglected. Within the parton model, the total inclusive cross-section for a hard scattering process between particles A and B giving rise to the quark q (regardless of any other reaction products X), can be written in the form:

$$\sigma(AB \to q + X) = \sum_{a,b} \int_0^1 d\tau \int_\tau^1 \frac{dx_a}{x_a} f_{a/A}(x_a, Q^2) f_{b/B}(\tau/x_a, Q^2)\ \hat{\sigma}(ab \to q + X) \quad (1.10)$$

where:

- the indices a, b run over all parton species: all quark and antiquark flavors and gluons.
- x_a is the fraction of the hadron momentum carried by parton a.
- $\tau = x_a \cdot x_b$, which, in a Lorentz frame where masses can be neglected compared to the three momenta, can be written as $\tau = \hat{s}/s$ where s is the center of mass energy for the A-B hadron system and $\hat{s}$ is the center of mass energy of the a-b parton system.
- $f_{a/A}(x_a), f_{b/B}(x_b)$ are the parton densities, or structure functions, for a, b in A, B and these represent the probability of finding parton a,b with a certain momentum fraction x_a, x_b in hadron A, B

- $\hat{\sigma}(ab \rightarrow q + X)$ is the elementary cross-section for the subprocess $a + b \rightarrow q + X$ averaged over initial parton colors and summed over final parton colors.

- Q^2 is the square of the momentum transfer between the incoming and outgoing partons.

The quark distribution functions for the proton have been measured in deep inelastic lepton-nucleon scattering experiments in processes such as $eA \rightarrow eX$, $\mu A \rightarrow \mu X$, $\nu_\mu A \rightarrow \mu^- X$, $\bar{\nu}_\mu A \rightarrow \mu^+ X$, with a large momentum transfer between the lepton and the nucleon. To obtain the gluon distribution, a more comprehensive set of data was needed since deep inelastic scattering is not very sensitive to gluon distributions. A representation in common use is the so called Duke and Owens set of distribution functions [18]. A global analysis of deep inelastic scattering, and J/ψ , Υ, and high-mass dilepton production was performed in order to determine a set of nucleon parton distributions. Both the proton and pion distribution functions have been measured experimentally in high energy collisions and it appears that, using different beam particles allows us to probe the relative importance of the different elementary processes (a recent review on structure functions can be found in reference [19]).

Historically, the J/ψ was the first charmonium state seen, as it was discovered simultaneously in e^+e^- and p-nucleus collisions. e^+e^- annhilation has been the classic channel for producing and studying heavy quarks, due to the superior signal to background ratio.

e^+e^- collisions can only produce $J^P = 1^-$ states directly, χ states are typically obtained through the $\psi(2S)$ radiative decays in e^+e^- machines. Hadron-hadron collisions, on the other side, can produce all charmonium states directly. There have been many experiments to study hadronic production of charmonium states, with the J/ψ being the most studied. It is now known that a good fraction of the J/ψ are not directly produced but are the decay products of higher mass charmonium states (χ, $\psi(2s)$ or ψ') and therefore the inclusive J/ψ production is not a good probe of $c\bar{c}$ hadroproduction. χ states are much better candidates: there is only one $c\bar{c}$ state (the ψ') with mass

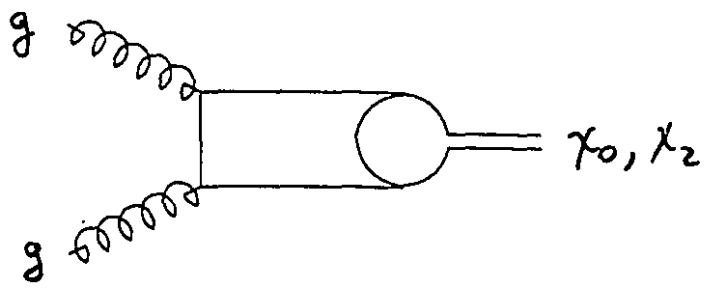

Figure 1.2: The two gluon fusion diagram

higher that the χ and less than $D\bar{D}$, and the ψ' has a fairly small decay width to $\chi's$. There are two main candidates for a successful description of the present hadroproduction data: the "color singlet" model and the "color evaporation" model. These models make predictions for for χ and J/ψ production as will be outlined in the next two sections.

1.3.1 Color singlet model

This model requires that the initial quark and antiquark or gluons form directly a bound state $c\bar{c}$ in a color singlet. At lowest order, $\mathcal{O}(\alpha_s^2)$, the only possible process involves the fusion of two gluons to form a C=+1 color singlet state, as shown in Figure 1.2.

The matrix element, describing the transition from the initial to the final state, is obtained by crossing symmetry, using the decay amplitude of charmonium decaying into two gluons. Due to Yang's theorem[21] a spin odd particle cannot decay into a symmetrical state of two massless spin-1 quanta, the transitions $gg \rightarrow \chi_1$, $gg \rightarrow \psi$ are forbidden. The two gluon fusion cross-section for χ_0 and χ_2 can be written in the form[20]:

$$\hat{\sigma}(gg \rightarrow {}^3P_j + X) = \frac{8\pi^2}{M_{\chi_j}^3}(2J+1)\Gamma({}^3P_j \rightarrow gg) \tag{1.11}$$

where M_{χ_j} is the mass of the χ state with spin J. $\Gamma(\chi_j \rightarrow gg)$ is the decay width for the elementary process $\chi_j \rightarrow gg$ and can be written as:

$$\Gamma(\chi_0 \rightarrow gg) = \frac{6\alpha_s^2}{M_{\chi_0}^4}\left|\frac{d\Phi(0)}{dr}\right|^2 \quad (1.12)$$

$$\Gamma(\chi_1 \rightarrow gg) = 0 \quad (1.13)$$

$$\Gamma(\chi_2 \rightarrow gg) = \frac{8\alpha_s^2}{5M_{\chi_2}^4}\left|\frac{d\Phi(0)}{dr}\right|^2 \quad (1.14)$$

where $\left|\frac{d\Phi(0)}{dr}\right|$ is the derivative of the charmonium radial wave function evaluated at the origin, to be calculated by solving the non-relativistic Schroedinger equation based on the potentials described in Section 1.2. There are some unavoidable uncertainties in the determination of the absolute cross-sections, with major contributions coming from the charmonium wave functions and the value of α_s, the QCD coupling constant. The uncertainty can be eliminated by looking at relative yields of the charmonium states. At lowest order, the two gluon fusion model predicts the following ratios for the χ cross-sections:

$$\sigma(\chi_0) : \sigma(\chi_1) : \sigma(\chi_2) = 3 : 0 : 4 \quad (1.15)$$

In the color singlet model the lowest order diagrams contributing to J/ψ and χ_1 production are of the order $\mathcal{O}(\alpha_s^3)$. At this order the charmonium states can be produced by quark-antiquark annihilation, quark(or antiquark)-gluon scattering, and gluon-gluon scattering and three gluon fusion. The corresponding diagrams are shown in Figure 1.3. The cross-sections for charmonium production for these processes have been calculated by several authors [22],[23]. The process $gg \rightarrow c\bar{c}g$ is thought to dominate J/ψ production at high p_t while the three gluon fusion process ($ggg \rightarrow c\bar{c}$) is thought to dominate at high x_F ($x_F = \frac{2P_L^*}{\sqrt{s}}$ where P_L^* is the longitudinal component in the center of mass frame of the particle momentum with respect to the beam direction and $\sqrt{s}$ is the available energy in the center of mass frame). These two processes have been studied in detail[23] in conjunction with the nuclear dependance of the J/ψ cross-section. The quark (or antiquark) gluon scattering process can only contribute to the χ but not to J/ψ production. The processes q-g and g-g scattering at order $\mathcal{O}(\alpha_s^3)$ present some

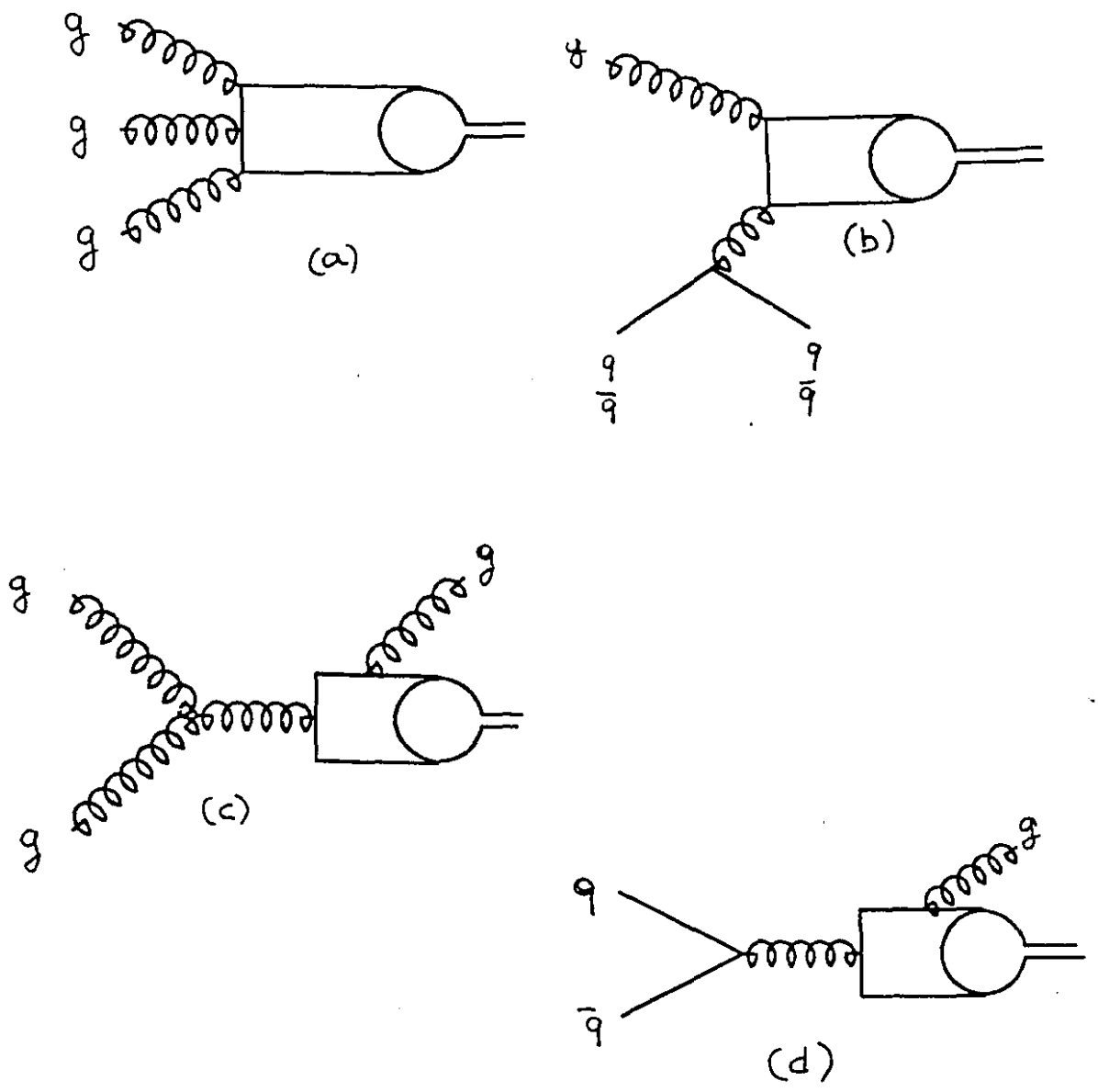

Figure 1.3: The color singlet diagrams at order $O(\alpha_s^3)$: a) three gluon fusion , b) quark-gluon scattering, c) gluon-gluon scattering, d) quark-antiquark annihilation

calculational difficulties due to infrared divergencies. In principle, when the $c\bar{c}$ pair has a small transverse momentum, it is possible to consider the gluon as part of the incident hadron and consequently factorize out the divergencies of these processes into the distribution function of the gluon involved in the $\mathcal{O}(\alpha_s^2)$ process. A simple procedure was used[22]: a cut-off was imposed on the divergent p_T distributions at $p_T \sim 2$ GeV/c. The cross-section for the $q\bar{q} \rightarrow \chi g$ process was found[22] to be at least one order of magnitude smaller than the other $\mathcal{O}(\alpha_s^3)$ processes. The absolute normalizations of these diagrams are uncertain and usually the predictions are fit to the shape of the observed $\frac{d\sigma}{dp_T}$ distribution. The J/ψ p_T distributions predicted by this model for high p_T are in agreement with the data. Numerically, a large effective QCD scale, $\Lambda \sim 500$ MeV, is necessary to explain the observed J/ψ yields, in particular at high p_T. In this model, 35% of J/ψ production is attributed to the direct production through the $g-g \rightarrow \psi-g$ process and the remainder to χ states radiative decays. The relative contribution of the different diagrams to χ production is unknown and no predictions are available for χ production at order $\mathcal{O}(\alpha_s^3)$.

1.3.2 Color evaporation model

This model assumes that, in the hard collision between partons, an unbound $c\bar{c}$ pair is produced which materializes into the physical meson by radiating one or more soft gluon. The diagrams for the lowest order processes are shown in Figure 1.4.

The states that remain after color evaporation can be charmonium states or pairs of charmed mesons when M($c\bar{c}$) is above charm threshold. According to the semilocal duality hypothesis[24], the production of $c\bar{c}$ bound states is approximately given by the free $c\bar{c}$ cross-section integrated from $m = 2m_c$ to $m = 2m_D$. The cross-section for a bound $c\bar{c}$ state O can be written in the form:

$$\sigma(AB \rightarrow O + X) = \int_{4m_c^2}^{4M_D^2} dm^2 \frac{d\sigma}{dm^2}(AB \rightarrow c\bar{c} + X) \qquad (1.16)$$

where m_c is the unbound charm quark mass, M_D is the mass of the lightest charmed meson and $\frac{d\sigma}{dm^2}$ is the cross section for free $c\bar{c}$ production. The left hand side represents

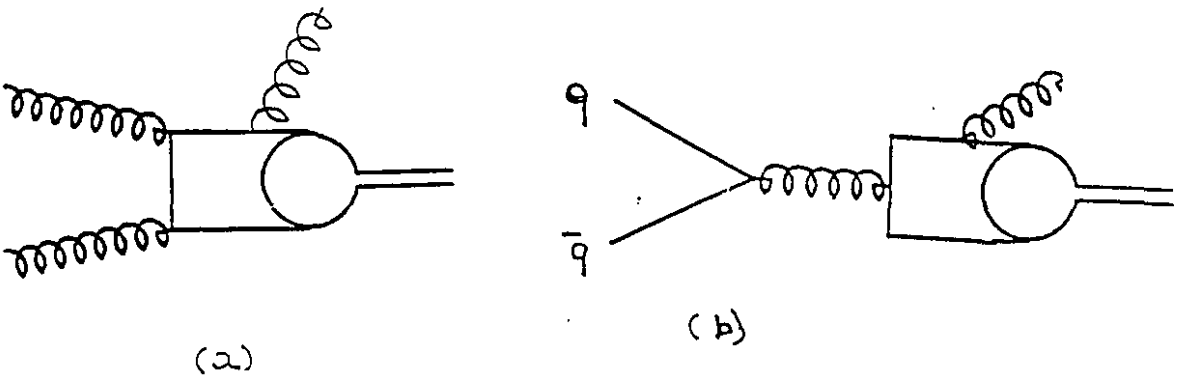

Figure 1.4: The color evaporation diagrams at lowest order: a) two gluon fusion, b) quark-antiquark annihilation

a sum over all resonant states. The model does not make any prediction for the relative production of charmonium states; a common assumption [25] is that the χ cross-sections are proportional to the spin factors (2J+1):

$$\sigma(\chi_0) : \sigma(\chi_1) : \sigma(\chi_2) = 1 : 3 : 5 \tag{1.17}$$

This model also implies that all the states are observed in the same proportion over the entire range of x_F and p_T.

Another model which has been proposed involves both constituent annihilation into bound states and into the $c\bar{c}$ continuum[26]. The cross-section is assumed to be the sum of a color singlet production mechanism (as presented in the previous section) and a color non-singlet mechanism producing a free $c\bar{c}$ which materialize into physical bound state by emitting a gluon. The cross-section for producing heavy quark bound states of mass M_i, by the nonsinglet mechanism, was calculated by multiplying the cross-section for producing a free $c\bar{c}$ state by R_1/R_2, where R_1 is the rate of producing charmonium from a free $c\bar{c}$ pair by emitting a gluon and R_2 is the rate of capture of a light quark by the heavy quark to form a charmed meson. So far the calculation has been done only for protons, for which the gluon contribution is dominant:

$$\sigma(pp \rightarrow M_i + ...) = \int d\tau F_{gg}(\tau)\sigma(gg \rightarrow c\bar{c}, M_i)\frac{R_1^{M_i}}{R_2^{M_i}} \tag{1.18}$$

where:

- $F_{gg}(\tau)$ is the excitation function which gives the probability for the colliding gluons to have enough energy to produce the desired particle:

$$F_{gg}(\tau) = \tau \int_{\tau}^{1} f(x) f(\tau/s) dx/x \tag{1.19}$$

- $f(x)$ is the gluon density, representing the probability of finding a gluon with a certain momentum fraction x in the proton.

- x is the fraction of the hadron momentum carried by the gluon.

- $\tau = \hat{s}/s$ where s is the center of mass energy for the A-B hadron system and $\hat{s}$ is the center of mass energy for the two gluon system.

- $\sigma(gg \rightarrow c\bar{c}, M_i)$ is the cross section for producing a free $c\bar{c}$ pair as calculated using the lowest order QCD.

Comparing color singlet production with the new mechanisms, the latter is found to be dominant. The values of the absolute χ cross-sections at our energies are not available as of this time, but the ratio of χ_1/χ_2 cross sections due to non color singlet production are assumed to follow the spin statistical weights as shown in Equation 1.17.

It is also possible to get information about charmonium production mechanisms by studying angular correlation function for the various decay products[27]. More specifically, in the case of the χ production, there are predictions for the decay $\chi \rightarrow \psi\gamma$ followed by the decay $\psi \rightarrow \mu^+\mu^-$. The angular distribution of the photon and the μ^+ can be written as:

$$I = \sum_{\lambda,\lambda'=0,\pm 1} W_{\lambda\lambda'}(\theta,\phi) V_{\lambda,\lambda'}(\theta^*\phi^*) \tag{1.20}$$

where:

- θ and ϕ are the polar and azimuthal angles of the J/ψ measured in the rest frame of the χ (x,y,z), where the xz plane is spanned by the initial hadrons (beam+target).

- θ^* and ϕ^* are the polar and azimuthal angles of the μ^+ measured in the rest frame of the ψ (x'y'z'), where the z' axis is chosen opposite to the photon momentum direction.

It was assumed that χ states are produced by gluon fusion or quark annihilation and that the average tranverse momenta of the partons is negligible. The form of the angular distributions, V and W, depends on the spin, J, of the χ meson and also on whether the production mechanisms was quark annihilation or gluon fusion. Therefore, by looking at the angular distributions, it may be possible to extract the relative contributions of gluon and quark fusion subprocesses.

As a conclusion from this theoretical review, it appears that a coherent model, to be confronted with all the charmonium hadroproduction data available presently or in the near future, doesn't exist. Charmonium hadroproduction holds the potential for providing a useful tool for a deeper understanding of the subnuclear world. Nevertheless it doesn't seem that much theoretical work, exploiting the advances in the formulation of QCD, has been done on the topics in the past few years.

1.4 Existing experimental results

The χ states are usually detected through their radiative decay into $J/\psi\ \gamma$. The branching fractions for these decays are [9]:

$$BR(\chi_0 \rightarrow \psi\gamma) = (0.66 \pm 0.18)\%$$
$$BR(\chi_1 \rightarrow \psi\gamma) = (27.3 \pm 1.6)\%$$
$$BR(\chi_2 \rightarrow \psi\gamma) = (13.5 \pm 1.1)\%$$

Therefore, given that the χ_0 branching fraction is about 30 times smaller than those of χ_1 and χ_2, χ_0 production is less often observed. The χ masses have been very accurately determined and the present world average values [9] are:

$$M(\chi_0) = (3415.1 \pm 1.0)\ \mathrm{Mev/c^2}$$

$$M(\chi_1) = (3510.6 \pm 0.5)\ \mathrm{Mev/c^2}$$

$$M(\chi_2) = (3556.3 \pm 0.4)\ \mathrm{Mev/c^2}$$

The study of charmonium states hadroproduction presents great experimental difficulties. In fact, given that the cross-section for these processes are fairly small, it is desirable to use a high luminosity beam and, to maximize the percentage of produced events which are in the geometrical acceptance of the apparatus and therefore can be reconstructed, it is necessary to use an apparatus with large solid-angle coverage. Therefore a spectrometer with large aperture and capable to sustain high interaction rates is needed. Moreover, for the χ production it is necessary to distinguish two states with very similar masses, since the χ_1/χ_2 mass difference is only 45 MeV/c^2. This implies that both the energy and the position of the photons have to be determined with great accuracy, and this in a regime of high flux and over a fairly wide range of photon energies. As a consequence, as it will be seen in the remainder of this chapter, where the previous χ hadroproduction experiments are described, the overall amount of experimental information available on the χ production is rather limited.

1.4.1 Experiments at Fermilab

Experiment E369

Experiment E369 was performed at Fermilab by a collaboration of physicists from Fermilab, Harvard University, University of Illinois, University of Oxford and Tufts University. χ production[28] was observed using a 217 GeV/c π^- beam incident on beryllium and liquid hydrogen targets. The Chicago Cyclotron Magnet Spectrometer, shown in Figure 1.5, was used to detect and identify the particles associated with dimuon production. The trigger required two penetrating particles in diagonally opposite quadrants of a scintillation counter hodoscope located downstream of a steel hadron absorber. The photons were detected using a lead glass array of 76 elements (each 6.35x6.35x61 cm). The dimuon mass spectrum is shown in Figure 1.6a; a peak of 160 J/ψ events was observed above background. Combining the reconstructed photons with

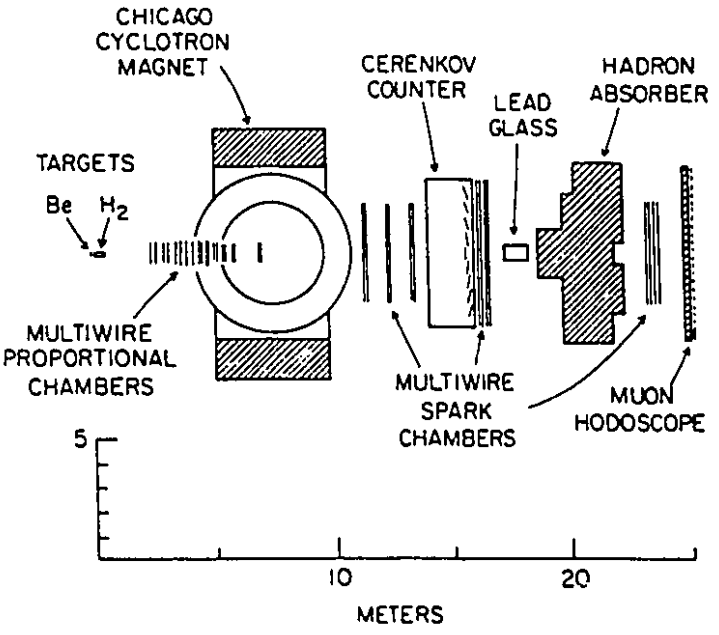

Figure 1.5: The E369 spectrometer

the J/ψ candidates, the invariant mass spectrum shown in Figure 1.6b was obtained. A 2.6 standard deviation excess above background at ~3.5GeV/c^2, was observed. Fitting the invariant mass distribution with a gaussian plus a background shape, the excess was found to be 17.2 ± 6.6 events. Attributing the excess to the process $\chi \rightarrow \psi\gamma$ and correcting for acceptance and reconstruction efficiencies, the fraction of J/ψ coming from χ radiative decays was found to be:

$$R = \frac{\sum_j \sigma(\chi_j) \cdot \mathrm{BR}(\chi_j \rightarrow \psi\gamma)}{\sigma(\psi)} = 0.70 \pm 0.28 \qquad (1.21)$$

This early result seemed to confirm some of the theoretical expectations that a large fraction of the J/ψ hadronic cross-section was in fact the result of χ production and decay.

Experiment E610

Experiment E610 was the follow-up experiment to E369. χ production[29] was observed using a 225 GeV/c π^- beam incident on beryllium target. It was performed at Fermilab using the Chicago Cyclotron Magnet Spectrometer (shown in Figure 1.5),

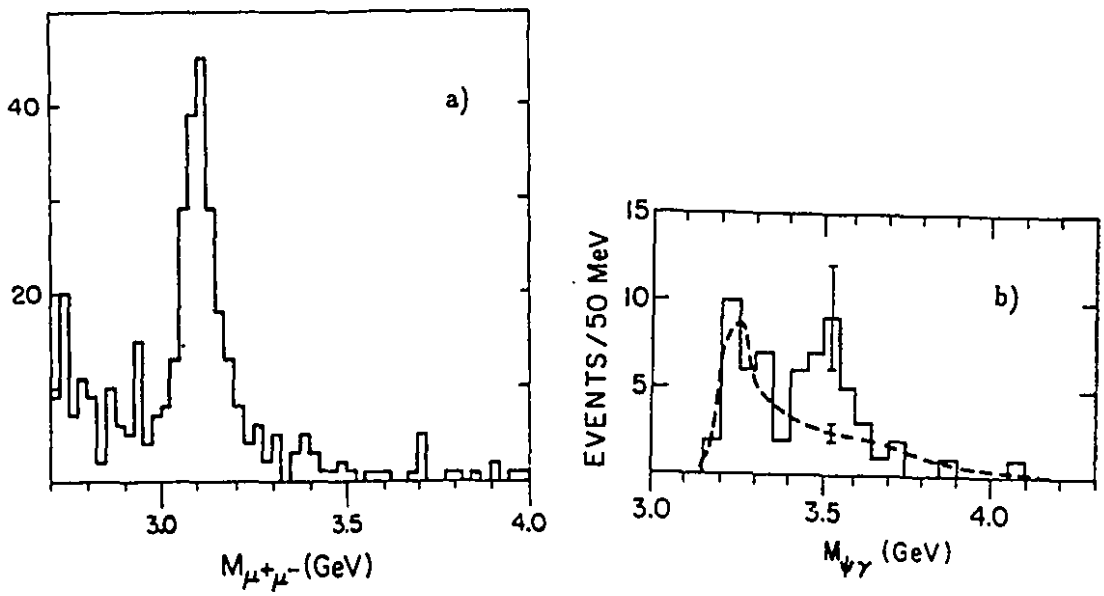

Figure 1.6: Results of E369: a) the $\mu^+\mu^-$ invariant mass spectrum, b) the J/ψ -γ invariant mass spectrum

with two major modifications: the spark chambers were replaced by drift chambers and the photon calorimeter was completely redesigned and enlarged. The photon detector consisted of a tranverse and a longitudinal array of lead blocks and, in-between them, a proportional tube array used to measure the shower position, as shown in Figure 1.7. The dimuon mass spectrum is shown in Figure 1.8a. A gaussian fit to the peak with an exponential background gave 1056 ± 36 J/ψ events above background. Photons in the energy range 5-30 GeV were combined with the J/ψ candidates, to obtain the invariant mass spectrum shown in Figure 1.8b. The number of χ events above background was found to be 80 ± 15. Correcting for photon reconstruction efficiency, the fraction of J/ψ 's produced via χ radiative decays was found to be:

$$R = 0.37 \pm 0.09 \tag{1.22}$$

The background-subtracted signal was fit using two gaussians centered at $\chi(3510)$ and $\chi(3555)$. Correcting for acceptances and branching ratios, the ratio of χ production

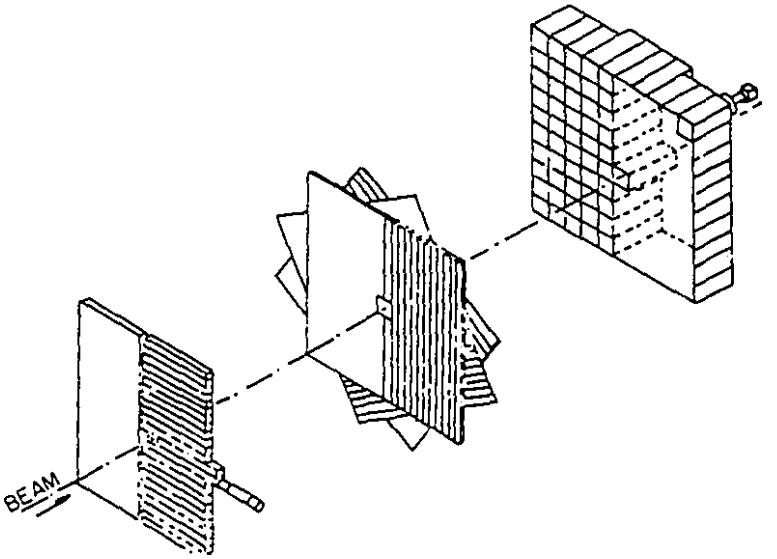

Figure 1.7: The E610 photon detector

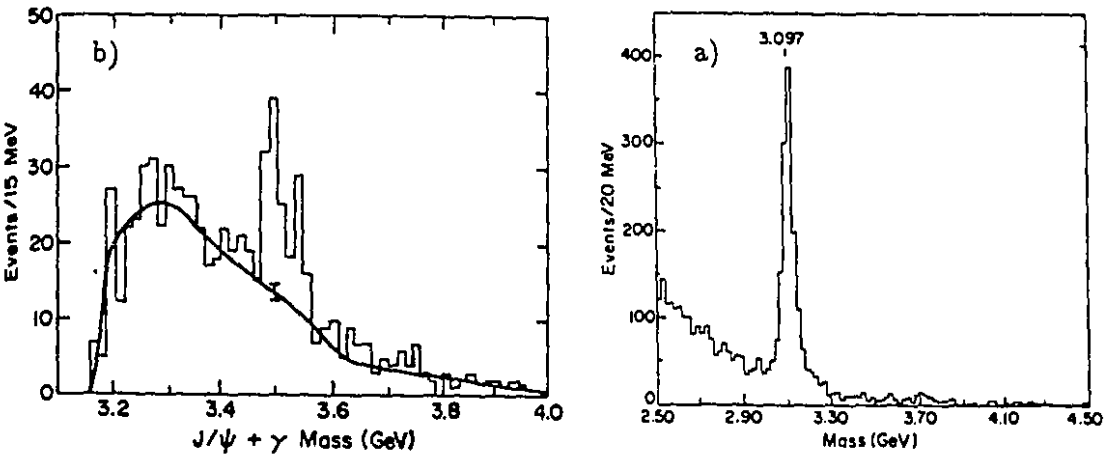

Figure 1.8: Results of E610: a) the $\mu^+\mu^-$ invariant mass spectrum b) the J/ψ -γ invariant mass spectrum

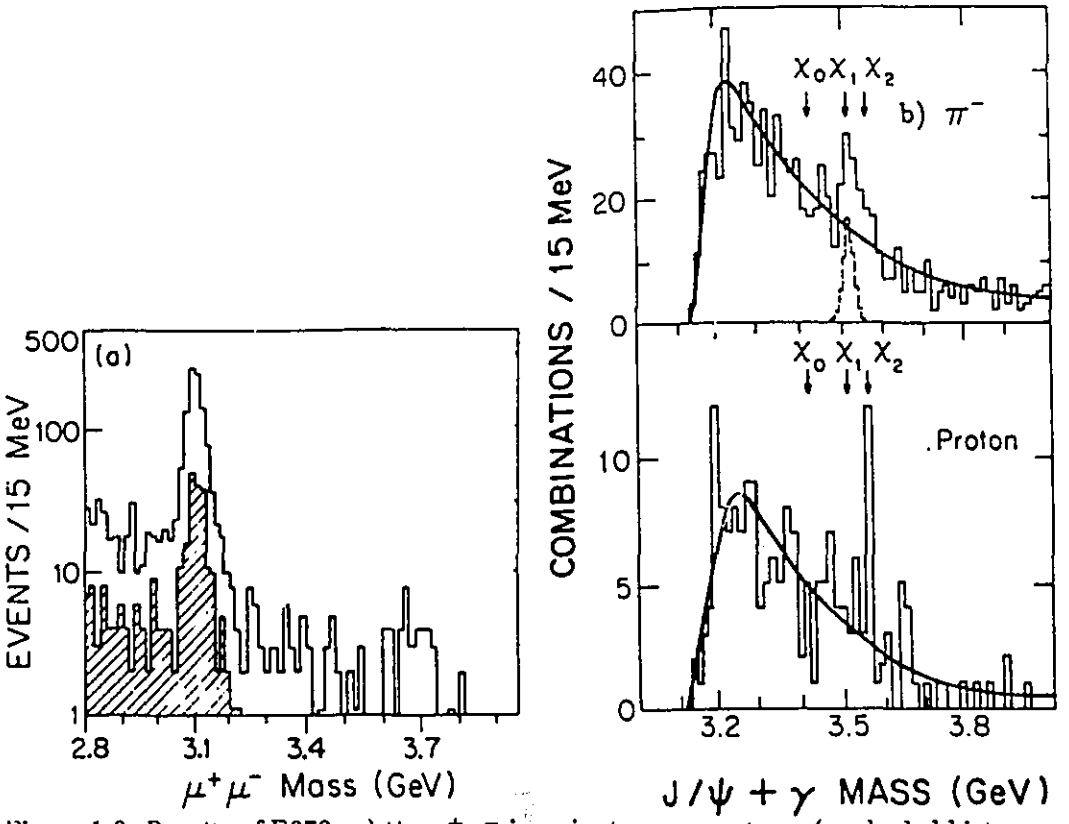

Figure 1.9: Results of E673: a) the $\mu^+\mu^-$ invariant mass spectrum (unshaded histogram is from π^- data, shaded histogram is from proton data), b) the J/ψ -γ invariant mass spectra

cross-sections was found to be:

$$\frac{\sigma(\chi(3555))}{\sigma(\chi(3510))} = 0.9 \pm 0.4 \tag{1.23}$$

Experiment E673

Experiment E673 studied χ production using a 190 GeV/c π^- beam and proton beams of 200 and 250 GeV/c[30]. It was the first attempt to compare charmonium production using both pion and proton beams in the same experiment. The experiment was actually a continuation of E610 and used the Chicago Cyclotron magnet spectrometer in the same configuration. Three Cherenkov detectors in the beam line were used to identify the beam particle type. The dimuon invariant mass spectra obtained for π^- and proton beams are shown in Figure 1.9a. Gaussian fits with polynomial backgrounds yielded 157 ± 17 J/ψ events for the proton beam and 908 ± 41 J/ψ events

for the π^- beam. Combining the J/ψ candidates with photons reconstructed in the electromagnetic calorimeter, the mass spectra shown in Figure 1.9b were obtained. A constrained two-gaussian fit to the background-subtracted plots was done to determine the number of reconstructed χ's. The fraction of J/ψ 's produced through χ radiative decays was found to be:

$$R = 0.31 \pm 0.10 \qquad \text{for pions} \qquad (1.24)$$

$$R = 0.47 \pm 0.23 \qquad \text{for protons} \qquad (1.25)$$

Correcting the number of observed χ_1 and χ_2 events for acceptance, reconstruction efficiencies and branching ratios, the ratios of the χ production cross-sections were found to be:

$$\frac{\sigma(\chi_1)}{\sigma(\chi_2)} = 0.96 \pm 0.64 \qquad \text{for pions} \qquad (1.26)$$

$$\frac{\sigma(\chi_1)}{\sigma(\chi_2)} = 0.24 \pm 0.28 \qquad \text{for protons} \qquad (1.27)$$

Using in addition the known J/ψ cross-section (from experiment NA3 [31], extrapolated to E673 energies), the χ cross-sections for $x_F > 0$ were determined to be:

$$\sigma(\chi(3510)) = 65 \pm 28 \text{ nb} \qquad \text{for pions} \qquad (1.28)$$

$$\sigma(\chi(3555)) = 67 \pm 34 \text{ nb} \qquad \text{for pions} \qquad (1.29)$$

$$\sigma(\chi(3555)) = 134 \pm 68 \text{ nb} \qquad \text{for protons} \qquad (1.30)$$

The apparent dominance of the χ_2 in the proton beam led the authors to suggest that simple gluon fusion in the singlet model, dominated by the two-gluon χ_2 production, could account for the bulk of the χ production in proton interactions. This is to be contrasted with the π^- beam data, where the results indicated that a mixture of all the possible mechanisms was responsible for χ production. The very low statistics of the proton induced χ signal (Figure1.9b) should however be noted.

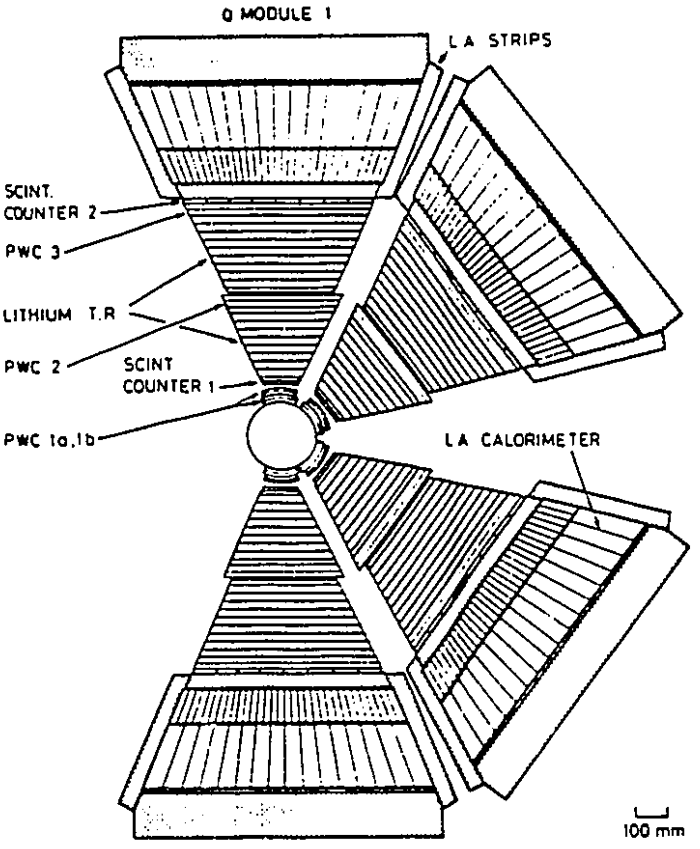

Figure 1.10: The R806 apparatus

1.4.2 Experiments at CERN

Experiment R806

χ production was studied at the CERN Interacting Storage Rings in proton-proton collisions at $\sqrt{s} = 62\ GeV$[32]. The apparatus consisted of four modules, each covering a solid angle of 1 sr. 50° to 130° in polar angle and 40° in azimuth, as shown in Figure 1.10. The J/ψ was observed through its decay into electron-positron pairs. The energies of the two electrons were measured by segmented lead-liquid argon calorimeter, which also helped reject the hadronic background. The invariant mass distribution for electron-positron pairs is shown in Figure 1.11a. Seven hundred forty eight (748) J/ψ candidates were selected based on the requirement $2.67 \leq M_{e^+e^-} \leq 3.52 GeV/c^2$. The estimated background in this sample is 129. Of these 748 events, 205 J/ψ candidates had at least one reconstructed photon. These photons were combined with the J/ψ 's after constraining the e^+e^- pair to be 3.1 GeV/c^2 and the resulting

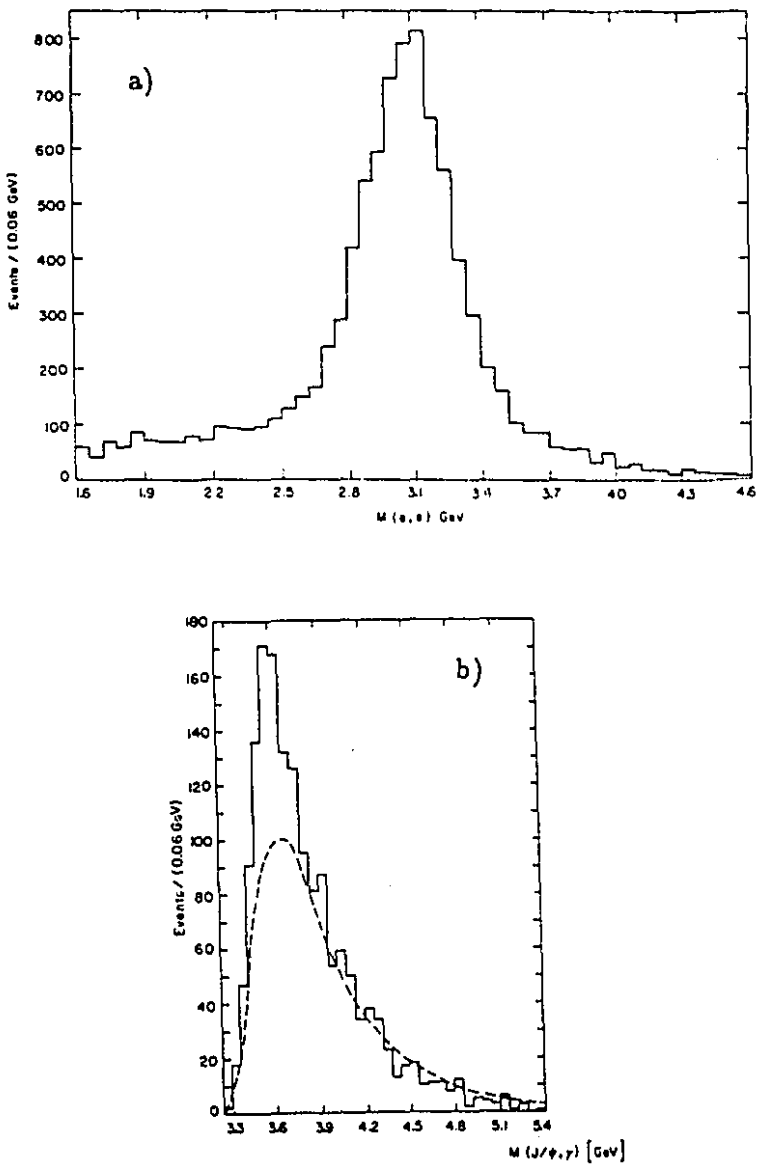

Figure 1.11: R806 results: a) electron-positron invariant mass distribution b) J/ψ -γ invariant mass distribution

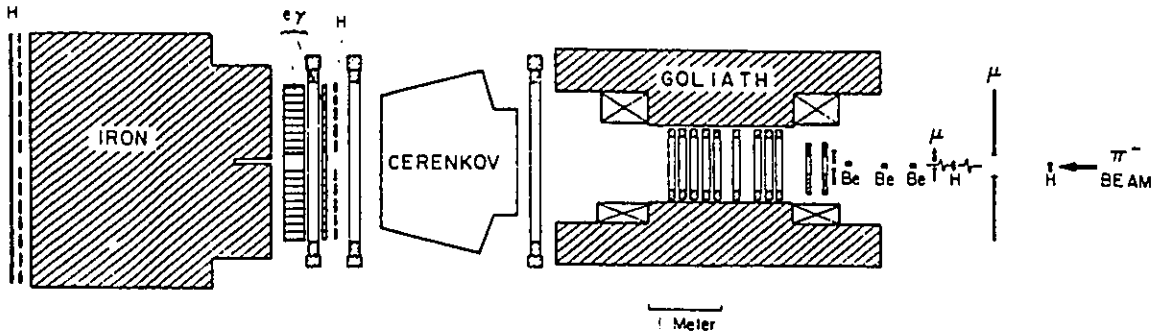

Figure 1.12: The WA11 experimental layout

invariant mass distribution is shown Figure 1.11b. After the corrections, the fraction of J/ψ 's coming from χ radiative decays was found to be:

$$R = 0.47 \pm 0.08 \tag{1.31}$$

It should be observed however that this result is extremely sensitive to the evaluation of the background, given that the signal and the background both peak at the same mass, and therefore a small change in the evaluation of the background could significantly affect the estimate of the signal.

Experiment WA11

χ production was studied at the CERN Super Proton Synchotron (SPS) in π^--Beryllium interactions at 185 GeV/c[33]. The experimental setup is shown in Figure 1.12. The trigger selected events with two muons in diagonally opposite quadrant of the hodoscopes. The data sample consisted of 50,037 dimuons in the mass range 2.95 to 3.25 GeV/c^2, containing 44,750 J/ψ 's. Photons were detected by their conversion into e^+e^- pairs. The e^+ and e^- momenta were reconstructed by the charged particle tracking system. An e^+e^- pair was labeled a photon candidate if the invariant mass, $M_{e^+e^-}$, was less than 25 MeV/c^2. The J/ψ -γ invariant mass spectrum is shown in Figure 1.13. Clearly this technique allows the resolution of the χ_1 and χ_2 peaks. The

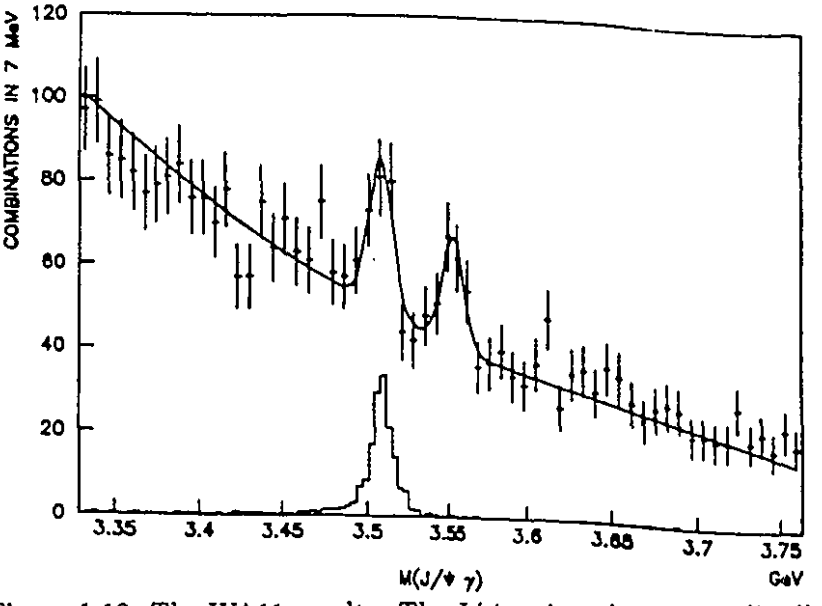

Figure 1.13: The WA11 results: The J/ψ -γ invariant mass distribution

price paid for excellent mass resolution is low detection efficiency; nevertheless this experiment was able to determine the percentage of J/ψ 's separately coming from χ_1 and χ_2 radiative decays:

$$R_1 = \frac{\sigma(\chi_1) \cdot \mathrm{BR}(\chi_1 \rightarrow \psi\gamma)}{\sigma(\psi)} = 0.177 \pm 0.035 \pm 0.015 \tag{1.32}$$

$$R_2 = \frac{\sigma(\chi_2) \cdot \mathrm{BR}(\chi_2 \rightarrow \psi\gamma)}{\sigma(\psi)} = 0.128 \pm 0.023 \pm 0.015 \tag{1.33}$$

Using a total J/ψ cross-section of 116 nb[33], the cross-sections for χ_1 and χ_2 production by π^-'s were found to be:

$$\sigma(\chi_1) = 65 \pm 19 \text{ nb} \tag{1.34}$$

$$\sigma(\chi_2) = 96 \pm 29 \text{ nb} \tag{1.35}$$

The ratio of χ_1 to χ_2 cross-sections led the authors to conclude that neither the quark-antiquark fusion, nor the gluon-gluon fusion model could alone explain the data, while the color evaporation was compatable with the experimental results.

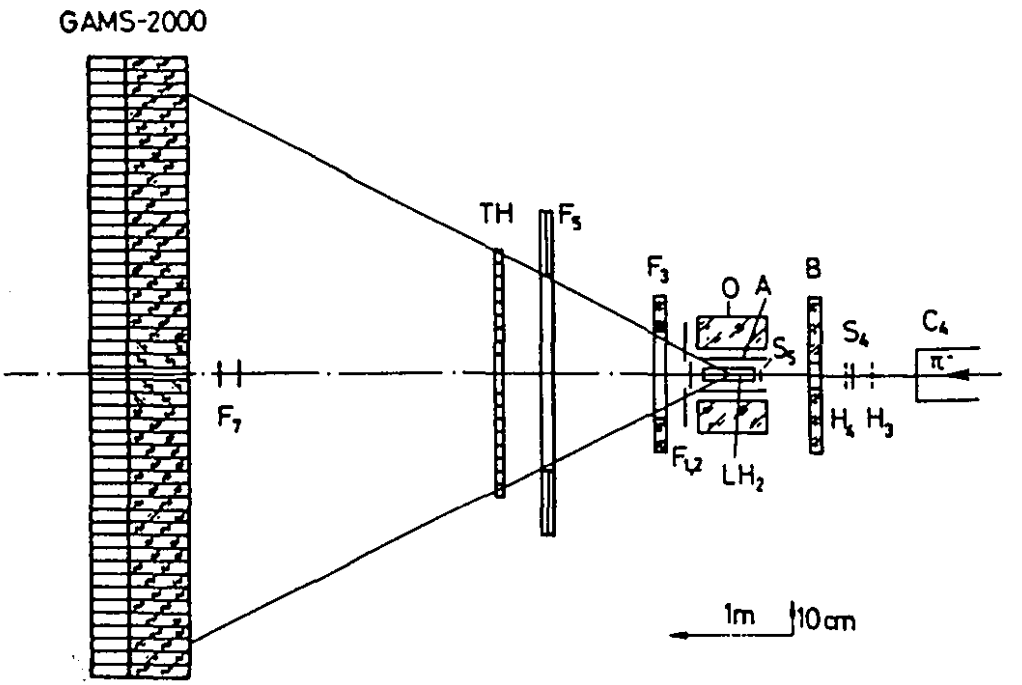

Figure 1.14: The GAMS2000 experimental layout

1.4.3 Experiments at Serpukov

Experiment GAMS2000

χ production was studied near threshold in the reaction $\pi^- p \rightarrow \chi + ...$ at the 70 GeV IHEP proton synchotron[34]. A π^- beam of 38 GeV/c was transported onto a liquid hydrogen target. The experimental layout is shown in Figure 1.14. J/ψ particles were identified by their decay into electron-positron pairs. The electrons and photons were reconstructed using GAMS2000, a hodoscope spectrometer and a lead glass matrix of 48x32 lead-glass counters. The e^+e^- invariant mass distribution is shown in Figure 1.15a. It shows a peak corresponding to J/ψ production with 40 J/ψ candidates in the mass range $2.8 \leq M_{e^+e^-} \leq 3.4$ GeV/c^2. Combining those events with the reconstructed photons, the mass spectrum of Figure 1.15b was obtained. It shows a peak containing 10 events in the mass region $M_{J/\psi-\gamma} \sim 3.5$ GeV/c^2.

After the appropriate corrections, the fraction of J/ψ 's coming from χ radiative

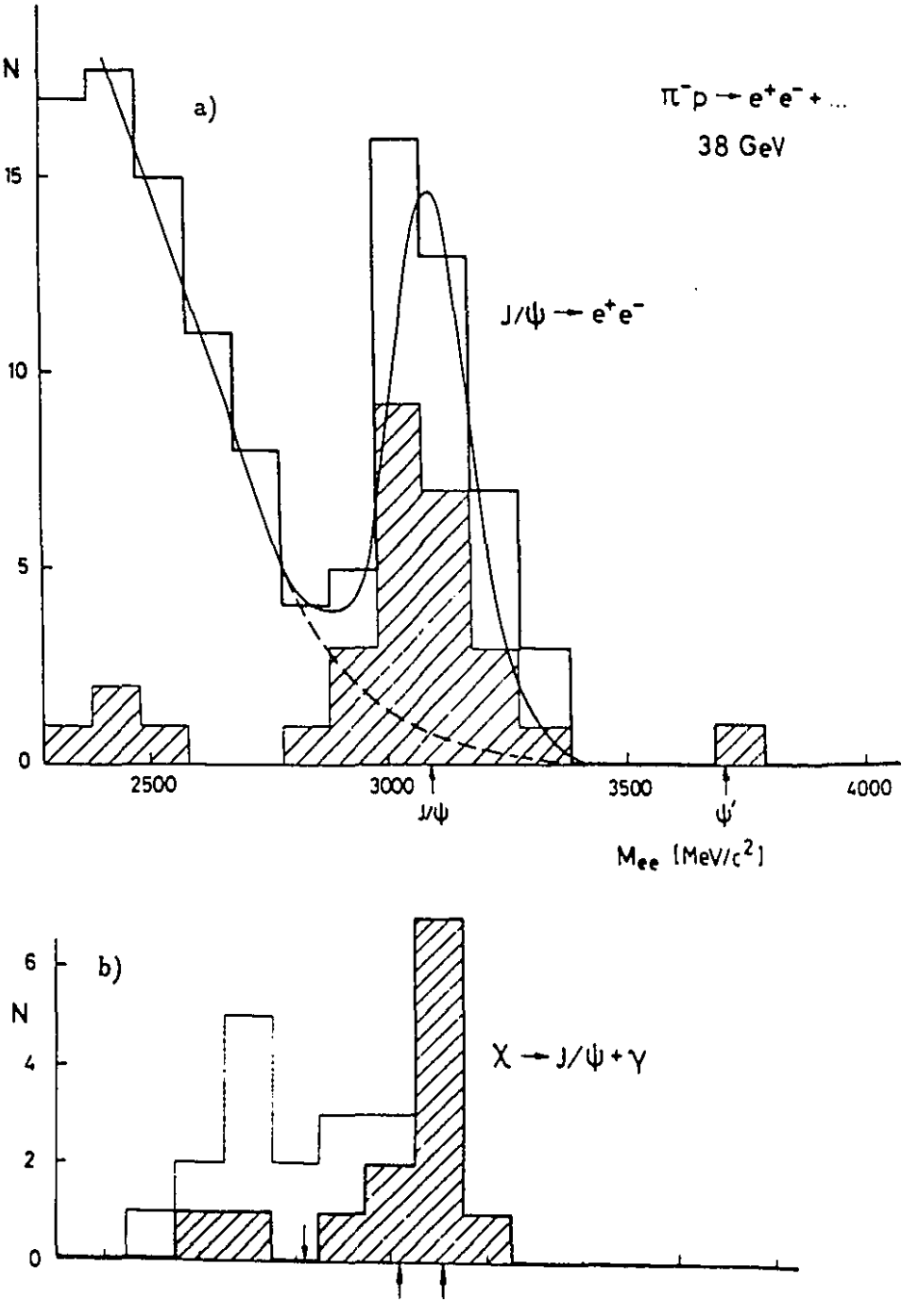

Figure 1.15: The GAMS2000 results: a) e^+e^- invariant mass spectrum, b) J/ψ -γ invariant mass distribution (shaded histograms correspond to a set of different requirements used in the event selection).

decays was found to be:

$$R = 0.44 \pm 0.16 \tag{1.36}$$

Using the χ_1/χ_2 ratio measured by WA11 with π^- beam and the probability of the decays the cross section was evaluated:

$$\sigma_{x_F>0}(\pi^- p \rightarrow \chi + ...) = 28 \pm 11\text{nb} \tag{1.37}$$

As a conclusion of this experimental review, it appears that, although many experiments have been performed in the attempt to accurately measure χ production and relative χ_1 to χ_2 yields, not much experimental data is available. The χ production induced by pion beam was measured by WA11 with good accuracy but rather statistically limited sample. Basically no measurement is available for χ production by protons, especially with respect to the χ_1 to χ_2 relative yields.

Chapter 2

Experimental setup

2.1 Overall layout

The Fermilab experiment E705 was performed by a collaboration of physicists from University of Arizona, University of Athens, Duke University, Fermilab, Florida A&M University, McGill University, Northwestern University, Prairie View A&M University, Shandong University, University of South Alabama, and University of Virginia. The first physics run of E705 was conducted in the Proton West beam line from July 1987 through February 1988.

The experiment layout is shown in Figure 2.1. The origin of the coordinate system is placed in the midpoint of the analysis magnet. The positive z-axis is directed downstream along the direction of the beam, the positive x-axis points in the horizontal direction to the left, looking downstream along the beam, and the positive y-axis points upward.

The experiment studied dimuon and direct photon production in interactions of positive and negative 300 GeV/c pions and protons incident on a natural lithium target. Two threshold Cerenkov counters were used to identify the beam particle type. A set of 19 Proportional Wire Chamber planes and 28 Multiwire Drift Chamber planes was employed, together with a dipole analysis magnet, to reconstruct the charged particles produced in the interaction. The electromagnetic calorimeter was used to determine the energy and position of photons, electrons, and positrons. The muon hodoscope, consisting of four planes of scintillation counters located behind blocks of steel and concrete, was employed in the identification of muons and in the definition of the

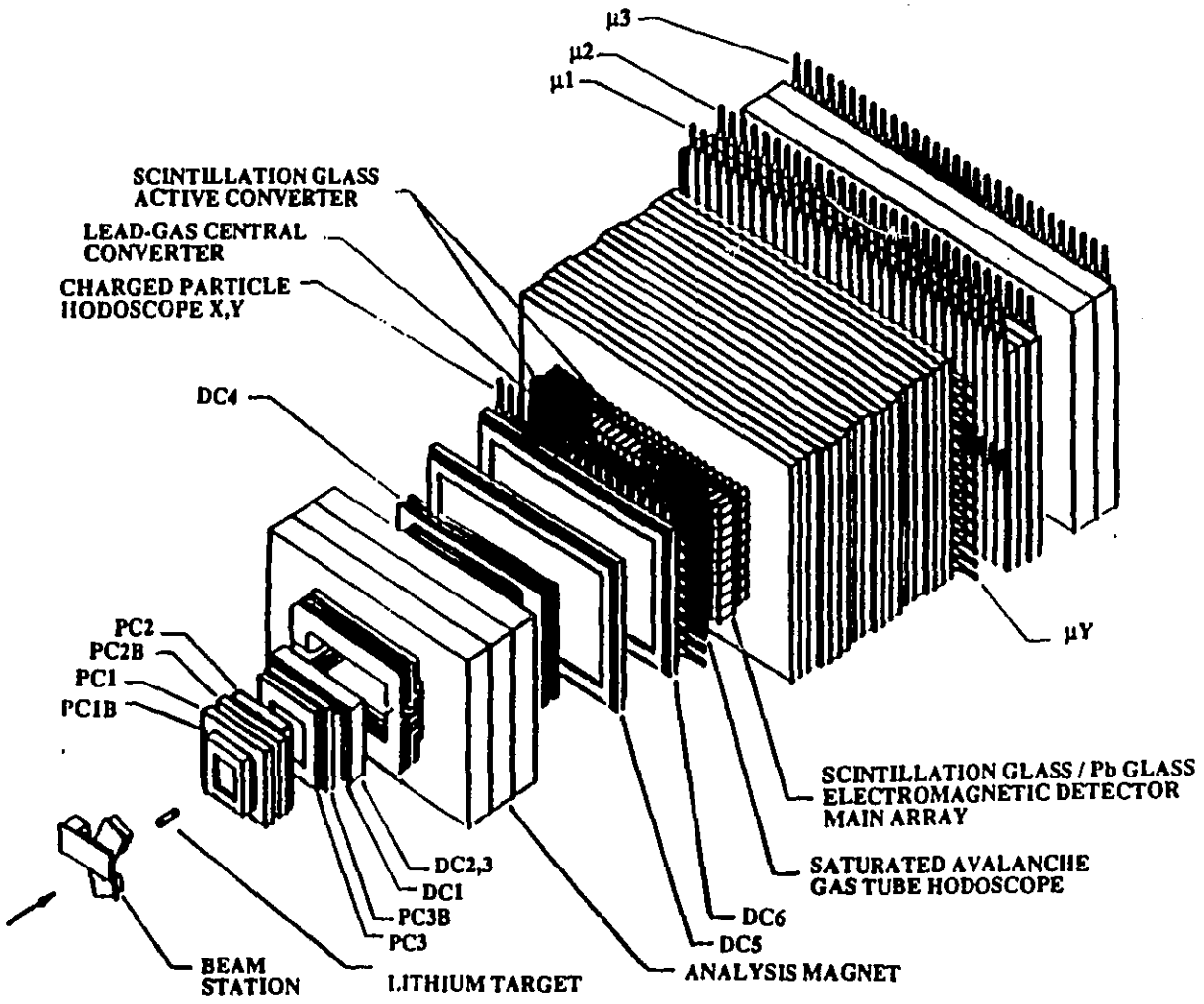

Figure 2.1: The E705 spectrometer layout

dimuon trigger.

2.2 Beam detectors

2.2.1 The Beam line

The Fermilab Accelerator produced 800 GeV/c proton beam which was then extracted for 23 seconds out of 57 seconds and split to three major experimental areas: neutrino, meson and proton. Each of these beam lines had further splits to enable several experiments to run simultaneously. In the Proton West beam line, in Figure 2.2, a fraction of the primary proton beam of average intensity 1.5×10^{12} particles per spill, impacted a *Be* production target to produce secondary particles which were collected through the aperture of the dipole magnet PW6W2.

The beam line was designed to operate in two different modes to deliver positive and negative secondary beams. In the secondary or "charged" mode the primary beam hit the *Be* target at an angle and the PW6W2 magnet was used to select the negative (or positive, depending on the desired beam charge) tracks while diverting to a dump the positively (or negatively) charged tracks. By the combination of the dipole magnets and a collimator, referred to as "momentum slit", a fairly monochromatic 300 GeV/c beam was achieved ($\Delta p/p < 5\%$). In the tertiary or "neutral" mode, the production beam hit the target at zero angle and the PW6W2 magnet was used to sweep away most charged tracks, letting through only neutral tracks. The final beam, consisting of $\bar{p}$ and π^- were produced by the decays $\bar{\Lambda} \rightarrow \bar{p}\pi^+$ and $\bar{K^0} \rightarrow \pi^-\pi^+$. When this second method was used to extract negative particles, the beam had lower yields than the "charged" one, but it presented the advantage of higher percentage of $\bar{p}$ (8% instead than 1.5%).

Another type of beam generated was an electron beam for the purpose of calibrating the electromagnetic detector. The neutral mode was used and a lead plate, EMAKER, was inserted in the neutral beam line to convert photons to electron-positron pairs. By using PW6W3 and the Momentum Slit, the momentum of the beam could be selected.

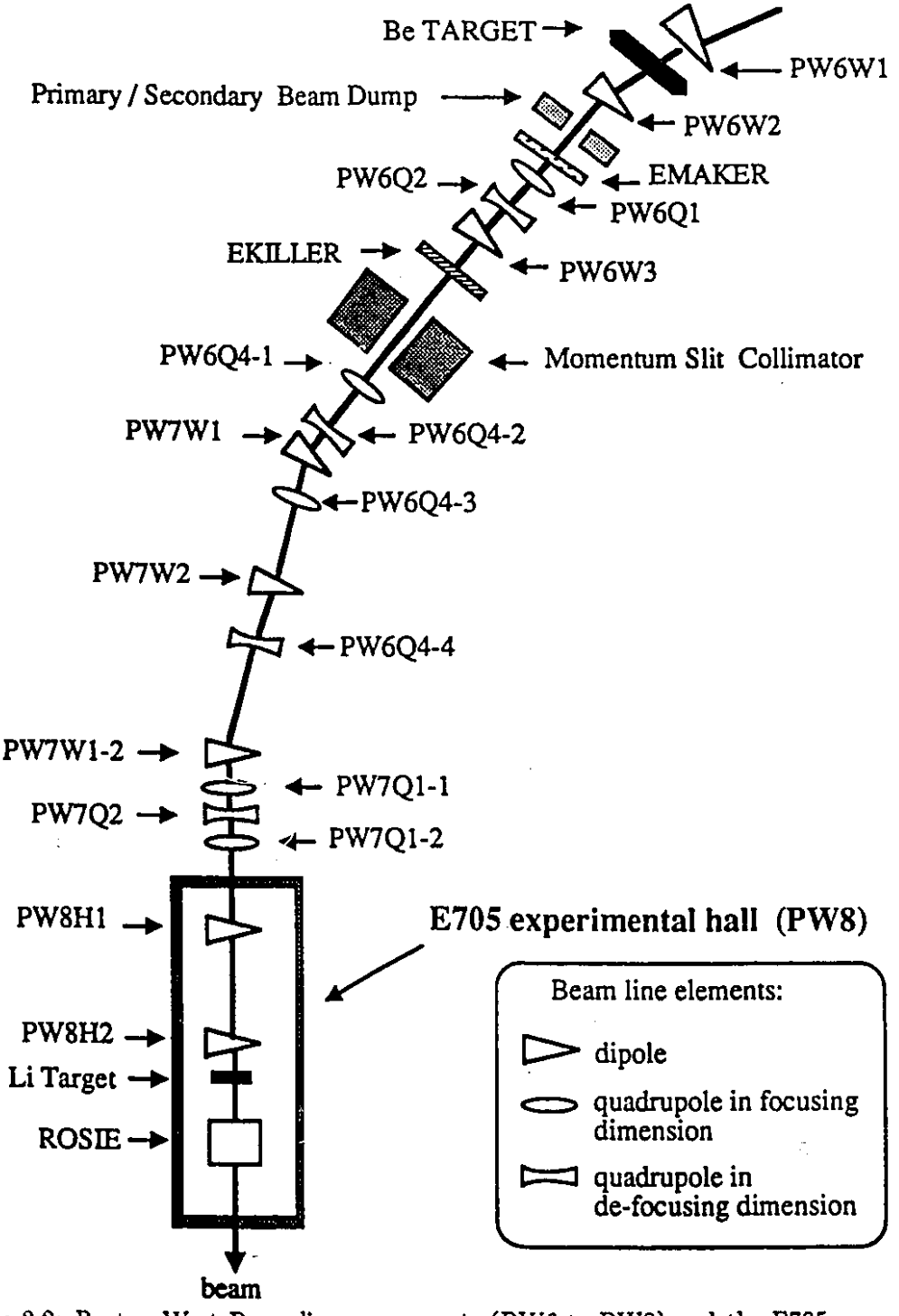

Figure 2.2: Proton West Beam line components (PW6 to PW8) and the E705 experimental hall magnets

Beams of 2, 6, 10, 30, 60, and 100 GeV/c were used periodically to calibrate the detector.

The intensity of the beam was controlled by the primary and secondary line collimators and was measured by a secondary emission monitor (SEM). The beam profile was monitored by segmented wire ionization chambers (SWICs) positioned throughout the beam line.

Two threshold Cerenkov counters located in the PW8 area upstream of the experimental setup were used to tag the beam particles. The counters were filled with a mixture of 80% helium and 20% nitrogen as radiator. The light was focused by a 33 cm diameter mirror on a RCA 31000M photomultiplier. In the normal 300 GeV/c running, using a gas pressure of 1.8 psia it was possible to discriminate between incoming pions and protons. Pions were defined if a signal was present in any of the two Cerenkov counters, while proton were defined if no signal was present. During calibration runs, to distinguish electrons from pions, the Cerenkov pressure was adjusted according to the different beam energies.

2.2.2 Beam chambers

The beam trajectories upstream of the experimental target were determined by using a set of multi-wire proportional chambers referred to as Beam chambers (BC1, BC2, BC3). Each Beam Station consisted of three planes with 128 wires: one Y plane with wires stretched along the x axis and two planes (U and V) with wires rotated by $+60^0$ and -60^0 respectively from the x direction. Each plane was made of 128, 12.5 μm diameter, tungsten wires. The chambers were run with a gas mixture of 77% argon, 16.7% isobutane, 6% methylal and 0.3% freon. The signals of the Beam Station were recorded by readout system, due to W. Sippach of Nevis Lab. The characteristics of the beam chambers are shown in Table 2.1.

Table 2.1: Beam Chambers

Chamber	Z position (cm)	Wire spacing (cm)	θ_{xy}[1] (rad)
BC-1 Y	-6714.635	0.1	0.
BC-1 U	-6729.875	0.1	-1.047
BC-1 V	-6722.255	0.1	1.047
BC-2 Y	-4260.380	0.1	0.
BC-2 U	-4252.760	0.1	-1.047
BC-2 V	-4245.140	0.1	1.047
BC-3 Y	-1029.594	0.1	0.
BC-3 U	-1021.974	0.1	-1.047
BC-3 V	-1014.354	0.1	1.047

2.2.3 Beam and Veto counters

Each beam chamber had a scintillator hodoscope associated with it. The beam hodoscopes were used to define the beam in the trigger logic. Each hodoscope consisted of 8 scintillation counters positioned parallel to the x-axis having a width gradually increasing from the center to the sides (ranging from 0.8 cm to 2.3 cm). Each hodoscope covered an area of 13 × 13 cm^2. A scintillation counter, T1, placed after the last beam station and before the target, was also used to detect beam particles and to define the overall timing for beam definition and triggering.

The muon flux along the beam line was reduced by spoiler magnets. In addtion, a Veto wall was installed, before the lithium target, to minimize the trigger rate from muon halo associated with the beam and upstream interactions. This wall was made of two scintillation counter hodoscopes, VX and VY, oriented in the vertical and horizontal direction respectively. The VX wall consisted of 22 scintillation counters covering an area of 408 × 147 cm^2 with a rectangular hole in the center of 25.4 × 8.8 cm^2 for the beam to go through. The VY wall consisted of 18 scintillation counters covering an area of 306 × 153 cm^2 with a 8.8 × 25.4 cm^2 beam hole.

[1] θ_{xy} is defined as the angle between the wires and the horizontal x axis.

2.3 Target

The target design was based on considerations of the radiation length and interaction length of the material used. A low Z (atomic number) material was selected to reduce the conversion rate of photons into e^+e^- pairs relative to the interaction rate. The thickeness of the target was determined by requiring it to be 10% of a nuclear interaction length. The target was a cylinder of natural lithium (94% ^7Li and 6% ^6Li), 33 cm long and 5 cm radius. The choice of lithium was motivated also by the consideration of it being almost an isoscalar material. An isoscalar target is desirable since, containing the same number of protons (uud) and neutrons (udd), at a parton level the interactions of the beam particle with u and d quark of the target were equally probable, making the interpretation of the results more straightforward. The target was mounted on a motorized table that could be moved, under computer control, in the direction transverse to the beam. This feature of the target was used during calibration and alignment runs, when the beam particles were allowed to go through without interacting.

2.4 Charged particle spectrometer

2.4.1 Multiwire proportional chambers

Large angle tracks MPWC

A set of three proportional chambers, PC1, PC2 and PC3, were part of the tracking system upstream of the analysis magnet. All of the planes in these chambers had their beam regions desensitized. These chambers, together with the upstream drift chambers, determined the path of the charged tracks before they were deflected by the analysis magnet. Each chamber consisted of three planes (four in the case of PC1): one X plane with wires stretched along the y axis and two planes (U and V) with wires rotated by an angle $+\theta_{xy}$ and $-\theta_{xy}$ respectively from the x direction. The chambers used gold-plated tungsten wires of diameter 15 or 20μm with spacing of 1.5 or 2 mm, depending on the chamber. The high voltage cathode planes were 0.0025" copper-beryllium wires with

Table 2.2: Multiwire Proportional Chamber system

Chamber	Z position (cm)	Wire spacing (cm)	θ_{xy} [1] (rad)	Aperture (cm^2)	Dead region radius (cm)
PC-1	-405.	0.15	0.29	54× 29	5.08
PC-2	-334.	0.15	0.29	76× 40	5.08
PC-3	-265.	0.2	0.29	106× 50	6.35
PC-1B	-427.	0.075	0.49	60× 30	0.
PC-2B	-380.	0.075	0.49	75× 40	0.
PC-3B	-244.	0.1	0.49	90× 50	0.

1 mm spacing and they were kept at a high voltage of around 4. kV. The gas used in the MWPC was a conventional "Magic gas" mixture of 77% argon, 16.7% isobutane, 6% methylal, 0.3% freon. A circular region, at the center of each plane, was de-sensitized to minimize high occupancy rate due to the beam and target fragments; this was achieved by an electroplating procedure which doubled the radius of the wires and therefore decreased the electric field by a factor of two. The signal of every wire was amplified by a commercial (Nanometric) N-277D amplifier and was recorded by a N-278 latch. The details of the characteristics for each chamber are shown in Table 2.2.

Small angle MPWC

Three more proportional chambers were located between the target and the magnet: PC1-B, PC2-B, PC3-B. They were implemented to detect the small angle tracks which could not be detected by the other proportional chambers, which were desensitized in the central region. Each chamber consisted of three planes of sense wires: one X plane with wires stretched along the y axis and two planes (U and V) with wires rotated by an angle $+57.3^0$ and -57.3^0 respectively from the x direction. The chambers used gold-plated tungsten/rhenium wires of diameter 12.5 μm with spacing of 0.75 or 1 mm,

[1] θ_{xy} is defined as the angle between the U and V plane wires and the horizontal x axis. By convention, θ_{xy} is positive for U view and negative for V view.

depending on the chamber. The high voltage cathodes were 25μm graphite-coated kapton planes. After few weeks of running, because of the high beam rate, severe damage occurred to the graphite coating and all cathode planes had to be replaced by aluminized kapton. This problem made the chambers unavailable for much of the data and therefore they are not used in the analysis presented in this thesis. The characteristics of each chamber are shown in Table 2.2 and more details on their construction and their performance can be found in reference [35].

2.4.2 Drift chambers

Three large drift chambers were located upstream of the analysis magnet (DC1, DC2, DC3) and three downstream (DC4, DC5, DC6). Each of the front drift chambers had 3 planes X, U, V while each of the rear drift chamber had four planes, two X's (referred to as X and X') , and two other planes, U and V, rotated by $+16.7^0$ and -16.7^0 respectively from the vertical axis. The drift chambers were of two construction types. DC1, DC5, and DC6 had sense gold-plated tungsten wires of 25μm diameter (with the exception of DC1: 20μm) ground and cathode planes of 63.5 μm copper-beryllium wires at negative voltages (the same as field shaping wires). DC2, DC3, and DC4 consisted of planes of sense wires kept at positive voltages alternating with field shaping grounded wires sandwiched between cathode aluminium foils. The gas used was a 50% argon, 50% ethane mixture. The signal from each wire was amplified and converted to ECL levels by the LeCroy 7790 amplifiers and sent to a LeCroy TDC (Time to Digital Converter) which recorded the drift time. All drift chambers had their central regions desensitized. Detailed characteristics for each of the drift chambers are shown in Table 2.3.

2.4.3 Analysis Magnet

The analysis magnet, referred to as "Rosie", was a dipole magnet which, in conjunction with the proportional and drift chamber, measures the momenta of the charged particles. It had an aperture of 185 cm horizontally and 91 cm vertically and a 150 cm

Table 2.3: Drift Chamber system

Chamber	Z position (cm)	Wire spacing (cm)	θ_{xy} [1] (rad)	Aperture (cm^2)	Dead region [2] (cm)
DC-1	-216.	0.6	0.29	51× 102	6.35
DC-2	-194.	1.27	0.29	51× 102	6.35
DC-3	-180.	1.27	0.29	51× 102	6.35
DC-4	175.	1.95	0.29	203× 102	30.5 × 15.2
DC-5	277.	1.95	0.29	335× 168	30.5 × 15.2
DC-6	381.	1.95	0.29	335× 168	30.5 × 15.2

length along the z-axis. Its center was located 533.3 cm downstream of the target and the operating current was 2100 Amperes. This current corresponded to an integrated field length ($\int B \times dl$) of 25.55 KG·m or a transverse momentum "kick" of 0.766 GeV/c. To reduce the fringe field downstream of the magnet, and its effect on the calorimeter, an steel mirror plate (22 cm thick) was placed on the downstream end of Rosie.

2.4.4 Charged particle hodoscope

Two scintillation counters hodoscopes, CPX and CPY, were located downstream of the rear drift chambers and measured the X and Y position of charged tracks respectively. These hodoscopes provided fast signals to be used in the multiplicity trigger and were used in the reconstruction procedure to remove some of the tracking ambiguities.

The CPX hodoscope consisted of two rows, for a total of 184 vertically-oriented counters. Each counter was 1 cm thick, 4 cm wide, and 100 cm long. They formed a 350×200 cm^2 wall with a 30×15 cm^2 beam hole. They were coupled to photomultiplier tubes with transistorized bases. The output signal from each photomultiplier on the top row was summed with the signal from the corresponding counter in the lower row. The logical signals from the CPX counters were summed and discriminated to supply

[1] θ_{xy} is defined as the angle between the U and V plane wires and the horizontal x axis. By convention,θ_{xy} is positive for U view and negative for V view.

[2] For DC-1, DC-2 and DC-3 the radius of their circular dead region is reported, while for DC-4, DC-5 and DC-6 the dimensions of their rectangular dead regions are reported.

a CPX$\geq$2 signal to the fast trigger logic when two or more counters were lit. Also, the discriminated signals from CPX counters were recorded for each event and were used in the charged particle tracking (as reported in Section4.4).

The CPY hodoscope consisted of two vertical columns for a total of 48 counters, each being 1 cm thick, 8 cm wide, and 200 cm long. They formed a wall $400 \times 180 cm^2$ with a $30 \times 15 cm^2$ square hole. Signals from the CPY were used to defined the interaction trigger together with the CPX signals.

2.5 Electromagnetic calorimeter

The electromagnetic calorimeter was placed 10 m downstream of the target, behind the tracking system. Its purpose was to measure the energies and positions of photons and electrons. It consisted of a large glass array, referred to as Main Array, and, in front of it, a photon converter, referred to as the Active Converter. The converter was used to initiate the showers, so that their centroids could be measured. The converter also gave useful information on the longitudinal development of the shower, which was used as a basis for rejecting hadrons. The converter consisted of different devices in the two different regions shown in Figure 2.3. In front of the outer region of the Main Array, the Active Converter consisted of vertically mounted glass blocks used to initiate the electromagnetic showers and measure the deposited energy. Between the Active Converter and the Main Array there was a Gas Tube Hodoscope, used to measure the shower profile and therefore determine the shower position. In the central region, a Lead Gas Converter, consisting of a sandwich of several layers of lead plates and proportional tubes, served the purpose of both initiating the shower and measuring the shower profile. The entire calorimeter rested on a moving table, inside a climate controlled house whose temperature was kept constant within $\pm 0.06^\circ$ C. The whole house could be moved horizontally and vertically so that each Main Array block could be centered on the electron beam for calibration purposes. In the following sections, the details of the devices forming the electromagnetic detector will be described.

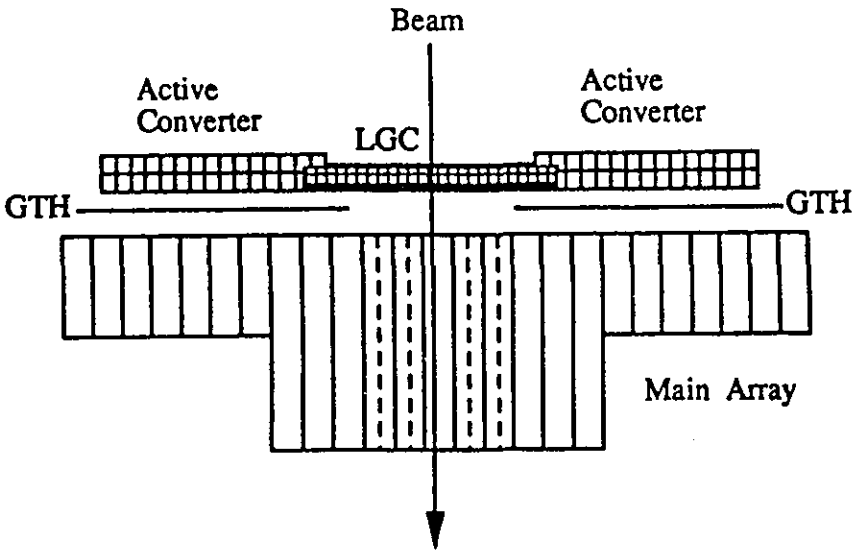

Figure 2.3: Top view of the electromagnetic calorimeter

2.5.1 Main array

The Main Array consisted of 392 glass blocks covering an area of 371x195 cm^2, as shown in Figure 2.4 The blocks were arranged to leave a 30x15 cm^2 hole in the center to avoid interaction of very energetic hadrons produced at small angles with respect to the beam and the beam itself. Two different materials and two different sizes were used for the glass blocks. In the central area of the detector, the blocks were made of scintillation glass (Ohara Optical SCG1-C); while in the outer region lead glass (SF5) was used. The properties of these two types of glass are summarized in Table 2.4. This choice was motivated by several considerations: energy resolution, radiation damage and financial limitations. In the lead glass, light derives from Cerenkov radiation produced by relativistic electrons and positrons. In the scintillation glass, in addition to Cerenkov light there is also scintillation light due to the Ce_2O_3 scintillator. In a test performed at SLAC by the E705 collaboration [36], the light yield from scintillation glass was found to be 5.1 times that of the SF5 glass. This, in principle, results in better energy resolution for the scintillation glass. Also, the SCG1-C was found to be 150 times more resistant to radiation damage [37], which would result in a darkening of the glass and

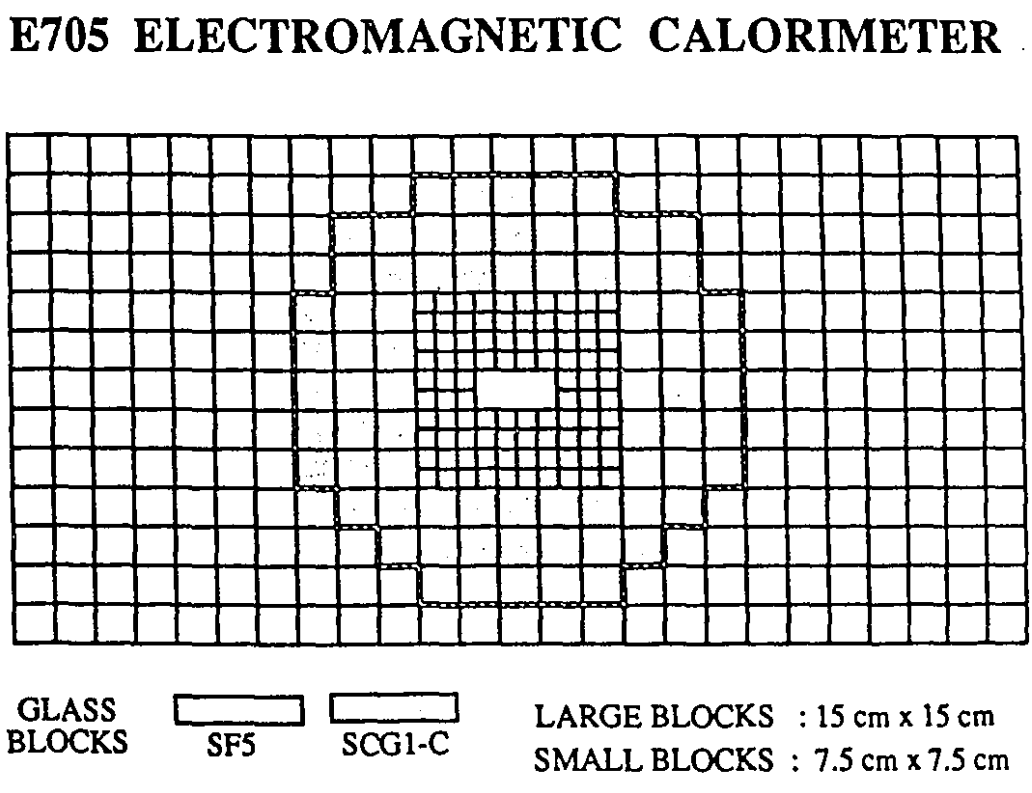

Figure 2.4: Front View of the Main Array

Table 2.4: Summary of the characteristics of the glass types used in the E705 Main Array.

	SCG1-C		SF5	
Composition (by weight)	BaO	43.4%	PbO	55%
	SiO_2	42.5%	SiO_2	38%
	Li_2O	4.0%	K_2O	5%
	MgO	3.3%	Na_2O	1%
	K_2O	3.3%		
	Al_2O_3	2.0%		
	Ce_2O_3	1.5%		
Radiation Length	4.25 cm		2.47 cm	
Interaction Length	45.6 cm		42.0 cm	

a consequent degradation of energy resolution. On the other hand, SF5 presented the advantage of a more favorable ratio of radiation length to interaction length so that, for a given number of radiation lengths, there is a smaller probability for a hadron to interact. Also SF5 was a less expensive material. The SCG1-C blocks came in two different sizes. Most of the blocks, had a cross-section of 15x15 cm^2 and a length of 89 cm, corresponding to 20.5 radiation lengths. In order to achieve better segmentation in the busy central region of the detector, blocks with a smaller cross-section (7.5x7.5 cm^2) were used. The SF5 blocks surrounded the scintillation blocks; their cross-section was 15x15 cm^2 and their length was 41.45 cm, corresponding to 18 radiation lengths. The light obtained from the glass was collected to the photomultipliers: EMI 9791KB 5" photomultipliers for the large blocks and RCA6342A 3" tubes for the small blocks. An optical coupling gel (Dow Corning 92-3067) provided the seal between the tube and the glass. The high voltage to the photomultiplier was supplied by LeCroy 1440 power supplies. The signals from the phototubes were carried by RG-8 cables, 200 ns long, to the inputs of the custom made Precision Charge Cards, where the charge was integrated and sent to ADCs and to TDCs systems.

The precision Charge Amplifier/ADC cards [38] were especially made for E705 in order to perform in high rates and to cover a large dynamic range of energies with

high accuracy. Each card consisted of 16 channels continuously integrating the input signals. The charge pulses from the glass block phototubes were split into high and low frequency components in order to prevent the low frequency noise from contributing at the integration-shaping stage. The high frequency component was amplified and integrated by a resistor-capacitor circuit. Two copies of the integrated pulses were produced, one being sent to a Cluster Finder trigger and the other to LeCroy 4290 TDCs. Another copy of the pulses was delayed by 400 ns to wait for a trigger decision and then sent to the digitization section of the cards. There the voltage pulse charged two sample-and-hold capacitors, C1 and C2, via two JFET switches. When a trigger occurred, one switch opened just before the signal of interest appeared on the delay line output, so that the C1 voltage reflected the state of the charge integrating amplifier output just "before" the event of interest was integrated. The other switch opened 250 ns later, so that the voltage on C2 reflected the state of the integrator output "after" the interaction of the event of interest. A differential amplifier subtracted the "before" from the "after" level. After subtraction, the resulting pulses were sent to a single 5200 Analog Device 12-bit ADC. Before reaching the ADC they were amplified by a factor of 8 if the level was such that the digitized value would have been less than 1/8 of the full scale, or by 1 otherwise. This provided an effective sensitivity of 15-bits, increasing the maximum range to 32760 counts. The voltage level of capacitor C1 was also digitized in 3 bits, giving information about the "before" state of the charge integrating amplifier, often referred to as "before bit". A 16-bit word was formed by the 12 bits of the digitized difference, the 3 "before bits", and one bit set to 1 when the analog output had been multiplied by 8. The digitized values for the 16 channels of each board were then sent to a FIFO to await read-out through CAMAC.

The signals from the front output of the Charge Cards were sent to a LeCroy 4290 TDC system. The TDCs operated in a common stop mode, using the ADC signal as a start and the trigger pulse as a stop. The TDCs were used to identify glass blocks with energy deposition not associated with the interaction of interest.

The gains of the photomultiplier tubes were monitored with a light pulser system.

The light source consisted of an array of 96 green Hewlett Packard HLMP-3950 light emitting diodes (LED). Optical filters were used to vary the light intensity from 0-100%. Bundles of optical fibers brought the light from the LED array to the glass blocks. For the Main Array blocks, each fiber was attached to the block surface opposite to the photomultiplier, while for the Active Converter blocks it was mounted in the middle of the block. Three Litronix BPX 66 PIN diodes were used to monitor the LED light level. The pulser was operated during the run of the experiment at about 2 Hz.

2.5.2 Glass Converter

The Glass Converter consisted of two layers of vertically arranged SCG1-C scintillation glass blocks. Each block had a cross-section of 7.5x7.5 cm^2 and was 97.5 cm long. Particles traversing the two layers, were going through ~15 cm of glass equivalent to 3.45 radiation lengths, sufficient to initiate the shower of most electrons, positrons, and photons. An RCA 6342A photomultiplier was mounted on the free end of each block. The signals from the phototubes were sent to the Charge Cards (described in the previous section) for charge integration and digitization.

2.5.3 Gas Tube Hodoscope

The Gas Tube Hodoscope (GTH)[39] was built to determine the position of the electromagnetic showers in the outer region of the electromagnetic calorimeter and was positioned between the Glass Converter and the Main Array. The GTH consisted of two panels, 156x197 cm^2 each, positioned at the left and the right outer regions of the Main Array. Each panel consisted of two planes of 216 conducting polystyrene tubes, vertically arranged and sandwiched between three sheets of 1.6 mm copper-clad G-10. The two outer copper layers, adjacent to the tube planes, were etched into horizontal strips 0.86 cm wide and measured Y-coordinate. The tubes were of single and double width, with a wire stretched along their center, set at +2100 volts. The wire-to-wire spacing was 0.88 cm and 1.76 cm for the single and double width tubes respectively.

The boundary between the single and double width tubes was at ±85 cm from the center of the calorimeter. The tubes were filled with a gas mixture of 50/50 Argon/Ethane. The two layers of tubes were ganged together, as were the two layers of strips. The signals were carried by RG8 cables to LeCroy 2280 ADCs.

2.5.4 Lead Gas Chamber

The Lead Gas Chamber (LGC)[40] was positioned in front of the central region of the Main Array. The LGC was an 8-layered sampling device with each sampling section consisting of 1.2 mm lead, 10 mm aluminum extrusion proportional tubes, copper-clad horizontal strips, and 1.6 mm fiberglass board. A 1.3 cm sheet of steel, followed by 8 mm of lead were placed in front of the whole LGC assembly. The device had a total thickness of 4.2 radiation lengths and spanned an area of 1.03x1.95 m^2 with an 30x14 cm^2 hole in the center. The LGC was used both as active converter and shower position detector. The X coordinate was given by the proportional tubes and the Y coordinate by a copper-clad printed circuit board of horizontal strips picking up capacitively the signals in the tubes. There were two planes of tubes: a top and a bottom, each having 104 tubes. Each tube had a 50 μm gold-plated tungsten wire stretched inside it, set at +1850 volts. The wire-to-wire spacing was 9.92 mm. The gas consisted of a mixture of 50/50 Argon/Ethane. The cathode strips were 1.25 cm wide and they were arranged in two groups. The eight wires at the same x position and at different depths were ganged together, as were the eight corresponding strips. The wire and strip signals were brought by RG8 coaxial cables to LeCroy 2280 ADCs. Pedestals were subtracted online, and only clusters of channels above a preset threshold were written to tape.

2.6 Muon detector

The muon detector was placed behind the electromagnetic calorimeter and consisted of four planes of scintillation counters, μY, $\mu 1$, $\mu 2$, and $\mu 3$, positioned within copper, steel

and concrete absorber material. The muon detector was designed to detect muons with at least 6 GeV/c momentum, which was the minimum momentum required for a muon to penetrate the absorbers and reach the last hodoscope. All muon counters were made of NE114 1 cm thick plastic scintillator.

The μ_Y and $\mu 1$ planes were located behind the first shield, which consisted of a layer of copper and one of steel. The copper shield was 40 cm thick and covered only the central part of the hodoscope for a total surface of 183x290 cm^2. The steel wall covered the entire hodoscope surface and was 310 cm thick. The μ_Y plane consisted of 96 horizontally-arranged counters in four columns of 24 counters each. It covered a total area of 620x285 cm^2 with a 40.6x40.6 cm^2 hole in the center. The counters were of two sizes: 187x13 cm^2 for the outer-column counters and 129x13 cm^2 for the inner-column counters. The $\mu 1$ plane consisted of 60 counters, vertically arranged in two rows of 30 counters each, covering a total area of 618x290 cm^2 with a 40.6x40.6 cm^2 hole in the center. Each counter measured 20x145 cm^2.

Proceeding downstream, the $\mu 2$ hodoscope was located behind a steel absorber 61 cm thick. The $\mu 2$ hodoscope was composed of 62 scintillators, arranged vertically in two rows of 31 counters each, covering a total area of 617x315 cm^2 with a 40.6x40.6 cm^2 hole in the center. The counters were arranged so that between two adjacent counters, in the same row, there was a 1 cm region of overlap. Each counter measured 20x145 cm^2.

The $\mu 3$ hodoscope was located behind a 90 cm concrete absorber. It consisted of 62 counter arranged vertically in two rows of 31 counters each and it covered an area of 723x352 cm^2 with a 87.6x40.6 cm^2 hole in the center. The counters were arranged so that between two adjacent counters, in the same row, there was a 3 cm region of overlap. Each counter measured 26.7x176.0 cm^2.

2.7 Trigger system

The trigger system was designed to select the events of interests and reduce the amount of data recorded to tape. The primary goals of the experiment were to measure the

Table 2.5: Percentage of the various data triggers written to tape

Trigger type	% to tape
Interaction	1.1
Dimuon	69.2
Single Photon	12.8
Diphoton	11.6
Two vee	4.3
LED	1.0

production of high mass dimuons (J/ψ decays in particular) and, at the same time, measure the production of high p_T neutral particles (direct γ, π^0, η) in hadronic interactions. During the 1988 run, data were collected based on six triggers to satisfy the different goals of the experiment:

- The interaction trigger was used to insure that an interaction had occurred in the target.
- The dimuon trigger was used to select events with two opposite-sign muons with high mass.
- The photon trigger was used to select events with high p_T showers in the electromagnetic calorimeter (more details are given in[42]).
- The diphoton trigger was implemented to study the production of two prompt photons. It selected events with two high p_T showers in opposite quadrants of the calorimeter.
- The two-vee trigger was implemented to select events with two "vee" decays occurring between PC2 and PC3.
- The LED trigger was used to track the gains of the glass blocks.

The percentage of the various data triggers written to tape, averaged over the entire run, is reported in Table 2.5. In the following sections the interaction and dimuon

triggers will be described in detail since they were used to collect the data analized in this thesis.

2.8 Interaction trigger

The interaction trigger was defined as the coincidence of a beam particle with at least two hits from the CPX hodoscope planes.

A beam particle was defined using the BY, T1, and the HALO counter signals, as shown in Figure 2.5. The discriminated pulses from the BYi counters, set to a width of 10 ns, were both OR'ed and summed together to form six pulses, named BY1, BY2, BY3 and $\sum$BY1, $\sum$BY2, $\sum$BY3 respectively. To define a proper beam particle the BY counter signals had to be in coincindence with T1 (which defined the absolute timing of the experiment). In order to reject halo particles the coincidence of the two veto planes, referred to as HALO, was used as a veto. Beam was than defined as:

$$B = T1 \cdot BY1 \cdot BY2 \cdot BY3 \cdot \overline{HALO} \tag{2.1}$$

The accelerator delivered the beam particles as a train of equally spaced bunches, referred to as "buckets". The separation between buckets was about 19 ns. The beam rate was 4 MHz, at the beginning of the run, and increased steadily to reach 6 MHz for the second half of the run. Given the high beam rate and the beam structure of the accelerator, the secondary beam could have more than one particle within a bucket. The multiple particle buckets had higher probability to interact in the target and they could cause errors in the calculation of the beam normalization. These buckets were removed from the data sample, but to keep the useful beam rate as high as possible only buckets with more than two particles were rejected. The beam normalization was corrected offline to take into account the cases of double occupancy. The $\sum$BYi signals were sent to discriminators with thresholds set to select more than two particles. Therefore the vetoed beam was defined as:

$$BV = B \cdot (\overline{\sum BY1 > 2} + \overline{\sum BY2 > 2} + \overline{\sum BY3 > 2}) \tag{2.2}$$

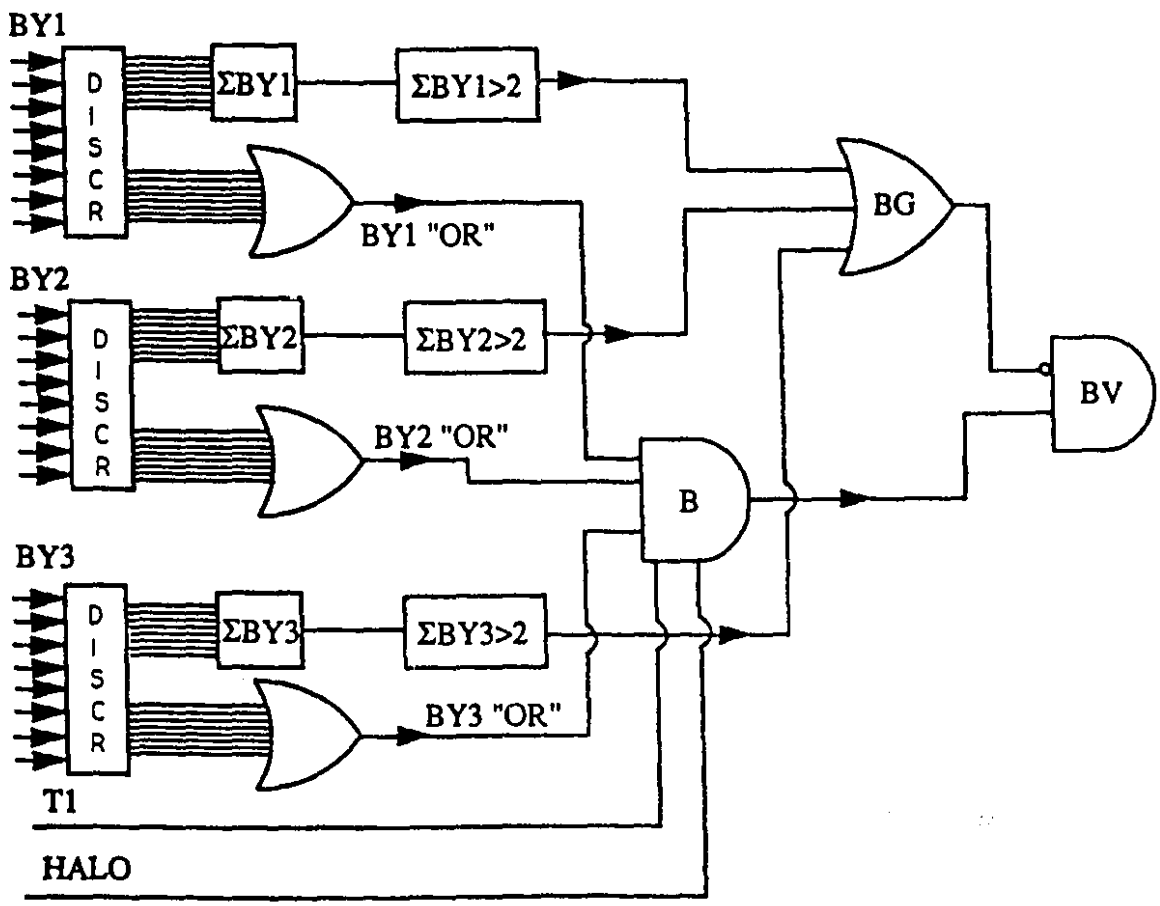

Figure 2.5: Beam trigger logic

The beam particle type was identified based on the two threshold Cerenkov counter signals. The Cerenkov counters were set to give light only for 300 GeV/c momentum particles with mass below that of the proton mass. The signals of the two Cerenkovs, C1 and C2, were discriminated and used to define a pion (π) or a proton (p):

$$\pi = BV \cdot (C1 + C2) \qquad p = (BV \cdot \overline{C1}) \cdot (BV \cdot \overline{C2}) \tag{2.3}$$

Finally, the signals from the CPX counters were summed and the result was sent to a discriminator with a threshold set for two hits. The interaction trigger was then defined as:

$$INTERACTION = (\pi + p) \cdot (CPX > 2) \tag{2.4}$$

2.9 Dimuon trigger

The dimuon trigger consisted of two stages: two muons in different quadrants were required by the first level, referred to as the fast trigger; at the second level a fast online processor [43] performed the computation of the invariant mass of the dimuon system, selecting events with apparent mass ≥ 2.4 GeV/c^2.

2.9.1 Fast trigger

The fast trigger was satisfied if two muons were detected in different quadrants of the muon detectors. A single muon was defined as the triple coincidence, as illustrated in Figure 2.6, by the following exprssion:

$$TC_i = \mu 1_i \cdot (\mu 2_i + \mu 2_{i+1}) \cdot (\mu 3_i + \mu 3_{i+1}) \tag{2.5}$$

The coincidences were grouped in four quadrants in the following way:

$$Quadrant\,1 \;\; = TC\,1 \;to\,15 \tag{2.6}$$

$$Quadrant\,2 \;\; = TC\,16 \;to\,30 \tag{2.7}$$

$$Quadrant\,3 \;\; = TC\,31 \;to\,45 \tag{2.8}$$

$$Quadrant\,4 \;\; = TC\,46 \;to\,60 \tag{2.9}$$

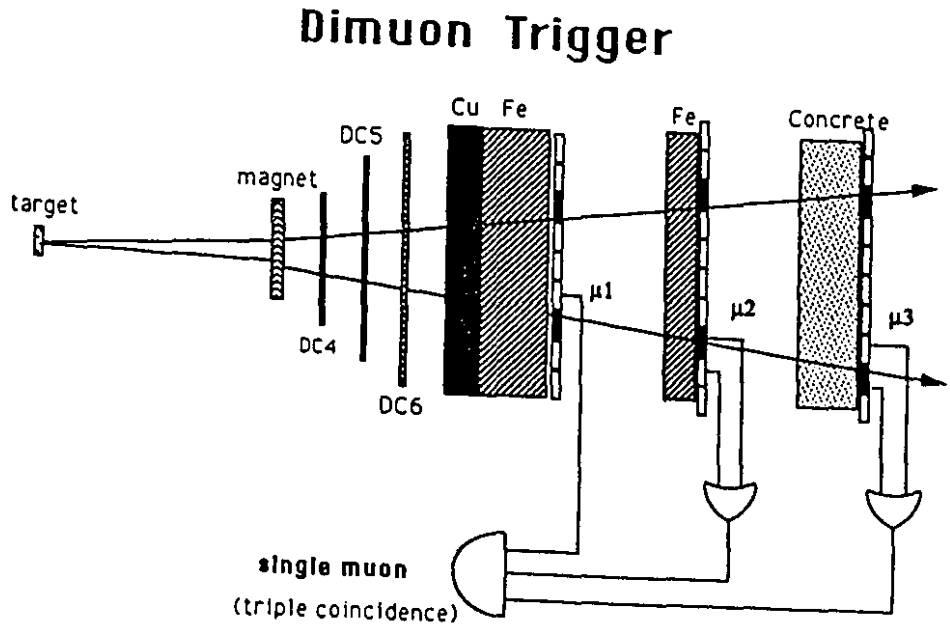

Figure 2.6: Scheme of the dimuon trigger defintion

Then the dimuon trigger was formed if at least two triple coincindences from different quadrants were present at the same time as an interaction trigger. The dimuon trigger rate was approximately 10^{-3} relative to the interaction rate. The major contribution to the fast dimuon trigger was due to muons coming from pion and kaon decays.

2.9.2 Trigger processor

The trigger processor[43] selected high mass dimuons by performing a fast track reconstruction and calculating a mass for every opposite sign track pair. The tracks were found using the x and x' planes of the rear drift chambers. Using only the position of the drift chamber wires, tracks were reconstructed which pointed toward lit CPX counters and muon triple coincidences. The Y trajectory of the track was estimated by using the μY counter information. If more than one μY counter was consistent with a track, the trigger processor attributed to the track the counter which generated the

largest angle between the two muons. This was done in order to reduce the loss of events due to an underestimate of the mass. The tracks were assumed to originate in the target center and the momenta were calculated using this assumption. Once all the tracks were found and the mass had been calculated for all the combinations of opposite-sign tracks, events with mass lower than 2.4 GeV/c^2 were rejected. This value of the mass cut rejected 75% of the dimuon triggers while accepting 90 $\pm$ 5% of the J/ψ events.

2.10 Data acquisition system

The data was collected from the electronics by Smart Crate Controllers which resided in standard CAMAC crates. The Controllers were designed specially for the experiment [41] in order to achieve a high data collection rate. The controllers executed lists of CAMAC instructions in order to initialize, read, and clear the modules that resided in their crates. The lists were pre-loaded into the Controllers from a VAX 11/780 computer via RS-232 lines. The data from the Controllers was sent to a VME-bus based system, containing a set of ACP modules (Fermilab Advanced Computer Project) [1]. These Motorola 68020-based computers had 2 megabytes of memory and they were responsible for assembling into a single record the data arriving in parallel from the Smart Crate Controllers, and then holding the event in memory until it was recorded to magnetic tapes. Thanks to the parallel architecture and the fast list execution, the time to service a single trigger was less than a 1 msec. From the VME-crate the data was sent to a PDP 11/45 computer via a CAMAC branch highway. The PDP wrote the data to two tape drives. For peak running conditions, a tape was written every 10 minutes. A fraction of the events was also transferred from the VME-crate to the VAX, for monitoring programs checking the various devices during the data taking.

2.11 Data sample

The data were taken from August 1987 to February 1988. At about 6 MHz beam rate, the interaction rate was of about 700 KHz and the number of dimuon triggers per interaction was approximately 10^{-3}. A total of about 140 millions good quality dimuon events were written to tape, as shown in Figure 2.7 as a function of time. These triggers divide into roughly equal positive and negative beam sample. The negative beam was 98.5% π^- and 1.5% $\bar{p}$, while positive beam was 40% π^+, 60% p.

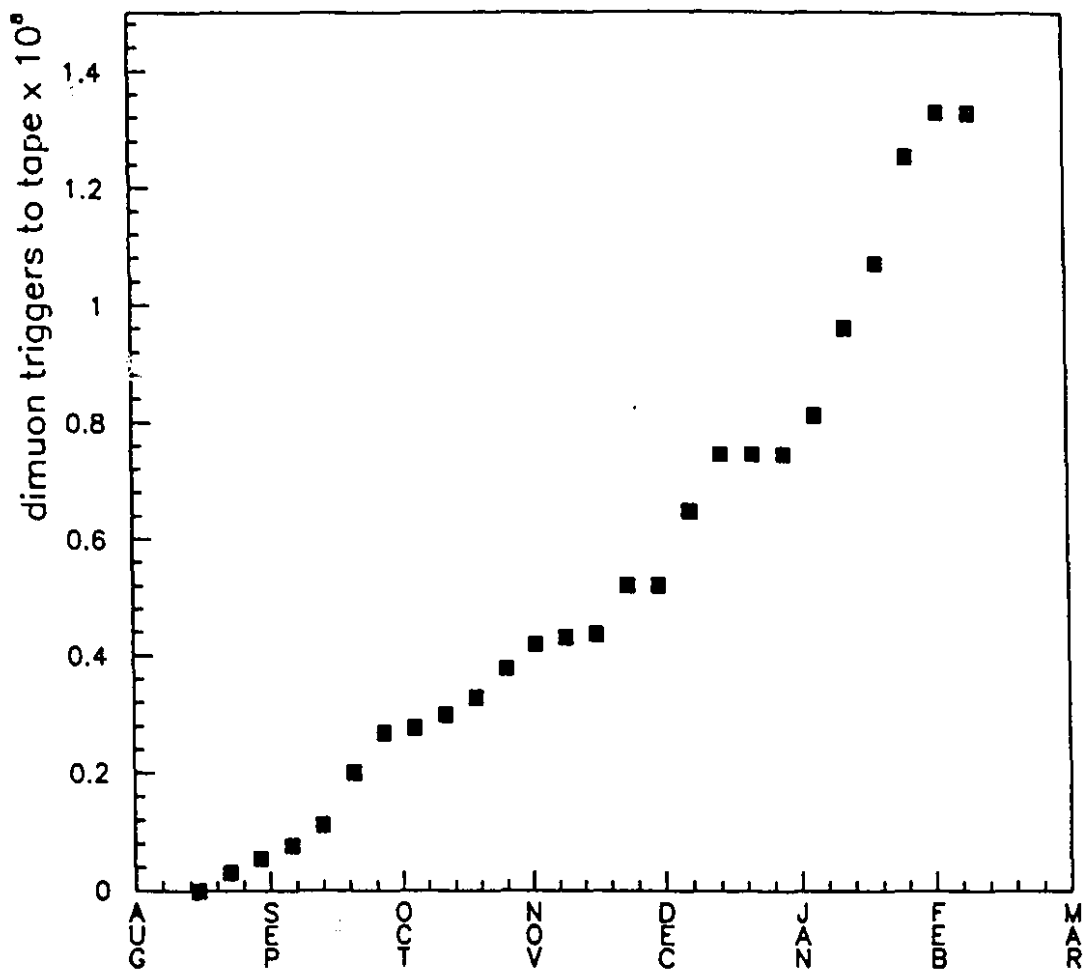

Figure 2.7: Dimuon triggers written to tape as a function of time

Chapter 3

Calibration and Alignment of the Spectrometer

Special sets of data were collected to study in detail each component of the detector to determine their characteristic parameters and evaluate their performance. In Section 3.1 the detailed study to determine the alignment constants and efficiencies of the beam chambers will be described. In Section 3.2 the performance of the various elements of the charged particle spectrometer will be discussed. Finally, in Section 3.3 the electromagnetic calorimeter calibration procedure will be presented and the energy and position resolution obtained analyzing calibration events will be reported.

3.1 Beam chambers

3.1.1 Alignment method

During the data taking, special runs were performed with the target out, so that the beam chamber alignment could be checked with respect to the rest of the spectrometer. The alignment was done in three steps:

1. Using U and Y hits, the position of the expected V hit was computed and compared with the position of the closest V hit. A triplet was defined by the existence of a V hit within a predefined tolerance ($\pm$ 1 wire-spacing). The position of the planes relative to each other was adjusted iteratively to maximize the number of triplets.

2. Using the combination of Y,U, and V hits, space points were defined in each chamber. Space points in the three beam chambers were used to reconstruct beam tracks. The beam tracks were then projected into each plane. The residual

difference between the beam track projection and the closest hit is shown in Figure 3.1 for all the beam chambers. Keeping the position of one chamber fixed, the position of the other two chambers was varied, until the residual distributions were centered at zero. This step was done iteratively since the chamber positions define the space location of the beam tracks which are used as reference lines for the alignment. This procedure converged after few iterations. The chamber resolution can be inferred from the widths of the residual distributions and it was found to be about 250 μm. Such a value is consistent with what one expects for a uniform distribution of hits within a cell:

$$\sigma = \frac{wire - spacing}{\sqrt{12}} = 290\ \mu m$$

where $wire - spacing$= 1.0 mm in the case of the beam chambers.

3. The beam track was projected into the PCBs, located downstream of the target, and the difference between the projected track position and the PCB space points was plotted. The beam chambers were then moved as a whole until their alignment was consistent with that of PCBs. This procedure provided an absolute alignment for the beam chambers since the PCBs had been previously aligned with the rest of the spectrometer.

The alignment parameters were determined periodically throughout the run and they were fairly stable.

3.1.2 Beam chamber efficiency

Using alignment tapes, the beam chamber efficiencies were estimated by checking for planes not participating in the definition of the reconstructed beam tracks. The efficiency of the beam chambers was monitored throughout the run as shown in Figure 3.2, there is no evidence of systematic variation with time. The average value, over the entire run, for each beam chamber plane efficiency is shown in Table 3.1. The errors

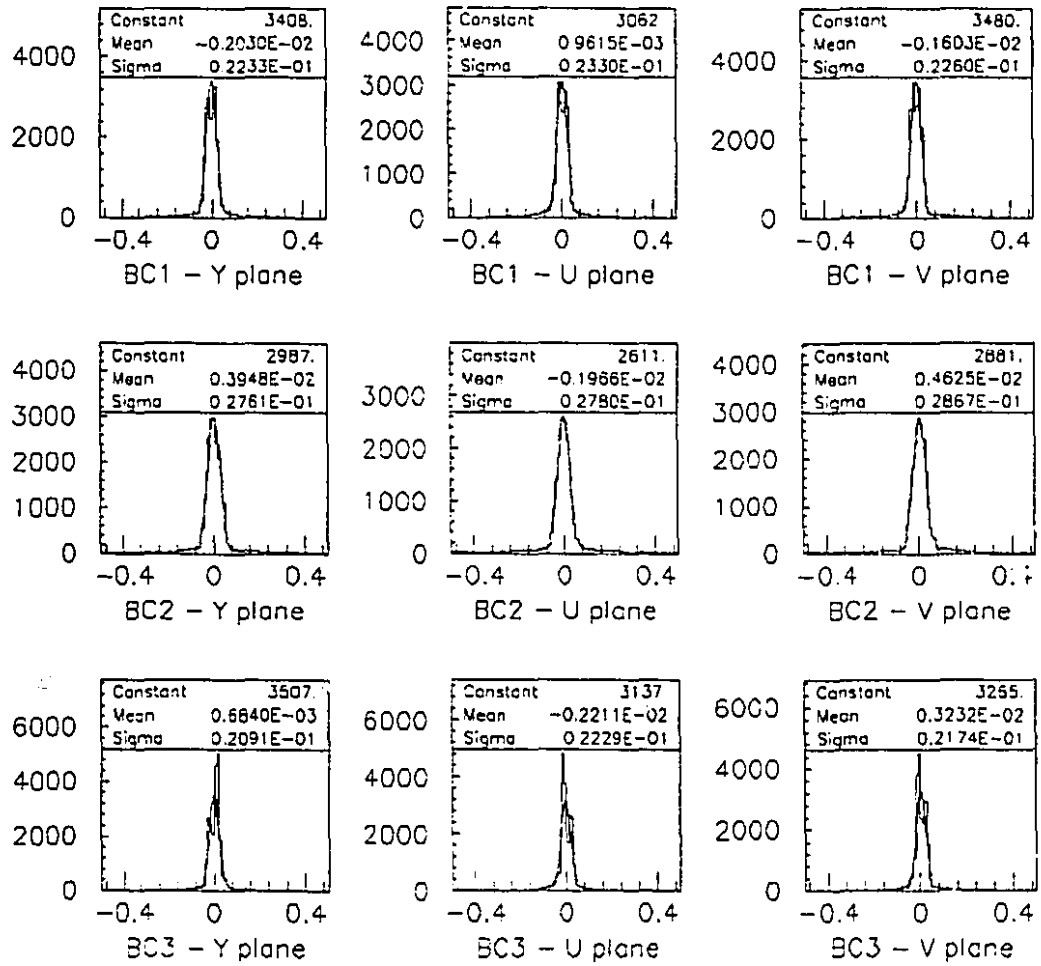

Figure 3.1: Beam station residuals (cm)

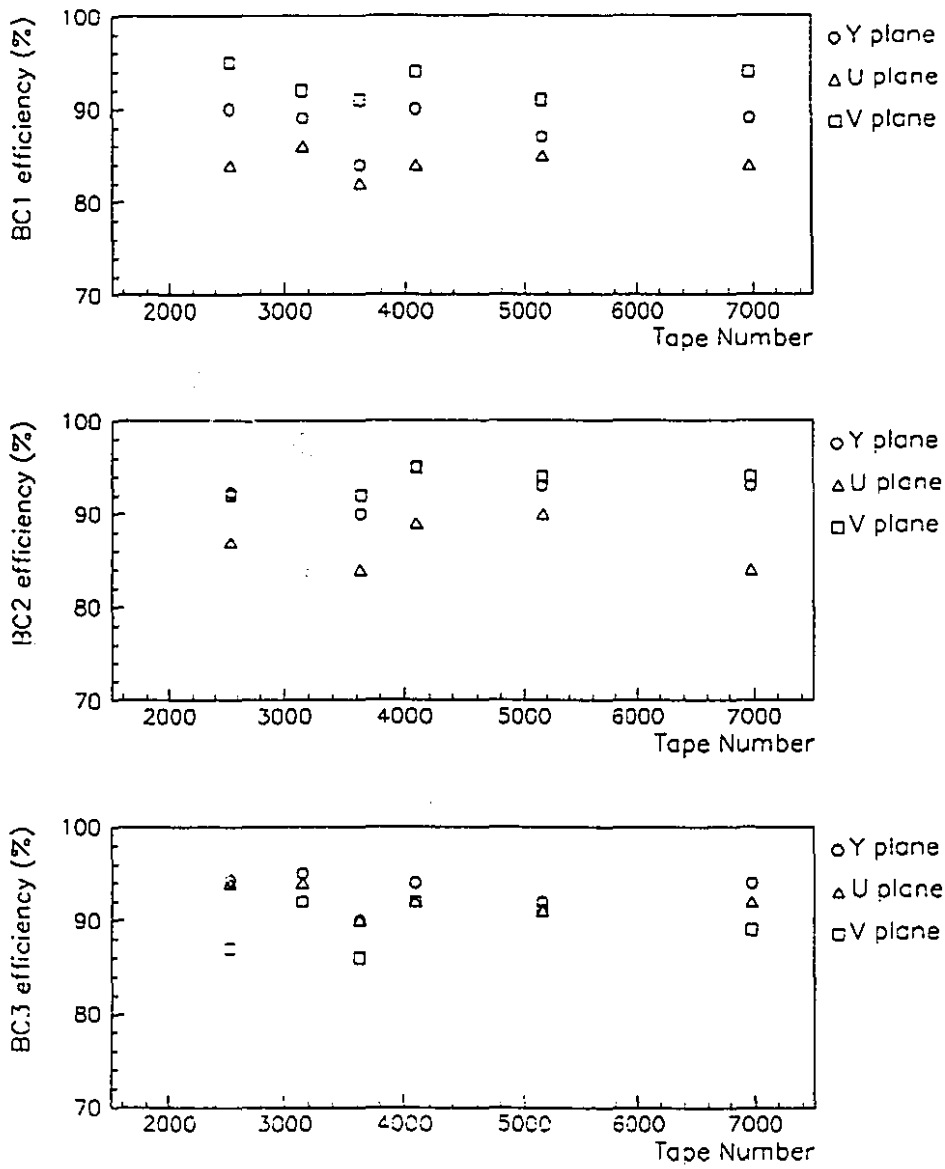

Figure 3.2: Beam station efficiency versus tape number

Table 3.1: Summary of the beam station efficiencies

Chamber	Y plane efficiency (%)	U plane efficiency (%)	V plane efficiency (%)
BC-1	88 ± 2	84 ± 1	93 ± 2
BC-2	89 ± 3	87 ± 3	93 ± 1
BC-3	93 ± 2	92 ± 2	90 ± 2

listed represent the variances on the arithmetic mean ($\sigma^2 = \frac{1}{n-1}\sum_{i=1}^{n}(\epsilon_i - <\epsilon>)^2$) and they are mainly due to fluctuations during the data acquisition period.

3.2 Charged particle spectrometer

3.2.1 Front and rear chamber alignment method

Precise position and efficiency measurements for the front and rear chambers were determined using special runs in which the analysis magnet was turned off. The tracks of the particles coming from interactions in the target were used as straight line references to evaluate the relative position of the front and rear chambers. In the proportional chambers, the position of the first wire for each plane was set so that the residuals of the track projected position and the hit position were centered at zero. In the drift chambers, the time corresponding to a zero drift distance, T_0, was determined for each wire. A correction was applied to compensate for the non-uniform drift speed within the cell. The distribution of the residuals, defined as the difference between the track projection and the hit position, is shown in Figure 3.3 for all the planes for one of the proportional chambers and one of the drift chambers. The intrinsic resolution of each plane was estimated from the width of the residual distribution. Table 3.2 summarizes the resolution for all the chambers. These numbers represent the averages for all of the planes within a given chamber.

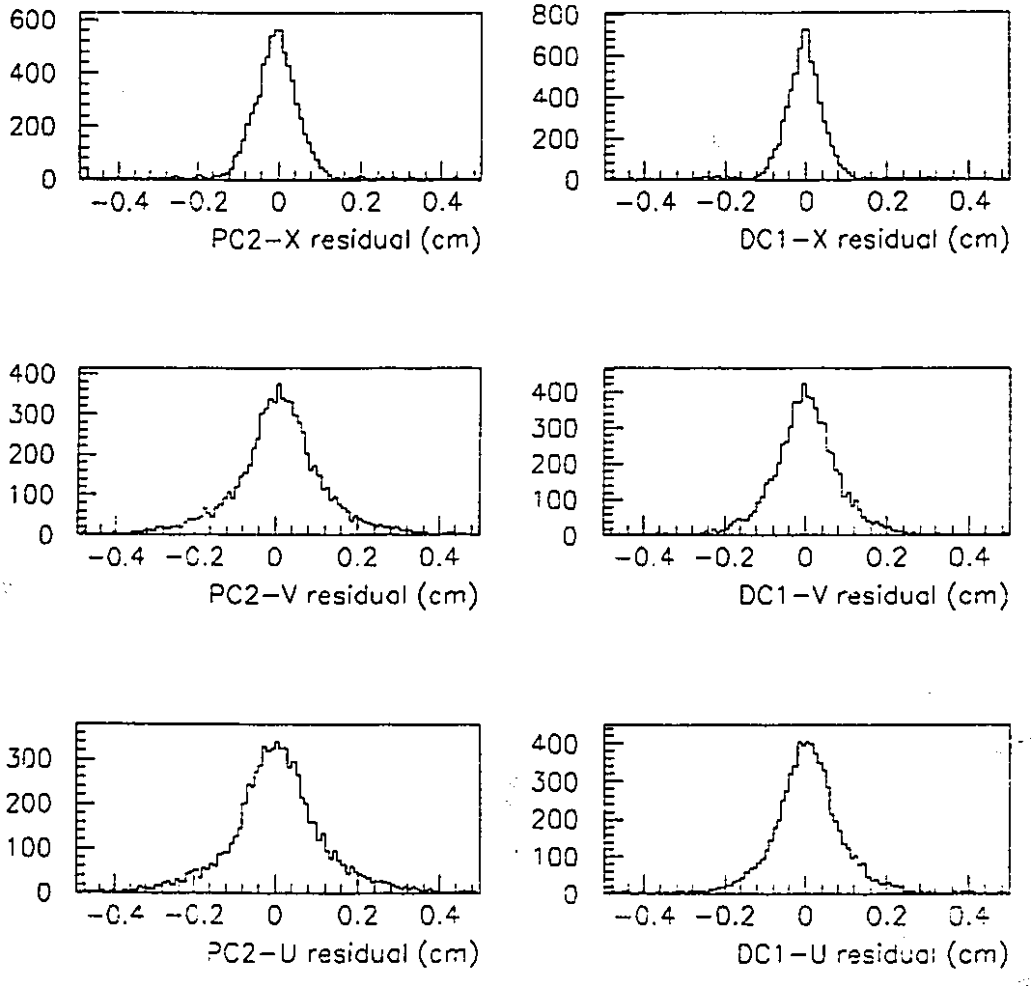

Figure 3.3: Residual distribution for PC2 and DC1 planes in X, U, V view

Table 3.2: Summary of the front and rear chamber resolutions

Chamber	Average resolution (μm)
PC-1	660 ± 50
PC-2	670 ± 40
PC-3	740 ± 40
DC-1	420 ± 40
DC-2	390 ± 10
DC-3	360 ± 20
DC-4	660 ± 40
DC-5	480 ± 70
DC-6	660 ± 80

3.2.2 Chamber efficiency

To measure the chamber efficiencies, tracks were selected which intersected the live region of all the chambers. The reconstructed track was projected into each plane for which the efficiency was to be determined, and a search made for nearby hits. The tolerance used to decide whether the hit was present or not was the quadrature sum of the track projection error and the spatial resolution of the plane in question. Chamber efficiency was monitored throughout the run and time variations were found to be ±5% [44] . Table 3.3 shows the efficiency for each of the planes averaged over the entire data collection period.

3.2.3 Muon counter efficiency

To estimate the μ_1, μ_2, μ_3 and μ_Y efficiencies photon triggers were analyzed, so as to avoid the bias present in the dimuon events where the presence of signals in all counter planes had already been required by the trigger.

Muon candidates were selected by requiring three of the four planes of the muon counter hodoscope to be consistent with a reconstructed charged particle track.

Each muon track was then projected into the counter plane of interest and the

Table 3.3: Efficiencies for the front and the rear chambers

Chamber	X plane eff (%)	V plane eff (%)	U plane eff (%)	X' plane eff (%)
PC-1	84	79	73	69
PC-2	82	91	81	-
PC-3	87	77	80	-
DC-1	90	89	87	-
DC-2	93	89	89	-
DC-3	93	91	93	-
DC-4	89	85	85	88
DC-5	93	90	87	91
DC-6	90	85	85	85

Table 3.4: Summary of the muon counter efficiencies

Counter	Efficiency (%)
μ_1	91.4 ± 2.4
μ_2	97.0 ± 1.1
μ_3	96.0 ± 0.7
μ_Y	92.0 ± 3.7

efficiency was defined as the percentage of tracks with a muon counter lit within the tolerance (for more details see reference [45]). Muon counter efficiencies were carefully monitored throughout the run. The muon counter efficiencies, averaged over the entire run, are shown in Table 3.4. The errors reported represent variances on the arithmetic mean ($\sigma^2 = \frac{1}{n-1}\sum_{i=1}^{n}(\epsilon_i - < \epsilon >)^2$) and they are mainly due to fluctuations during the data collection period. The lower efficiency of μ_1 and μ_Y is due to gaps in between counters in the hodoscope plane; these were not present in the μ_2 and μ_3 walls.

3.3 Electromagnetic calorimeter

Special calibration runs based on electron or positron beams of known energy were used to determine the gain constants for the electromagnetic detector elements. During the calibration runs, the target was moved out of the beam line and the glass house was moved so that the beam was centered sequentially on to each Main Array glass block. The nominal beam energies used for the calibration runs were 6, 10, 30, 60, 100 GeV. The Cerenkov counter information was used to separate the electrons from pions. Pion contamination in the beam varied between 3% at the lower energies and 50% at 100 GeV. Pion background in the final sample of tagged electrons was estimated to be less than 1%. At the beginning of each calibration, beam line elements were used to deflect the beam so that it traversed the live region of all the upstream chambers. A further deflection by Rosie combined with the track measurement by the downstream chambers then allowed the evaluation of the mean value and the width of the beam momentum distribution. This information was found to be in agreement with predictions obtained from a simulation of the beam transport line. The momentum spread of the beam was typically $\Delta P/P = 0.7\%$.

3.3.1 Calibration procedure

One of the main tasks in the calibration of any apparatus is to determine the parameters needed to convert the raw data to the desired physical quantities. In the case of the electromagnetic calorimeter the gain constants, used to convert ADC counts of the measured pulse height into energy, had to be determined. As a first step, the gain constants for the electromagnetic detector were established online by referring the observed pulse height to the nominal beam energy. Using a special trigger, which required only a beam particle tagged as an electron, calibration events were also written to tape to allow further offline analysis.

Online gain setting

The settings of the photomultiplier high voltage gains were chosen to reach a good compromise between the aim of optimizing the resolution (which would imply large gain) and the necessity of measuring high energy showers. To measure most of the kinematically attainable photons, the gains were set radially; in the small block region the least ADC count was made to correspond to 8.3 MeV, in the region of large SCG1-C blocks to 5 MeV, and in the lead glass region to 3.3 MeV. Using the 30 Gev beam, the high voltage of each photomultiplier was set online while keeping the analysis magnet off. The values of the high voltage were subsequently adjusted to compensate for the effect of the fringe field from the magnet. For this purpose, the LED pulse height measured with magnet-off was compared to the magnet-on pulse height and the gains of each phototube were modified accordingly.

Offline gain determination

30 GeV calibration electron showers in the calorimeter blocks were analyzed offline to get the best possible value of the gains. Events with more than one reconstructed beam track were removed from the sample. An iterative procedure was used to calculate the calibration constants which relate pulse height to energy for each block. Starting with the values of the gains determined online from the nominal energy of the beam, a fit was performed to minimize the χ^2 defined as:

$$\chi^2 = \sum_{n=1}^{N_{ev}} (E - E_n)^2 \tag{3.1}$$

where E is the beam energy, E_n is the sum of the energy deposited in the Active Converter and in the Main Array blocks for the n-th event.

For the generic n-th event, the energy deposited in the k-th element of the electromagnetic detector is related to the pulse height measured:

$$E_{k_n} = G_k P_{k_n} \tag{3.2}$$

where:

- G_k is the gain factor for the detector element k

- P_{k_n} is the pulse height of the detector element k in the n-th event

Only the beam-centered block gain constants (in the Main Array and in the Active Converter) were treated as unknown in the minimization procedure of a given block. More specifically, in terms of the glass gain constants for individual blocks different equations were written for the regions covered by the two different Active Converters:

1) In the region of the Glass Converter, using the index a for targeted Main Array block, b for the hit Front Converter block, c for the hit Back Converter block, we can write for the n-th event:

$$E_n = E_{a_n} + \sum_{i=1,}^{N_a} E_{i_n} + E_{b_n} + \sum_{j=1,}^{N_b} E_{j_n} + E_{c_n} + \sum_{l=1,}^{N_c} E_{l_n} \qquad (3.3)$$

where:

- the index i runs over the N_a neighbors of the Main Array block a

- the index j runs over the N_b neighbors of the Front converter block b

- the index l runs over the N_c neighbors of the Back Converter block c

The measured energy in the Glass Converter was affected by glass attenuation, therefore a correction was applied to account for the different attenuation of light for particles entering the Converter at different vertical positions. To optimize the resolution, the attenuation coefficients were included among the fitted parameters. The energy deposition measured in the block b of the Active Converter, hit by the beam at a certain distance d from the phototube, was written as:

$$E_{b_n} = (d + k_0)^{k_1} G_b P_{b_n} \qquad (3.4)$$

where k_0 and k_1 are parameters which were empirically determined from the calibration, since the energy deposited in a specific Active Converter block was measured for three different values of the distance d from the phototube (corresponding to three different targeted Main Array blocks).

2) In the LGC region the tubes in the X-view were used to determine the energy deposited in the Lead Gas Converter. Using the index a for targeted Main Array block, b for the hit tube in the X view of the LGC we can write:

$$E_n = E_{a_n} + \sum_{i=1,}^{N_a} E_{i_n} + E_{b_n} + \sum_{j=1,}^{N_b} E_{j_n} \tag{3.5}$$

where:

- the index i runs over the N_a neighbors of the Main Array block a
- the index j runs over the N_b neighbors of the hit tube b in the X view of the LGC (4 on each side).

Before doing the calibration, the LGC tube to tube relative gains were determined by looking at a large number of standard data events taken just before or after the calibration. Assuming that the interaction dynamics produce a smooth average profile of the energy deposition in the tubes, a smoothing procedure fpr the profile was used to establish the relative tube gains. The relative tube gains obtained in such a fashion were used as input to the calibration procedure, which was used to determine the overall gain constants for the four different quadrants of the LGC (each quadrant was connected to a different power supply, therefore four different gain constants had to be determined). The energies are related to the measured pulse heights as shown in Equation 3.2. For the purpose of calibrating a given block, only the Main Array targeted block and one LGC gain constant were treated as unknown.

In addition to the gain, two correction factors were also determined as a result of the calibration procedure for each Main Array block. Because of the attenuation of light in the Main Array blocks, the Main Array energy measured at the phototube will depend upon the longitudinal distribution of the shower development. Parametrizing in terms

of z, the shower-maximum depth position[1] in the Main Array, one can write:

$$E_{MA} = E_{MA_{measured}}(1 + \frac{\lambda_m}{z}) \tag{3.6}$$

where λ_m is a constant which depends on the glass quality of the Main Array block m. Empirically it was found that the inverse depth can be well represented by the ratio of the energy measured in the Active Converter to the energy measured in the Main Array. In fact, a shower that starts later deposits less energy in the converter and more energy in the Main Array, farther back in the blocks (therefore closer to the photomultipliers), than an early-developing shower. Since the light would have to go through less glass, more of it would reach the photomultiplier giving a larger signal. We can then write:

$$E_{TOT} = \alpha_m E_{MA} + \beta_m E_{AC} \tag{3.7}$$

The factors α_m and β_m were determined block by block for electrons at the different calibration energies and a slow variation with energy was found. To take this into account the factors α_m and β_m corresponding to an arbitrary value of the energy were obtained by linear interpolation between two nearby known energy points (more details on the calibration procedure can be found in [46]).

After a set of gain constants was obtained for all of the blocks, such values were used as input for the next iteration until convergence was reached. In this procedure some of the gain constants were overdetermined since the active plane elements cover more than one Main Array block. The final set of gain constants was then determined by averaging the different values obtained for each detector element. The 30 GeV electron beam energy spectrum, obtained using the final set of calibration constants, is shown in Figure 3.4 for the four different regions of the detector. Looking at the energy spectra for different Main Array blocks and making a gaussian fit to the distributions, the mean energy value for each block can be extracted. As shown in Figure 3.5 (for a subsample of blocks selected randomly) this calibration procedure fixes the energy scale for each block to better than 1%. It should be noted in fact that although the χ^2 procedure,

[1] Defined as the depth where the shower deposits the maximum amount of energy.

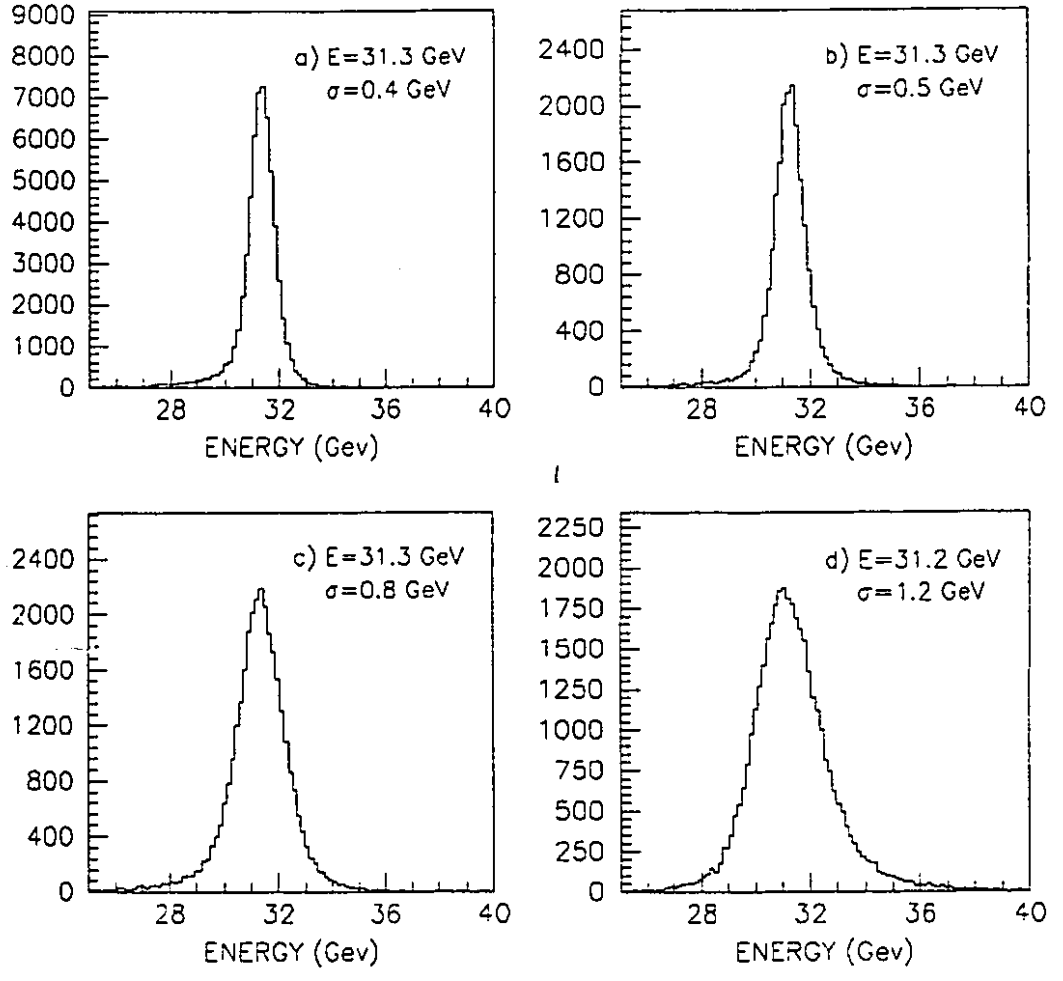

Figure 3.4: Reconstructed energy spectrum for a 30 GeV calibration run in the different regions of the detector; a) SF5 blocks, b) Large SCG blocks with GTH as position hodoscope, c) Large SCG blocks with LGC as position detector, d) Small SCG blocks.

Table 3.5: Summary of the energy resolution in the four different regions of the detector. The mean beam energy of each calibration run is also indicated.

Region	σ_E (GeV) E=6.6 GeV	σ_E (GeV) E=10.6 GeV	σ_E (GeV) E=31.2 GeV	σ_E (GeV) E=60.5 GeV
Small SCG	0.433±0.005	0.558 ± 0.006	1.153±0.008	2.10±0.03
Large SCG (LGC)	0.374±0.004	0.451 ± 0.004	0.853±0.006	1.42 ±0.01
Large SCG (GTH)	0.184±0.03	0.217 ± 0.02	0.507±0.02	0.94 ±0.02
SF5	0.197±0.002	0.232 ± 0.002	0.453±0.003	0.840±0.007

as defined in Equation 3.1, minimizes the width of the energy distribution for all Main Array blocks, it does not guarantee that the central energy value found for each block is the same for all the blocks.

3.3.2 Energy resolution

The ability to calibrate the detector using electrons/positrons of known energy in the calorimeter enabled us to investigate the energy resolution for electromagnetic showers for a wide range of energies. The fractional energy resolution, σ_E/E, was extracted from the width of the calibration energy spectra. The contribution to the width due to the momentum spread of the electron beam was estimated from the deflected electron runs to be 0.7 %. After removing it in quadrature, the energy resolution obtained for the four different regions of the detector at different energies is shown in Table 3.5.

The measured fractional energy resolution is usually parametrized as:

$$\frac{\sigma_E}{E} = a + \frac{b}{\sqrt{E}} \tag{3.8}$$

In Figure 3.6 the plot σ_E/E for different calibration runs versus $1/\sqrt{E}$ and a least-squares straight-line fit are shown. Table 3.6 summarizes the values obtained for a and b in the different regions of the detector. The SCG resolution had been measured in a test performed earlier by the E705 collaboration at the Stanford Linear Accelerator Center ([48]). The measurement comparable to the SLAC results is the one for the large

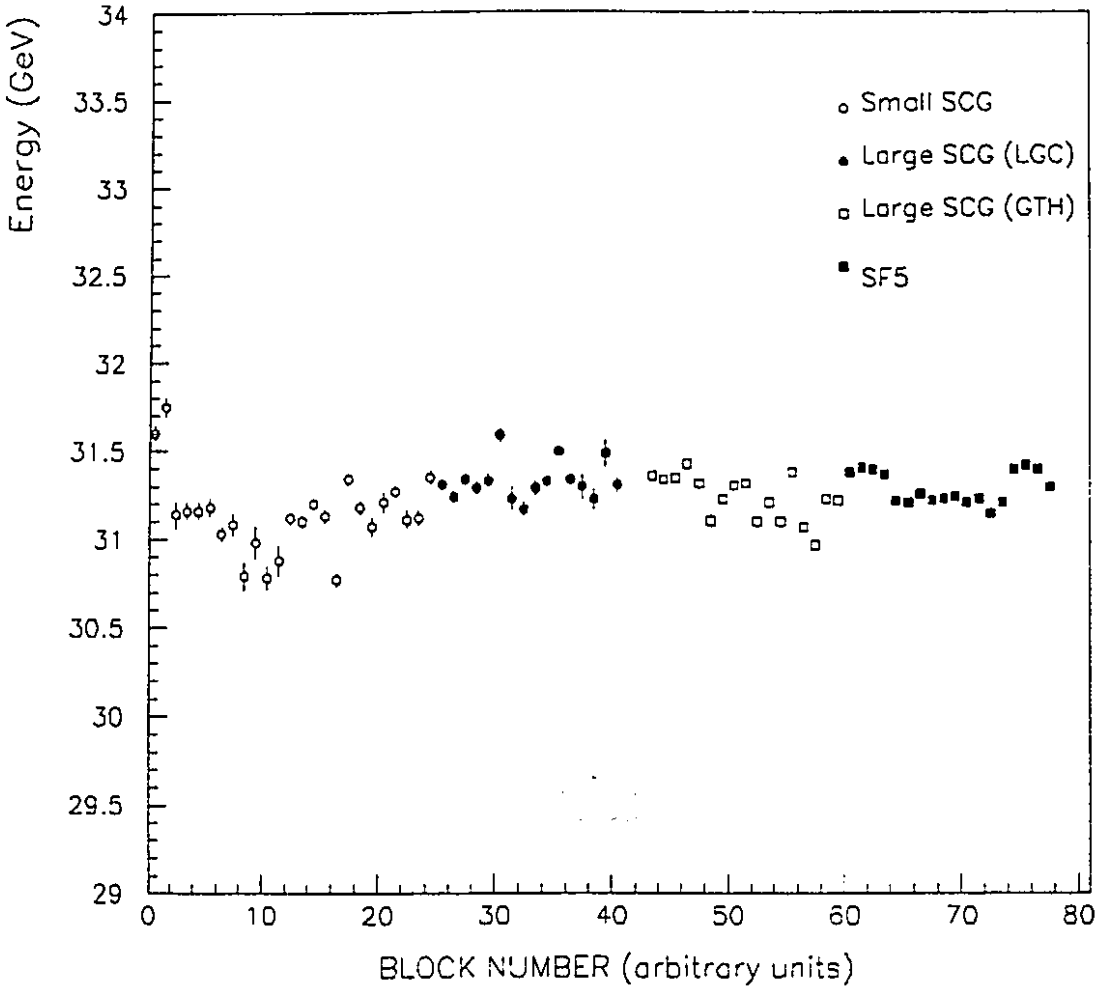

Figure 3.5: Mean energy for 30 GeV calibration run. Each point represents a different targeted Main Array block

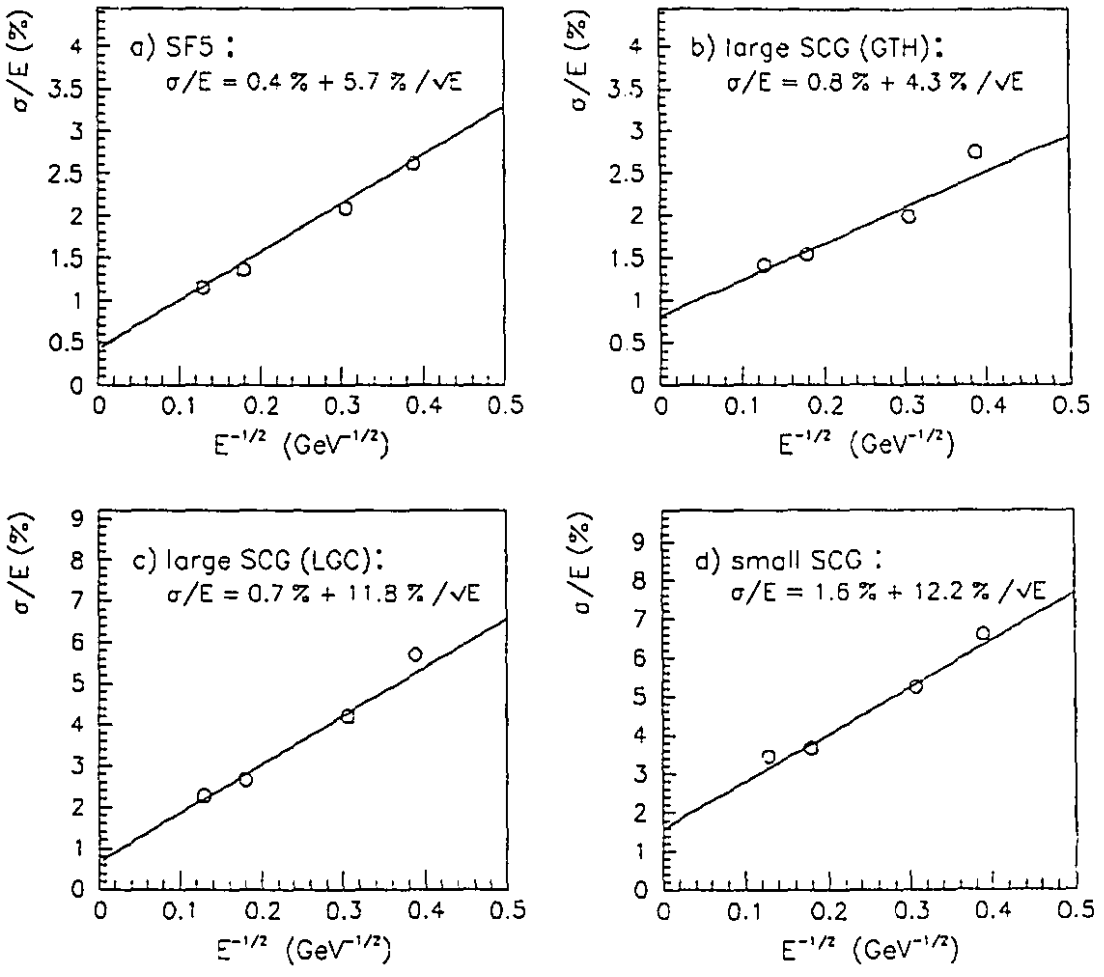

Figure 3.6: Fractional energy resolution versus the inverse of the square root of the energy (E). A linear fit to the data is also shown.

Table 3.6: Summary of the resolution constants in the different regions of the detector.

Region	a	b $(GeV^{1/2})$
Small SCG1-C	1.573±0.003	12.20 ± 0.08
Large SCG1-C (LGC)	0.694±0.001	11.77 ± 0.03
Large SCG1-C (GTH)	0.806±0.001	4.29 ± 0.02
SF5	0.433±0.001	5.71 ± 0.01

SCG1-C behind the GTII hodoscope where it was found that $\sigma/E = (0.64+3.9/\sqrt{E})\%$. The small difference from the SLAC measurement can be attributed to the difference in material of the two hodoscopes and to the 1.3 cm thick steel in front of the active converter during the E705 run. The poor energy resolution of the LGC accounts for the worse resolution in that region. The choice of the LGC was motivated by the better segmentation of the device with respect to the Glass Converter, to ease the pattern recognition in the busy central region. Also the transverse development of electromagnetic showers in the LGC was smaller, enabling the reconstruction of showers with small spatial separation as for photons coming from high pt π^0 decays. Another advantage of the LGC detector was that it had less interaction lengths than the Glass Converter region. Previous measurements [49] of the SF5 resolution gave comparable results.

3.3.3 LED triggers

LED triggers were used throughout the run to monitor the gain and pedestal stability.

Gain monitoring

Once the calibration constants were determined, LED data were used to track the gain variation in between calibrations, by comparing the detector response to LED flashes. The stability of the LED system was monitored using the pulses coming from three PIN diodes. To get the gain constants at a specific point in time, the gain

calibration constants were updated in the following way:

$$g_{current} = g_{calibration} \frac{LED_{calibration} PIN_{current}}{LED_{current} PIN_{calibration}} \tag{3.9}$$

where LED is the mean pulse height of the glass response to the LED pulse, PIN is the mean pulse height recorded by the PIN diode, referred to calibration or current time. This procedure was tested by determining the gains for two calibration runs taken in different times. The first set of gains was corrected with this method and compared with the second set. It was found that it was possible to extrapolate gains over the entire run with an accuracy of ±2% [47].

Pedestal correction

The pedestal is the effective zero level for a channel, that is the number of ADC counts corresponding no energy deposited. Pedestal values for each block were extracted using LED trigger events with the filter wheel closed (when no LED light was transmitted). These events were recorded throughout the run by pulsing the LED during the off-spill portion of the accelerator cycle. Out of the beam spill, pedestal fluctuations were found to be of the order of few ADC counts, corresponding to energy values of 5-20 MeV.

Special runs were also dedicated to record LED triggers during the beam spill, making use of a special trigger which vetoed all interactions in a window from 250 ns before to 250 ns after the LED pulse. The in-spill pedestals were found to be different from the ones extracted out of the spill. This effect was observed by plotting the pedestal distribution in each block as a function of the spill clock time, measured relative to the beginning of each spill. In Figure 3.7 the pedestal recorded in one SCG block and one SF5 block is shown as a function of clock time.

The difference between the in-spill pedestal distribution (corresponding to $t \leq 24$ s) and out-of-spill ($t \geq 24$s) is evident for both blocks, although the effect is more evident in the SCG block. A detailed study found the pedestals to be dependent on interaction rate and glass type and to be decreasing with distance from the center of the calorimeter (as

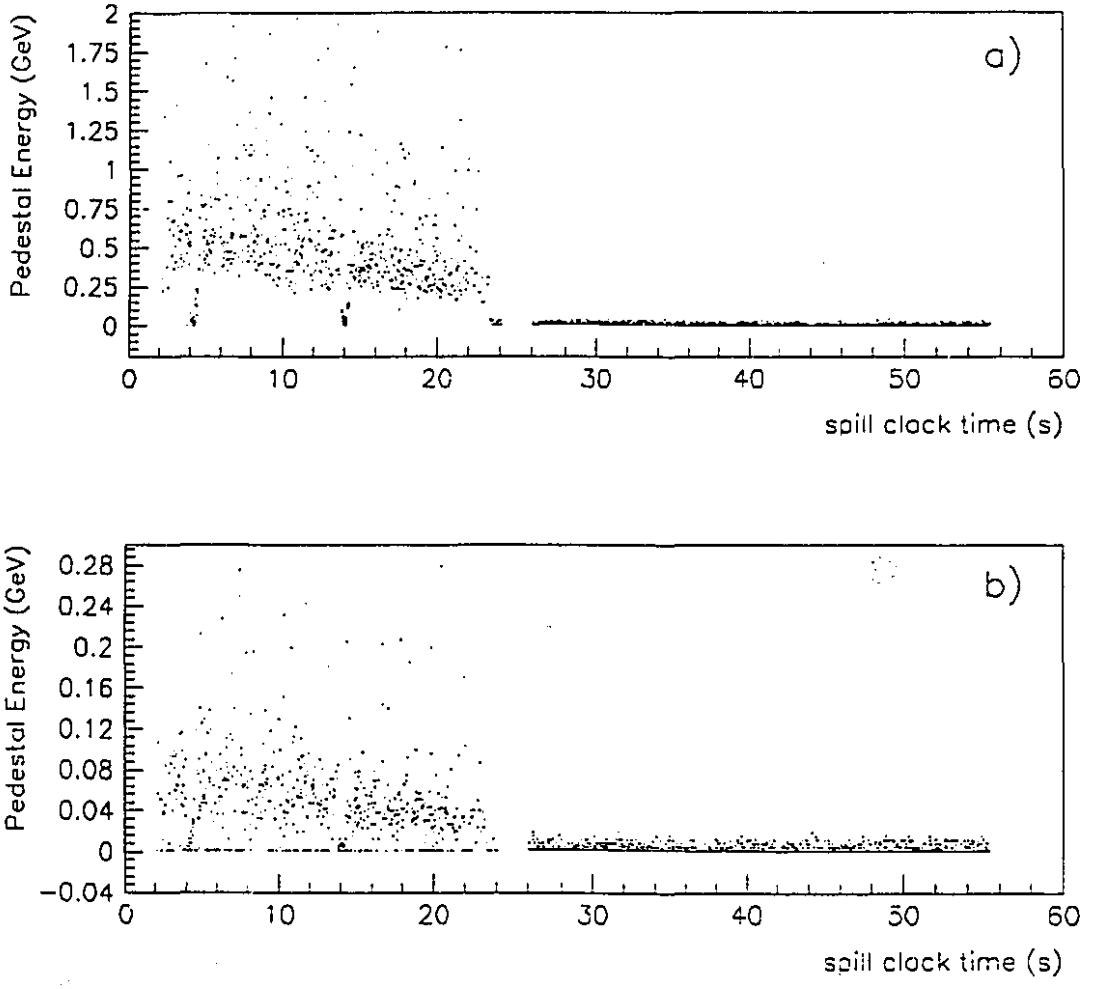

Figure 3.7: Pedestal energy as a function of spill clock time for block 384 (small SCG) and block 169 (SF5).

reported in reference [47]). This effect was eventually traced to an incorrect behaviour of the newly designed electronics employed for the glass readout and an "after the fact" correction procedure was then attempted. Event by event, the interaction rate could be measured using the value set for the Before Bit. For each block of the Main Array, the value of Before Bit was set proportional to the energy deposited in a block before the triggering interaction time. The Before Energy in each block, a three bit field, was then measured in units corresponding to 1/8 of the energy full-scale (12 GeV for SF5, 19 GeV for large SCG1-C, 31 GeV for the small SC1G-C blocks). Using in-spill LED triggers, the pedestal energy distribution, as a function of total Before Energy in the event, could be measured for each block. As shown in Figure 3.8, for one SCG block and one SF5 block, a strong correlation between the pedestal shift and the Before Energy was found. A pedestal subtraction could be made as a function of Before Energy using correction factors extracted from in-spill LED triggers. The corrected energy after pedestal subtraction is shown in Figure 3.9 as a function of E705 clock time for one SCG and one SF5 block. Even if the correction removed some of the systematic in-spill pedestal shift, the broadening of the pedestal energy distribution for in-spill events compared with the out-of-spill ones, indicated that not all of the effect could be removed and that the energy resolution of the detector in the data would be degraded. The method used to determine the energy resolution in the data will be described in the next chapter.

3.3.4 Position resolution

During calibration, the precise impact location of the electron/positron beam in the calorimeter was determined by using the beam chamber information. Therefore the position resolution of the tube hodoscopes could be investigated for several shower energies, by studying electron calibration runs and comparing the position of the shower as determined from the electromagnetic calorimeter information and from the position of the beam track projected on to the glass. The distributions of the residuals between the beam track projection and the shower position, for the X and Y view of both

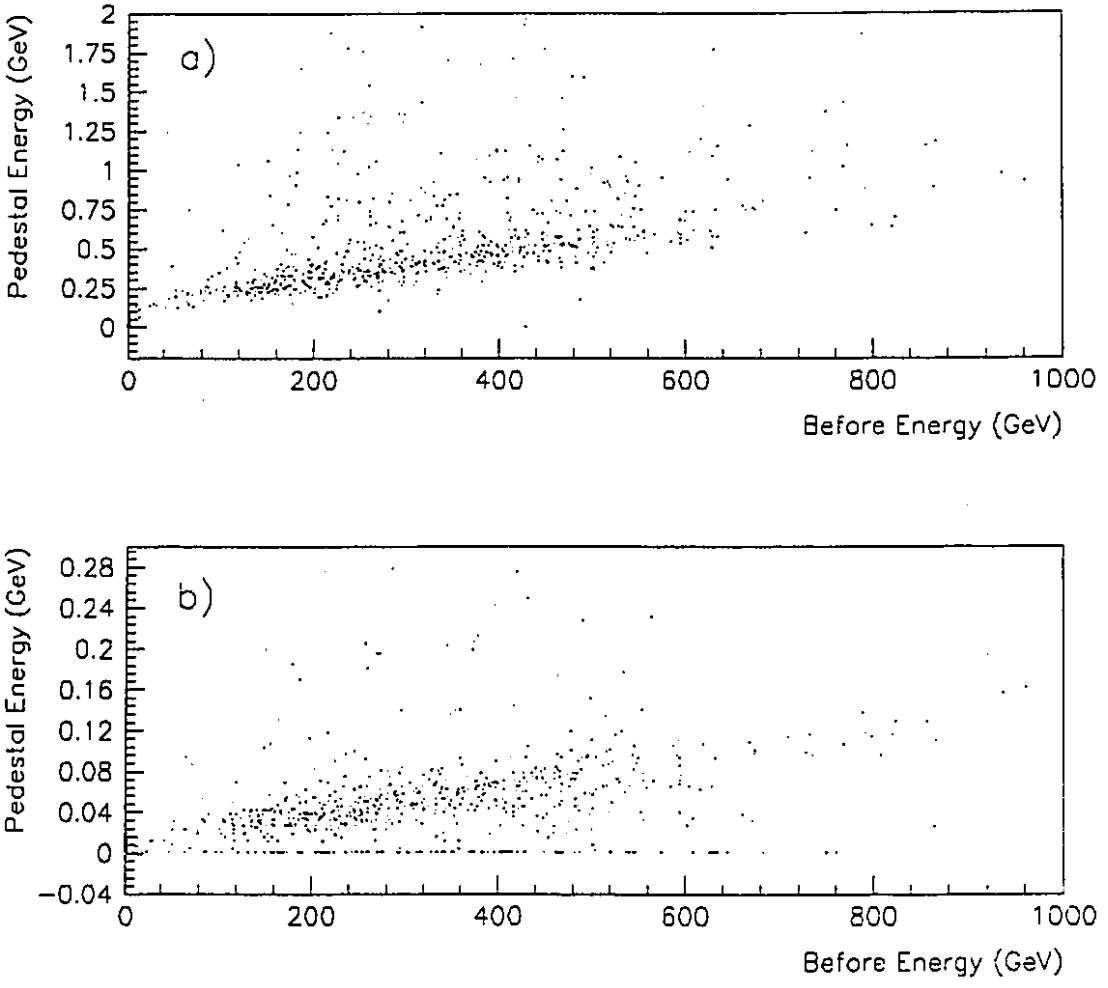

Figure 3.8: Pedestal energy as a function of "Before Bit" for block 384 (small SCG) and block 169 (SF5).

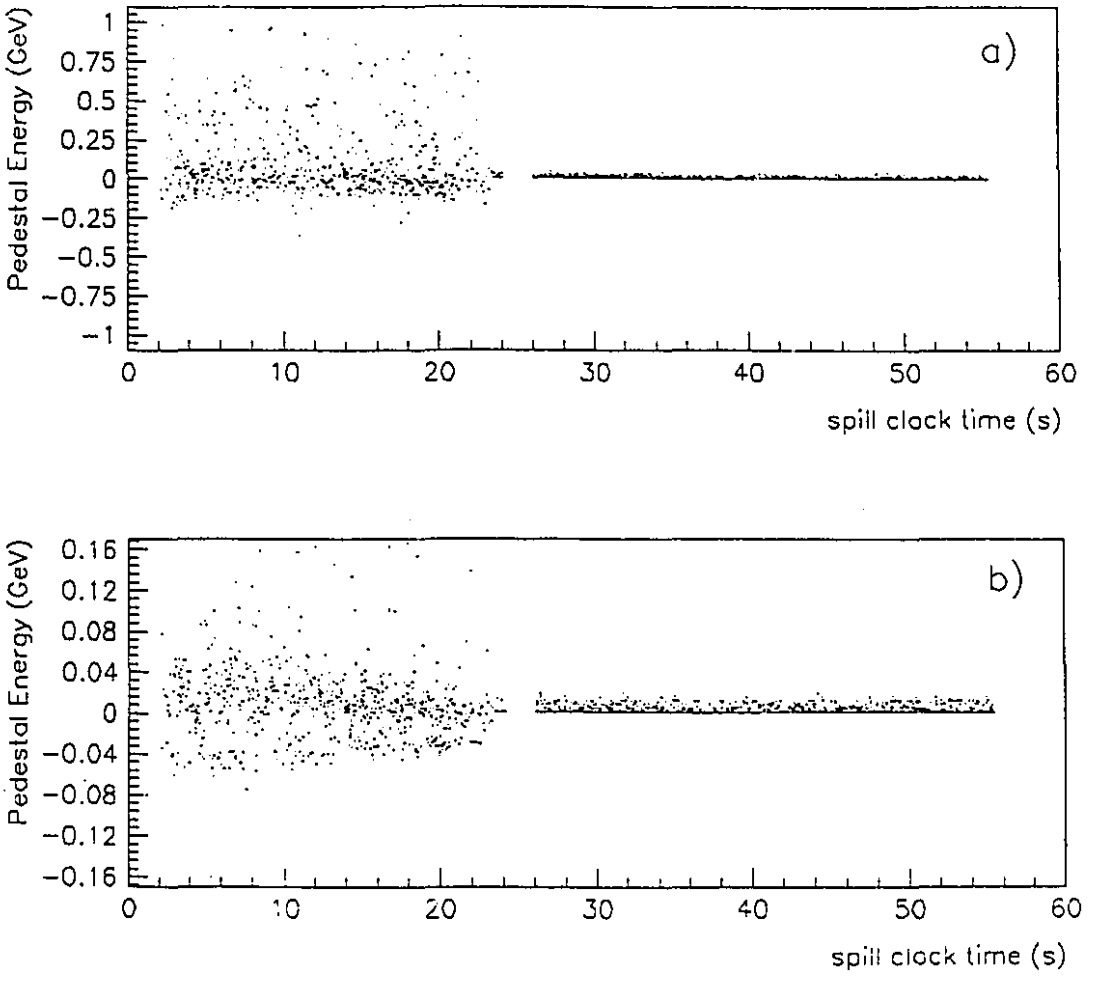

Figure 3.9: Corrected pedestal energy as a function of "Before Bit" for block 384 (small SCG) and block 169 (SF5).

hodoscopes, are shown in Figure 3.10. A Monte Carlo simulation was done to evaluate the effect of multiple scattering in the spectrometer upon the residual distribution. After unfolding the estimated beam projection error, values for position resolution in the different regions of the detector as function of energy were obtained and are shown in Figure 3.11.

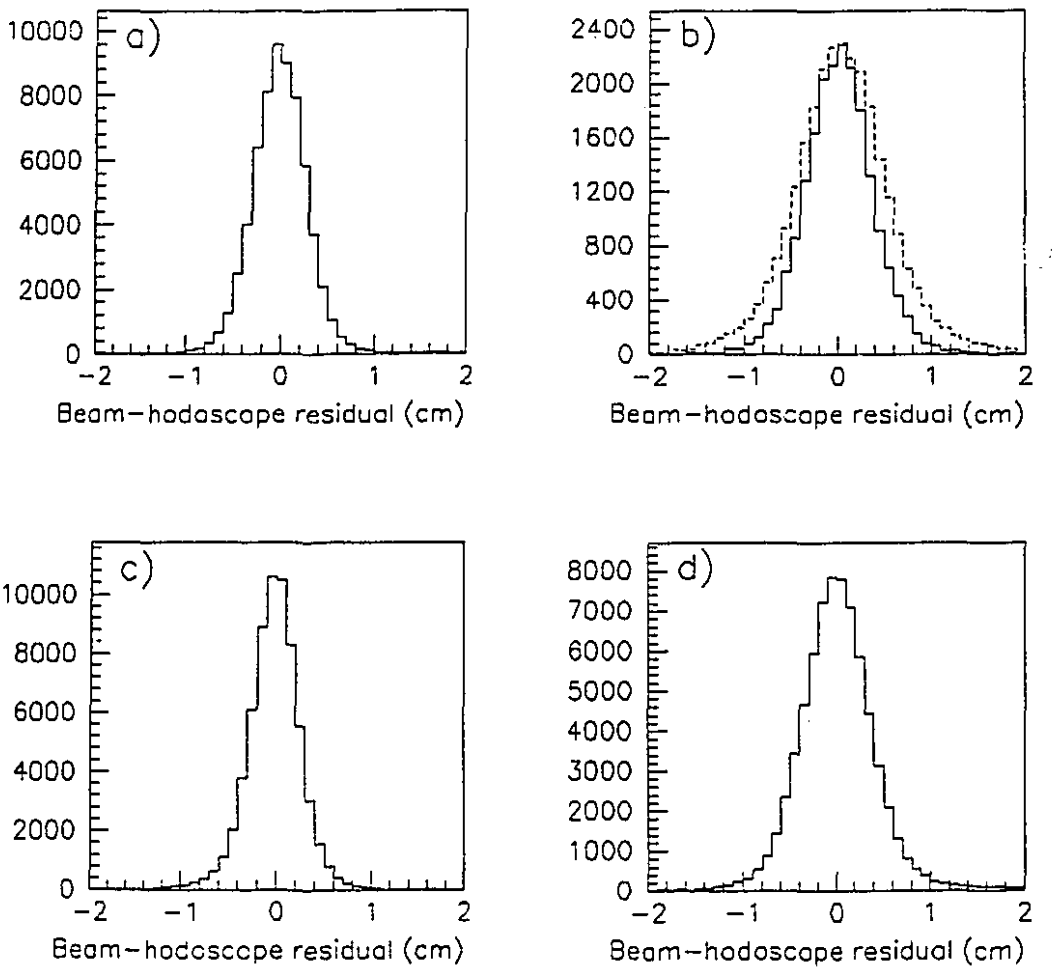

Figure 3.10: Difference between the beam track projection into the glass and the reconstructed shower position for 30 GeV calibration electrons in the different region of the detector: a) LGC X view; b) GTH X view (full line single tubes, dotted line double tubes); c) LGC Y view; d) GTH Y view.

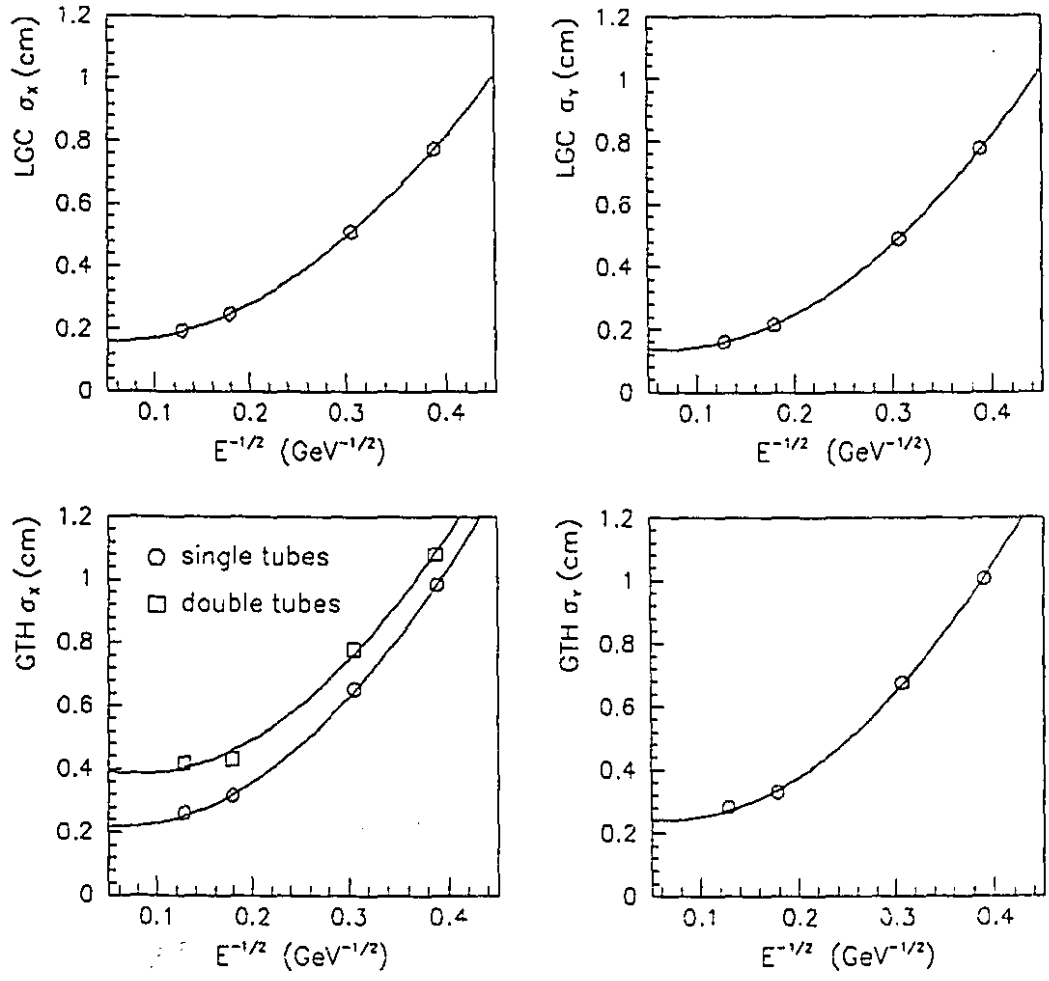

Figure 3.11: Position resolution versus the inverse of the square root of the energy. The line shows a quadratic fit to the data.

Chapter 4

Charged particle reconstruction

This chapter describes the algorithm used to reconstruct the trajectories of the charged particles in the spectrometer. The analysis of the raw data to reconstruct charged particles was performed on the Fermilab ACP parallel processor system. The computer program, written to interpret the raw data and convert them into physical quantities, consisted of a set of routines driven by a main program. The input to these routines were the hits in the proportional and drift chambers and the latched signals from the charged particle hodoscope and muon counters. The trackfinding technique used was the "track road" method, where one candidate track was chosen by starting with two points and predictions were made to look for further points belonging to the track candidate. If additional points were found, they were added to the track, otherwise the track candidate was dropped. When the charged particle reconstruction was finished, the information on the beam trajectory, the interaction vertex and the charged particles four-momenta was added to the raw event data, which was then recorded onto an output tape. The reconstruction of charged tracks proceeded in the following sequential steps:

- Beam tracking.
- Front tracking.
- Interaction vertex reconstruction.
- Rear tracking.
- Linking rear and front tracks.

- Momentum and Charge determination.

In the following sections all of these steps will be described in detail and the results on the tracking efficiency and momentum resolution (obtained by a Monte Carlo simulation of the charged particle spectrometer) will be presented.

4.1 Beam tracking

The trajectory of the beam particles was reconstructed using the information of the three beam chambers (BC1, BC2 and BC3). The first step involved the reconstruction of space points defined by the combination of hits in two or three views. Using U and Y hits, the position of the expected V hit was computed and compared with the position of the closest V hit. A triplet was defined by the existence of a V hit within a predefined tolerance ($\pm$ 1 wire-spacing). In each chamber all possible YUV triplets were reconstructed and their coordinates were stored as space points. Then all possible doublets defined as the combination of two hits (UY,VY,UV) were formed and stored as space points. All the hits participating in a triplet were excluded from contributing to doublets. The space points in the three beam chambers were used to reconstruct tracks. Using the space points in BC1 and BC3 a track candidate was defined and projected into BC2. If a space point was found in BC2 within the tolerance, defined as four times the sigma of the BC2 space point, the track was fit, using the space points from all three chambers. If two of the reconstructed tracks shared two hits in more than one chamber, the two tracks were considered duplicates and the track with the worse chisquare was dropped. The beam tracks were stored in the beam track bank, in order of increasing chisquare, up to a maximum of five tracks. Typical beam track multiplicities, number of hits on the beam track, and χ^2 values from the beam track fitting are shown in Figure 4.1. Due to electronic noise and chamber inefficiencies and a small amount of real double tracks, about 50% of the events had more than one reconstructed beam track. Using these chamber information only, it was impossible to identify the beam responsible for the interaction, but at the vertex reconstruction

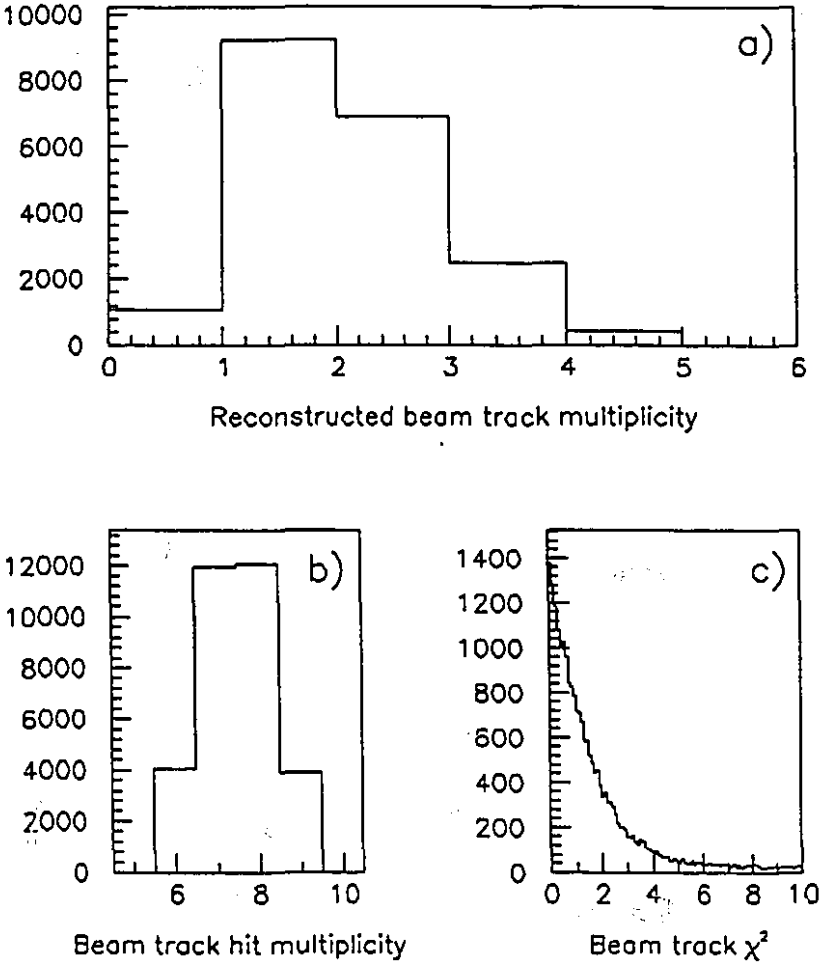

Figure 4.1: Reconstructed beam tracks: a) Beam track multiplicity, b) Number of hits on the beam track, c) χ^2 from the beam track fitting.

level (as described in section 4.3) this ambiguity was removed. The distributions for the X and Y projections at the middle of the target ($z_{target} = -533.$ cm) are shown in Figure 4.2.

4.2 Front tracking

Tracking upstream of the analysis magnet involved three MWPCs and three DCs for a total of 19 planes: 7 in the X view , 6 in the U view, 6 in the V view. The first step of the front tracking was to reconstruct track projections, called view tracks, in each of the three views (X,U,V) separately. Once all view tracks were reconstructed, the algorithm matched them to form space tracks.

4.2.1 View tracks

As a first step, the hits of each plane we reordered in ascending order. In each view, a pair of hits belonging to 2 different planes (called seed planes) were used to define a track candidate. The view track candidate was projected into all the other planes to search for other hits if it satisfied the following conditions:

- The track slope was within the spectrometer angular acceptance.
- The track projection into the middle of the magnet was within the acceptance o the magnet.
- The track was pointing to the target within the projection error.

The track candidate was projected into each plane and all hits found within the tolerance (defined to be ± 3 mm for MPWCs and ± 1 wire spacing for DCs) were selected. If at least four hits belonging to the track were found, a chisquare fit to a straight line was performed. The χ^2 distribution for view track candidates is shown in in Figure 4.3. If the χ^2 was ≤ 4, the view track was stored. For $4 \leq \chi^2 \leq 8$, the hit contributing the largest value to the chisquare was removed. Then if the number of hits left was ≥ 4,

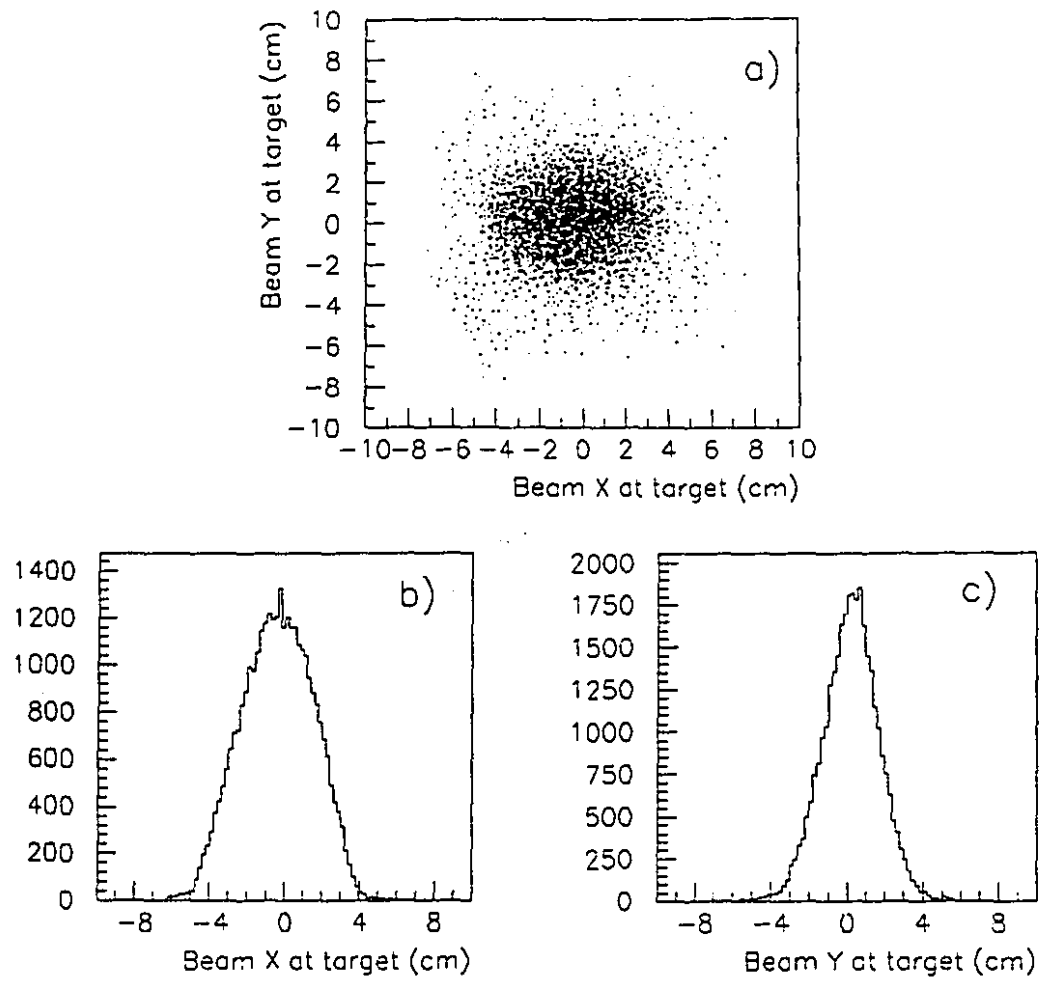

Figure 4.2: Reconstructed beam tracks projected into the middle of the target: a) Y versus X coordinate, b) X coordinate, c) Y coordinate.

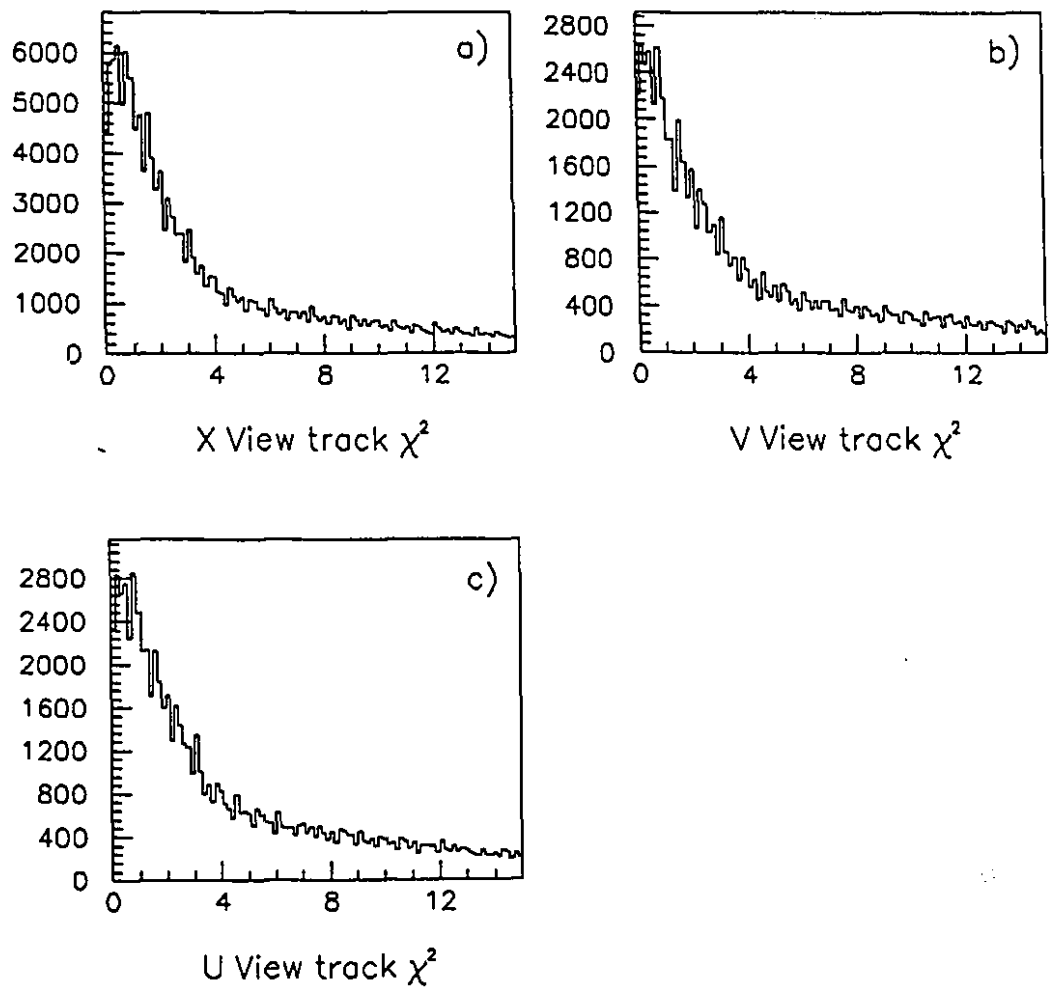

Figure 4.3: Front view track χ^2 distribution: a)X view, b)U view, c) V view.

the track was refit to see if the new χ^2 was acceptable or not. For $\chi^2 > 8$, the view track was dropped.

Several passes were made using as seed planes all possible combinations of the 7 (or 6) planes of each view, excluding combinations of adjacent planes. After all the view tracks were formed, they were cross-checked for common hits. If two view tracks shared two or more wires, the one with the smaller number of hits was droppped; if they had the same number of hits, the one with the worse χ^2 was dropped.

The same procedure was repeated for all three views. Typical distributions of view track multiplicity and the number of hits found for each track are shown in Figure 4.4.

4.2.2 Space tracks

The space tracks were reconstructed by matching the view tracks in two passes. In the first pass, combinations were tried by taking as "seed" U and V view tracks. If a "seed pair" formed a track candidate within the magnet aperture and projected back to the target, a search among the X view tracks was made. A space track was found if the following requirements were satisfied:

1. The difference between the x slope computed using U and V view tracks and the X view track slope was < 10 mrad.

2. The difference between the x intercept computed using U and V view tracks and the X view tracks intercept was < 0.5 cm.

3. The total number of hits on the space track was ≥ 8.

4. The "pseudo-χ^2" was required to be ≤ 15, where "pseudo-χ^2" was defined as the χ^2 (see equation 4.1) computed using the view track fit parameters (intercepts and slopes).

If any of the view tracks had been already used to form another space track, the two tracks were compared and the track with the worse pseudo-chisquare was dropped.

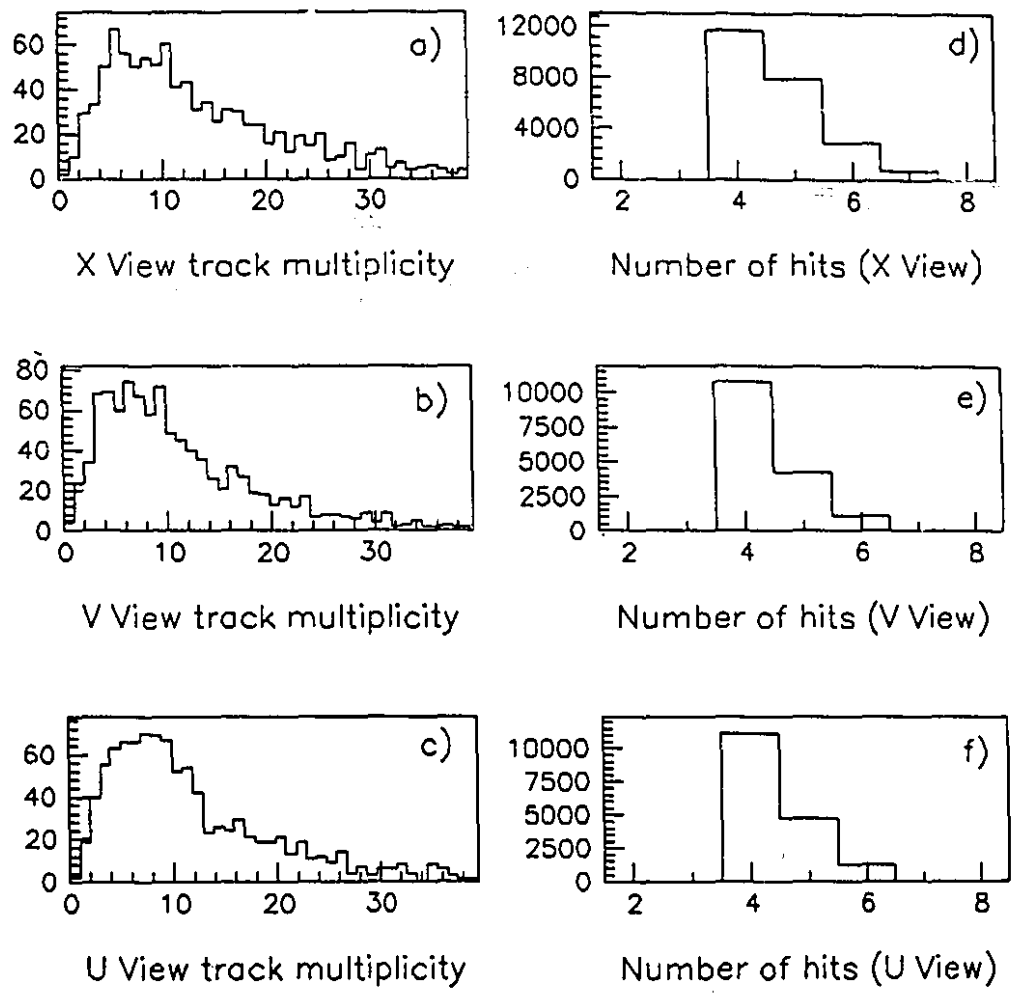

Figure 4.4: Front view track multiplicity distribution and number of hits on the tracks: a)-d) X view, b-e)U view, c-f) V view.

After all possible space tracks candidates were formed using all three view tracks, a second attempt to make space tracks was made by using a pair of tracks in two seed views and looking for hits in the search view. All possible combinations of the X, U and V views were used as seed views. The pair of seed view tracks were projected into all the search planes. If at least two hits were found within the tolerance, they were used, along with the hits of the seed view tracks, to compute the "pseudo-χ^2". If the "pseudo-χ^2" was ≤ 15 and the total number of hits on the space track was ≥ 8, the track was kept as a space track candidate.

Finally, the track slopes and intercepts were determined by minimizing the following χ^2:

$$\chi^2 = \frac{1}{N-4}\sum_i \left(\frac{X_i - x_i}{\sigma_i}\right)^2 \tag{4.1}$$

$$x_i = (a_x z_i + b_x) * cos(\alpha_i) - (a_y z_i + b_y) * sin(\alpha_i) \tag{4.2}$$

where:

X_i = location of the hit in the plane i

x_i = track projected location at plane i

N = number of hits on the track

i= index over the N planes

a_x, a_y = slopes of candidate track in X and Y projections

b_x, b_y = intercepts of candidate track in X and Y projections

α = angle of the orientation of the plane (see Table 2.2, 2.3).

Minimizing this χ^2, a system of equations was obtained and the space track parameters, a_x, a_y, b_x and b_y, were uniquely defined. The χ^2 distribution for space track candidates is shown in in Figure 4.5a.

For $\chi^2 \leq 5$, the track was stored in the front track bank. For $5 \leq \chi^2 \leq 15$, the hit contributing the largest value to the chisquare was removed. If the number of hits on

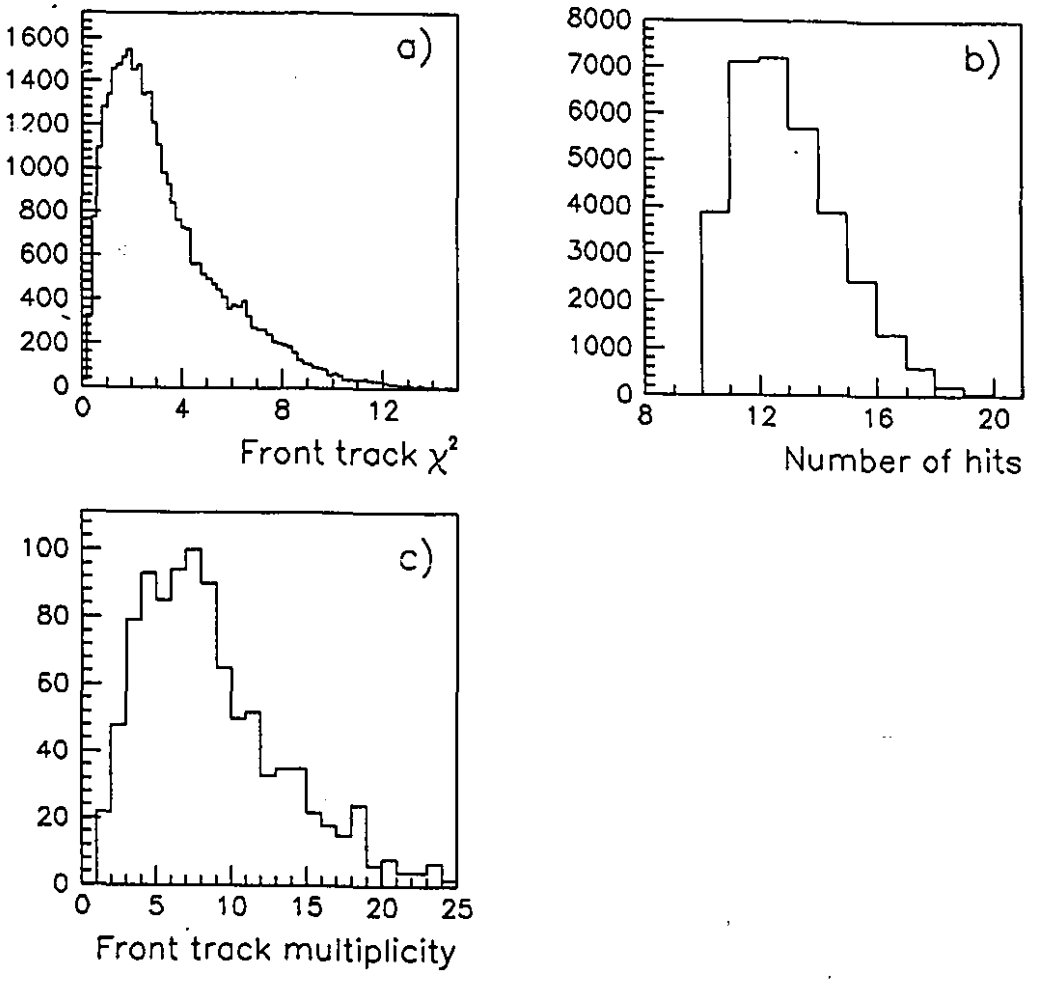

Figure 4.5: Front space tracks: a) χ^2 distribution, b) Number of hits on final sample, c) Number of front tracks per event.

the track was ≥ 8, the track was refit to see if the new χ^2 was acceptable or not. For $\chi^2 > 15$ the space track was dropped. The distribution of the number of hits on the final sample of front tracks is shown in in Figure 4.5b. On average 8.8 front tracks/event were reconstructed and the distribution of the front track multiplicity is shown in in Figure 4.5c.

4.3 Vertex reconstruction

Using the front tracks, two different methods were used to reconstruct the interaction vertex depending on whether the beam trajectory information was available or not.

4.3.1 Vertex reconstruction using beam and front tracks

If at least one beam track was reconstructed, the interaction vertex coordinates were found using the beam trajectory and the front tracks.

At first, the beam particle which actually produced the interaction was identified as the beam track which could be associated with the largest number of front tracks. Each of the beam tracks was projected into the target at different values of the Z-coordinate (16 different steps were made through the 33 cm long target). At each Z-coordinate, a circle was defined with a radius set to 3 times the projection error of the beam and the front track combined, as illustrated in Figure 4.6. At all the Z-coordinates within the target, the number of front tracks within the circle was evaluated for all the beam tracks. The beam track associated with the largest number of front tracks was flagged as the one causing the interaction if at least three tracks were pointing to it (referred to as interacting beam in the following). If the front track multiplicity associated with the beam was ≤ 2 the vertex was reconstructed without using the beam track information, as described in the next section.

Using the interacting beam track and the front tracks associated with it, the vertex

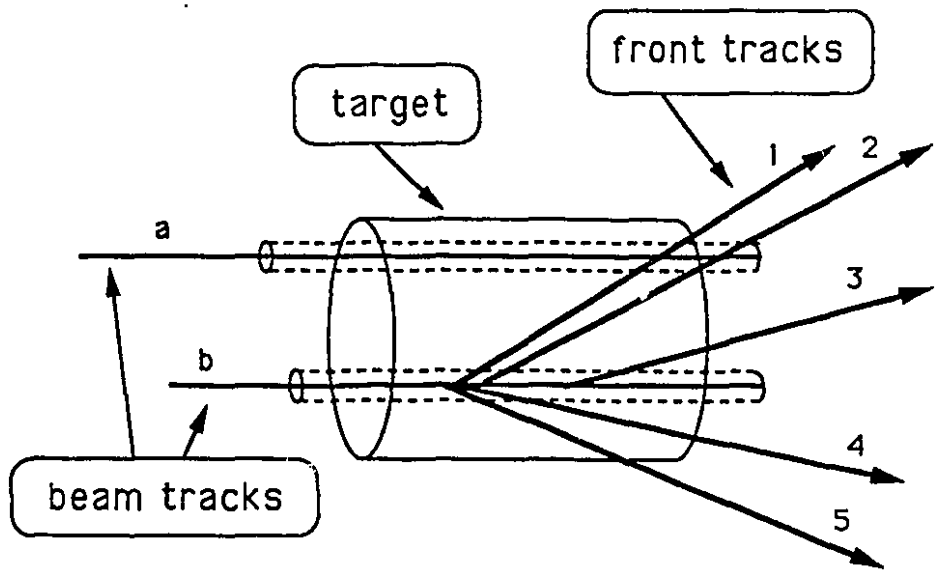

Figure 4.6: Vertex reconstruction: identification of the trajectory of the beam particle which produced the interaction.

z coordinate (z_v) was determined by minimizing the following χ^2:

$$\chi^2 = \sum_i \frac{(x_i - \mathcal{X}_B)^2}{\sigma_{x_i}^2 + \sigma_{\mathcal{X}_B}^2} + \frac{(y_i - \mathcal{Y}_B)^2}{\sigma_{y_i}^2 + \sigma_{\mathcal{Y}_B}^2}. \tag{4.3}$$

with : $$x_i = a_{x_i} \cdot z_v + b_{x_i} \qquad y_i = a_{y_i} \cdot z_v + b_{y_i} \tag{4.4}$$

$$\mathcal{X}_B = \mathcal{A}_{\mathcal{X}_B} \cdot z_v + \mathcal{B}_{\mathcal{X}_B} \qquad \mathcal{Y}_B = \mathcal{A}_{\mathcal{Y}_B} \cdot z_v + \mathcal{B}_{\mathcal{Y}_B} \tag{4.5}$$

where:

- i= index over all selected tracks.
- a_{x_i},a_{y_i}= x, y slopes of the i-th track.
- b_{x_i},b_{y_i}= x, y intercepts of the i-th track.
- σ_{x_i},σ_{y_i}= x, y projection errors for the i-th track calculated at z=-533.5 (the middle of the target).
- $\mathcal{A}_{\mathcal{X}_B}$,$\mathcal{A}_{\mathcal{B}_B}$= x, y slopes of the interacting beam track.

- $\mathcal{B}x_B$,$\mathcal{B}y_B$= x, y intercepts of the interacting beam track.

- σx_B,σy_B= x, y projection errors of the interacting beam track calculated at z=-533.5 cm (the middle of the target).

The vertex x and y coordinates, x_v and y_v, were determined as the interacting beam projection at z_v (using equation 4.5). Using this method the vertex resolution was found to be 2 cm in the direction of the beam (Z direction) and of 250 μm in the transverse projection (x,y).

4.3.2 Vertex reconstruction using only front tracks

If no beam track was reconstructed or none of the reconstructed beam tracks could be flagged as having caused the interaction, the vertex coordinates were determined by using only the front tracks. The vertex was reconstructed by minimizing the following χ^2:

$$\chi^2 = \sum_i \frac{(a_{x_i} \cdot z_v + b_{x_i} - x_v)^2}{\sigma_{x_i}^2} + \sum_i \frac{(a_{y_i} \cdot z_v + b_{y_i} - y_v)^2}{\sigma_{y_i}^2} \qquad (4.6)$$

where:

- i is the index running over the front tracks.

- a_{x_i},a_{y_i}= x, y slope of the track i.

- b_{x_i},b_{y_i}= x, y intercept of the track i.

- σ_{x_i},σ_{y_i}= x, y projection error of the track i calculated at z=-533.5 (the middle of the target).

- x_v, y_v, z_v is the x, y, z location of the vertex.

Two iterations were made to determine the vertex coordinates. At first, the vertex location was determined by using all the front tracks. The tracks giving a contribution to the χ^2 greater then 70 were removed as they were not pointing to the vertex. Then the fitting procedure was repeated using the remaining front tracks to get a more accurate

determination of the vertex. By using this method, the achieved vertex resolution was 1 mm on the determination of x_v and y_v and 5 cm in the determination of z_v.

4.4 Rear tracking

The tracking downstream of the analysis magnet involved the three drift chambers for a total of 12 planes: 6 in the X view, 3 in the U view, 3 in the V view. First X-view tracks were reconstructed, then the X-hits belonging to a track were used together with all the hits in the U or the V views to form Y-coordinates. Using the Y coordinates, two-dimensional YZ tracks were reconstructed. The space tracks were obtained by combining the X and Y view tracks.

4.4.1 X-view tracks

X view tracks were reconstructed by using a pair of hits belonging to the seed planes to define a track candidate. All possible combinations of one of the two planes in DC4 and one of the two in DC6 were used as seed planes. The view track candidate was projected into all the other planes to search for other hits, if it satisfied the following requirements:

- The track slope was within the spectrometer angular acceptance.
- The track projection at the middle of the magnet was within the acceptance of the magnet.

The track candidate was projected into each plane and hits within the tolerance (defined to be ± 3 mm) were selected. To reject out-of-time tracks and to reduce the combinatorial background, the information of the scintillation counters was used:

a) When dealing with the search for muon tracks, the muon hodoscope was used. The track was projected to each of the muon counter planes, the residual between the track projection and the center of the closest lit counter was computed. The

track was flagged as a muon if:

$$|\mu 1 \quad \text{residual}| \leq 19 \text{ cm}$$

$$|\mu 2 \quad \text{residual}| \leq 22 \text{ cm}$$

$$|\mu 3 \quad \text{residual}| \leq 27 \text{ cm}$$

b) When a search was made for all possible charged tracks, each track candidate was projected onto the CPX counter plane. The residual between the track projection and the center of the closest lit counter was computed. The track was stored as an X-view candidate if:

$$|\text{CPX} \quad \text{residual}| \leq 10 \text{ cm}$$

If at least 4 hits belonging to the track were found and at least one hit in each chamber, a chisquare fit was performed. For $\chi^2 \leq 8$, the view track was stored. For $8 \leq \chi^2 \leq 16$, the hit contributing the largest value to the χ^2 was removed. Then, if the number of hits left was ≥ 4, the track was refit to see if the new χ^2 was acceptable or not. For $\chi^2 \geq 16$, the view track was dropped. The distributions of the χ^2, the number of hits on the tracks and the number of reconstructed X-view tracks per event, are shown in Figure 4.7.

4.4.2 Rear space tracks

Each X-view track was used in combination with all the U and V hits to make a list of all possible Y hits. YZ tracks were reconstructed by using a pair of hits to define a track candidate. The track candidate was projected into all the other rear planes to search for other hits belonging to the track if:

- The track candidate was within the spectrometer angular acceptance (rear Y-slope ≤ 400 mrad).
- The track candidate, projected back into the middle of the magnet, was within the magnet acceptance.

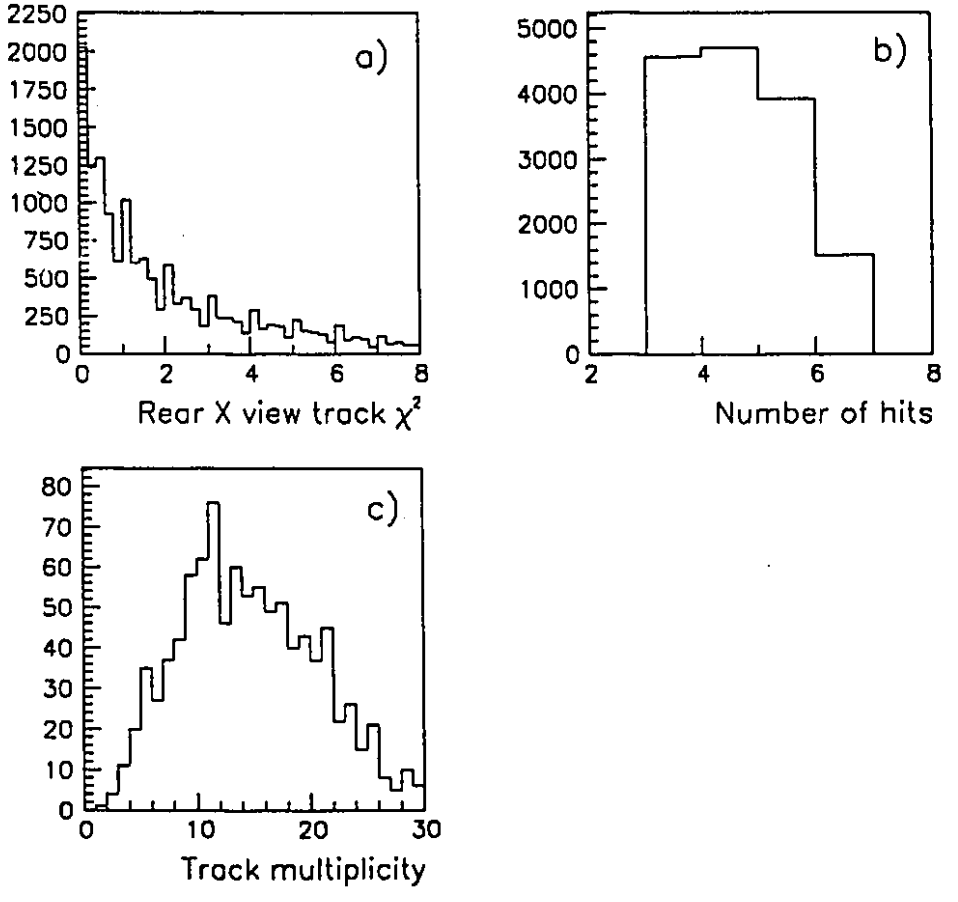

Figure 4.7: Rear X-view tracks: a) χ^2 distribution, b) Number of hits on final sample, c) Number of rear X-view tracks per event

- The slope of the front line connecting the projection of the rear track into the middle of the magnet to the center of the target was calculated. The track was kept if the difference between the Y-slope of the rear candidate and the front line was $\leq$ 30 mrad.

- When the tracking was used to reconstruct muon tracks, the YZ track was projected onto the μ_Y counter plane and the track was flagged as a muon if:

$$|\mu_Y \text{ residual}| \leq 19 \text{ cm}$$

If at least three hits belonging to the track were found (the tolerance was defined to be $\pm$3 mm), the pseudo-χ^2 was calculated. If the pseudo-χ^2 was $\leq$ 15, the hits were kept as a YZ track candidate. For each X-view track only the YZ candidate with the largest number of hits was kept. If more than one YZ candidate was found with the same number of hits, the one with the smallest value of the pseudo-χ^2 was stored. Finally the space track parameters were extracted by a chisquare fit as defined in Section 4.2.2 using all the rear plane hits belonging to the track. The χ^2 distribution, the number of hits on the reconstruted rear space tracks and the number of reconstructed tracks per event, are shown in Figure 4.8.

4.5 Linking rear and front tracks

Linking track segments upstream and downstream of the magnet allowed the determination of the particle trajectory throughout the spectrometer. To a good approximation, the magnetic field of the dipole magnet bent the tracks in the X-view only. The bending of the tracks in the field was considered as a simple bend at the magnetic center plane of the magnet. For each rear track, all front tracks were scanned to find the proper front-rear track pair. A front-rear match was found if:

- The Y-slope difference between rear and front segments was $\leq$ 20 mrad.

- The front and the rear track were extrapolated to the magnetic center plane and the projected difference was required to be $\leq$3 cm in the X-view and $\leq$6 cm in

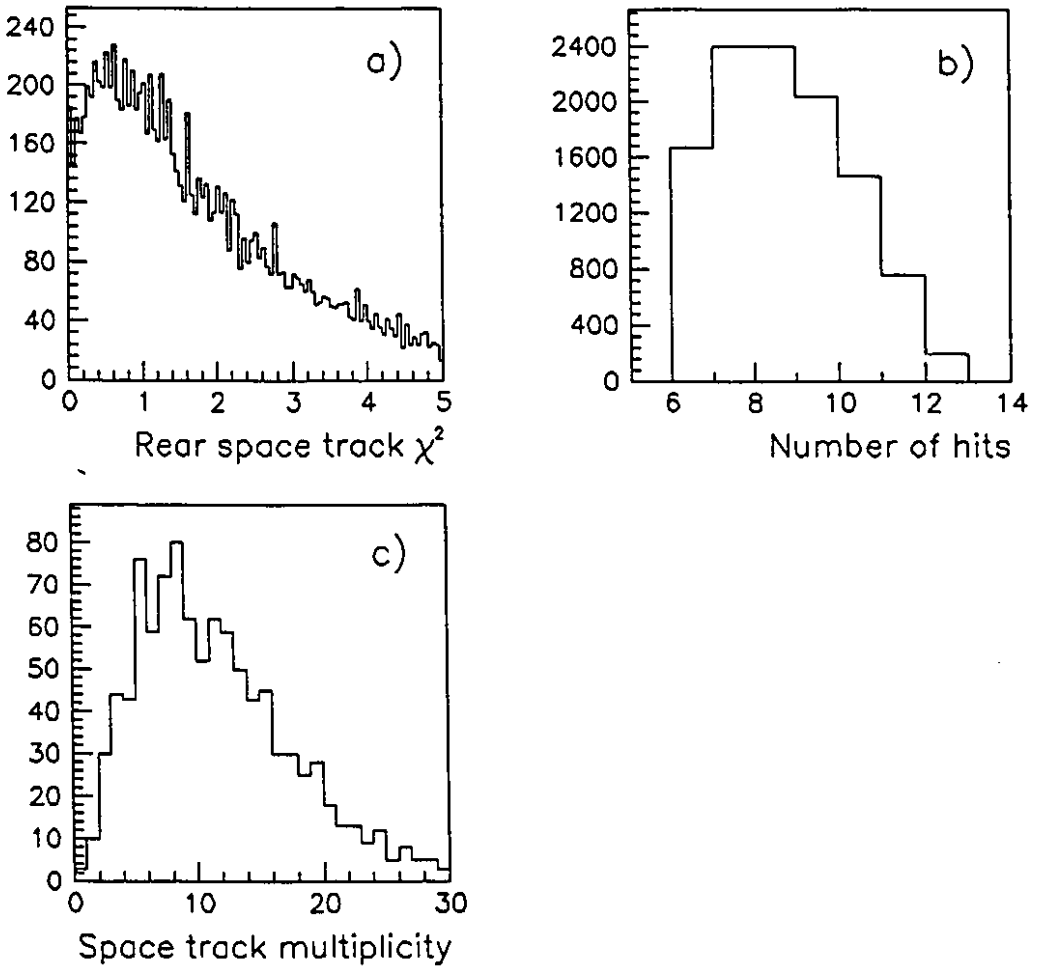

Figure 4.8: Rear space tracks: a) χ^2 distribution, b) Number of hits on final sample, c) Number of rear tracks per event

Y-view. The distribution of the projected difference is shown in Figure 4.9.

If more then one front-rear match was found, the one with the best link χ^2 was chosen, having defined link χ^2 as:

$$\chi^2 = (X_r - X_f)^2 + \frac{(Y_r - Y_f)^2}{9} \tag{4.7}$$

Where X_r, Y_r are the rear track X, Y projections into the middle of the magnet and X_f, Y_f are the front track X, Y projections into the middle of the magnet. The factor 9 in the denominator of the Y-component of the residual was used to take into account the different resolutions achieved by the tracking system for X and Y projections. If no candidate was found among the front space tracks, the rear projection at the middle of the magnet and the vertex were used to define a road to search for hits in the front chambers. If at least 7 hits were found, a least squares fit was performed as described in section 4.2.2. If the chisquare was ≤ 5 the track was stored in the front track bank and the rear track was considered to be matched.

If it was not possible to reconstruct a front track to link with the rear segment, the track was then classified unmatched. A pseudo-front segment, defined as the line connecting the rear projection at the middle of the magnet and the primary vertex, was assigned to the rear track.

4.6 Momentum and charge calculation

Particle momentum was calculated using the trajectories before and after the analysis magnet. The three components of the momentum were obtained by solving the following equations:

$$\sqrt{p_x^2 + p_y^2} = \frac{P_{kick}}{sin(\theta_{X_{in}}) - sin(\theta_{X_{out}})} \tag{4.8}$$

$$\frac{p_x}{p_z} = tan(\theta_{X_{in}}) \tag{4.9}$$

$$\frac{p_y}{p_z} = tan(\theta_{Y_{in}}) \tag{4.10}$$

where:

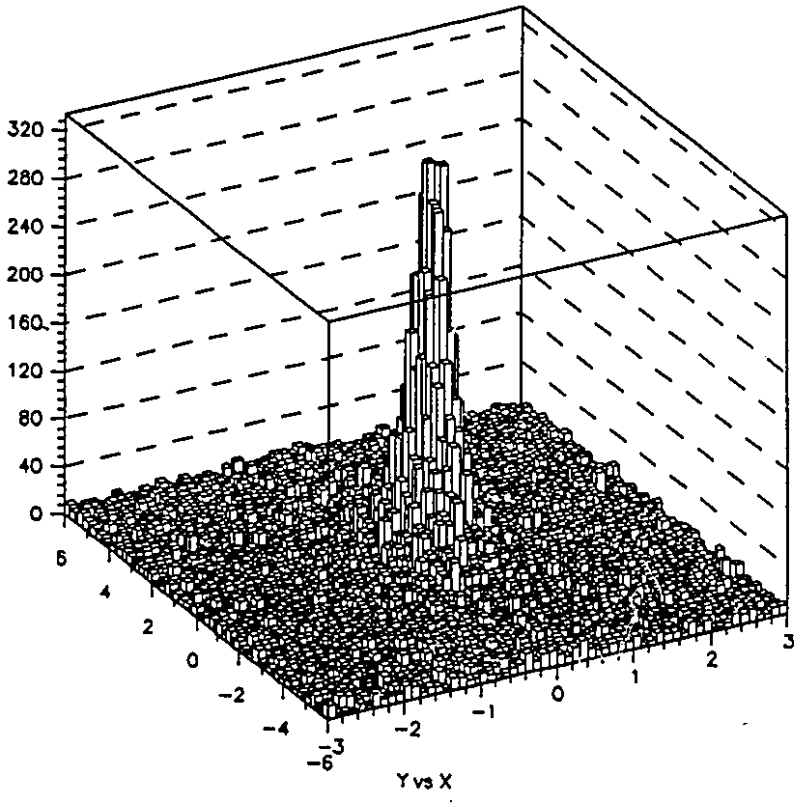

Figure 4.9: Difference between front and rear track projections at magnetic central plane: Y versus X

- P_{kick} = 766 MeV/c is the tranverse momentum kick of the magnet.
- $\theta_{X_{out}}$ is the outgoing angle in the XZ plane, determined using the X rear slope.
- $\theta_{X_{in}}$ is the incoming angle in the XZ plane, determined using the X front slope.
- $\theta_{Y_{in}}$ is the incoming angle in the YZ plane, determined using the Y front slope.

The charge of the particles was determined from the direction of the bend in the XZ plane.

4.7 Momentum resolution and tracking reconstruction efficiency

A Monte Carlo study was performed to determine the spectrometer momentum resolution and the track reconstruction efficiency. J/ψ events were generated, as described in Chapter 6, and the trajectory of each charged particle was propagated through the spectrometer. The hits were generated according to the measured resolution in each of the chambers (as reported in section 3.2.2). The chamber and counter efficiencies were taken into account by using the results presented in Chapter 3. The fractional momentum resolution, σ_P/P, was inferred by comparing the momentum of the generated particle and the reconstructed momentum. Grouping the tracks with respect to the value of their momenta, the distributions of the difference between the reconstructed momentum and the generated momentum were plotted. By fitting these distributions with a gaussian function, the value of the momentum resolution was determined as a function of momentum. When the MonteCarlo generated events consisted of only two muons from the J/ψ decay, this procedure would provide the intrinsic resolution of the spectrometer, which is shown in Figure 4.10 by the unfilled circle points. The data can be parametrized as σ_P/P=0.05 P (P measured in GeV/c). The presence of other particles accompanying the production was simulated by overlapping the hits of the Monte Carlo generated track to the hits recorded in a real dimuon trigger. The fractional resolution of the spectrometer, obtained from such a procedure, is shown in Figure 4.10 by the filled circle points. The degradation of the resolution, due to

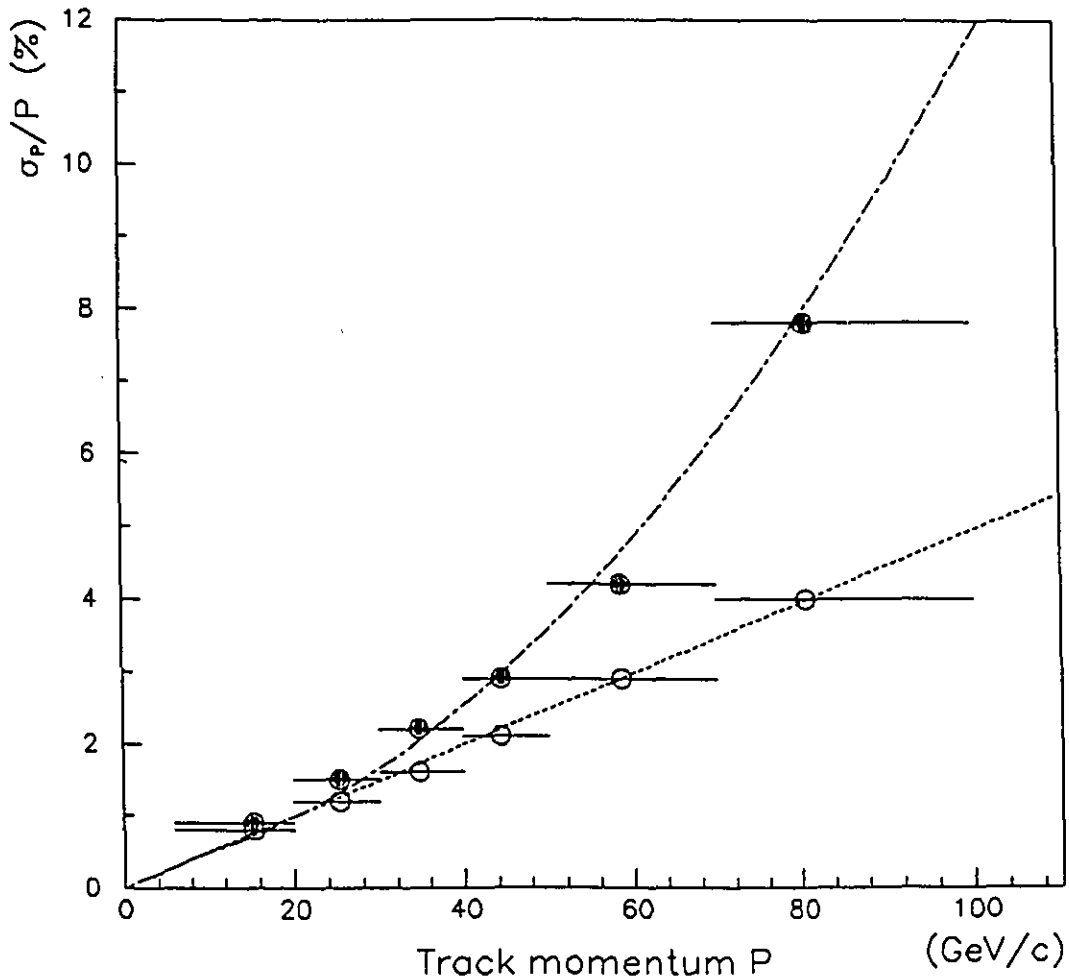

Figure 4.10: Monte Carlo simulation of σ_P/P: a) Intrinsic spectrometer resolution (open circles) b) Spectrometer resolution taking into account the presence of the underlying event (filled circles).

the presence of other tracks in the event, is more evident for high momentum tracks, which are in the central region of the detector, where the hit multiplicity is higher. The data can be parametrized as $\sigma_P/P = 0.2 + 0.02\ P + 0.001\ P^2$ (with P measured in GeV/c). The agreement between the momentum resolution predicted by the Monte Carlo and the momentum resolution measured in the data was checked by comparing the J/ψ width predicted by the Monte Carlo with the J/ψ signal reconstructed in the data; as described in Chapter 6, a very good agreement was found.

The efficiency of the tracking was evaluated using the same Monte Carlo simulation. Particles with trajectories intersecting the live region of all the chambers were selected. The efficiency was calculated as the ratio of the number of found tracks to the number of generated tracks. The track reconstruction efficiency was found to be $78 \pm 1\%$.

Chapter 5

Electromagnetic shower reconstruction

The electromagnetic detector reconstruction program is used to reconstruct showers in the glass, identify the ones which are consistent with being electromagnetic showers, and determine their energy and position in order to measure the photon four-momenta. The reconstruction of calibration particles such as electrons, π^0 's, and η's, which are abundantly produced in high energy interactions, was used to make detailed studies of the accuracy of the energy scale, the energy resolution achieved in the data and the reconstruction efficiency.

5.1 Description of the algorithm

5.1.1 Pedestal subtraction and decoding

The first step of the reconstruction program was the decoding of the information of the glass and the hodoscope. The ADC data for each block were examined and the mean pedestals, calculated as a function of Before Energy, were subtracted. Finally, each block ADC signal was multiplied by a gain constant to determine the energy deposited in the block. Pulse heights of the tubes and the strips of the LGC were also converted into energy using appropriate gain constants.

5.1.2 Clustering

Each Main Array block with energy $E \geq 300$ MeV and containing more energy than any of the 4 neighbouring blocks with a common boundary (or 5 if the block was near the large-small block boundary) was defined as the peak of a cluster. Blocks in the

innermost layer (around the beam hole) or in the outermost layer were not considered in this selection process.

Clusters were defined as the ensemble of the peak block and its neighbors (typically eight) to form 3x3 block arrays. At this stage, the energy assigned to each cluster was the sum of the energies contained in each block. If two or more clusters partially overlapped, the energy of the common blocks was divided proportionally to the energy contained in the peak block of each cluster.

5.1.3 Energy and position determination

To better redistribute energy for partially overlapping showers and better measure the shower position, a fitting procedure was used to match the measured shower shapes to predetermined shower transverse development patterns.

Pattern definition

A pattern consisted of a set of numbers which uniquely defined the energy and the position of a shower. Patterns were obtained by generating showers of known energy and position and sampling the average behavior of the generated showers. Using Monte Carlo methods, showers were simulated by EGS IV [50], a standard simulation package which tracked the electromagnetic cascade of each generated photon or electron through the various materials of the E705 calorimeter. Showers were generated for 5 different incident electron energies: 1, 2.45, 6.05, 14.9, and 36.6 GeV.

The transverse development of electromagnetic showers, which on average is different for the photons and electrons, is also dependent upon the angle of incidence into the calorimeter. Therefore three different set of tables were produced. In the first set, the incident particles were photons, while for the second and third sets electrons were generated according to two different running conditions: in one set, representing the standard data taking mode, where electrons produced in the target are deflected by the analysis magnet, events were generated with an incidence angle which depended

on their momentum. In the other set, representing calibration data, electrons were constrained to hit the glass at zero degree.

EGS showers were distributed randomly in one quadrant of the detector. The information for the other three quadrants was derived by using mirror symmetry. The quadrant was divided into 34 regions to take into account the different glass types and block sizes as well as the different incidence angles. For each region about 5000 showers were generated. Each region was divided into $1 \times 1\text{cm}^2$ cells and for each cell four different patterns were determined depending upon the fraction of energy deposited in the Active Converter plane. In order to minimize the number of parameters in the pattern, only five out of the nine blocks of a cluster were used. The patterns for the vertical position were derived by the horizontal position patterns, using the symmetry properties of the detector. The following ratios were defined:

$$\begin{aligned} p_1 &= \frac{E_1}{E_1+E_2+E_3} & p_4 &= \frac{E_4}{E_1+E_4+E_5} \\ p_2 &= \frac{E_2}{E_1+E_2+E_3} & p_5 &= \frac{E_5}{E_1+E_4+E_5} \\ p_3 &= \frac{E_3}{E_1+E_2+E_3} \end{aligned} \tag{5.1}$$

$$\begin{aligned} r_{12} &= \frac{E_1-E_2}{E_1+E_2} & r_{14} &= \frac{E_1-E_4}{E_1+E_4} \\ r_{13} &= \frac{E_1-E_3}{E_1+E_3} & r_{15} &= \frac{E_1-E_5}{E_1+E_5} \\ r_{32} &= \frac{E_3-E_2}{E_3+E_2} & r_{54} &= \frac{E_5-E_4}{E_5+E_4} \end{aligned}$$

where E_i is the energy in block i and the index $i = 1,2,3,4,5$ with the convention illustrated in Figure 5.1.

In a given cell, for a given position, the average and standard deviation for the p_i ratios were derived from the 5000 event sample. The mean was used to predict the individual shower energy and the standard deviation sigma was used to determine its accuracy, which is limited by fluctuations in shower development. For each energy, intervals for the variable r_{ij} were defined and an average position was determined by

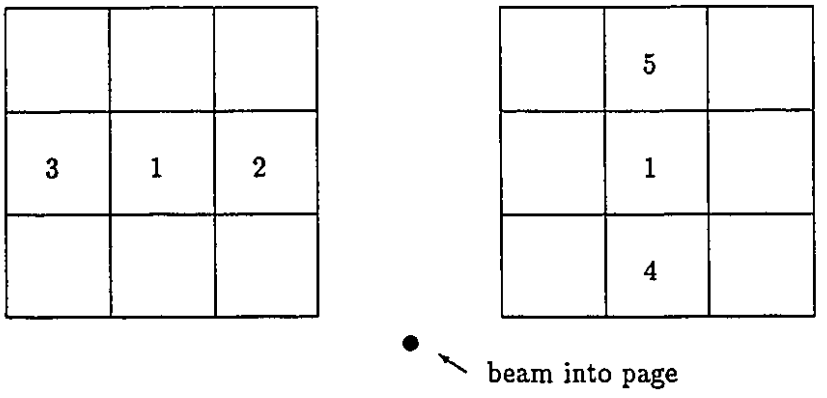

Figure 5.1: Indexing of blocks for tables

selecting showers with r_{ij} within each interval. The standard deviation for the position was also calculated. These tables were used to estimate shower position from the energy distributed in the five blocks (for more details see references [51], [47]).

Energy determination

An initial position for every cluster was estimated using the position patterns. The ratios R_{12}, R_{13}, R_{32}, R_{15}, R_{14}, and R_{45} (defined as r_{ij} in equation 5.1), were formed using the energies measured in the cluster blocks. The position was predicted by interpolating between the positions corresponding to the two pattern ratios r_{ij} closest to the measured R_{ij}. Using the sigmas from the tables, the position errors, Δr_{ij}, were also calculated. The position in x and y was calculated as the weighted average of the three possible determinations:

$$x = \frac{\frac{x_{12}}{\Delta x_{12}^2} + \frac{x_{13}}{\Delta x_{13}^2} + \frac{x_{32}}{\Delta x_{32}^2}}{\frac{1}{\Delta x_{12}^2} + \frac{1}{\Delta x_{13}^2} + \frac{1}{\Delta x_{32}^2}} \qquad y = \frac{\frac{y_{14}}{\Delta y_{14}^2} + \frac{y_{15}}{\Delta y_{15}^2} + \frac{y_{54}}{\Delta y_{54}^2}}{\frac{1}{\Delta y_{14}^2} + \frac{1}{\Delta y_{15}^2} + \frac{1}{\Delta y_{54}^2}} \tag{5.2}$$

The ratios P_1, P_2, P_3, P_4, and P_5, (defined as the p_i in equation 5.1) were then formed. Using P_1, P_2, and P_3 and interpolating between pattern tables, the predicted values for the energy in the three horizontal blocks, $\mathcal{E}_1$, $\mathcal{E}_2$, and $\mathcal{E}_3$ were extracted. Using then P_1, P_4 and P_5 the predicted values for the energy in the vertical blocks, $\mathcal{E}_4$, $\mathcal{E}_5$

were determined by applying the constraint that the energy assigned to the peak block using the vertical pattern would be the same as the one predicted using the horizontal pattern. By means of EGS studies, the predicted energy for the corner blocks was determined as the ratio of energies predicted for their nearest neighbors. The energy of each cluster was finally estimated by minimizing the χ^2 with respect to a scale factor required to make the shower pattern match the experimental pattern. The χ^2 was defined as:

$$\chi^2 = \sum_{i,j}(E_i - A\mathcal{E}_i)\, M_{ij}\, (E_j - A\mathcal{E}_j) \tag{5.3}$$

where A is the scale factor and M_{ij} is the inverse of the covariance matrix, which was empirically defined as:

$$M_{ij} = \frac{E_i E_j}{(max(E_i,E_j))^2} \quad \text{if blocks i and j were neighboring blocks} \tag{5.4}$$

$$M_{ij} = 0 \quad \text{otherwise}$$

The total Main Array energy attributed to each shower was the sum of the predicted energies over all the blocks. If a block was shared by several showers, the fitting procedure was repeated iteratively until the process converged (energy of last iteration within 1% of the previous one) or until 25 iterations had been tried. At each iteration a fractional energy error was calculated as:

$$\Delta E = \frac{\sqrt{\sum_i (E_i^{out} - E_i^{in})^2}}{E_{tot}^{out}} \tag{5.5}$$

where the index i runs over the five blocks for which the patterns were defined and the energies E_i^{in}, E_i^{out} are the energies assigned to the block i before and after the fitting. ΔE was used as a measurement of how well the lateral shape of the shower matched the pattern-predicted shape (section 5.3.1). For the case of blocks belonging to more than one shower, the sum of the block energy attributed to the different showers had to equal the actual measured energy for the block.

Position determination

Shower position, as determined from the glass block patterns, was used as starting value for a more accurate determination based on the tube hodoscopes: LGC information in the central region and GTH information in the wings. The X and Y positions were measured by looking at the profile of the energy distribution in the tubes and strips. A window was defined on the hodoscope in front of each cluster, centered on the hodoscope position predicted by the glass patterns. The window width was defined to be ± 3 times the position error, with a maximum width of ± 6 cm and a minimum of ± 3 cm. A search for hodoscope peaks within this window was done independently in the X and Y views using a deconvolution technique. This technique was used to share the energies deposited in the tubes by overlapping showers, before trying to extract the position information. The input signal was Fourier transformed and then divided by the expected pulse shape in the frequency space as derived from the 30 GeV electron calibration data. The resulting spectrum was then transformed back to position space and signal peaks extracted. Tubes were selected as peaks if their energy was greater than their neighbors' and above a threshold, which was set to 200 MeV in the LGC and 300 ADC counts in the GTH. Once all the peaks associated with a shower were found in both views, a match of peak i in the X-view with the peak j in the Y-view was made based on the asymmetry variable:

$$\begin{aligned} A_{ij} &= \frac{E_{X_i} - E_{Y_j}}{E_{X_i} + E_{Y_j}} && \text{for the LGC} \\ A_{ij} &= \frac{ADC_{X_i} - ADC_{Y_j}}{ADC_{X_i} + ADC_{Y_j}} && \text{for the GTH} \end{aligned} \qquad (5.6)$$

where E_{X_i} is the energy, ADC_{X_i} is the number of ADC counts found for peak i in X-view hodoscope and E_{Y_j} is the energy; ADC_{Y_i} is the number of ADC counts found for peak j in Y-view hodoscope. A hodoscope crossing was defined if the asymmetry A_{ij} was less then 0.25 for peaks located in the LGC and less than 0.35 for peaks located in the GTH. These values were chosen by looking at the asymmetry distribution for calibration electrons. If more than one hodoscope crossing was found, the position of the pair with smallest asymmetry was chosen. The final position was computed as the

weighted average of the positions determined by the glass and by the hodoscope.

5.2 Electron reconstruction

The main source of electrons were π^0 and η decays into two photons, followed by photon conversions in the target, generating e^+e^- pairs. In this section, and in the remainder of this thesis, the word "electron" will be used to mean electron or positron regardless of the charge of the particle. Electrons were reconstructed as tracks using spectrometer information and their momentum could be determined very accurately. Since electrons deposit all their energy in the electromagnetic calorimeter and their mass is negligible relative to their momentum, there is a near equality between p_{track}, the momentum measured by the spectrometer, and $E_{cluster}$, the energy determined by calorimeter. Therefore electrons were used extensively to study the accuracy of the electromagnetic detector energy scale.

The first step in the selection of candidate electron showers consisted of looking for tracks whose projection into the calorimeter was within 3 cm of a reconstructed shower. This criterion, by itself, was not sufficient to distinguish between electrons and hadrons. Hadron showers are not fully contained in the calorimeter therefore hadrons deposited only a fraction of their energy in the glass. Moreover, they typically deposit very little energy in the Active Converter plane. To optimize hadron rejection in the data, events from the electron calibration beam were compared with events from special calibration runs done with pure hadron beam (pions). Figure 5.2 shows the comparison of energy deposited in the Active Converter by 6.5 GeV electrons and pions. It appears that $\simeq 90\%$ of the hadrons could be rejected by requiring:

$$E_{AC} \geq 200.\ \text{MeV}. \tag{5.7}$$

Figure 5.3 shows the distributions of the energy, reconstructed by the calorimeter, for 6.5 GeV electrons and for pions interacting in the Active Converter plane.

The distribution of $\frac{E_{cluster}}{p_{track}}$ for all the showers reconstructed in the data and associated with a track is shown in Figure 5.4a. Electrons appear as a peak near $E/p = 1$,

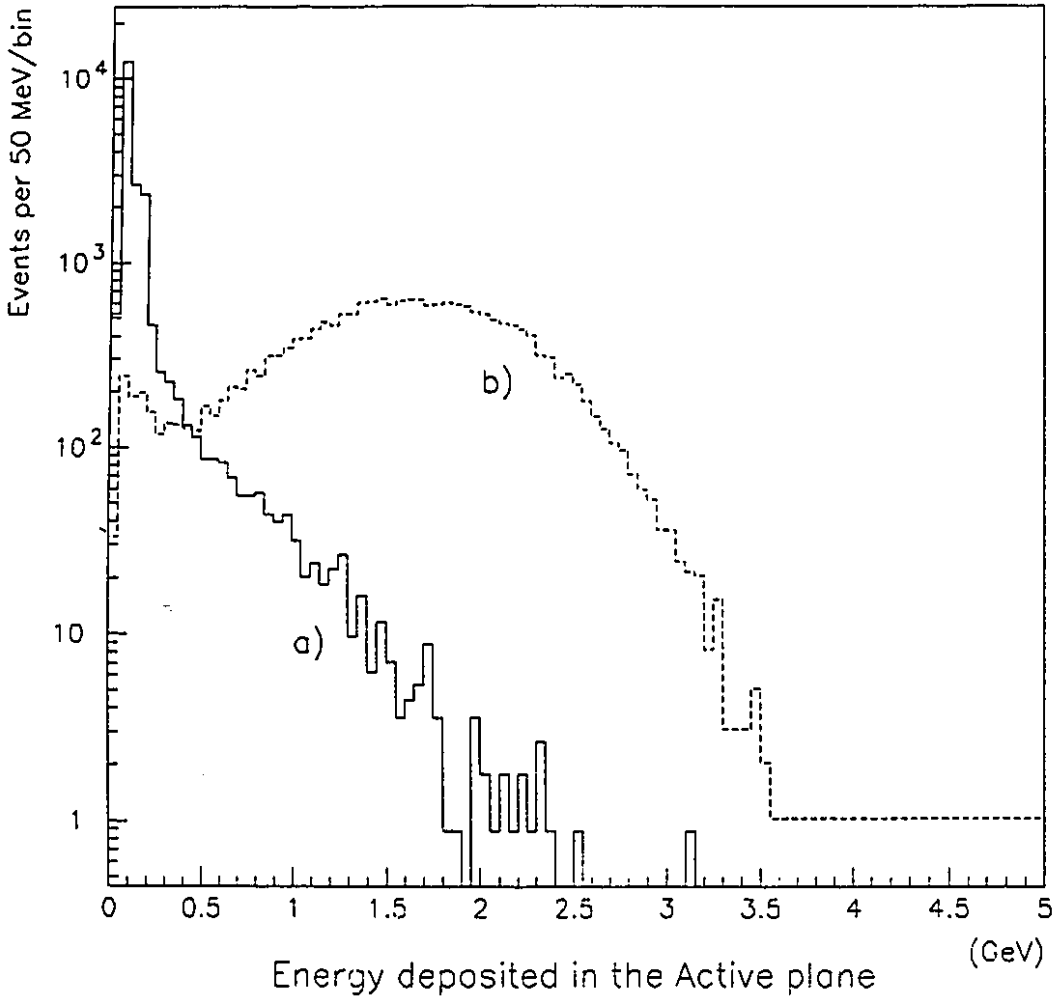

Figure 5.2: Energy deposited in the Active Converter plane: a) for 6.5 GeV energy pions, b) for 6.5 GeV electrons.

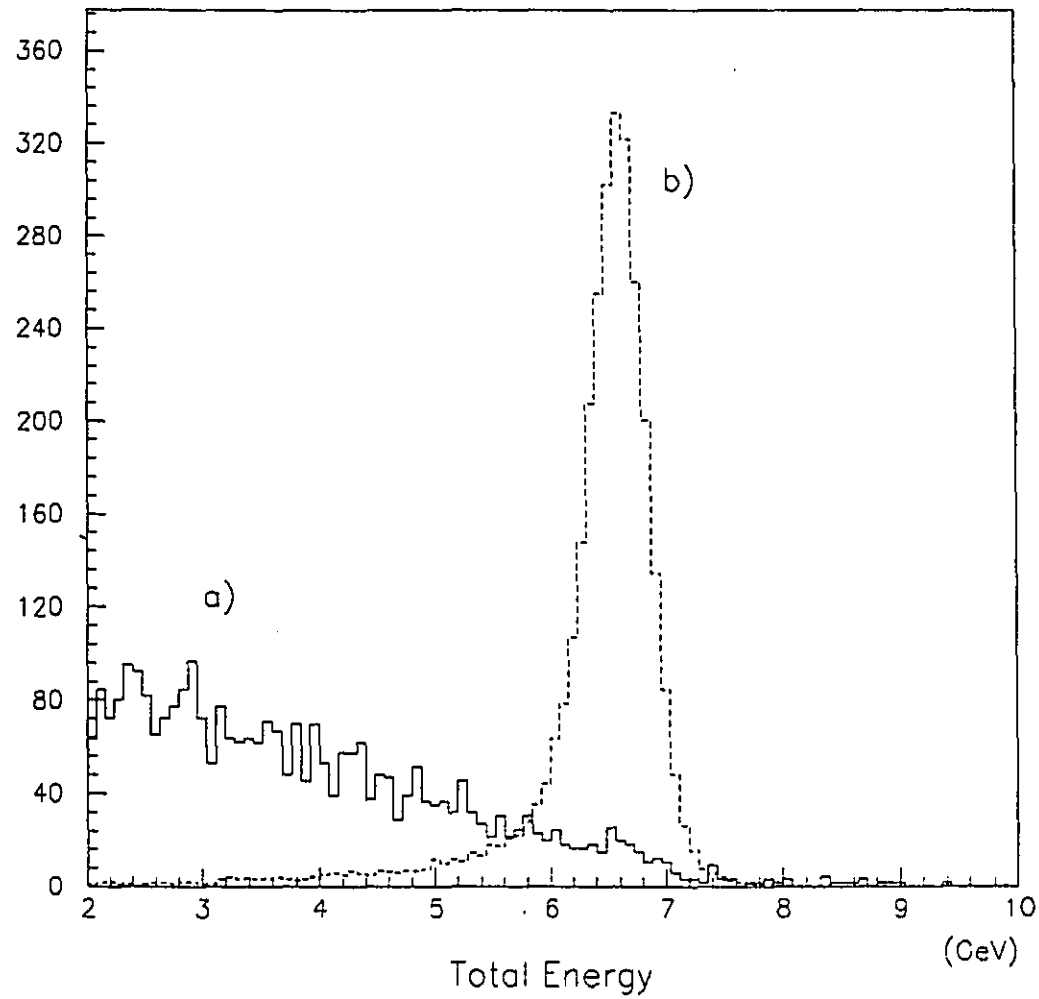

Figure 5.3: Total energy deposited in the electromagnetic calorimeter a) for 6.5 GeV energy pions, b) for 6.5 GeV electrons.

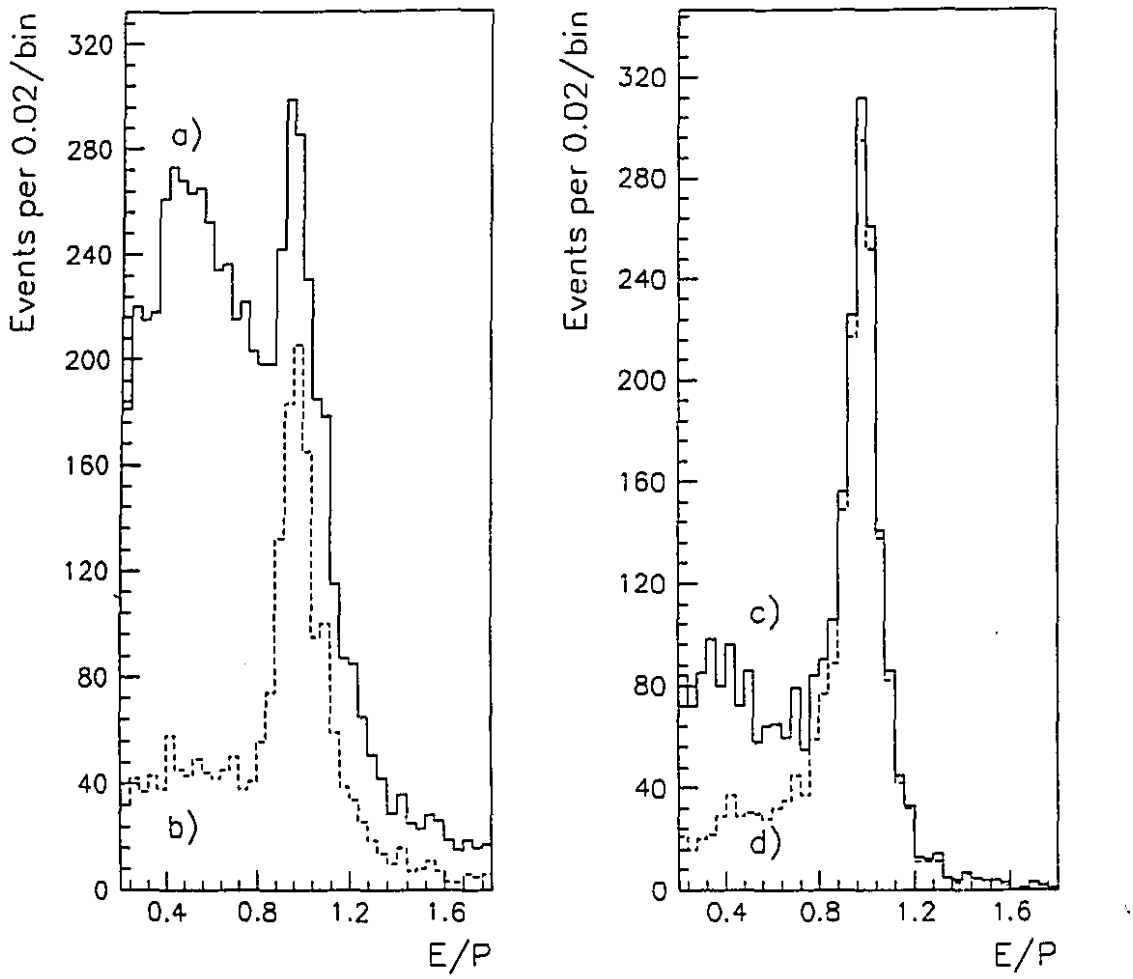

Figure 5.4: E/p signal: a) all showers in the SCG region associated with a track, b) all showers in the SCG region associated with a track requiring at least 200 MeV energy deposited in the Active Converter plane, c) all showers in the SF5 region associated with a track, d) all showers in the SF5 region associated with a track requiring at least 200 MeV energy deposited in the Active Converter plane.

Table 5.1: E/p for electron candidates

Region	E/p mean	E/p sigma	Average p (GeV/c)
Small	1.074 ± 0.002	0.091 ± 0.002	13.0
Large SCG LGC	1.088 ± 0.002	0.098 ± 0.002	9.7
Large SCG GTH	1.064 ± 0.001	0.085 ± 0.001	6.9
SF5	0.984 ± 0.001	0.077 ± 0.001	4.2

while hadrons appear in the the broader peak at lower values. In Figure 5.4b the same distribution is shown after the cut on the energy deposited in the active plane is applied (Equation 5.7). The hadronic peak is greatly suppressed using this requirement.

Looking for electrons in the data, showers were considered electron candidates if they could be associated with a track and had some energy deposited in the Active Converter plane (Equation 5.7). Electron candidate showers were tagged as electrons if they satisfied the requirement:

$$0.8 \leq \frac{E_{shower}}{p_{track}} \leq 1.2. \tag{5.8}$$

The hadron contamination, under the electron signal, is estimated to be of the order of 10%. By doing a background subtraction, the position and width of the electron E/p peak was accurately determined. The position of the peak provided information on the accuracy of the energy scale in the data. Since the momentum scale was known at the level of 0.25% (as it be will seen in Chapter 6), any shift of the peak position from unity indicated that the energy measurement was systematically wrong. The width of the peak was used to determine the energy resolution achieved in the data. The E/p plot was fitted using a 3rd degree polynomial for the background and a gaussian distribution for the electron signal. In Figure 5.5 the E/p spectrum is shown for the 4 different regions of the detector. The mean values and sigmas, extracted for the different regions by the fitting procedure, are shown in Table 5.1.

Resolutions measured in the data appeared to be worse than those reported in the previous chapter as derived from the calibration runs. The degradation is mainly due to the pedestal rate dependence: a detailed simulation of such an effect found the

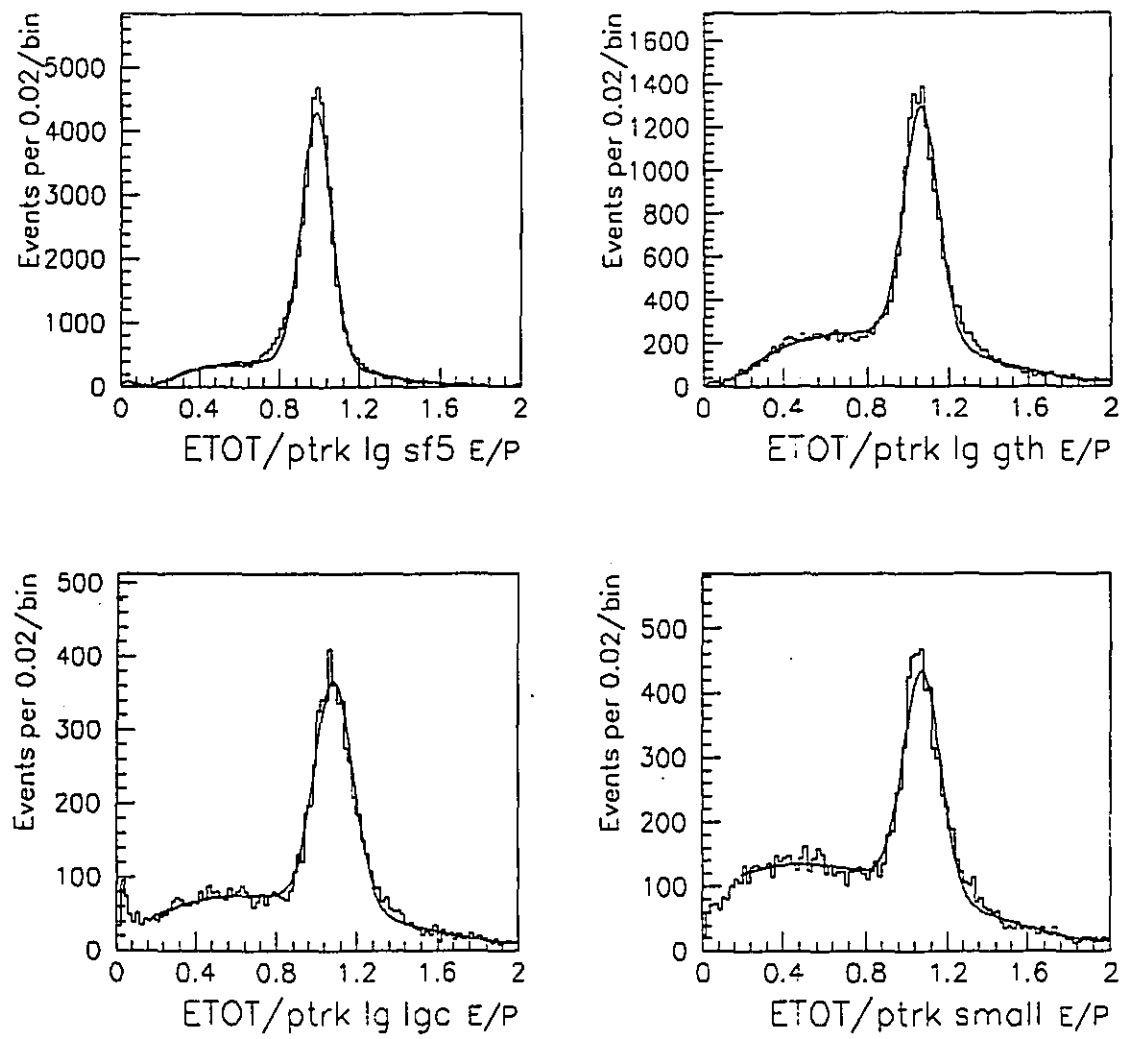

Figure 5.5: E/p signal for the 4 different regions of the detector: a) SF5 blocks, b) large SCG blocks behind GTH, c) large SCG blocks behind LGC, d) small SCG blocks.

Table 5.2: Correction constants for shower energy

Region	α	β (GeV)
Small	0.95	0.31
Large SCG LGC	0.92	0.
Large SCG GTH	0.94	0.
SF5	1.00	0.

degradation of the resolution measured in the data to be quantitatively consistent with the expected value [53].

Since the mean of the E/p distribution was found to be different from unity in the SCG region, a recalibration of the electromagnetic detector using electrons reconstructed in the data was necessary. E/p was studied in detail as a function of p, as shown in Figure 5.6. In the small SCG blocks the mismeasurement of energy was found to be dependent on the momentum of the track. Therefore an empirical correction was applied to the reconstructed energy according to the expression:

$$E_{true} = \alpha * (E_{reconstructed} - \beta) \tag{5.9}$$

The parameter β is a small positive offset for the small SCG blocks and it is attributed to a residual pedestal shift during the spill in this region where the dynamic pedestal effect was more pronounced. The parameter α is an overall renormalization constant to bring the mean value of the E/p to unity. The correction parameters were extracted by applying a linear fit to E/p as a function of p. In fact, assuming $E_{true} = p$:

$$\frac{E_{reconstructed}}{P} = a + \frac{b}{P} \tag{5.10}$$

where $a = 1/\alpha$ and $b = \beta$. Typical values of α and β for the different regions of the detector are shown in Table 5.2.

The E/p distribution was monitored and readjusted throughout the run, as shown in Figures 5.7, 5.8, 5.9, and 5.10, and the energy scale appeares to be correct at a level of $\pm 1\%$. The energy resolution was also studied as a function of the momentum in the four regions of the detector as shown in Figure 5.11.

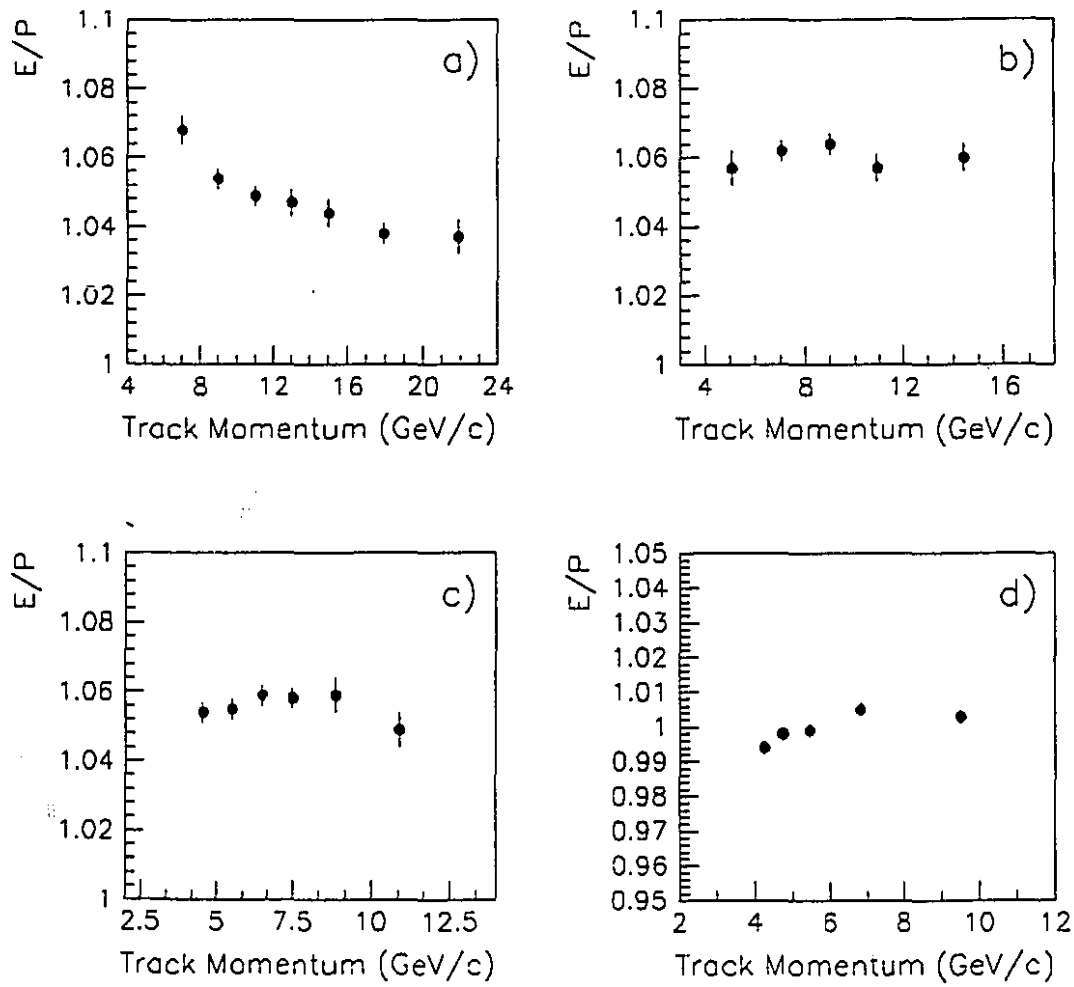

Figure 5.6: E/p signal as a function of track momentum: a) small SCG blocks. b) large SCG blocks behind LGC, c) large SCG blocks behind GTH, d) SF5 blocks.

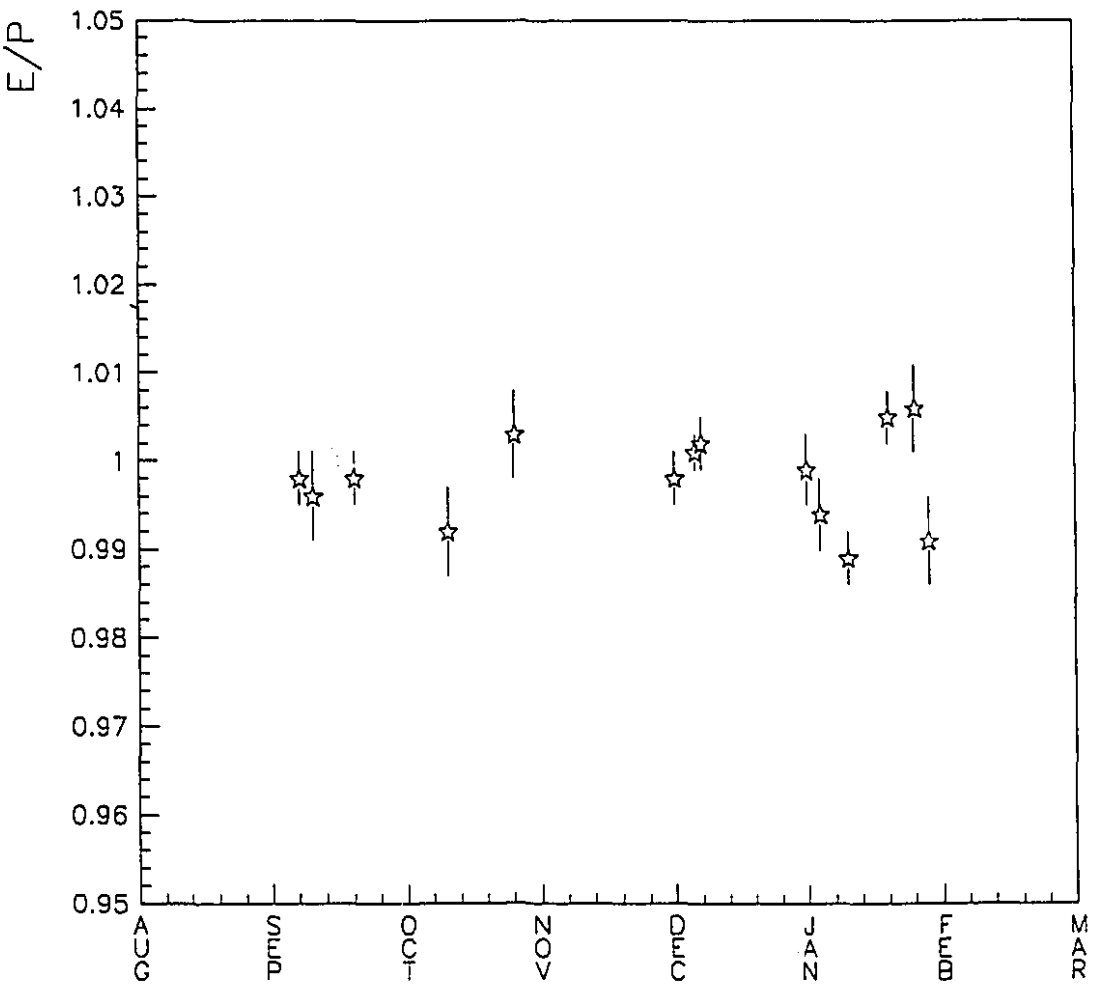

Figure 5.7: E/p signal as a function of time for showers in the Small SCG block region.

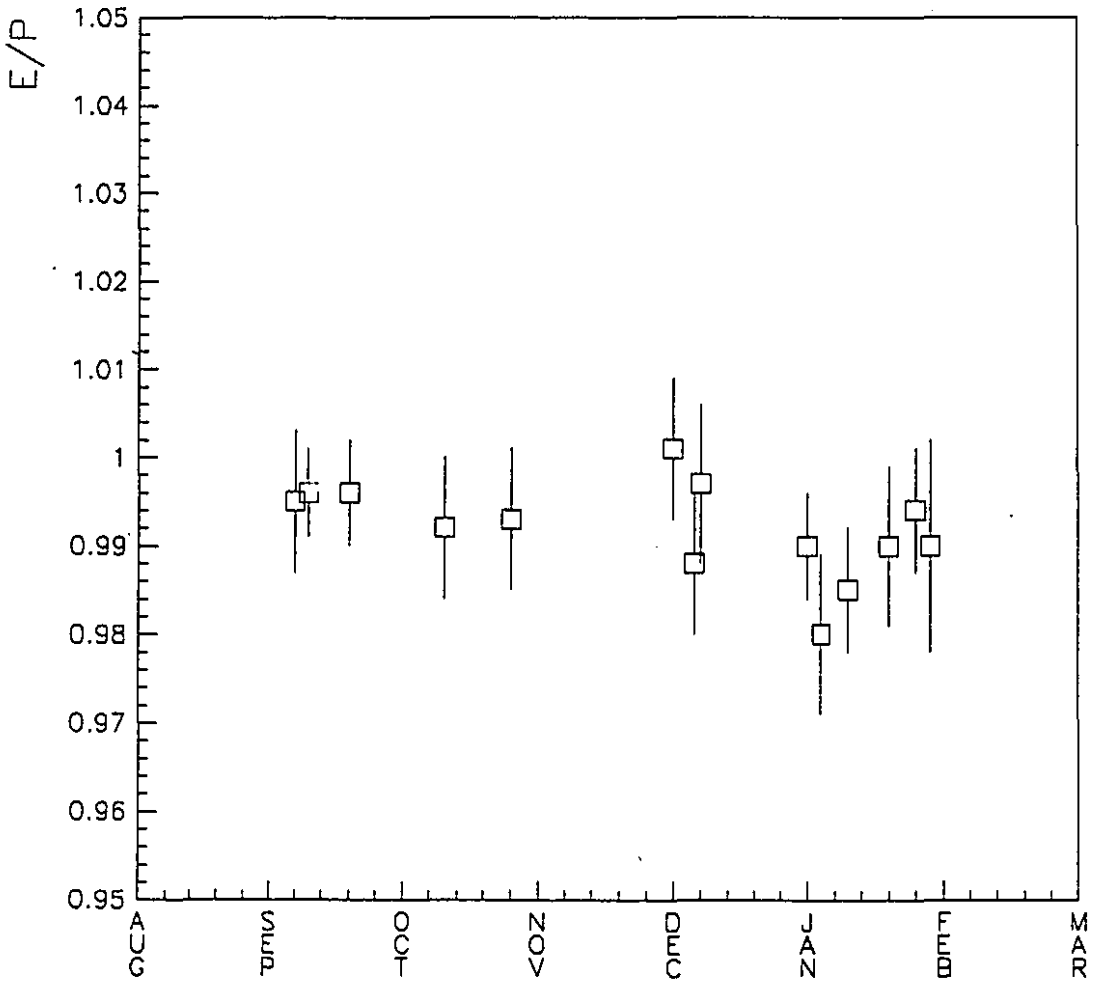

Figure 5.8: E/p signal as a function of time for showers in the Large SCG blocks located behind the LGC.

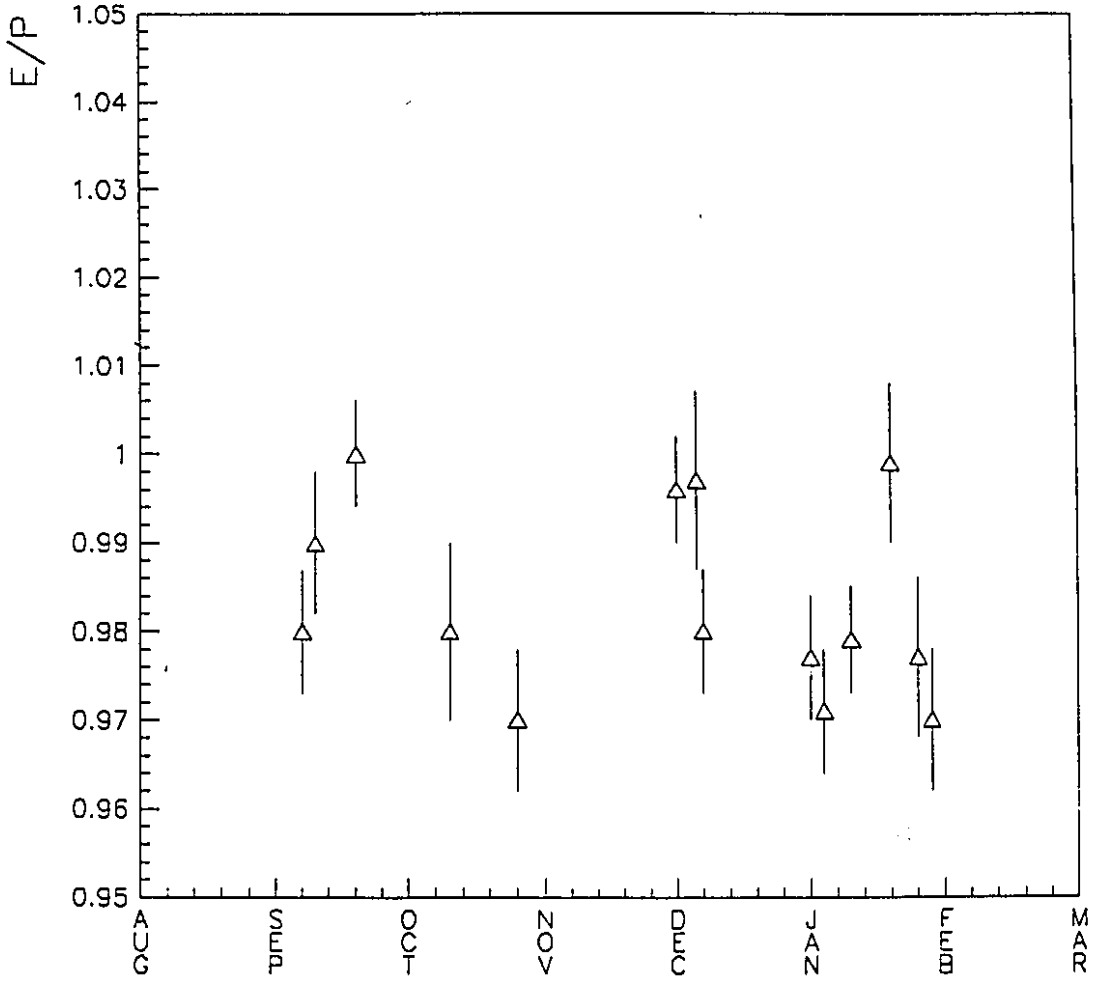

Figure 5.9: E/p signal as a function of time for showers in the Large SCG blocks located behind the GTH.

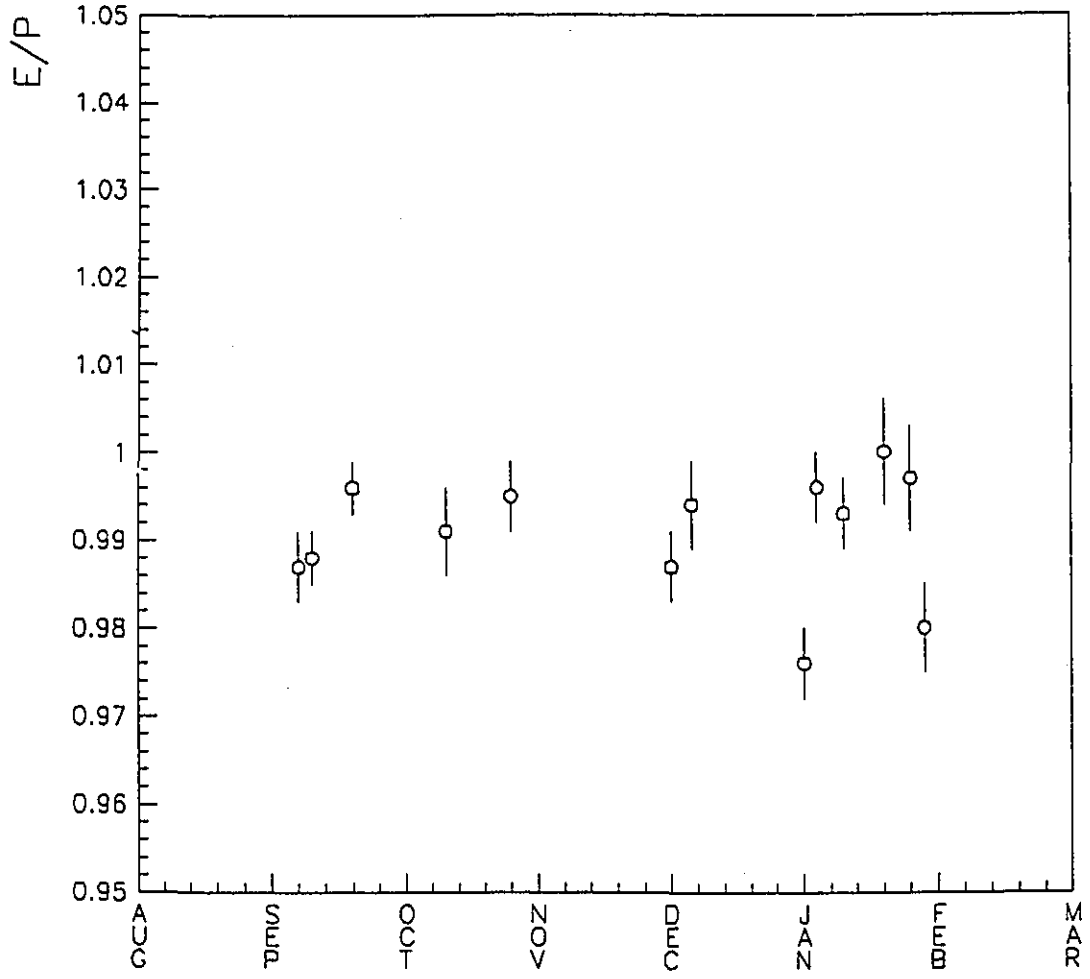

Figure 5.10: E/p signal as a function of time for showers in the SF5 block region.

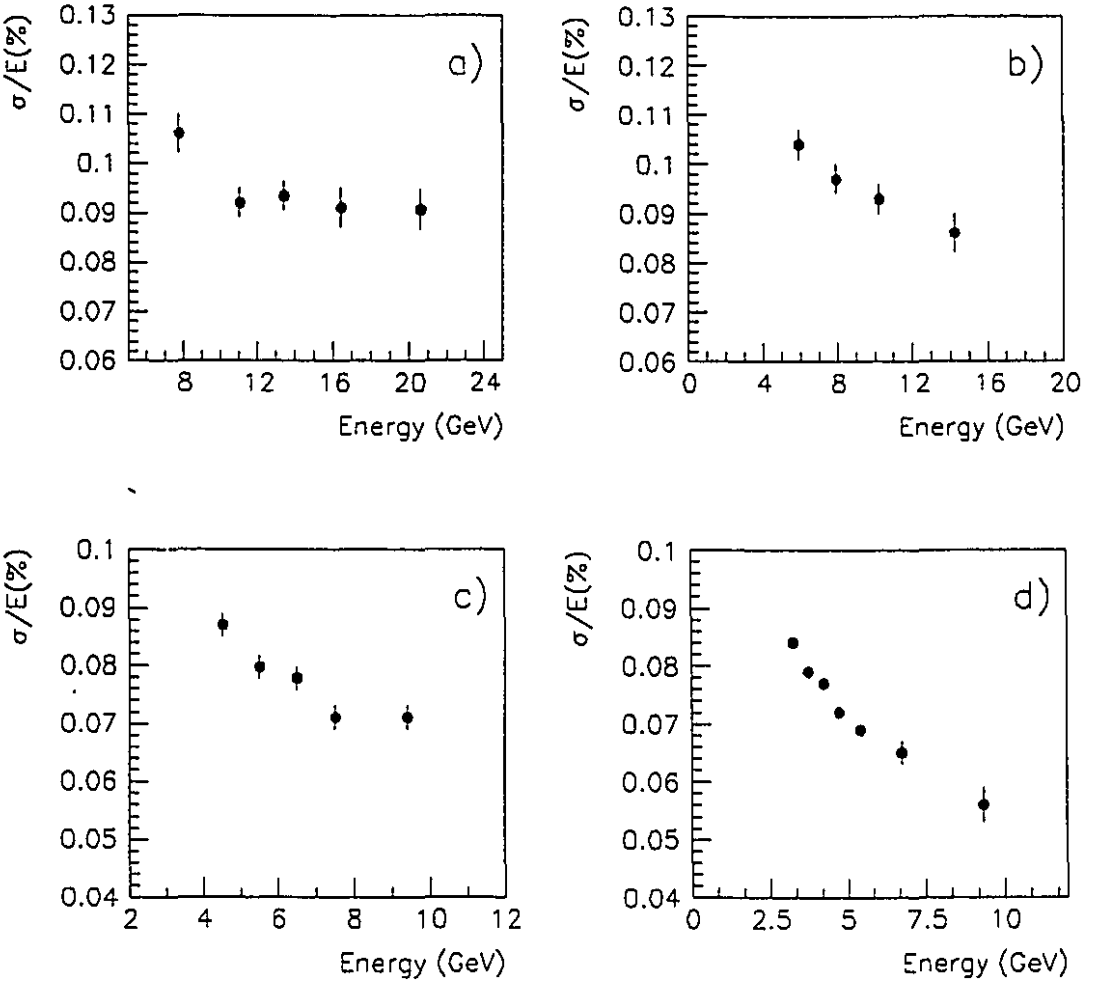

Figure 5.11: Energy resolution as a function of energy measured from E/P spectra in dimuon triggers for the four different regions of the detector: a) small SCG blocks, b) large SCG blocks behind LGC, c) large SCG blocks behind GTH, d) SF5 blocks.

5.3 Digamma combinations

Reconstruction of π^0 and η decays in the data provides further information on the accuracy of the energy scale, as determined from the electron reconstruction described in the previous section. Pizeros and etas were reconstructed through their decay in two photons. Selecting non-electron showers, all possible pair-wise combinations were made and their invariant mass $M_{\gamma\gamma}$ computed:

$$M_{\gamma_i\gamma_j} = \sqrt{2E_{\gamma_i}E_{\gamma_j}(1 - cos\theta_{ij})} \tag{5.11}$$

where E_{γ_i} and E_{γ_j} are the shower energies as measured by the calorimeter and corrected using Equation 5.9. θ_{ij} is the opening angle between the two photons computed from the positions of the two photons on the glass and the primary interaction vertex reconstructed using the charged tracks (given the short lifetimes of pizeros and etas, the distance between their production and decay points is negligible).

5.3.1 π^0 decays

Showers were selected as photon candidates if they satisfied the following requirements:

1. The shower in the glass was associated with a crossing in the position hodoscope.
2. The χ^2 from glass shower fitting was $\leq$10.
3. The fractional energy error (as defined in Equation 5.5) was $\Delta E \leq 0.2$.
4. The ratio between the energy deposited in the Active Converter plane and the square root of the total shower energy was $\frac{E_{ac}}{\sqrt{E}} \geq 0.15$ GeV$^{1/2}$. This empirical cut was chosen on the basis of EGS studies to optimize the rejection of hadronic showers without hurting the photon reconstruction efficiency.

To get a better understanding of the energy scale in the different regions of the detector, $\gamma\gamma$ combinations having both showers in the same region were selected and the corresponding invariant mass plots are shown in Figure 5.12. Using a polynomial function

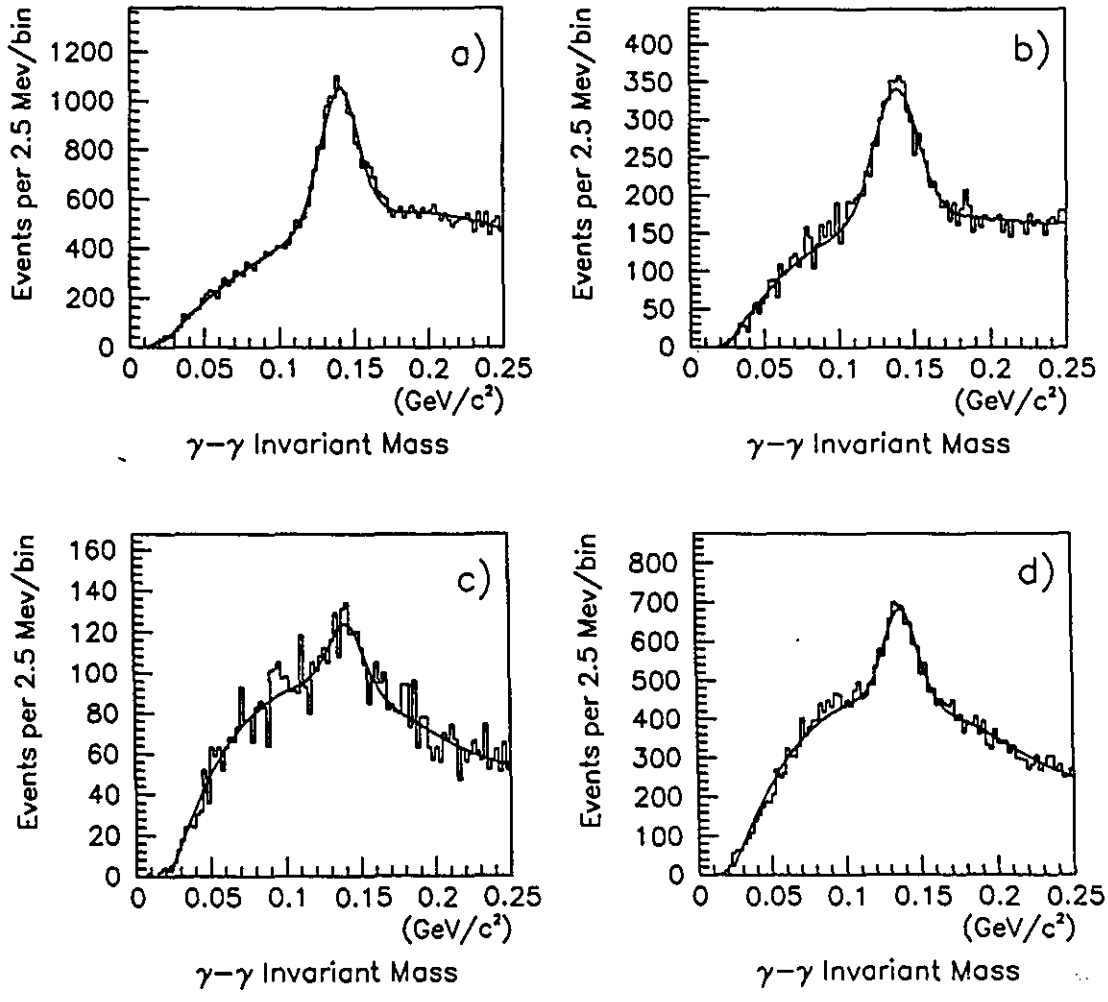

Figure 5.12: $\gamma\gamma$ invariant mass for the four different regions of the detector: a) small SCG blocks, b) large SCG blocks behind LGC, c) large SCG blocks behind GTH, d) SF5 blocks.

Table 5.3: π^0 mass in the different regions

Region	π^0 Mass (MeV)	π^0 mass sigma (MeV)
Small	138.4 ± 0.2	12.2 ± 0.3
Large SCG LGC	137.9 ± 0.5	14.3 ± 0.6
Large SCG GTH	142.5 ± 1.9	13.7 ± 2.0
SF5	137.6 ± 0.5	10.3 ± 0.5

to fit the background and a gaussian for the π^0 signal, the position and the width of the measured π^0 mass were determined for the four different regions of the detector, as shown in Table 5.3.

The measured π^0 width was checked against the prediction of a Monte Carlo simulation. Using the Pythia event generator [52], 25,000 events were generated. Each event was required to satisfy the interaction trigger and to have both photons in the electromagnetic calorimeter. The photons were then propagated through the electromagnetic detector using EGS. The energy and position resolution were taken into account by using the results of the electron studies. The π^0 signal obtained from the data (after background subtraction) is compared with the Monte Carlo prediction for the π^0 width in Figure 5.13. The Monte Carlo predicted π^0 width was found to be consistent with the measured one at the 3% level. This is an independent check that the energy resolution, as measured by reconstructing electrons, also represents well the measurement error for photon showers. Therefore the same technique will be used in Chapter 6 for photon showers coming from χ radiative decays.

In view of the deviations from the known π^0 mass (m=134.97 MeV/c^2)[9], the systematic error on the energy scale was estimated to be $\leq$3%. Combinations of photons with energy in specific intervals were selected to study the stability of the energy scale as a function of γ energy and the corresponding mass spectra are shown in Figure 5.14. The π^0 measured mass as a function of the energy of the two photons appeared to be fairly stable for $E_\gamma \geq 3.0$ GeV. Photons which when combined with other photons in the event, produced a mass combination in the range 100. MeV/$c^2 \leq M_{\gamma\gamma} \leq$180. MeV/$c^2$ were considered π^0 photon candidates.

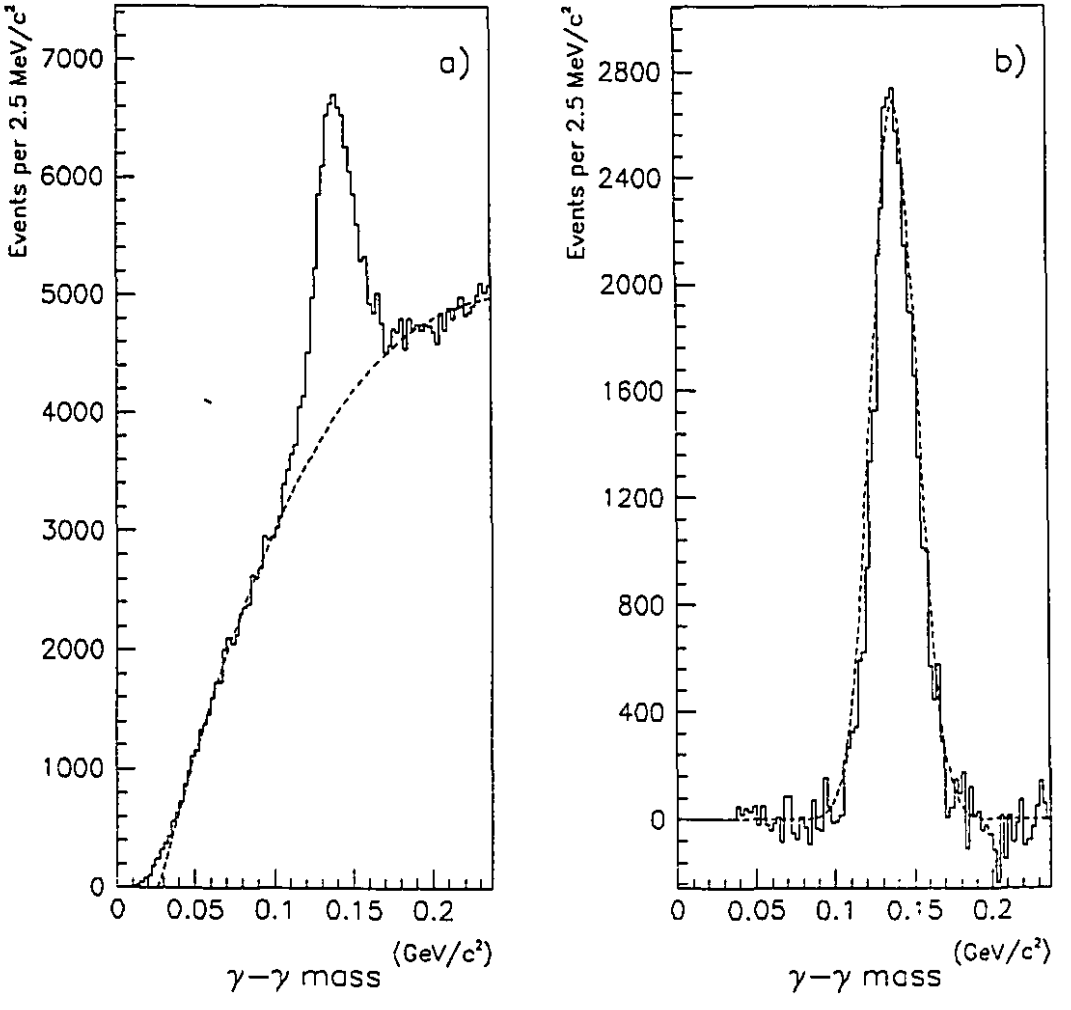

Figure 5.13: $\gamma\gamma$ invariant mass: a) All $\gamma\gamma$ combinations, b) background subtracted compared to the width predicted by the Monte Carlo simulation

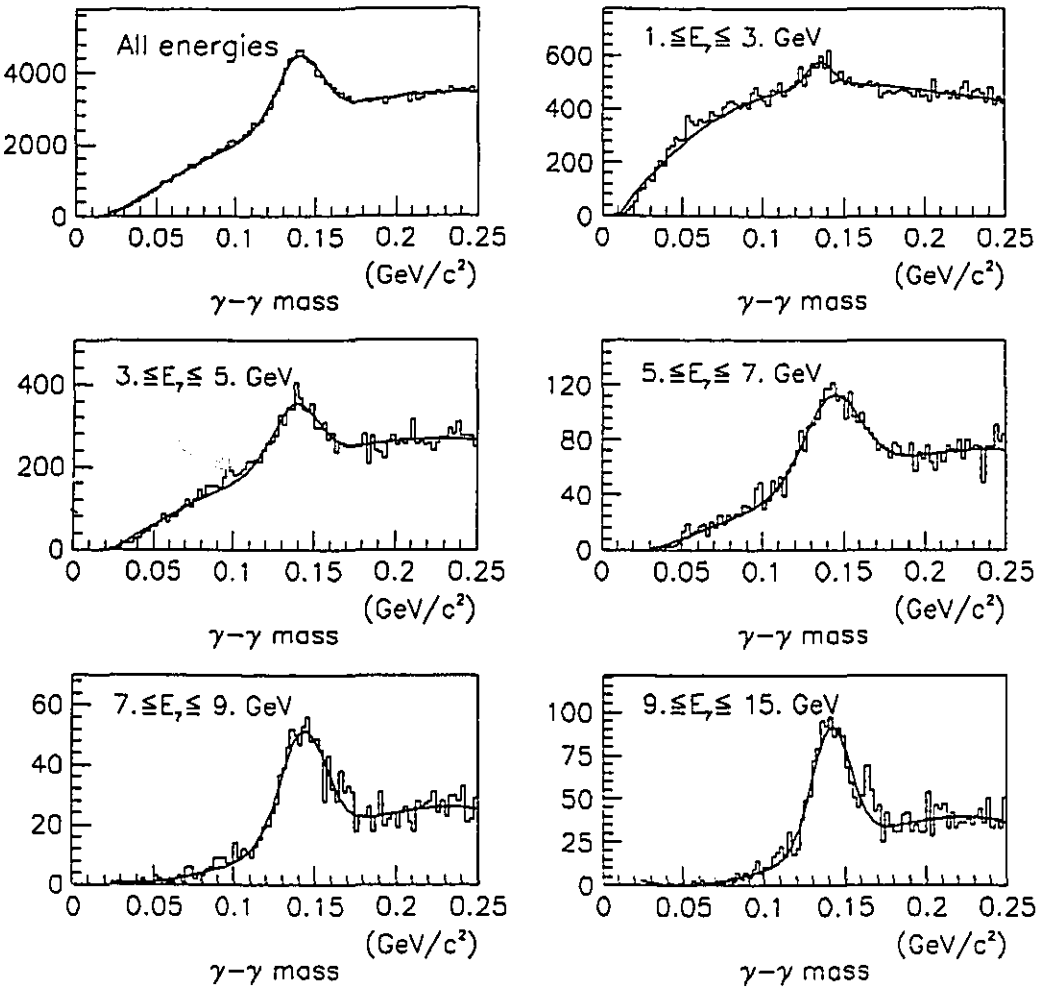

Figure 5.14: $\gamma\gamma$ invariant mass for different γ energy range

5.3.2 η decays

A signal for the decay $\eta \rightarrow \gamma\gamma$ was more difficult to observe since the η production cross-section and branching ratio into two photons are smaller than for the π^0, and consequently the expected signal-to-background ratio is less favorable. Therefore selection criteria for photon candidates were more restrictive:

1. The shower in the glass was associated with a crossing in the position hodoscope.
2. The χ^2 from glass shower fitting was ≤ 4.
3. The fractional energy error was $\Delta E \leq 0.15$
4. The ratio between the energy deposited in the Active Converter plane and the square root of the total energy was $\frac{E_{ac}}{\sqrt{E}} \geq 0.15$ GeV$^{1/2}$
5. There was no track projection within 5 cm of the shower
6. $E_\gamma \geq 5.$ GeV and the total energy of the parent particle $E_{\gamma_i} + E_{\gamma_j} \geq 15.$ GeV.

To reduce the combinatorial background even further, showers considered π^0 photon candidates were rejected. The $\gamma\gamma$ mass spectrum for the η region is shown in Figure 5.15. Using a polynomial function for the background and a gaussian for the η signal, the mass and width were measured: $M_\eta = 556 \pm 4$ MeV and $\sigma_{M_\eta} = 17 \pm 4$ MeV. The mass determination, when compared with the known value of the η mass of 549 MeV/c^2, is consistent with the believed energy scale systematic error of 3%.

5.4 Reconstruction efficiency

Photons converting in the target into electron-positron pairs provides useful information on the electromagnetic reconstruction efficiency. In fact, the conversion pairs could be identified by using solely the charged particle spectrometer information and this allowed a probe of the electromagnetic package reconstruction efficiency.

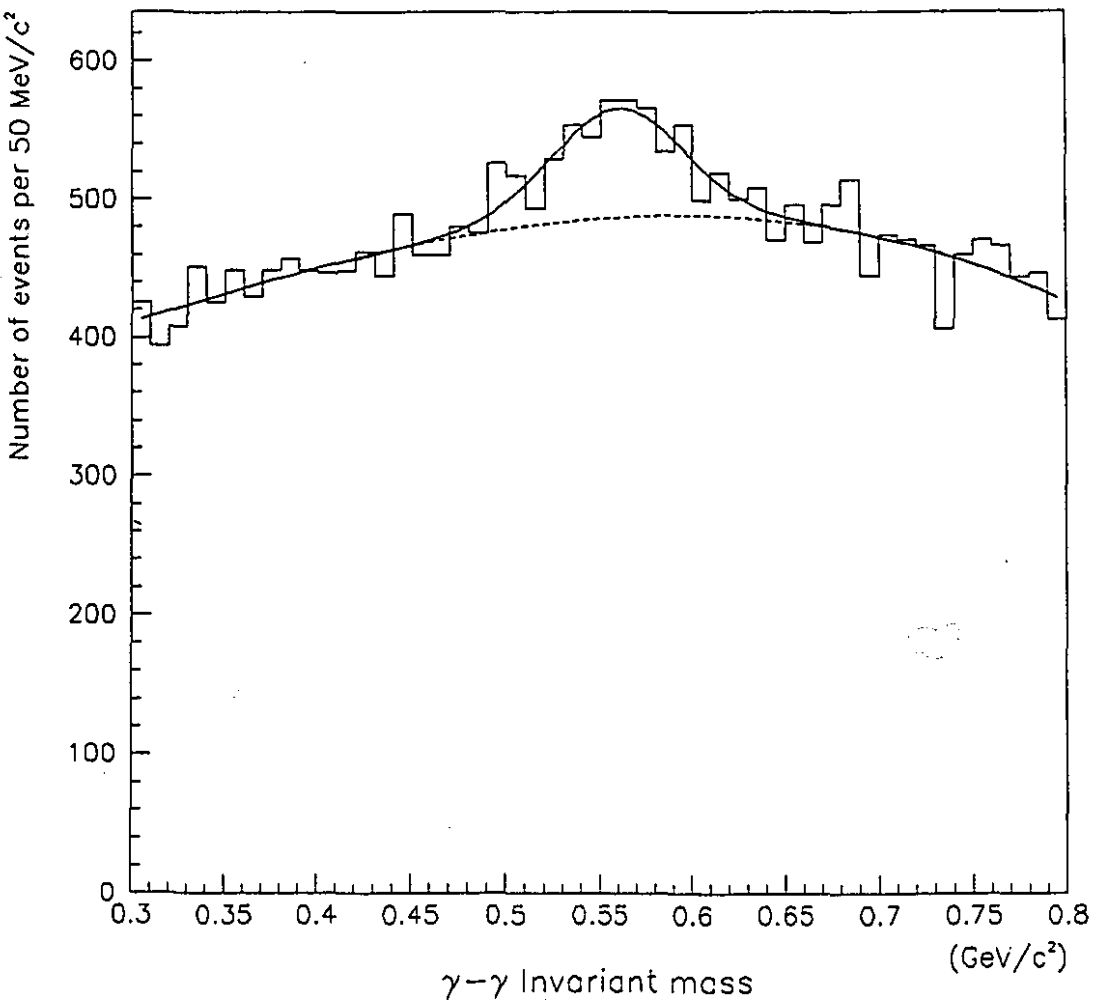

Figure 5.15: $\gamma\gamma$ invariant mass for $\eta(549)$ mass region

High energy photons, traversing a thickness Δz of a material having radiation length X_0, generate electron-positron pairs at a rate:

$$N_{e^+e^-} = N_\gamma(1 - e^{-\frac{7}{9}\frac{\Delta z}{X_0}}) \tag{5.12}$$

Given our 33 cm long natural lithium target (X_0=155 cm) and assuming that, on average, photons traverse half of the target, about 7% of the photons converted into electron-positron pairs within the target. Since about 8 photons/event are produced in a typical interaction at our energy, we expect 0.5 pairs/event to be produced (although only 10% of these will fall within the detector's acceptance). Particles produced in the decay of a massless parent particle, would be detected as a single track in the chambers upstream of the magnet given the very small opening angle of the decay. The effect of the analysis magnet would be to split the horizonthal projection but to leave the vertical projection untouched. Therefore to select e^+e^- pairs, a search was made for pairs of opposite sign satisfying the condition:

$$Y_{G_{pos}} - Y_{G_{neg}} \leq 10.\,\text{cm} \tag{5.13}$$

where $Y_{G_{pos}}$ is the impact position of the positive track at the glass and $Y_{G_{neg}}$ is the impact position of the negative track. Using the momenta determined by the charged particle spectrometer, the invariant mass for the candidate e^+e^- pairs was calculated and is shown in Figure 5.16. The clear peak at $M_{e^+e^-} \leq 10$ MeV is interpreted as a photon conversion signal. About 0.03 pair/event were reconstructed.

The distribution of $\frac{E_{cluster}}{p_{track}}$, requiring the shower to be within ± 3 cm of the track projection at the glass is shown in Figure 5.17. To minimize the hadronic background under the photon signal, a pair of low-mass opposite-sign tracks was identified as an e^+e^- pair if at least one of the two tracks, called "first" in the following, was identified as an electron by the electromagnetic calorimeter. About $8.9 \cdot 10^{-3}$ pairs/event satisfied this requirement.

The "second" electron of the pair was required to be within the electromagnetic detector geometrical acceptance. These e^+e^- pairs were used to determine the reconstruction efficiency for showers by the electromagnetic package by checking if the

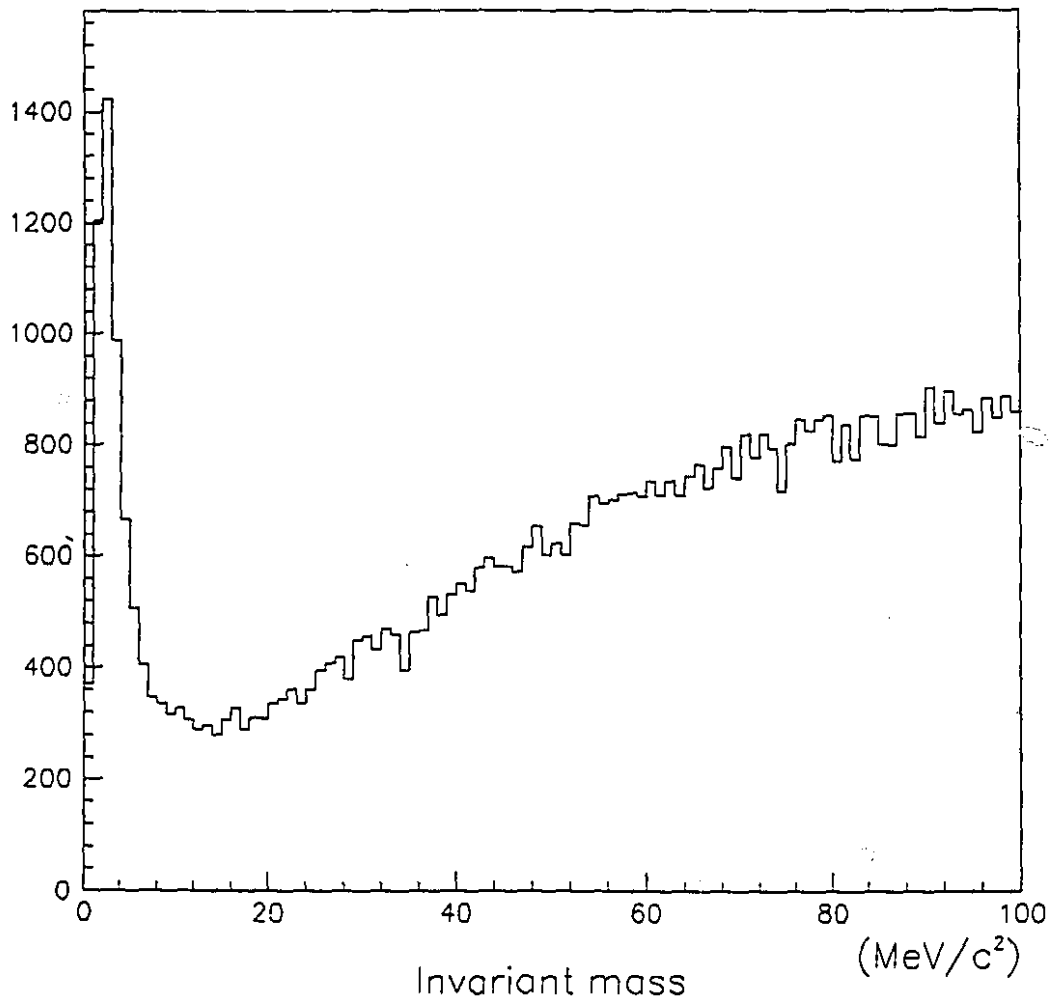

Figure 5.16: Opposite sign track invariant mass

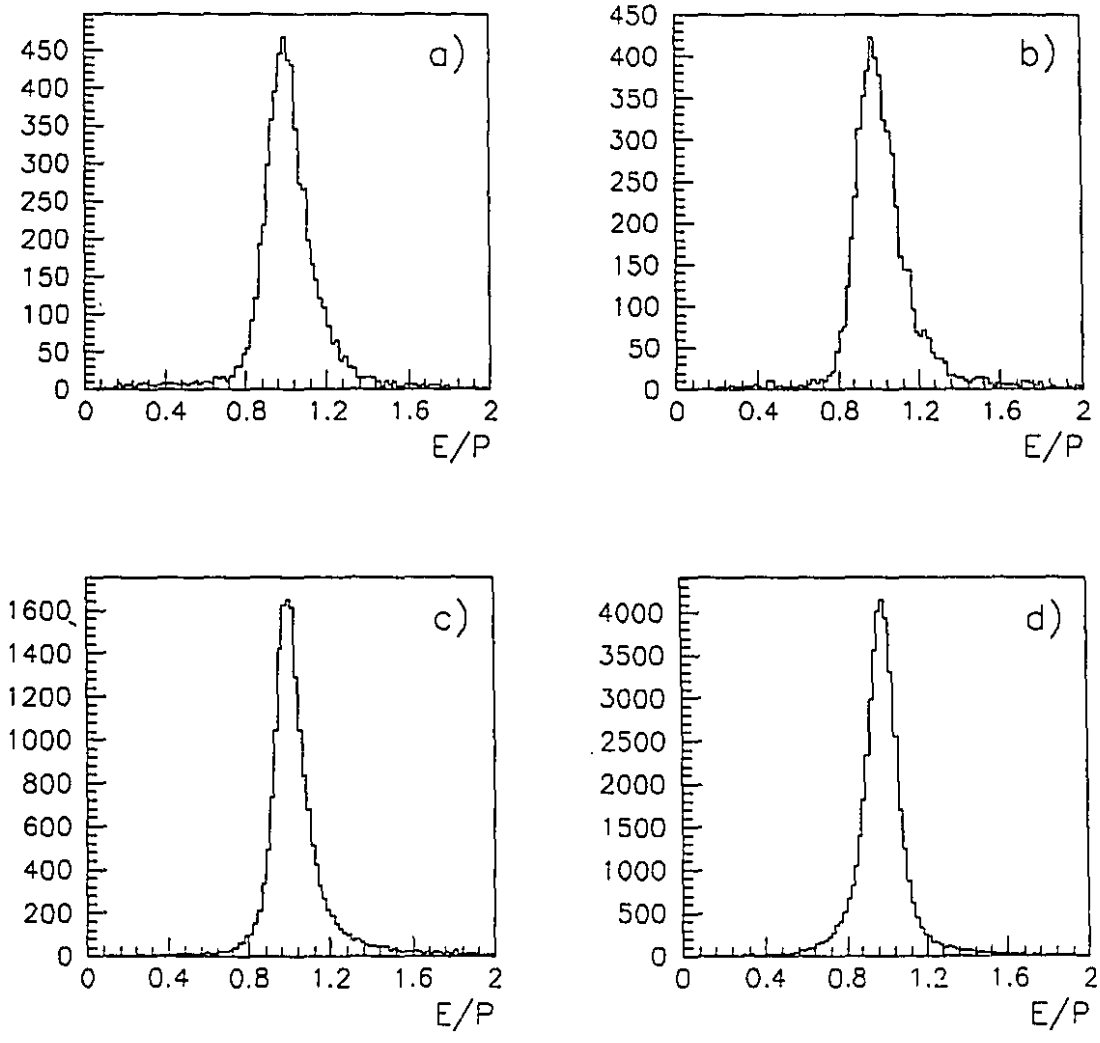

Figure 5.17: E/p signal for e^+e^- pair track candidates: a) SF5 blocks, b) large SCG blocks behind GTH, c) large SCG blocks behind LGC, d) small SCG blocks.

expected "second" electron of the pair was found:

$$\epsilon = \frac{\text{Number of "second" electrons reconstructed}}{\text{Number of "second" electrons expected}} \tag{5.14}$$

Since the average track multiplicity per event was 16, some of the identified pairs were not real e^+e^- pairs but random combinations of an electron with an oppositely charged track. This combinatorial background was estimated by two different methods using the sample of events containing an e^+e^- pair:

- Each electron in the pair sample was combined with all the tracks of the previous event. The probability for an electron to make a fake low-mass pair was found to be $(4.2 \pm 0.6)10^{-3}$. On average, 0.16 electrons per event were found, therefore the probability of having a fake pair was $(6.7 \pm 0.9)10^{-4}$/event. Compared with the found rate of 8.9 10^{-3}/event, the estimated percentage of fake pairs by this method was $(8 \pm 1)\%$.

- Each electron was combined with all the tracks of the same-sign in the event. The requirements used to select the e^+e^- pair sample were imposed and the probability of having a fake pair was estimated to be $(1.2 \pm 0.1)10^{-3}$. Therefore the estimated percentage of fake e^+e^- pairs by this method was $(14 \pm 1)\%$. Since same-sign pairs are less numerous than opposite-sign pairs, a further correction had to be applied. The same-sign average pair multiplicity is 6.4, the opposite-sign is 7.4. Taking this into account, the estimated background from opposite-sign fake pairs is $(16 \pm 1)\%$.

Averaging these two results, the estimated background from opposite sign fake pairs is $(12 \pm 4)\%$, corresponding to a correction factor of 1.14 ± 0.05 to the estimated efficiency:

$$\epsilon = 1.14 \frac{\text{Number of electrons found}}{\text{Number of electrons expected}} \tag{5.15}$$

The momentum distribution of the expected electrons in the four regions of the detector is shown in Figure 5.18. The same distribution for electrons identified by the

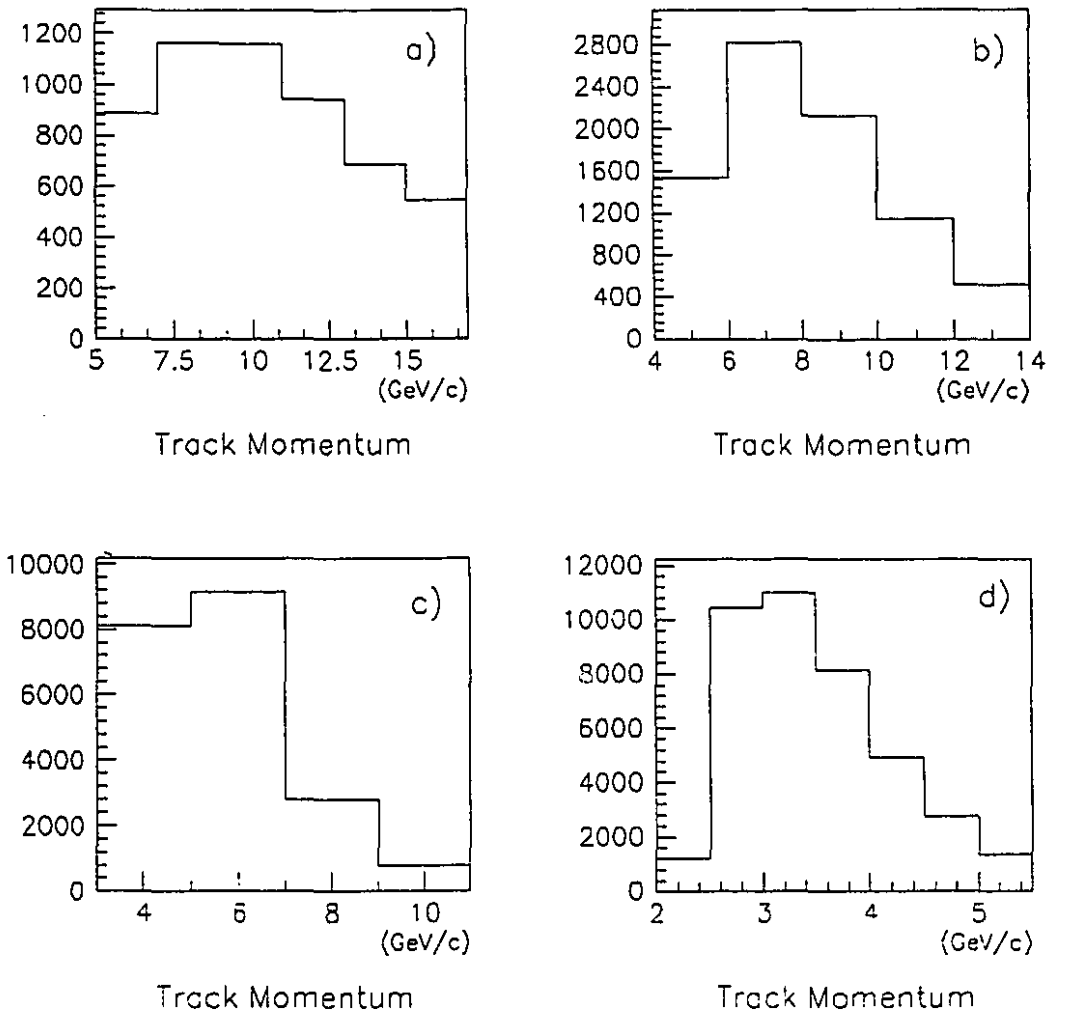

Figure 5.18: Momentum distribution for expected electrons in the four regions of the detector: a) small SCG blocks, b) large SCG blocks behind LGC, c) large SCG blocks behind GTH, d) SF5 blocks.

Region	efficiency (%)	corrected eff (%)
Small	35 ± 3	40 ± 3
Large SCG LGC	23 ± 2	26 ± 2
Large SCG GTH	35 ± 2	40 ± 3
SF5	49 ± 1	56 ± 3

electromagnetic package, as defined in the previous section, is shown in Figure 5.19. The ratio of the second distribution to the first gives a measure of the reconstruction efficiency as a function of momentum of the electron in the four regions of the detector. This distribution, corrected using Equation 5.15, is shown in Figure 5.20. The electron reconstruction efficiency, averaged over all the values of momentum, is shown in Table 5.4 for the four regions of the detector.

These results were used, together with the EGS simulation, to estimate the reconstruction efficiency for χ radiative decays (as reported in the next Chapter). More specifically, EGS was used to take into account the different longitudinal distributions of photon showers relative to electron showers: photons start their showers later and therefore deposit less energy in the Active Converter.

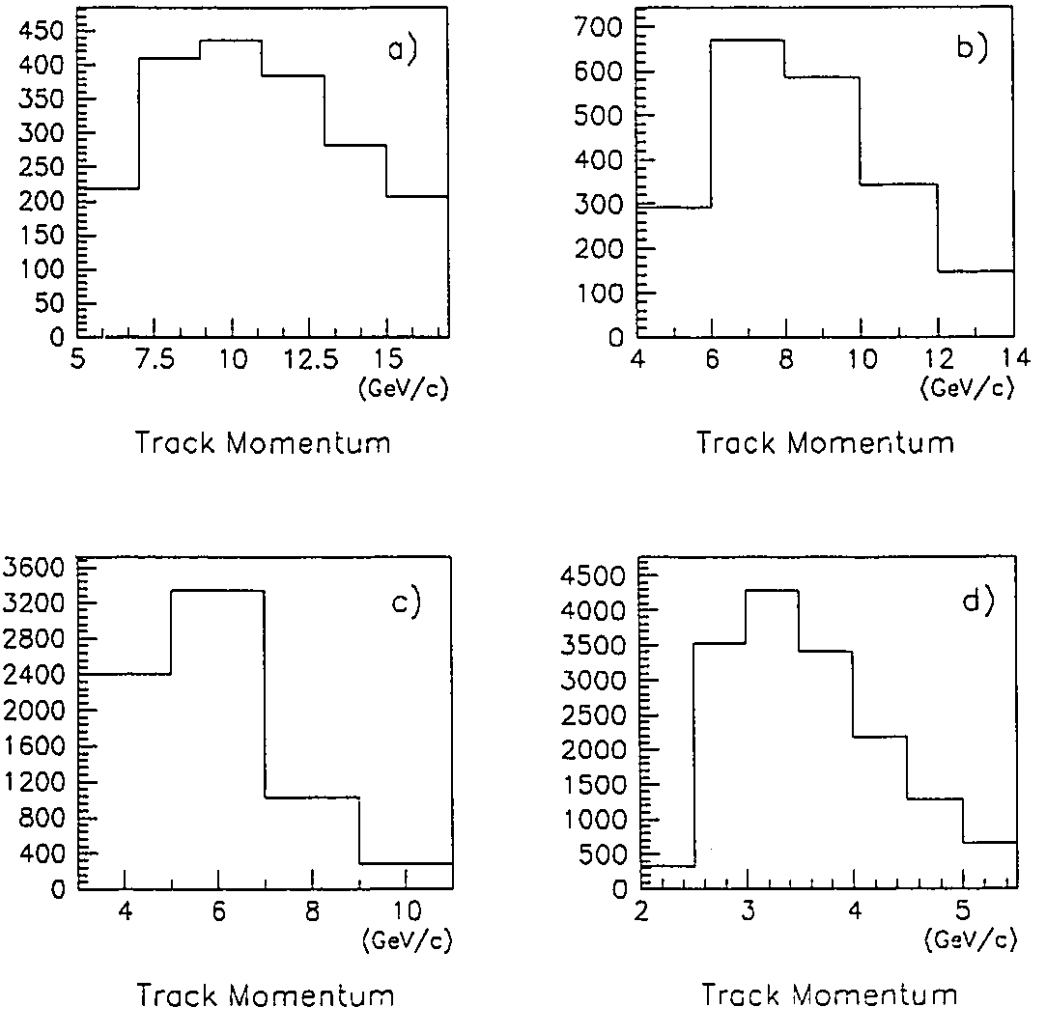

Figure 5.19: Momentum distribution for electrons found by the reconstruction program in the four regions of the detector: a) small SCG blocks, b) large SCG blocks behind LGC, c) large SCG blocks behind GTH, d) SF5 blocks

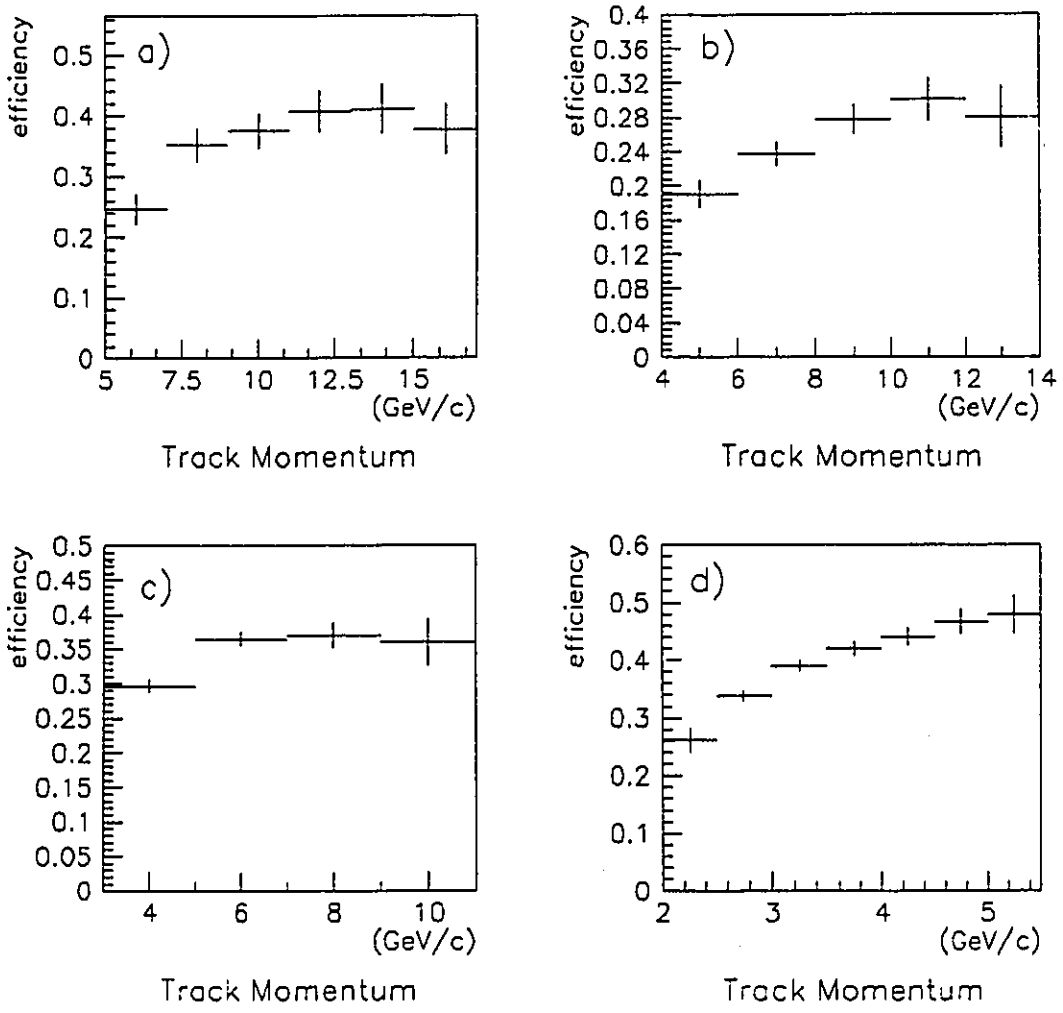

Figure 5.20: Reconstruction efficiency as a function of momentum in the four regions of the detector: a) small SCG blocks, b) large SCG blocks behind LGC, c) large SCG blocks behind GTH, d) SF5 blocks

Chapter 6

Analysis of dimuon events

The analysis of dimuon triggers to extract the radiative decays $\chi \rightarrow \psi\gamma$ was done in three steps:

- All the events were analysed to reconstruct muon tracks . Events containing at least one opposite-sign dimuon pair with invariant mass greater than 2.6 GeV/c^2 were kept for further analysis.
- In the second pass, cuts on the quality of the dimuon tracks were applied, to optimize the ratio of the J/ψ signal to background. Events with invariant mass in the interval 2.98–3.28 GeV/c^2 were selected as J/ψ candidates.
- Finally, J/ψ candidates were combined with all photon showers in the event. Using the $\psi\,\gamma$ invariant mass distribution, the χ signal and the background were evaluated.

6.1 Dimuon first pass analysis

In the first pass, all possible muon candidate tracks were found, using the chamber information. This analysis was performed on the Fermilab ACP parallel processor computer system. A filter program was used to pre-analyze the events and to make a fast selection based on a rough estimate of the dimuon invariant mass. The filter program used a similar algorithm as the trigger processor (section 2.9.2). Using the drift chamber TDC information, X-view tracks were reconstructed and using the projection of the beam trajectory into the middle of target, the muon four-momenta were calculated.

All possible pairs of opposite sign tracks were made. Only events with at least one pair with invariant mass $\geq$2.5 GeV/c^2, were considered for further analysis.

Events accepted by the filter were analyzed by the dimuon reconstruction program for complete analysis using the algorithm described in Chapter 4. Events containing a pair of fully reconstructed opposite sign tracks, with a corresponding invariant mass greater than 2.6 GeV/c^2, were selected. The dimuon mass spectrum for these events is shown in Figure 6.1a (full line), for 10% of the data sample. A clear peak at the J/ψ mass is evident.

6.2 Dimuon second pass analysis

The dimuon triggers were re-analyzed to reduce the number of events present in the background under the J/ψ peak and the number of J/ψ candidates was evaluated as described in the following sections.

6.2.1 Second pass selection criteria

The subsample of the data shown in in Figure 6.1, was used to optimize the J/ψ signal to background ratio. Criteria in selecting the best muon candidates were: a) the quality of the rear segment as a track (number of hits and χ^2) and as a muon candidate (muon residuals), b) the near equality of the front and rear Y-slopes c) the near equality of the front and rear X and Y intercepts.

An initial set of cuts was chosen, excluding the quantity under study (and all the variables correlated with the variable under study). Using the initial set of cuts the good muon events were selected as the tracks belonging to a J/ψ candidate. For each variable,the distribution for all tracks (shown as the full line in Figures 6.2-6.4) and for all good quality muons in the J/ψ mass region (shown as the dotted line in Figures 6.2-6.4) were compared.

As a result of the comparison this set of cuts was applied to the muon candidates:

- Each muon track was required to have momentum $\leq$ 320 Gev/c (given that beam

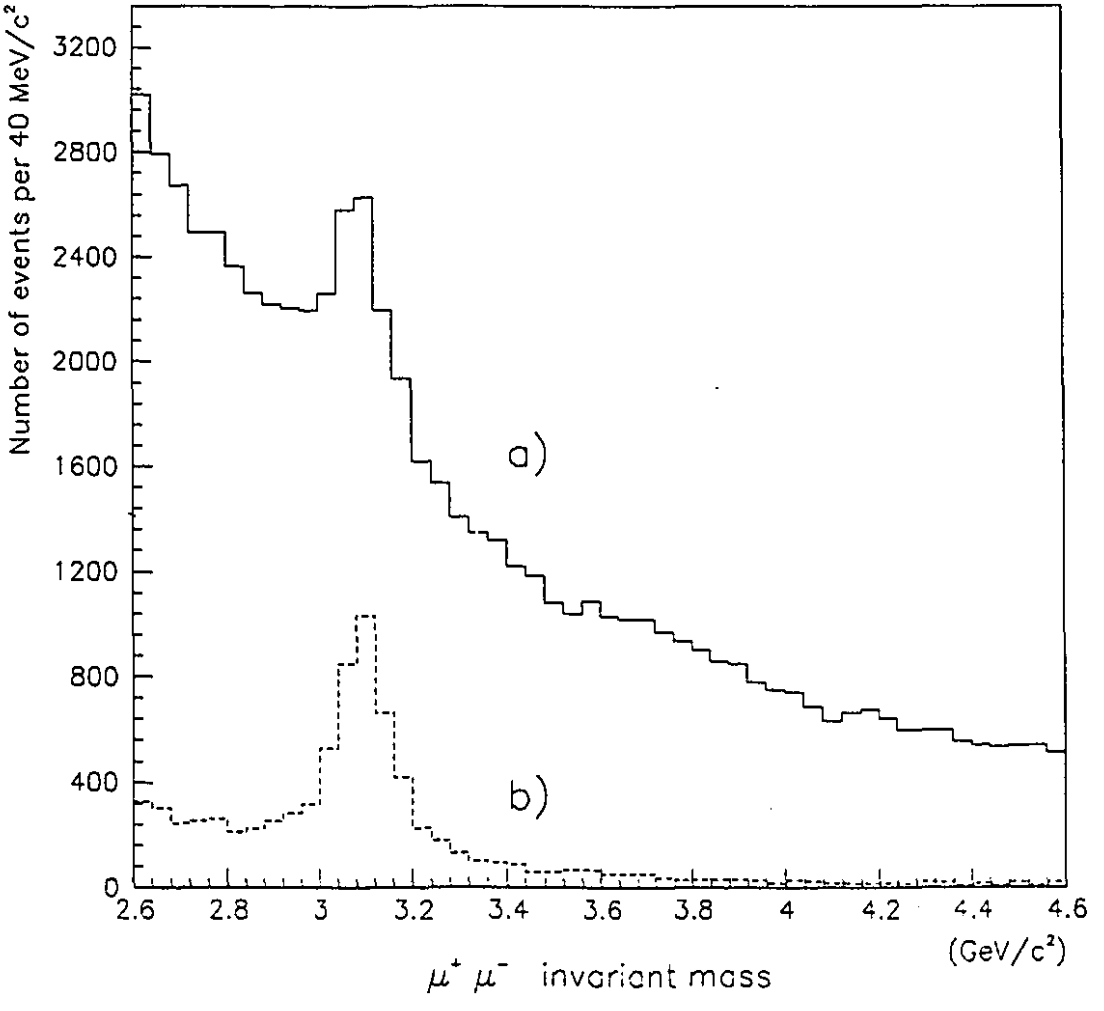

Figure 6.1: Dimuon mass spectrum from first pass analysis

momentum was 300 GeV/c, higher momentum corresponded to either fake, or badly measured tracks).

- Each muon track was required to have at least 7 (out of a possible maximum 12) hits on rear segment, as shown by the arrow on Figure 6.2a.

- The value of the χ^2 (per degree of freedom) obtained from the least square fitting of the rear space track (Figure 6.2b) was required to be ≤ 6 for each track.

- Each muon track candidate was required to point to a lit muon counter within a set distance, determined by Monte Carlo The Monte Carlo took into account projection uncertainties and multiple scattering:

$$|\mu Y \quad \text{residual}| \leq 16 \text{ cm}$$
$$|\mu 1 \quad \text{residual}| \leq 16 \text{ cm}$$
$$|\mu 2 \quad \text{residual}| \leq 20 \text{ cm}$$
$$|\mu 3 \quad \text{residual}| \leq 23 \text{ cm}$$

  The residual is defined by the difference between the track projection into the moun counter plane and the center of the closest lit counter (muon counter residual distribution are shown in Figure 6.3).

- The difference in upstream and downstream vertical slopes be less than 15 mrad:

$$|A_{Y_{front}} - A_{Y_{rear}}| \leq 15\text{mrad}$$

  where $A_{Y_{front}}$ is the front segment Y-slope and $A_{Y_{rear}}$ is the rear segment Y-slope (Figure 6.4a).

- The X and Y differences between the track front segment and the rear segment projection at the magnetic-center (z_{mag}=-4.8 cm), were required to be (Figure 6.4b and Figure 6.4c):

$$|X_f - X_r| \leq 1\text{cm}$$
$$|Y_f - Y_r| \leq 4\text{cm}$$

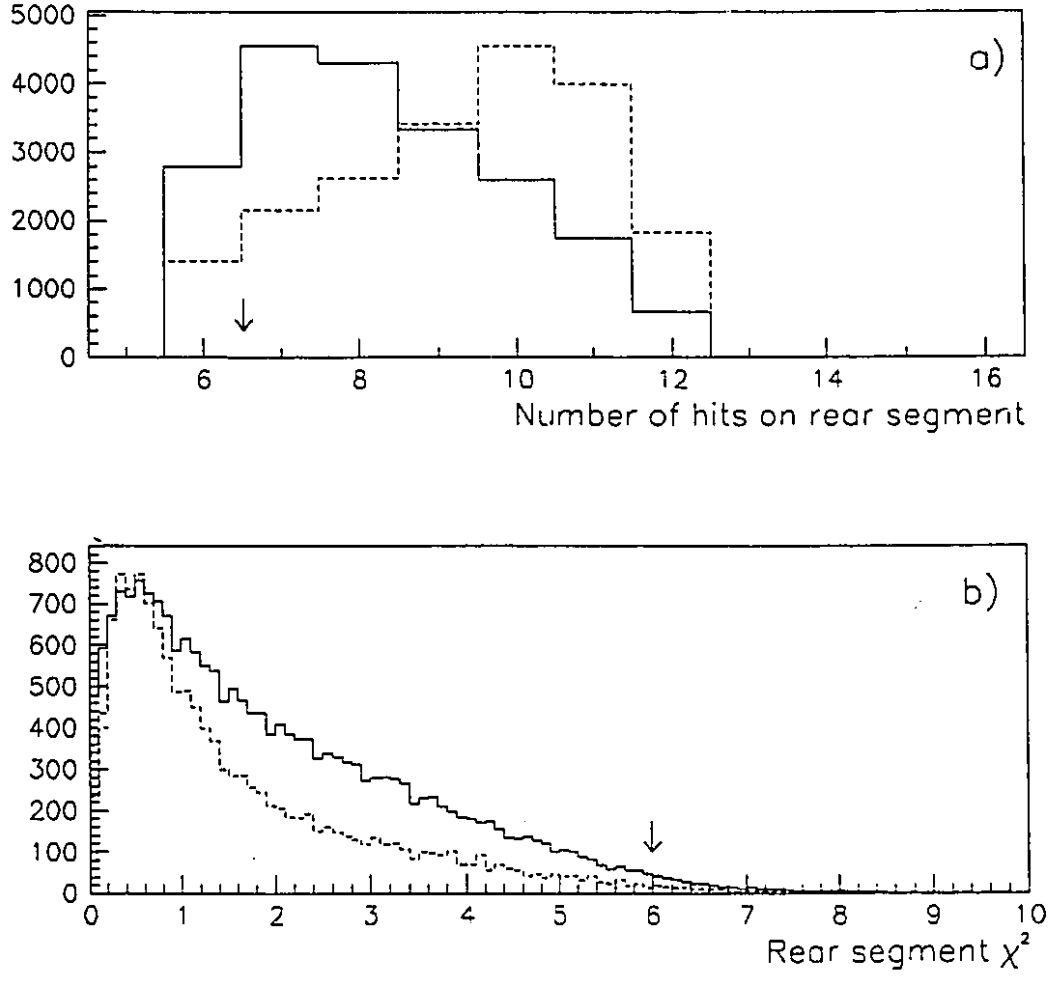

Figure 6.2: Rear segment χ^2 and number of hits (full line is all tracks dotted line is for good J/ψ muon tracks)

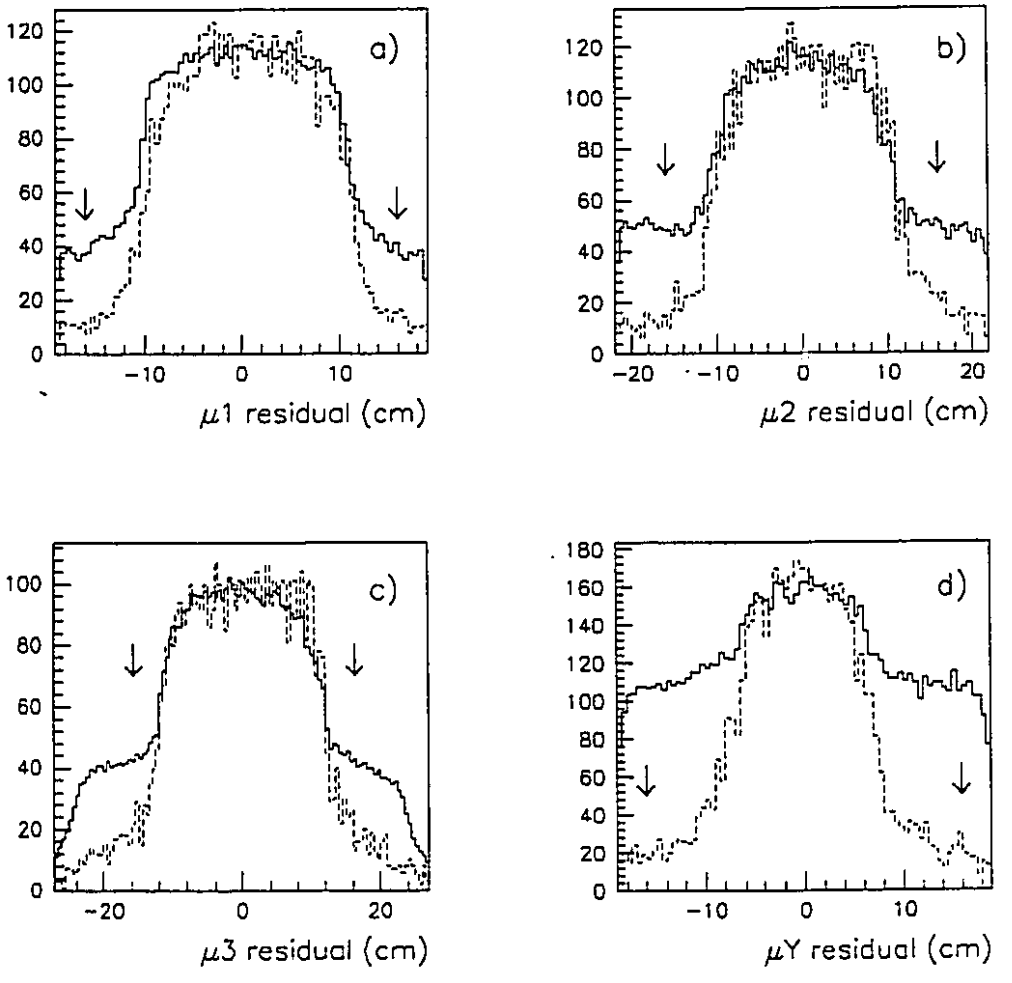

Figure 6.3: Muon residuals (full line is all tracks dotted line is for good J/ψ muon tracks)

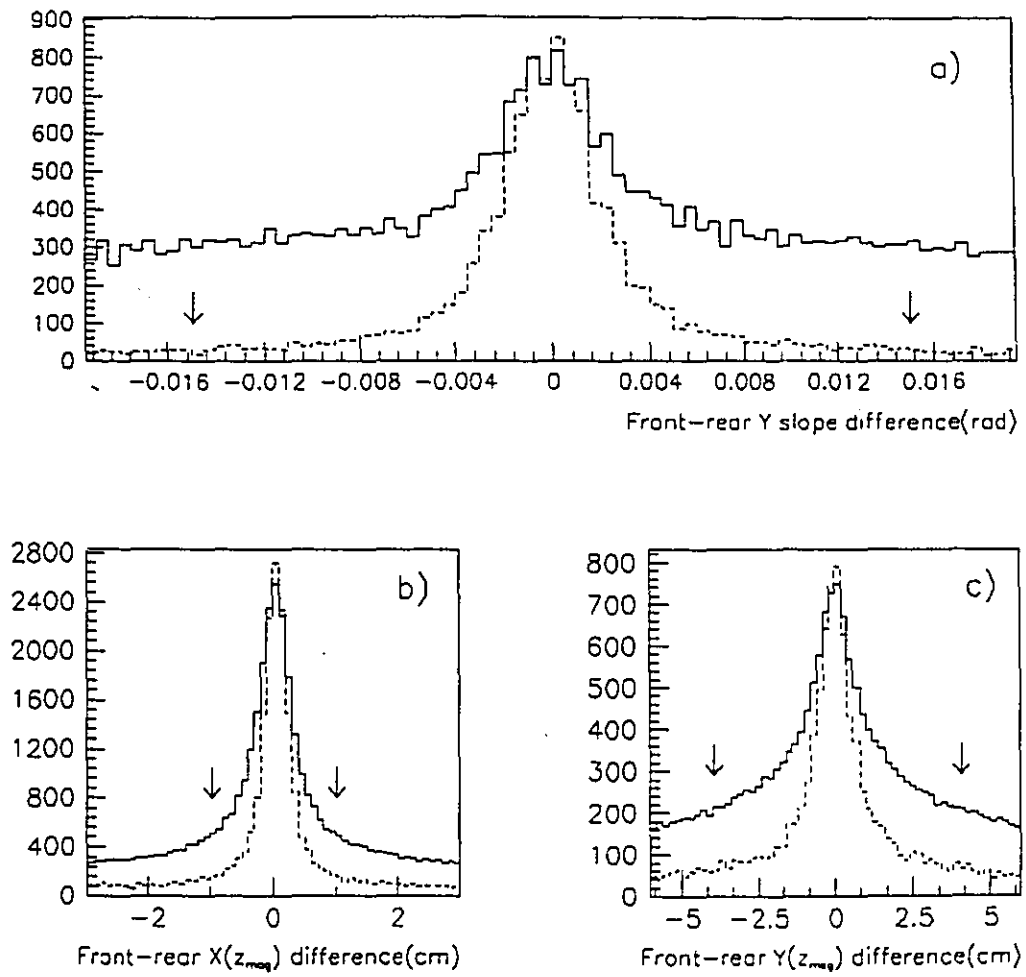

Figure 6.4: Front-rear difference at $z=z_{mag}$ and Y slope difference (full line is all tracks dotted line is for good J/ψ muon tracks)

where:

- $X_f = A_{X_{front}} \cdot z_{mag} + B_{X_{front}}$ is the projected location of the front X segment at the magnet middle plane.
- $X_r = A_{X_{rear}} \cdot z_{mag} + B_{X_{rear}}$ is the the projected location of the rear X segment at the magnet middle plane.
- $Y_r = A_{Y_{rear}} \cdot z_{mag} + B_{Y_{rear}}$ is the projected location of the rear Y segment at the magnet middle plane.
- $Y_f = A_{Y_{front}} \cdot z_{mag} + B_{Y_{front}}$ is the projected location of the front Y segment at the magnet middle plane.

The dimuon mass spectrum for the events satisfying these requirements is shown in Figure 6.1b (dotted line) for 10% of the data sample. The distributions, before and after the cuts, were fitted using an exponential function for the background and a double gaussian for the J/ψ signal (as described in more detail in the next section). This set of cuts, applied in the second pass, kept $(85 \pm 5)\%$ of the signal while rejecting $(90 \pm 5)\%$ of the background. Applying the same cuts to Monte Carlo generated events (see Section 6.4 for more details), a similar signal rejection factor was obtained.

6.2.2 J/ψ final sample

Events satisfying the second pass cuts were refit and the momentum recalculated by adding the constraint that the front segment originated at the interaction vertex. Figure 6.5a shows the dimuon effective mass for the full sample of events with mass greater than 2.5 GeV/c^2. A signal to background ratio exceeding 3:1 was achieved. Based on the results of the Monte Carlo studies (see Section 6.4 for a detailed description), the mass resolution of the experiment was evaluated as a sum of two gaussian functions:

$$f(M) = e^{-\frac{(M-M_\psi)^2}{2\sigma_1^2}} + Ce^{-\frac{(M-M_\psi)^2}{2\sigma_2^2}}$$

where:

- M_ψ is the J/ψ mass.

- σ_1 and σ_2 are the width of the two gaussians.

- C is a scaling factor between the two gaussians.

The parameters obtained by the double gaussian fit to the Monte Carlo generated events were:

$$\begin{aligned} M_\psi &= (3095.6 \pm 0.5)\ \mathrm{MeV/c^2} \\ \sigma_1 &= (38 \pm 1)\ \mathrm{MeV/c^2} \\ \sigma_2 &= (115 \pm 15)\ \mathrm{MeV/c^2} \\ C &= (0.34 \pm 0.03) \end{aligned} \tag{6.1}$$

In Figure 6.5b the Monte Carlo prediction for the J/ψ mass resolution is compared to the background-subtracted mass spectrum for the full sample of dimuon events. The double gaussian function represented well the effect of the numerous factors which degraded the mass resolution and the agreement between the data and the Monte Carlo simulation is very good. Dimuon invariant mass spectrum for each beam type is shown in Figure 6.6. The smooth curve is a fit to the data using the double gaussian function for the J/ψ signal plus an exponential background. The double gaussian width and relative scaling factor were fixed at the values obtained from the Monte Carlo simulation (Equation 6.1). The J/ψ mass obtained with this fitting procedure was $M_\psi = (3088.9 \pm 0.5)$ MeV/c^2. Comparing this value with the known value[9], 3096.9 MeV/c^2, we estimate that the momentum scale of our tracking system is correct to the level of 0.25 %. To obtain the best possible values of the J/ψ four-momenta, the four-momenta of the muons in the J/ψ region, defined to be 2980–3280 MeV/c^2, were rescaled so that they yielded an invariant mass of 3097 MeV/c^2. The number of J/ψ events, background corrected, is shown in Table 6.1 for the different beam types, together with the total number of events having a invariant mass $M_{\mu^+\mu^-}$ in the J/ψ region. These events were flagged as J/ψ candidates and used in subsequent

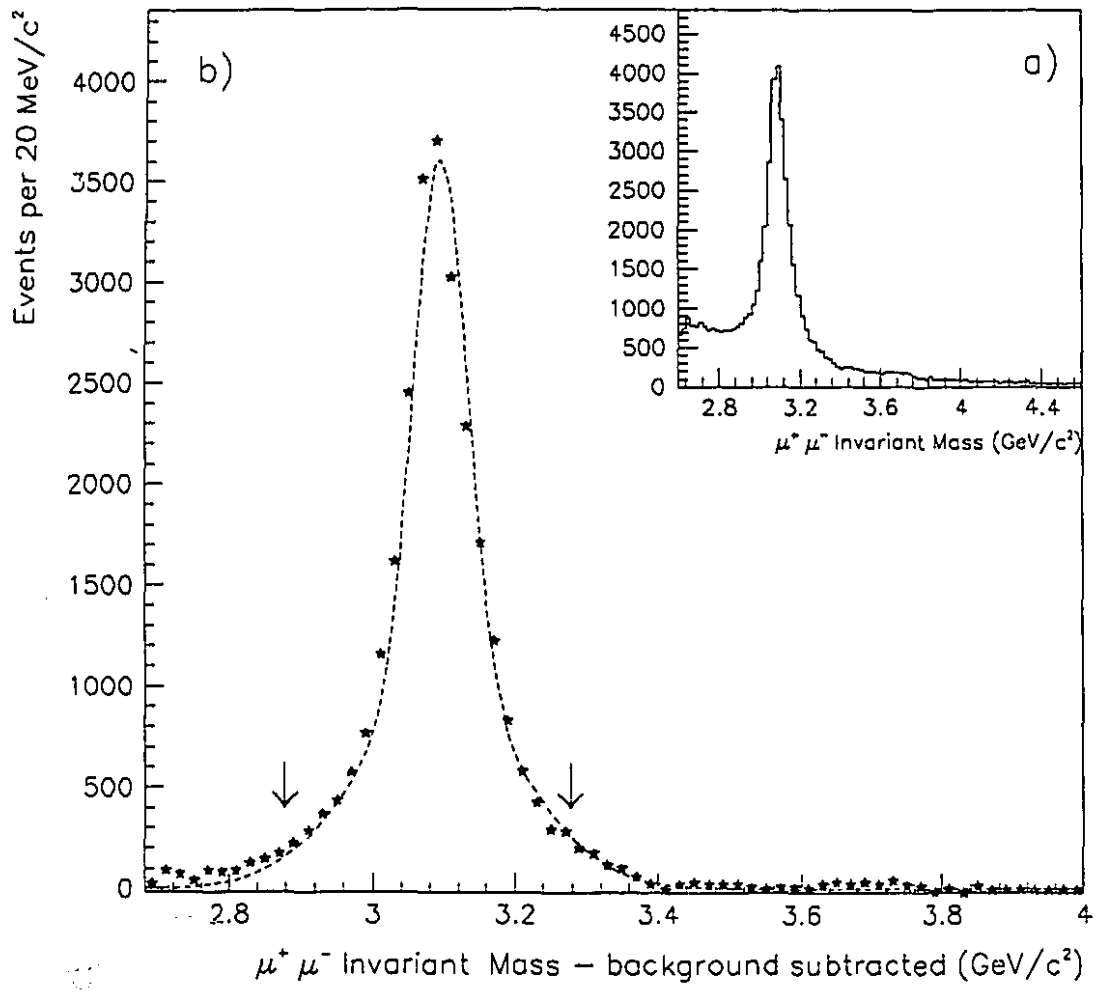

Figure 6.5: Dimuon final sample: a) invariant mass spectrum for all $\mu^+\mu^-$ combinations, b) background subtracted spectrum is compared to the Monte Carlo width prediction.

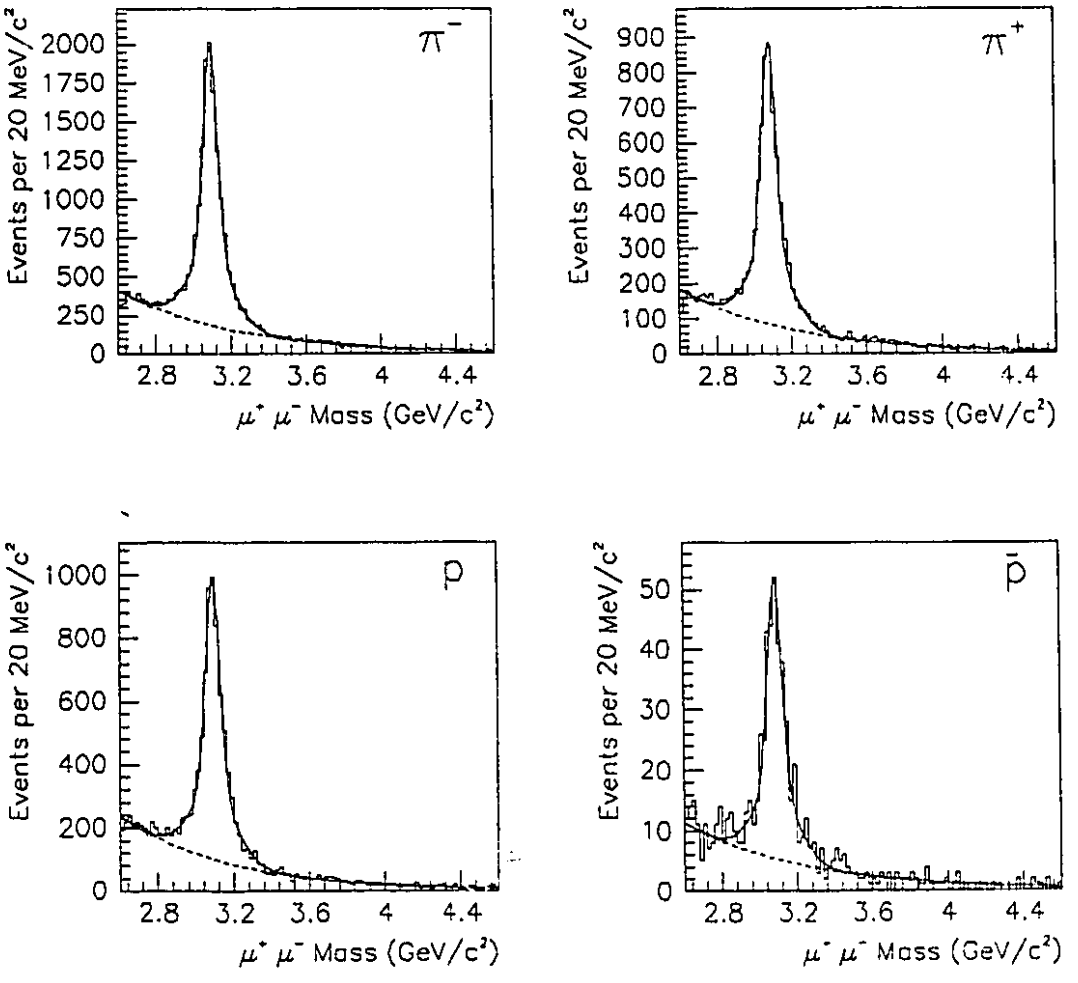

Figure 6.6: Dimuon final sample for different beam types

Table 6.1: Dimuon events with with $2.88 \leq M_{\mu^+\mu^-} \leq 3.28$ GeV/c^2

Beam type	Number of J/ψ candidates	Number of J/ψ 's (background subtracted)
π^-	16353	12470 ± 160
π^+	7147	5560 ± 90
p	8211	6090 ± 90
$\bar{p}$	439	320 ± 20

analysis. Such an event sample was also used to derive total and differential cross sections for the production ([55]).

6.3 $\psi\gamma$ invariant mass

As the last step of the dimuon event analysis, we reconstructed all possible electromagnetic showers using the electromagnetic package described in Chapter 5. Each J/ψ candidate was combined with all showers reconstructed in the same event which passed the electromagnetic shower cuts defined in Section 5.3.1. The J/ψ γ effective mass distribution is plotted, for the full data sample, in Figure 6.7 as a function of the difference $\Delta M = M_{\mu^+\mu^-\gamma} - M_{\mu^+\mu^-}$. Expected values of ΔM for the χ states are: $\Delta M_{\chi_0} = 0.318$ GeV/c^2, $\Delta M_{\chi_1} = 0.414$ GeV/c^2 and $\Delta M_{\chi_2} = 0.459$ GeV/c^2. Given the branching fractions, BR($\chi_0 \rightarrow \psi\gamma$) = 0.7 %, BR($\chi_1 \rightarrow \psi\gamma$) = 27.3%, and BR($\chi_2 \rightarrow \psi\gamma$) = 13.5% [9], one might expect comparable χ_1 and χ_2 signal and a much smaller χ_0 signal. Figure 6.7 shows an evident excess occuring in correspondance of the χ_1, χ_2 mass region. The background under the χ peak in the plot of Figure 6.7 is due to the high multiplicity of showers reconstructed in dimuon events (on average 3.3 showers per event). Possible sources of these showers include:

- $\pi^0 \rightarrow \gamma\gamma$ decays
- electrons and hadrons which passed the electromagnetic shower requirements (as seen in Section 5.2 10% of the hadrons passed our requirements).
- $\eta \rightarrow \gamma\gamma$ decays.

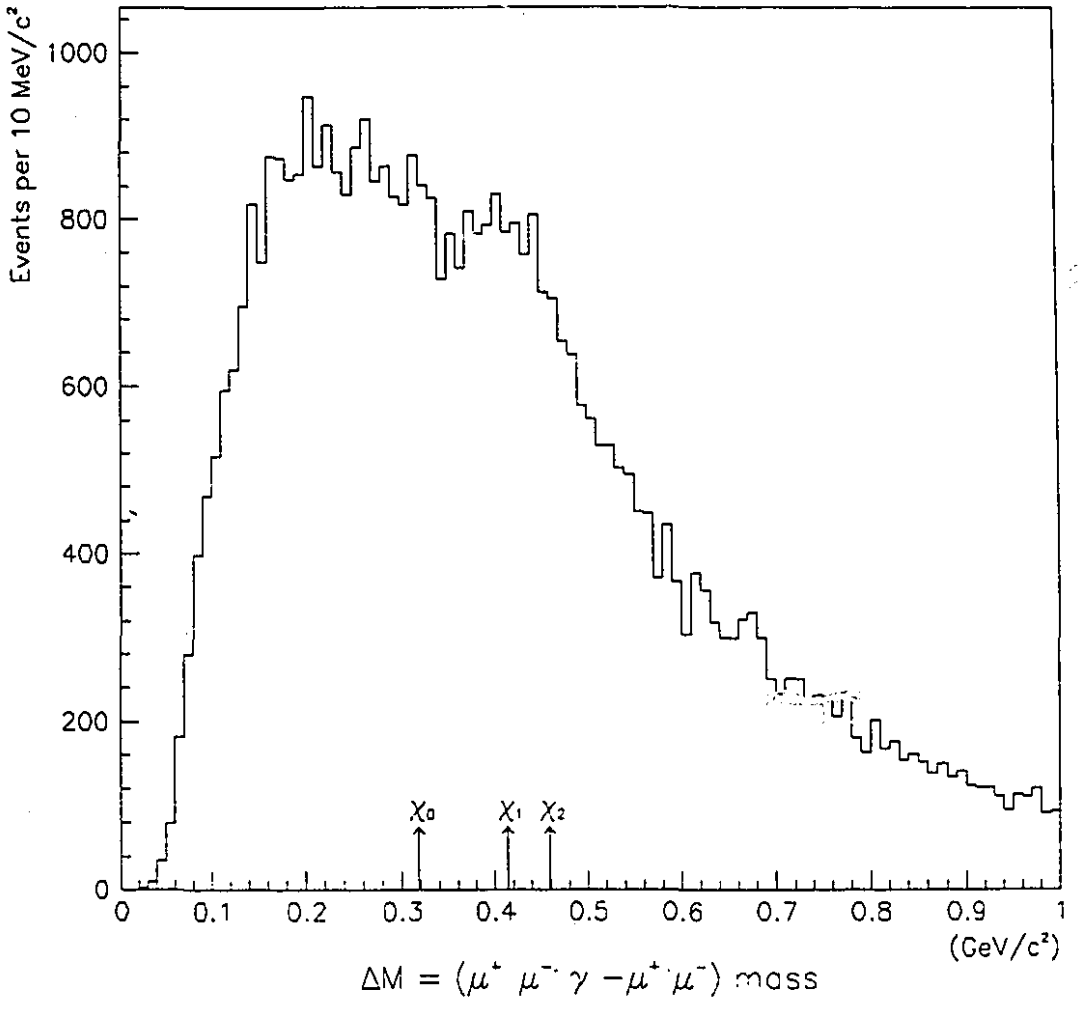

Figure 6.7: M ($\mu^+\mu^-\gamma$) - M ($\mu^+\mu^-$) mass spectrum for all electromagnetic showers.

Table 6.2: Parameters of the x_F and p_T fits to ψ cross section

beam type	n	x_0	$< p_T > (GeV/c)$
π^+, π^-	$2.34 \pm 0.12 \pm .5$	0.028 ± 0.06	1.071 ± 0.008
p	$4.89 \pm 0.21 \pm .5$	0.028 ± 0.05	1.005 ± 0.012

Therefore, to enhance the χ states while rejecting most of the background, the following 'χ quality' criteria were used:

- To eliminate π^0 decays, all photons, which when combined with another photon gave an invariant mass $M_{\gamma\gamma} \leq 180$ MeV/c^2, were rejected.
- To eliminate electrons and hadrons and the contamination due to hadron showers in the vicinity of a photon, showers within 8 cm of a projected track were rejected.

The J/ψ γ effective mass distribution for photons satisfying the "χ quality" criteria is shown in Figure 6.8. The following sections describe the extraction of the χ signals, the evaluation of the acceptance, and the estimation of the reconstruction efficencies.

6.4 χ Monte Carlo

A Monte Carlo program was used to evaluate the χ geometrical acceptance, the χ reconstruction efficiency and the expected width of the χ signal. The production of the desired reaction requires a model of the mechanisms involved. The χ production distributions have not yet been measured and therefore the J/ψ x_F and p_T distributions, as measured in our experiment, were used [54]:

$$E\frac{d^3\sigma}{dp^3} = Ap_T e^{-p_T^2/p_0^2}(1 - |x_F - x_0|)^n \qquad (6.2)$$

where the values for $< p_T >$, x_0, and n are listed in Table 6.2 for the different beam types. The χ's were generated using the above distributions, and then allowed to decay, isotropically in their center of mass frame, into J/ψ $\cdot\gamma$. The J/ψ was then decayed isotropically into $\mu^+\mu^-$. The muons were checked to see if they satisfied the trigger and subsequently they were sent through a simulation of the apparatus. Chamber and

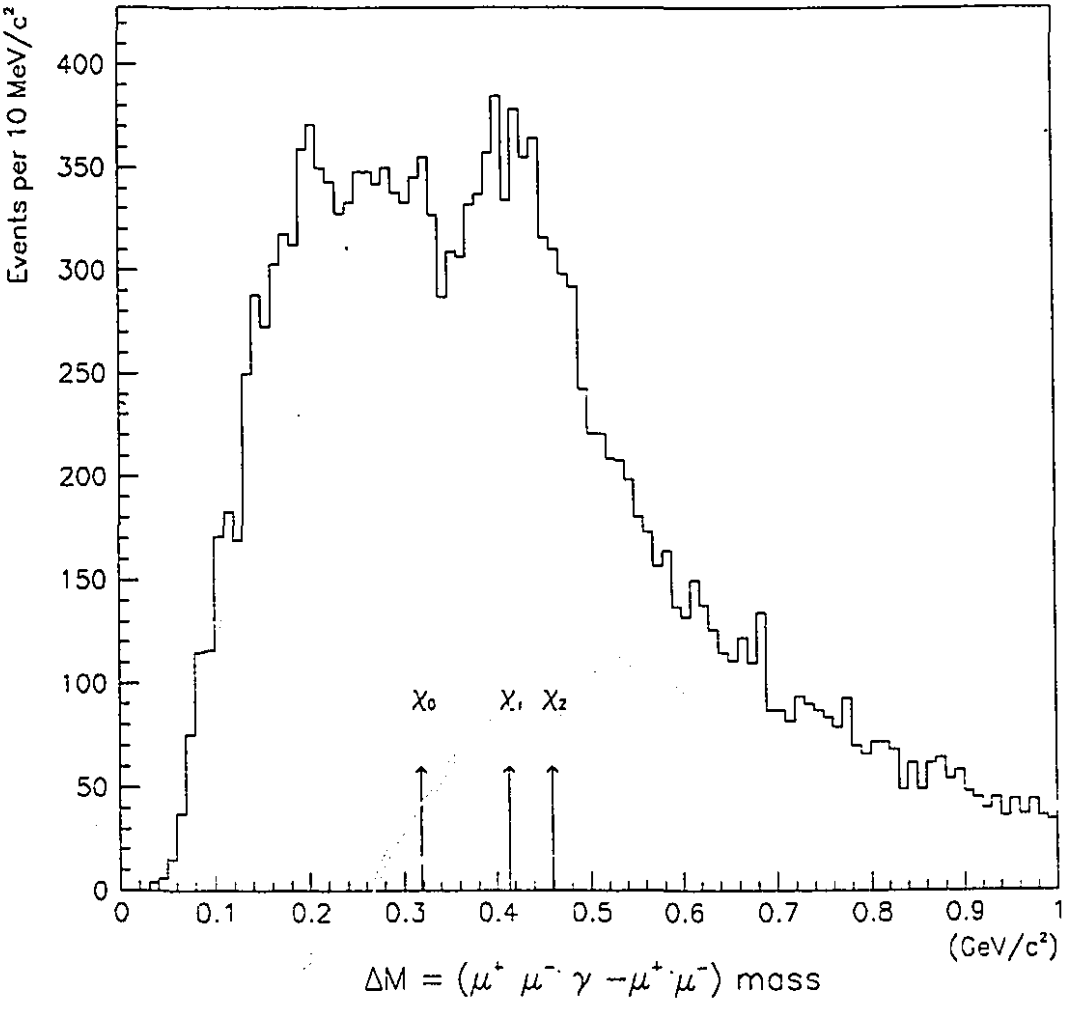

Figure 6.8: M ($\mu^+\mu^-\gamma$) - M ($\mu^+\mu^-$) mass spectrum for "χ quality" photons

counter efficiencies were taken into account by using the results described in Chapter 3. The presence of other particles accompanying J/ψ production was simulated by overlapping the hits of the Monte Carlo generated J/ψ tracks with hits recorded in a real dimuon trigger. The events were then analysed by the same algorithm used in the dimuon reconstruction program described in Chapter 4 and the second pass selection criteria, described in Section 6.2, were imposed to identify the simalted J/ψ 's. About 10% of the generated events had a fully reconstructed J/ψ (more details on the J/ψ simulation Monte Carlo are given in reference [45]). Photons within the detector acceptance were then run through the electromagnetic detector using EGS. Energy and position resolution were taken into account by using the results of the electron studies presented in Chapter 5. Finally, each photon was weighted by the detection efficiency, calculated using e^+e^- pairs as described in Chapter 5, to determine if it was to be included among the detected sample.

6.4.1 χ geometrical acceptance and reconstruction efficiency

The acceptance/efficiency of the spectrometer is defined as the ratio of the number of reconstructed events to the events actually produced. In the case of χ production, given that our reconstruction algorithm required the presence of a reconstructed J/ψ , the χ acceptance was calculated relative to the J/ψ acceptance. Events having a fully reconstructed J/ψ were used to calculate the χ acceptance, reconstruction efficiency and the expected width of the χ signal. Once the J/ψ was reconstructed, the photon was checked to see if entered the electromagnetic detector. Photons impacting the inner and outer most layers of the Main Array, or a dead region of the detector were removed. The χ acceptance was defined as:

$$A_\chi = \frac{\text{Number of } \chi \text{ with } \gamma \text{ accepted and } J/\psi \text{ reconstructed}}{\text{Number of } \chi \text{ with } J/\psi \text{ reconstructed}} \qquad (6.3)$$

The χ acceptance as function of x_F and p_T is shown in Figure 6.9 for pion and proton beams. The integrated χ acceptances were found to be:

$$A_\chi = 62 \pm 1\% \qquad \text{for pions}$$

$$A_\chi = 63 \pm 1\% \qquad \text{for protons}$$

Once the χ was accepted, the photon was propagated through the electromagnetic detector as described above and the χ reconstruction efficiency was evaluated as:

$$\epsilon_\chi = \frac{\text{Number of } \chi \text{ reconstructed}}{\text{Number of } \chi \text{ with } \gamma \text{ accepted and J}/\psi \text{ reconstructed}} \tag{6.4}$$

The χ reconstruction efficiency as a function of x_F and p_T is shown in Figure 6.10 for pion and proton beams. The reconstruction efficiencies take into account the 7% of the χ photons which converted before reaching the electromagnetic calorimeter (see Chapter 5 for more details). Finally, the integrated χ reconstruction efficiency was found to be:

$$\epsilon_\chi = 26.0 \pm 0.2 \pm 3.0 \qquad \text{for pions}$$

$$\epsilon_\chi = 26.1 \pm 0.2 \pm 3.0 \qquad \text{for protons}$$

where the first error is the statistical error due to the number of simulated events and the second is the uncertainty in the determination of the reconstruction efficiency using electron showers. The acceptance is the same for the χ_1 and χ_2. Varying, within reasonable limits, most of the parameters used in the χ Monte Carlo simulation didn't affect the χ acceptance, only exception was the χ angular distributions. The χ was decayed into $\psi\gamma$ in its center of mass according to the angular distribution $1 + \alpha cos^2\theta$, where θ is the angle between the photon and the incident beam particle ($\alpha = 0$ corresponds to the isotropic decay). Theoretical models predict values of α ranging from -1/3 to 1. Varying α between these limits produced variations in the χ acceptance of about 10% and this is taken to be the systematic error.

6.4.2 Expected width of χ signal

The observed width of the χ peak can be predicted from the Monte Carlo procedure of propagating both the photon and the J/ψ through the detector. Figure 6.11 shows the invariant mass spectrum derived from two different simulations:

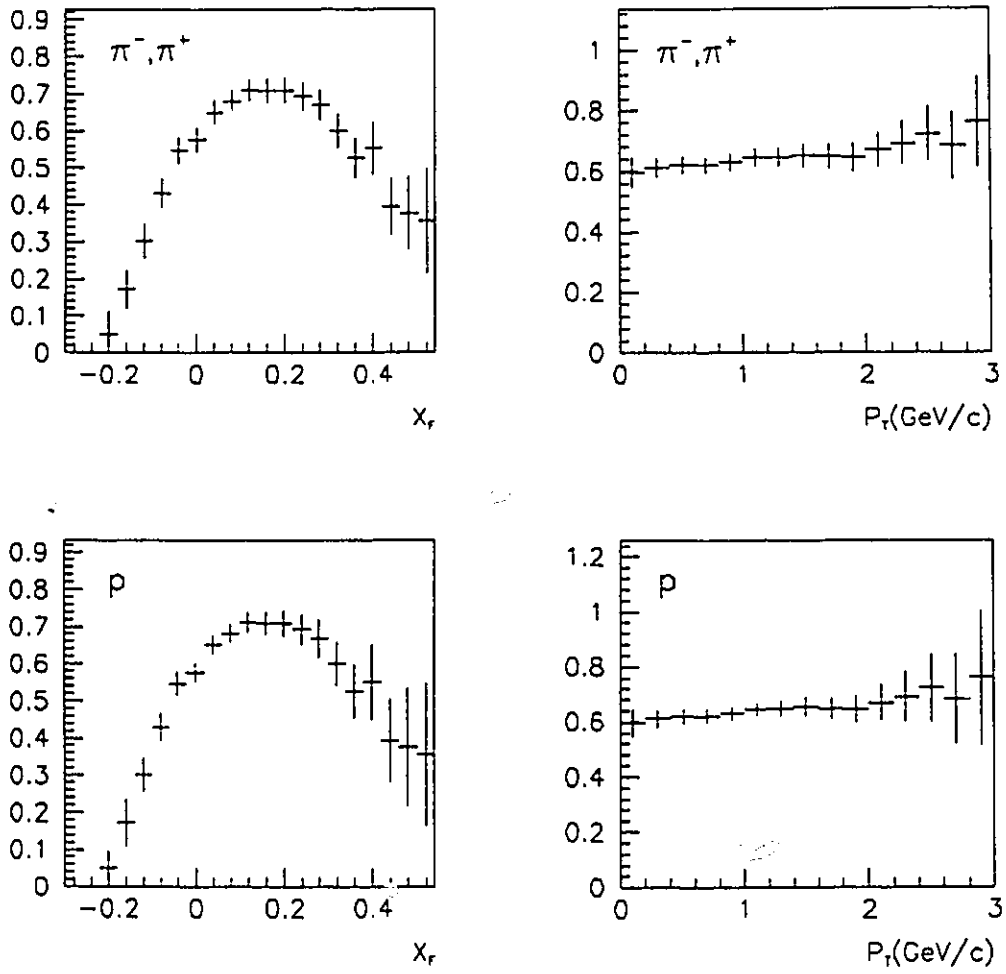

Figure 6.9: χ acceptance vs xf and pt

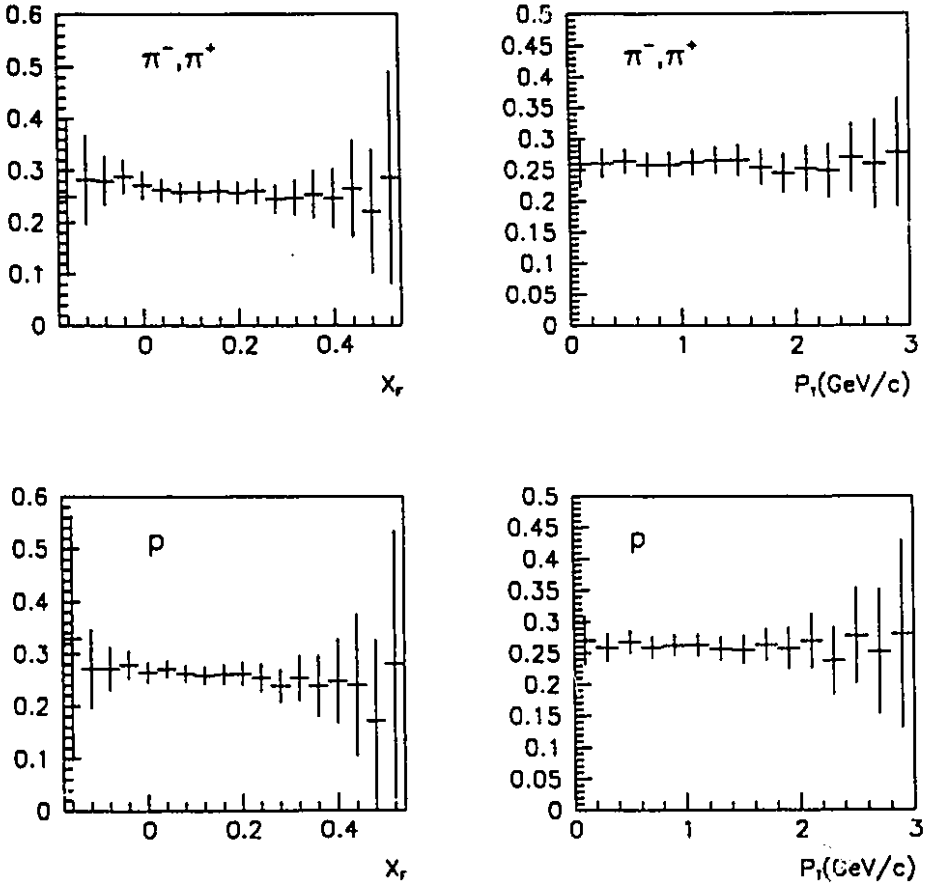

Figure 6.10: χ reconstruction efficiency vs x_F and p_T

a) Only the contribution to the χ width from the J/ψ reconstuction is taken into account.

b) Both contributions to the χ width from the J/ψ and γ reconstructions are taken into account.

The contribution of the muon tracking resolution to the χ width was estimated to be $\sigma_{\chi_{tracking}} = 7 \pm 0.5$ MeV/c^2. This follows from a gaussian fit to the plot in Figure 6.11a. The expected χ width was estimated by fitting the plot in Figure 6.11b where both muon tracking resolution and the photon energy resolution were accounted for. The expected χ width was found to be $\sigma_\chi = 30 \pm 3$ MeV/c^2. The error on this number was estimated by varying the parameters used in the χ Monte Carlo simulation. For the most part parameter variation only marginally affected the χ width. In contrast, it was found that the photon energy resolution factor affected the χ width significantly. From Chapter 5 the estimate of the error on the energy resolution was about 10% and this leads to a 10% uncertainty in the expected χ width.

6.5 Background sources to χ signal

To find the number of χ 's reconstructed, the background had to be estimated and subtracted. At this stage, the background was caused primarily by a J/ψ accompanied by an uncorrelated γ from the decay of a $\pi^0 \rightarrow \gamma\gamma$, where one of the two photons missed the detector or failed our reconstruction algorithm. Other sources of background include decays of charmonium states, other than χ's, having a J/ψ and a γ in the final state. The simulation of both of these backgrounds will be discussed in the following sections.

6.5.1 Uncorrelated background

The background due to J/ψ accompanied by an uncorrelated γ from the decay $\pi^0 \rightarrow \gamma\gamma$ produced in the interaction was simulated by combining each J/ψ in our sample with the photons from other 25 J/ψ candidates. A typical distribution of the background is shown in Figure 6.12. The shape of the background was then determined

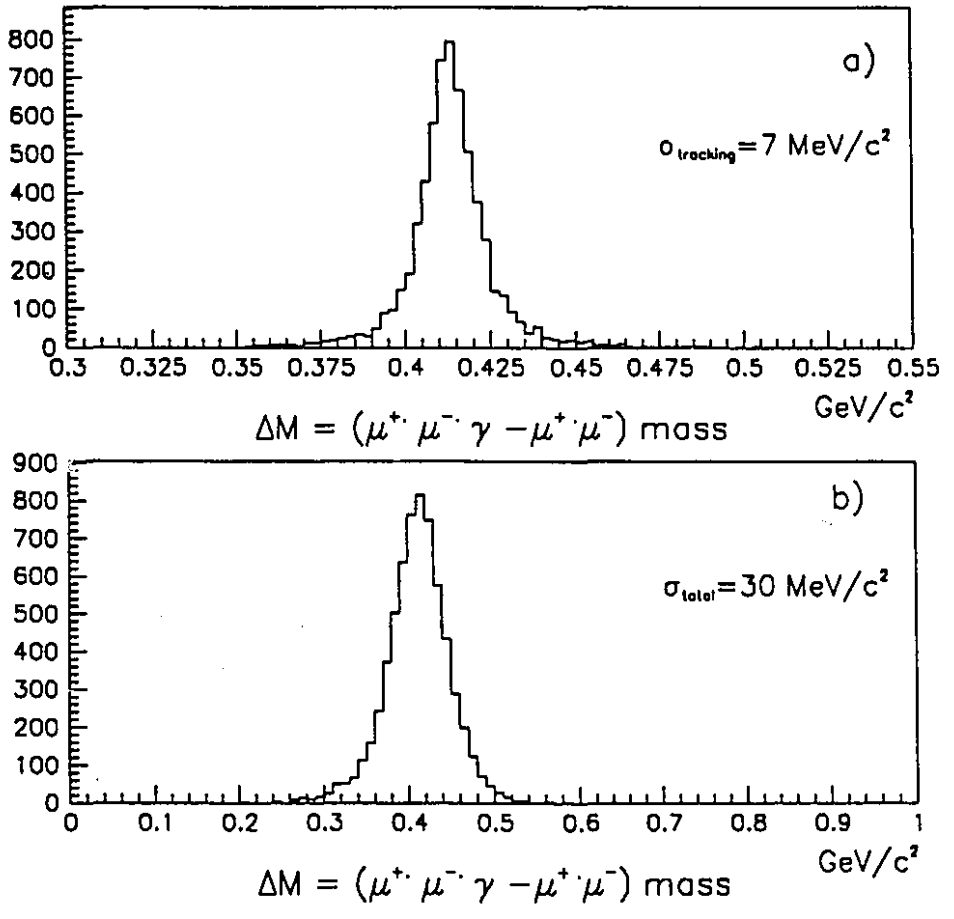

Figure 6.11: Monte Carlo M($\mu^+\mu^-\gamma$) - M($\mu^+\mu^-$) mass spectrum

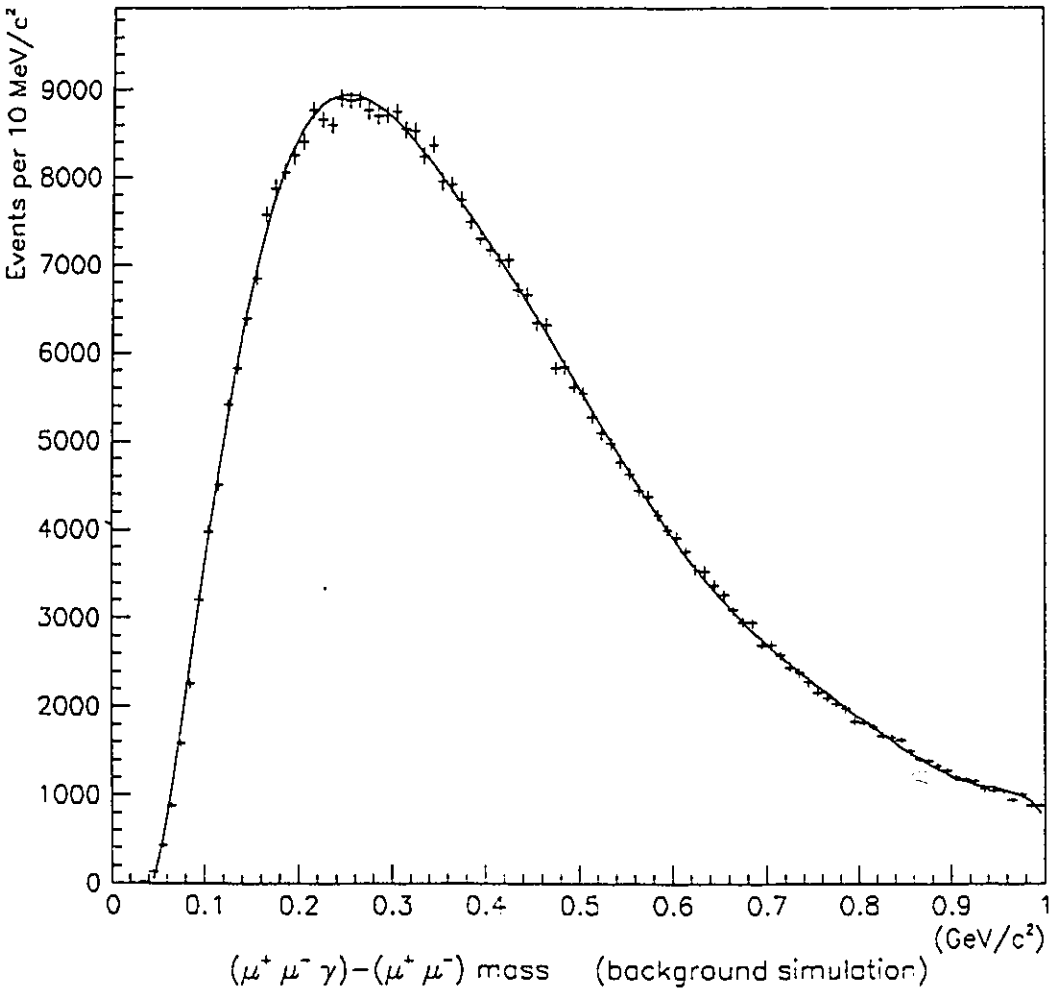

Figure 6.12: M($\mu^+\mu^-\gamma$) - M($\mu^+\mu^-$) mass spectrum for J/ψ combined with photons of other events.

using a 9th degree polynomial(shown by the line Figure 6.12).

6.5.2 Background due to ψ' decays

The $\mu^+\mu^-$ invariant mass plot shows a ψ' peak, as can be observed in the logarithmic scale distribution shown in Figure 6.13. The unbroken line is the fit based on 3 gaussian functions for the J/ψ and ψ' signals and an exponential background. The dotted line is the fitted background. The number of ψ' reconstructed is 370 ± 70. A Monte Carlo simulation was used to estimate the ψ' acceptance as described in Section 6.4, using J/ψ production distributions (see table 6.2). The combined ψ' acceptances and reconstruction efficiencies were found for all beam types ([45]):

$$\epsilon_A = 6.9 \pm 1.1\% \qquad \text{for pions}$$

$$\epsilon_A = 8.2 \pm 1.6\% \qquad \text{for protons}$$

Knowing $BR(\psi' \rightarrow \mu^+\mu^-) = 0.77 \pm 0.17\%$ ([9]), the number of ψ''sproduced can be estimated as:

$$N_{\psi'_{produced}} = \frac{N_{\psi'_{measured}}}{\epsilon_A \cdot BR(\psi' \rightarrow \mu^+\mu^-)} = (7 \pm 2)10^5 \qquad (6.5)$$

In order to estimate the contribution of ψ' decays into the J/ψ γ mass plot, a Monte Carlo simulation was done to evaluate the ψ and the photon acceptances for each of the channels.

ψ' decay into J/ψ π^0 π^0

Given the branching fraction $BR(\psi' \rightarrow \psi\pi^0\pi^0) = 8.6 \pm 1.2\%$ ([9]), the number of produced ψ''s decaying through this channel is:

$$N_{\psi' \rightarrow \psi\pi^0\pi^0} = (6 \pm 2)10^4 \qquad (6.6)$$

Only J/ψ 's decaying into $\mu^+\mu^-$ were actually recorded in the experiment. Using the Monte Carlo simulation the J/ψ was decayed isotropically into two muons and the two muons were propagated into the spectrometer, using the method described

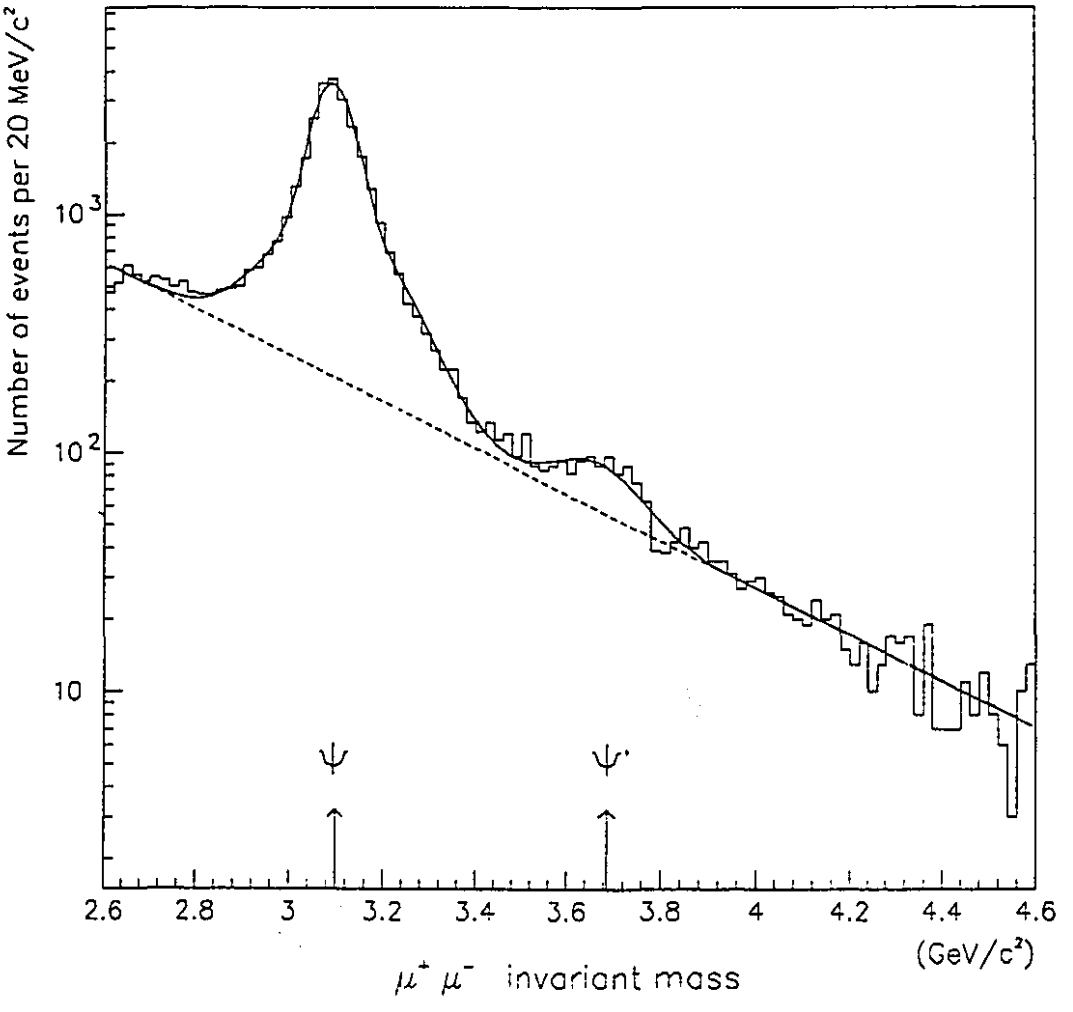

Figure 6.13: $\mu^+\mu^-$ mass spectrum.

in section 6.4. The J/ψ acceptance times reconstruction efficiency was determined to be $\epsilon_A = 6.0 \pm 1.2\%$ for pions and $\epsilon_A = 7.1 \pm 1.2\%$ for protons. Given BR($J/\psi \rightarrow \mu^+\mu^-$) $= 5.9 \pm 0.2\%$ ([57]), the expected number of ψ''s decaying into J/ψ $\pi^0\pi^0$ having the J/ψ fully reconstructed was estimated:

$$N_{\psi' \rightarrow \psi\pi^0\pi^0} = 220 \pm 70 \tag{6.7}$$

Knowing that π^0 decays into $\gamma\gamma$ with a branching fraction BR($\pi^0 \rightarrow \gamma\gamma$) $= 98.80 \pm 0.03\%$ ([9]), the final state of this ψ' decay will usually contain four photons. The accepted photon multiplicity is shown in Figure 6.14a. The energy spectrum for all photons generated by π^0 decays is shown in Figure 6.14b, the energy spectrum for photons within the detector acceptance is shown in Figure 6.14c. Finally, the invariant mass spectrum for photons satisfying the "χ quality" cuts is shown in Figure 6.14d.

ψ' decay into J/ψ η

Given the branching fraction BR($\psi' \rightarrow \psi\eta$) $= 2.7 \pm 0.4\%$ ([9]), the number of produced ψ' decaying through this channel is:

$$N_{\psi' \rightarrow \psi\eta} = (1.9 \pm 0.5)10^4 \tag{6.8}$$

Only J/ψ decaying into $\mu^+\mu^-$ were actually recorded in the experiment. Using the Monte Carlo simulation the J/ψ was decayed isotropically into two muons and the two muons were propagated into the spectrometer, using the method described in section 6.4. The J/ψ acceptance times reconstruction efficiency was determined to be $\epsilon_A = 6.0 \pm 1.2\%$ for pions and $\epsilon_A = 7.1 \pm 1.2\%$ for protons. Given BR($J/\psi \rightarrow \mu^+\mu^-$) $= 5.9 \pm 0.2\%$ ([57]), the expected number of ψ' decaying into J/ψ η with the J/ψ fully reconstructed was estimated:

$$n_{\psi' \rightarrow \psi\eta} = 70 \pm 20 \tag{6.9}$$

The η can either decay into $\gamma\gamma$, $\pi^0\pi^+\pi^-$ or $\pi^0\pi^0\pi^0$ with branching fractions: BR($\eta \rightarrow \gamma\gamma$) $= (38.9 \pm 0.8)\%$, BR($\eta \rightarrow \pi^0\pi^0\pi^0$) $= (31.9 \pm 0.4)\%$, and BR($\eta \rightarrow \pi^0\pi^+\pi^-$) $= (23.6 \pm 0.6)\%$ ([9]). The multiplicity of the accepted photons is shown in Figure 6.15a.

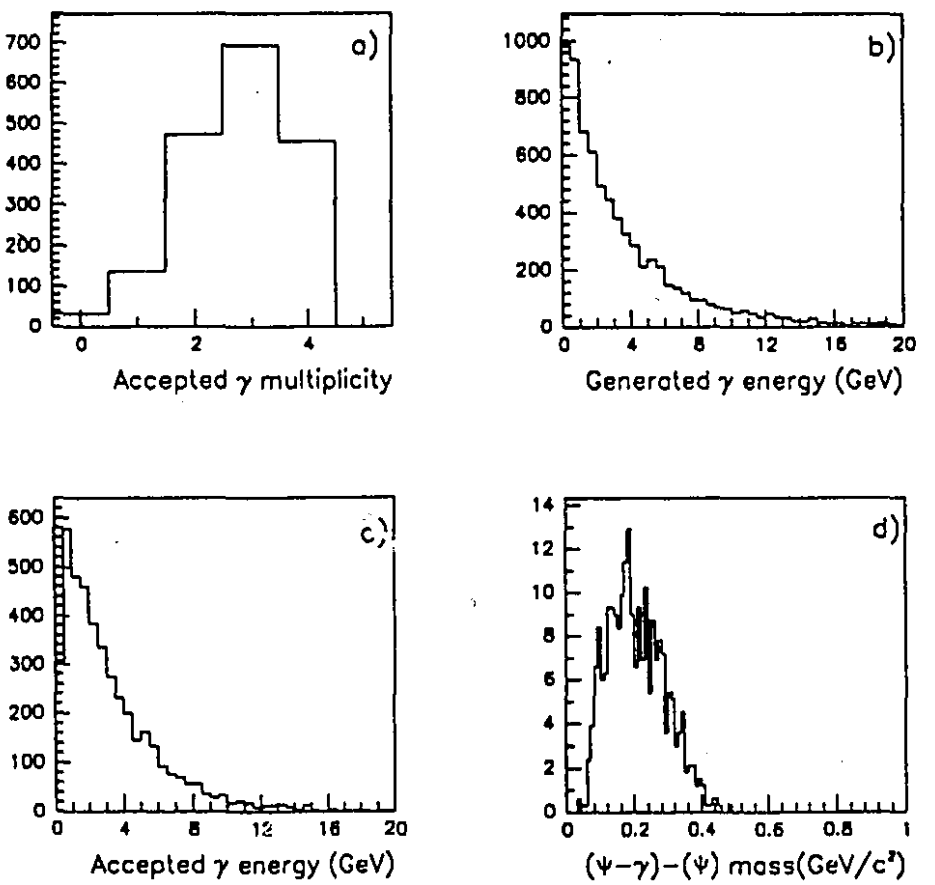

Figure 6.14: Monte Carlo events: $\psi' \rightarrow \psi\pi^0\pi^0$.

The energy spectrum for all the photons generated by the η decays is shown in Figure 6.15b, the energy spectrum for photons within the detector acceptance is shown in Figure 6.15c. Finally, the invariant mass spectrum for photons satisfying the "χ quality" cuts is shown in Figure 6.15d.

ψ' decay into $\chi\ \gamma$

Given the branching fractions $BR(\psi' \rightarrow \chi_1\gamma) = 8.7 \pm 0.8\%$ and $BR(\psi' \rightarrow \chi_2\gamma) = 7.8 \pm 0.8\%$ ([9]), the number of produced ψ''s decaying through these channels is:

$$N_{\psi' \rightarrow \chi\gamma} = (1.2 \pm 0.3)10^5 \tag{6.10}$$

Only χ decaying into J/ψ were actually recorded in the experiment through their subsequent decay into $\mu^+\mu^-$. Using the Monte Carlo simulation the ψ' were decayed into $\chi\ \gamma$ and subsequently the χ into $J/\psi\ \gamma$ according to the branching fraction for the χ radiative decays, using the method described in section 6.4.

The expected number of ψ''s decaying into $\mu^+\mu^-\gamma\gamma$ with the J/ψ fully reconstructed was estimated to be :

$$n_{\psi' \rightarrow \psi\gamma\gamma} = 100 \pm 30 \tag{6.11}$$

The multiplicity of the accepted photons is shown in Figure 6.16a. The energy spectrum for both photons is shown in Figure 6.16b, the energy spectrum for photons within the detector acceptance is shown in Figure 6.16c. Finally, the invariant mass spectrum for photons satisfying the "χ quality" cuts is shown in Figure 6.16d.

In Figure 6.17, the measured $J/\psi\ \gamma$ mass spectrum is compared with the shape of the background taking into account both the uncorrelated photon production (described in section 6.5.1 and represented by the dotted line) and the contribution due to ψ' decays (which is shown separately in Figure 6.17b). The data, shows an excess for low values of the invariant mass, although the contribution of the ψ' decays has decreased it somewhat. The remaining excess might be due to decays of undiscovered charmonium states, e.g. $1P_1$ decays. The uncorrelated background shape (shown by the dotted line) has a satisfactory agreement with the measured mass spectrum and since the excess at

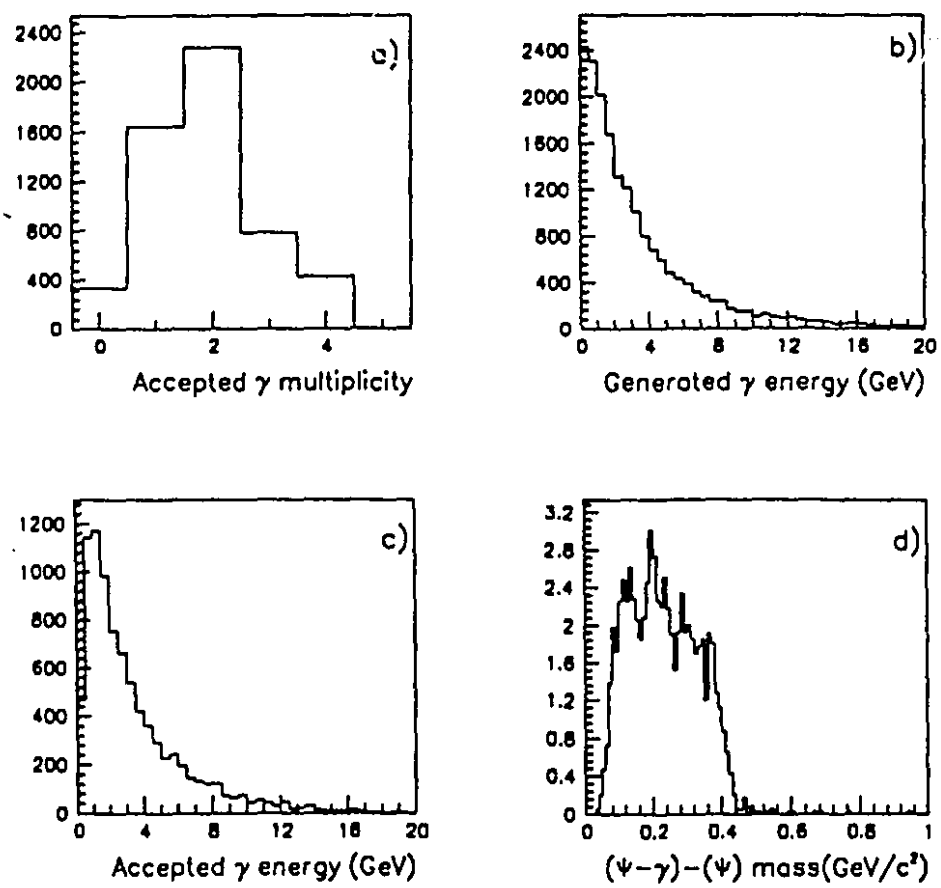

Figure 6.15: Monte Carlo events: $\psi' \rightarrow \psi\eta$.

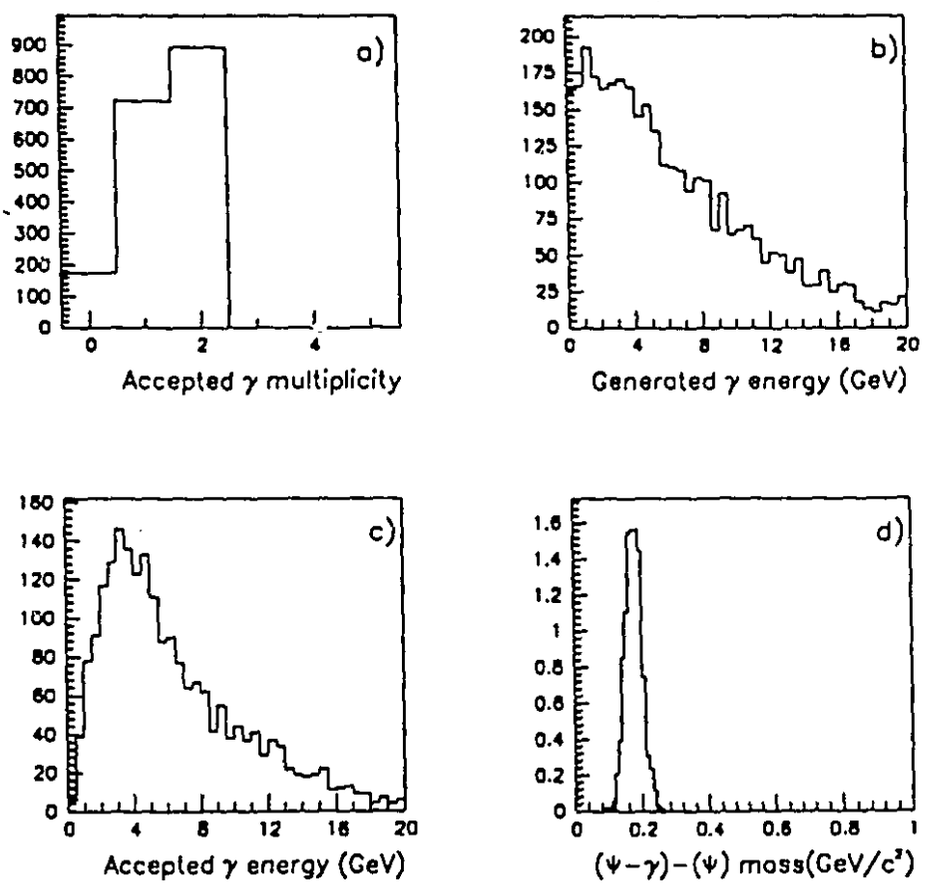

Figure 6.16: Monte Carlo events: $\psi' \to \chi\gamma$.

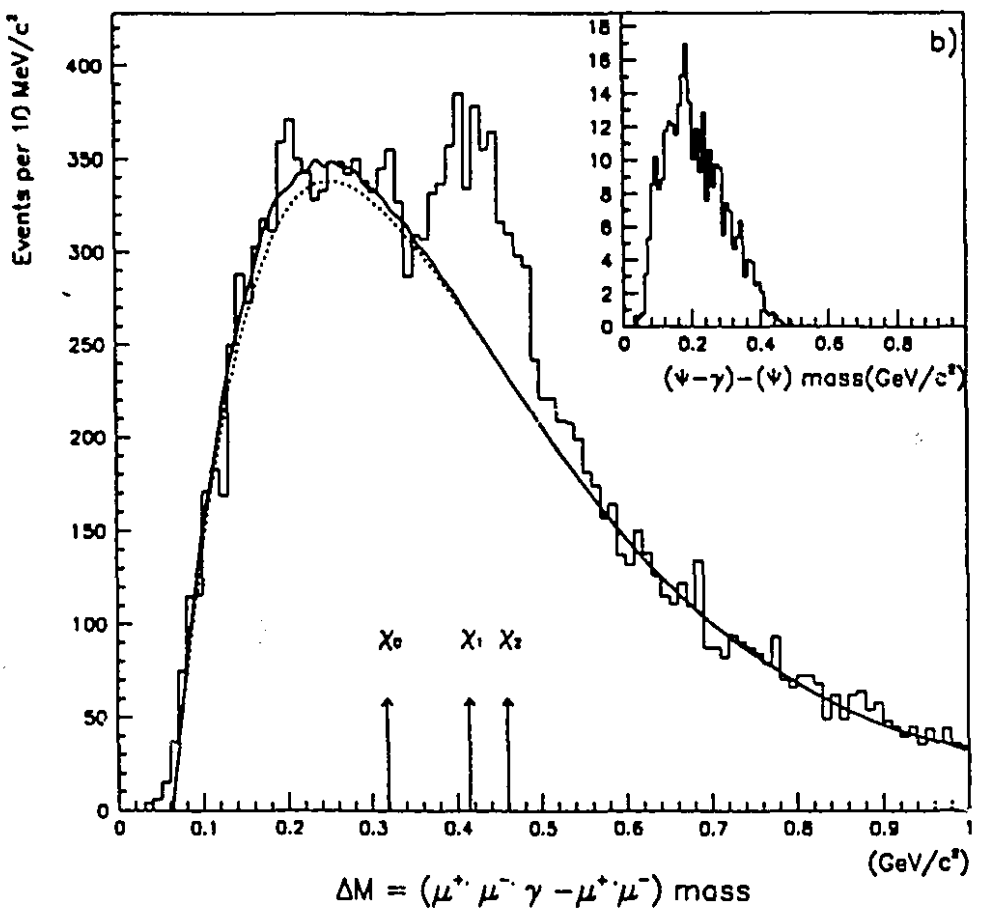

Figure 6.17: M($\mu^+\mu^-\gamma$) - M($\mu^+\mu^-$) mass spectrum: overlayed is the background shape (described in the text), b) invariant mass distribution of the background due to ψ' decays

low mass is fairly well understood, it is possible to extract an unbiassed estimate of the number of reconstructed χ events.

Chapter 7

Results and Conclusions

7.1 χ final analysis

The overall normalization of the background was adjusted by fitting the J/ψ -γ mass spectrum excluding the χ mass region, in the mass interval (0.55–1.)GeV/c^2. The J/$\psi\,\gamma$ invariant mass spectrum for the total sample is shown in Figure 7.1. The overlayed line is the background estimated from uncorrelated events. The excess at low mass is due to photons correlated with the J/ψ , mainly from ψ' decays. As shown in the previous chapter, this correlated background does not affect the mass spectrum in the χ mass region and therefore does not affect the estimate of the number of χ's. The background-subtracted plot is shown in Figure 7.2. The dashed curve represents the expected signal shape, based upon our estimate of the resolution, if only one resonant state, centered at the χ_1 mass, was produced. The data indicates a clear excess, indicating the presence of two states. The χ invariant mass plots for π^-, π^+ and proton beams are shown in Figure 7.3 and 7.4. The excess of background at low mass is attributed to various channels of ψ' decay, as discussed in Section 6.5.2: this is more evident for the pion beam spectra, as expected from the higher values of the ψ' cross section[54].

The Least-Squares method was used to fit the background-subtracted plots. The sum of two gaussian functions was used with the constraints that the widths be identical and the mass difference between the χ_1 and the χ_2 be the world average value[9]:

$$f(M) = \frac{N_\chi \cdot \rho \cdot \Delta_M \cdot e^{-\frac{(M-M_{\chi_1})^2}{2\sigma_\chi^2}}}{\sqrt{2\pi}\cdot(1+\rho)\cdot\sigma_\chi} + \frac{N_\chi \cdot \Delta_M \cdot e^{-\frac{(M-M_{\chi_1}-45.6)^2}{2\sigma_\chi^2}}}{\sqrt{2\pi}\cdot(1+\rho)\cdot\sigma_\chi}$$

where Δ_M is the bin width of plot of the invariant mass (10 MeV/c^2) and the fitted

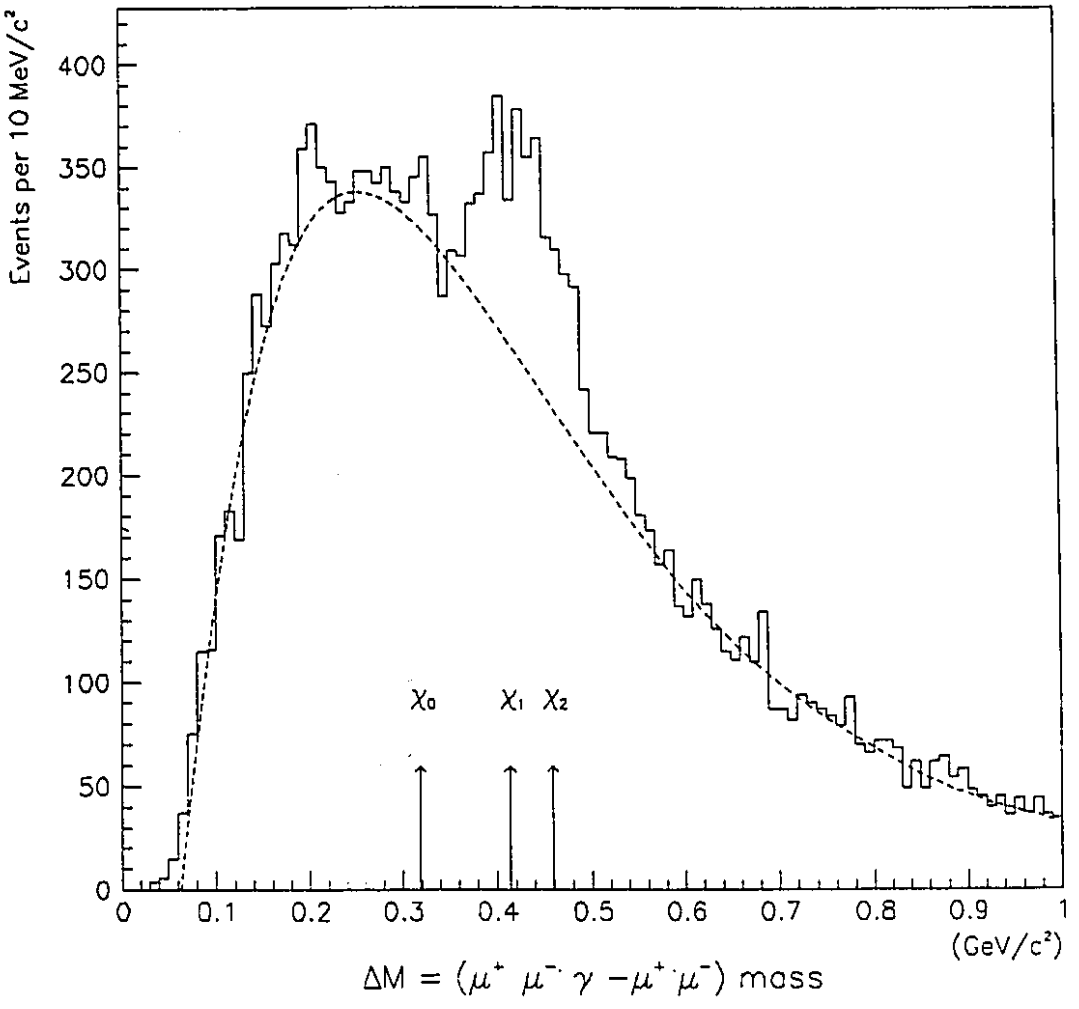

Figure 7.1: M($\mu^+\mu^-\gamma$) - M($\mu^+\mu^-$) mass spectrum for "χ quality" showers; overlayed is the background determination described in the text.

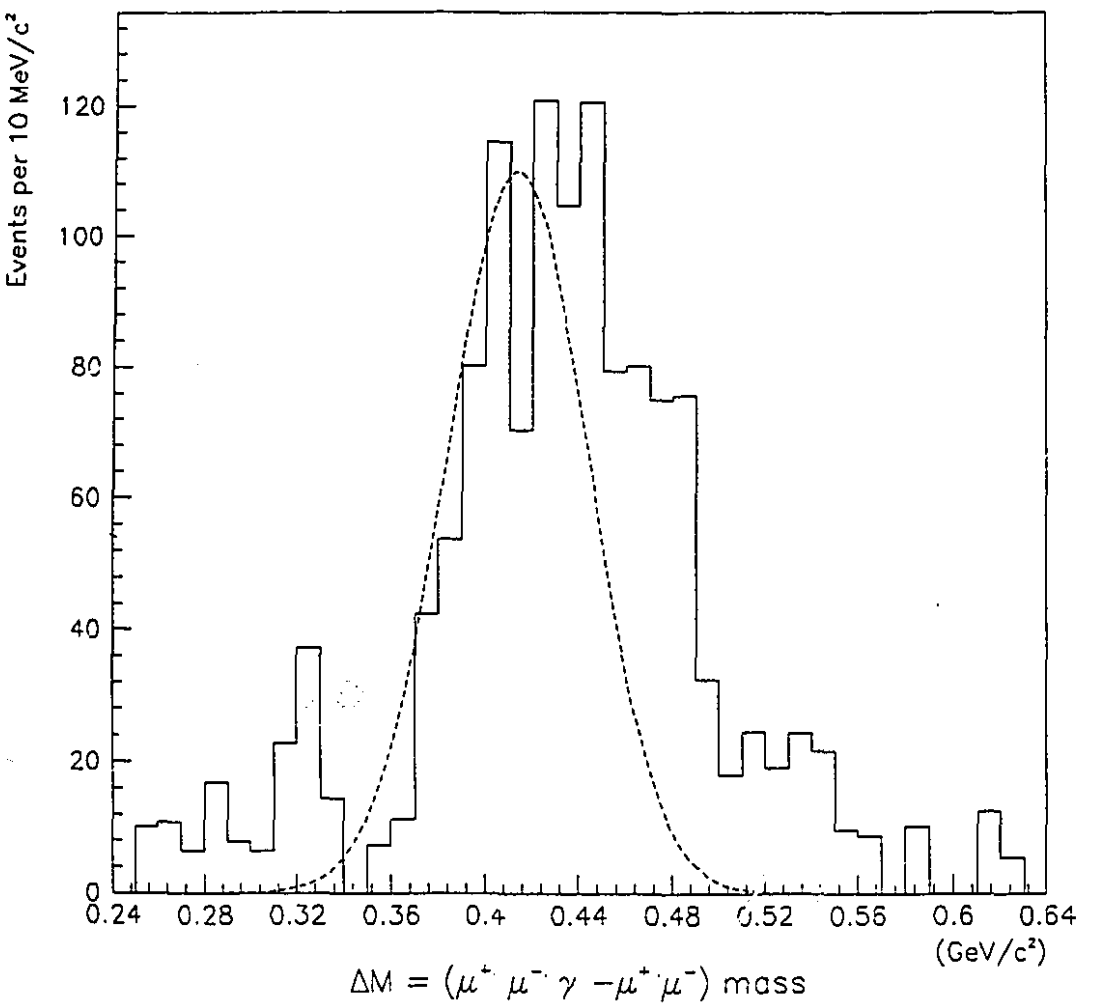

Figure 7.2: The M($\mu^+\mu^-\gamma$) - M($\mu^+\mu^-$) mass spectrum background subtracted is compared with the Monte Carlo prediction for χ_1 width.

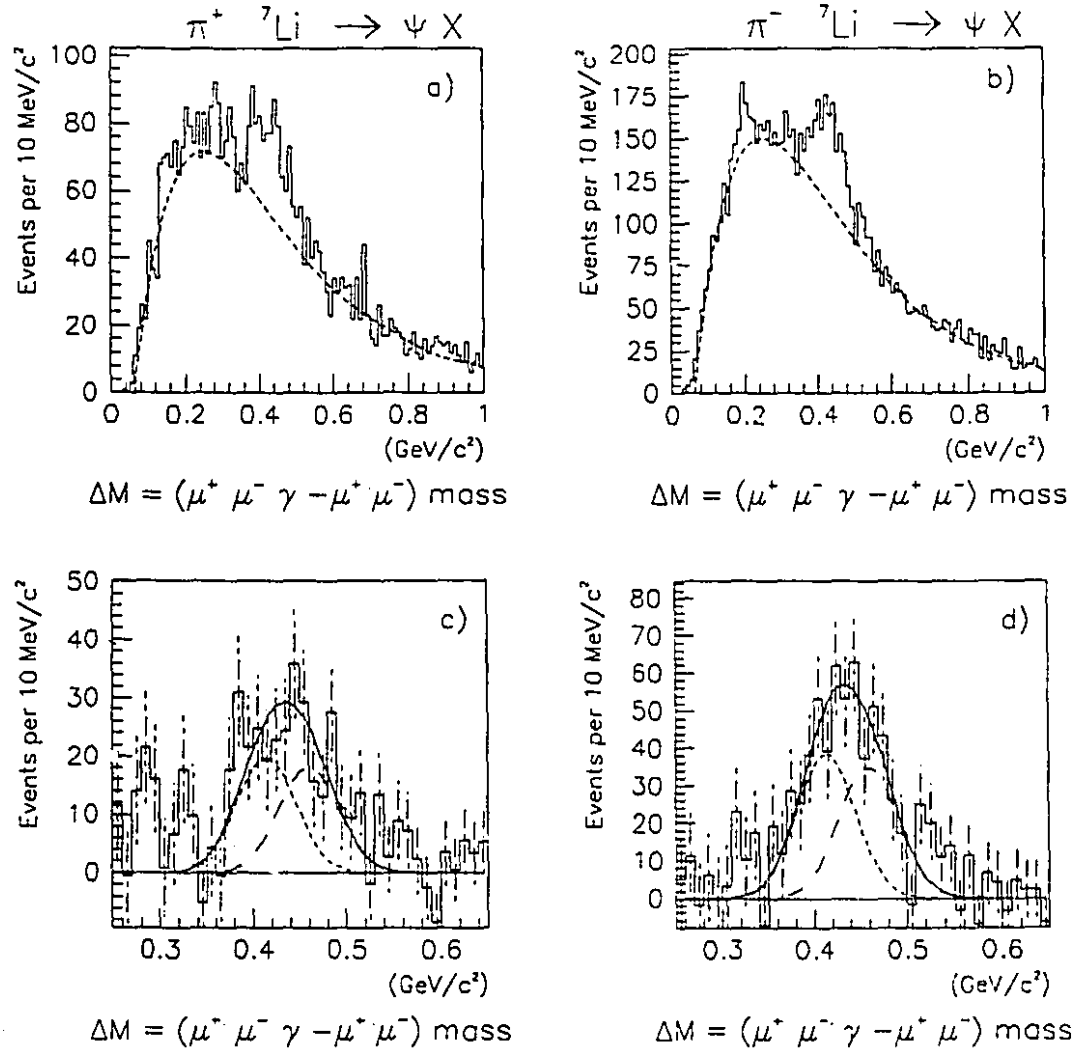

Figure 7.3: $M(\mu^+\mu^-\gamma)$ - $M(\mu^-\mu^-)$ mass spectrum induced by negative and positive pion beam: a) π^- beam overlayed is the background estimate, b) π^+ beam overlayed is the background estimate, c) π^- beam background subtracted plot with superimposed the double gaussian fit, d) π^+ beam background subtracted plot with superimposed the double gaussian fit.

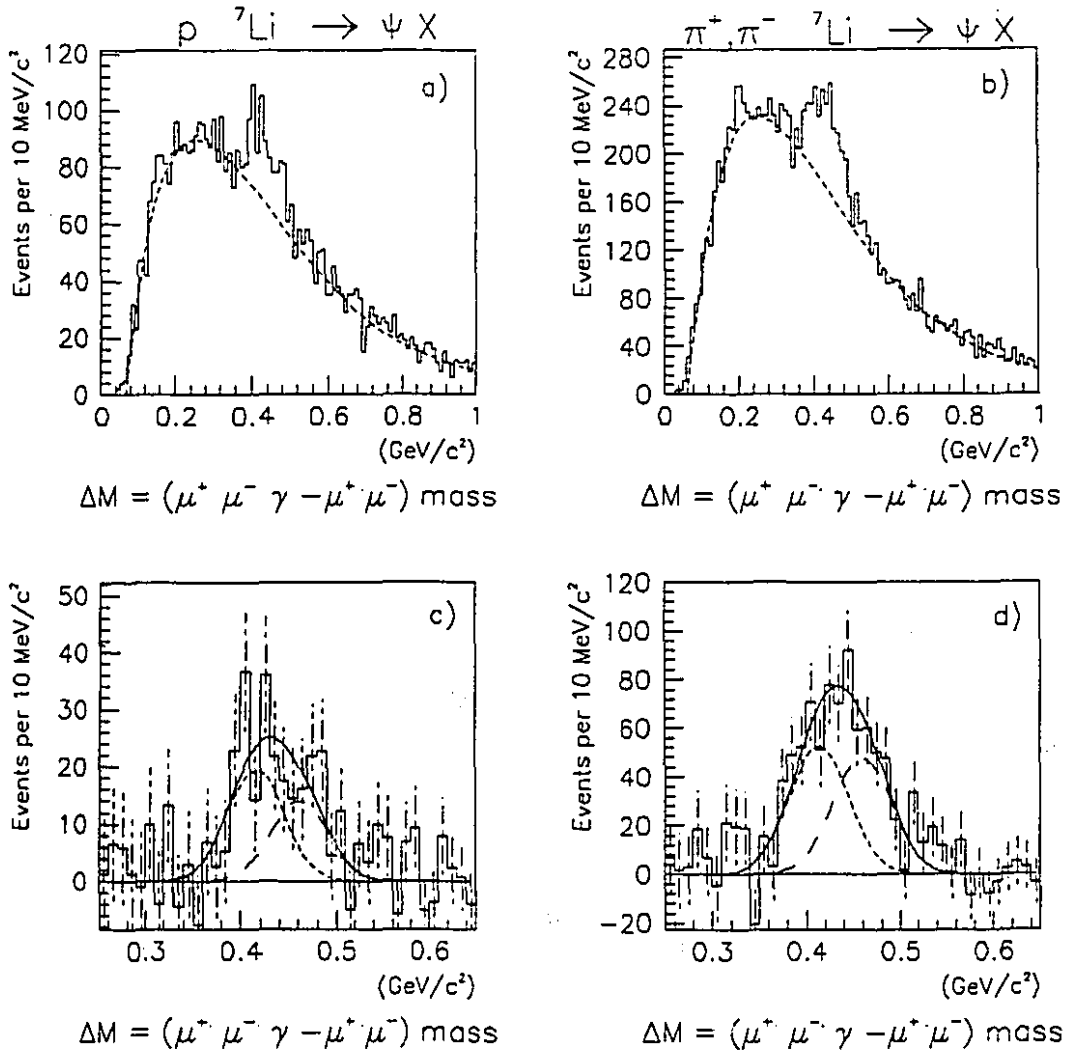

Figure 7.4: $M(\mu^+\mu^-\gamma) - M(\mu^+\mu^-)$ mass spectrum induced by proton and pion beam: a) proton beam overlayed is the background estimate, b) positive and negative pion beam overlayed is the background estimate, c) proton beam background subtracted plot with superimposed the double gaussian fit, d) positive and negative pion beam background subtracted plot with superimposed the double gaussian fit.

Table 7.1: Number of reconstructed χ's for the different beam types

Beam type	N_χ
π^-	590 ± 50
π^+	300 ± 35
p	250 ± 35

quantities are:

N_χ it the total number of reconstructed χ 's .

M_{χ_1} is mass of χ_1

σ_χ is the width of χ_1 and χ_2,

ρ is the ratio between the number of χ_1 events and the number of χ_2 events.

As discussed in detail in Appendix A, M_{χ_1} and σ_χ were included among the fitted parameters to be determined by the fit, in order to account properly for our experimental uncertainty in the actual values of those two quantities. More specifically, the accuracy of the energy scale had been determined by the procedure described in Chapter 4 from electrons, pizero and eta reconstruction, while the χ width was derived from the Monte Carlo simulation as described in Chapter 6. These estimates were used in the definition of the χ^2 as described in Appendix A. This method was tested for repeatability by applying different set of cuts to select the $\psi\gamma$ combinations and using different intervals to normalize the background. The results were found to be fairly consistent and well within the the quoted errors.

7.1.1 Percentage of J/ψ 's produced through χ radiative decays

When the fitting procedure, described in the previous section, was applied to the $\psi\gamma$ invariant mass distributions, the total number of reconstructed χ's (N_χ) was determined for the different beam types as reported in Table 7.1.

The total number of χ particles was corrected for acceptance and reconstruction

efficiency:

$$N_{\chi_{corrected}} = \frac{N_\chi}{A_\chi \epsilon_\chi} \tag{7.1}$$

Therefore the fraction, R, of ψ particles produced through the radiative decays of χ's has been estimated by:

$$R = \frac{N_{\chi_{corrected}}}{N_\psi} \tag{7.2}$$

The measured values of R for the different beam types are reported in Table 7.2 and are compared with results obtained by other experiments ([28], [29], [30], [32], [33], [34]) in Fig. 7.5 as a function of $\sqrt{\tau} = M_\chi/\sqrt{s}$ where $\sqrt{s}$ is the center of mass energy of the beam-target system. Our measurement of the fraction of J/ψ produced through

Table 7.2: Percentage of ψ from χ radiative decay.

	π^-	π^+	p
$R(\%)$	37 ± 3	40 ± 4	30 ± 4

χ radiative decays for pion beam is in agreement with WA11 results and all the other experiments, while for the proton beam our results disagree with R806 by more than one standard deviation.

7.1.2 J/ψ direct production cross-section

As discussed previously, it is now understood that J/ψ hadro-production can be due to either direct J/ψ production or the production of another charmonium state which decays into J/ψ . On the basis of the known branching fractions [9], it can be assumed that the only important contribution to indirect J/ψ production are decays from other charmonium states, i.e. from χ's and ψ's (it could also be shown that contributions from other channels, e.g. B decay into J/ψ , are negligible). Given that E705 was able to measure simultaneously both χ and ψ' production, it is then possible to quote a result for the cross-section of direct J/ψ production. E705 values[54] for the product

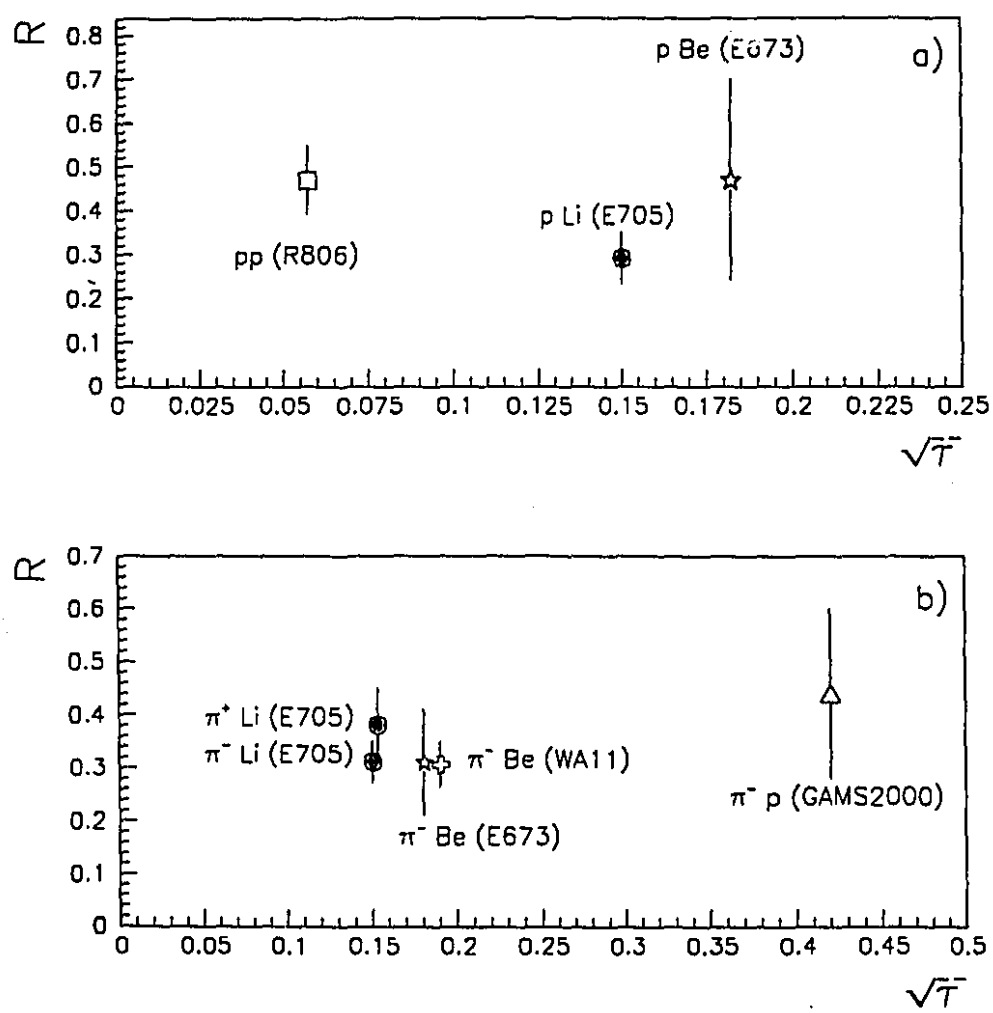

Figure 7.5: Fraction of J/ψ produced through χ radiative decay: E705 results are compared with world data.

Table 7.3: Total cross-section times branching ratio for ψ and ψ' production ($x_F > 0$)

beam type	$\sigma_A \times BR(\psi)$(nb/Li nucleus)	$\sigma_A \times BR(\psi')/\sigma_A \times BR(\psi)(\%)$
π^-	$71.4 \pm 1.0 \pm 7.3$	1.8 ± 0.3
π^+	$68.0 \pm 1.3 \pm 5.1$	1.9 ± 0.2
p	$58.2 \pm 1.1 \pm 6.0$	1.3 ± 0.2

of the inclusive cross-sections, $\sigma(\psi)$ and $\sigma(\psi')$, multiplied by the branching ratios, $BR(\psi, \psi' \rightarrow \mu^+\mu^-)$, are given in Table 7.3.

The cross-section per nucleus can be converted to cross-section per nucleon by using the following relation:

$$\sigma_{nucleon} = \frac{\sigma_{nucleus}}{A^\alpha} \tag{7.3}$$

where $\alpha = 0.93 \pm 0.01$ from a collection of world data compiled by L. Lyons[56]. Furthermore, in extracting the cross-sections, the values reported in Table 7.3 are multiplied by the the branching ratios:

$$BR(\psi \rightarrow \mu^+\mu^-) = (5.9 \pm 0.2)\% \text{ [57]} \tag{7.4}$$

$$BR(\psi' \rightarrow \mu^+\mu^-) = (7.7 \pm 1.7)10^{-3} \text{ [9]} \tag{7.5}$$

The measured values of the ψ and ψ' cross-sections per nucleon are shown in Table 7.4.

Table 7.4: Total cross-sections for ψ and ψ' production

beam type	$\sigma(\psi)$ (nb/nucleon)	$\sigma(\psi')/\sigma(\psi)$ (%)
π^-	$199. \pm 9. \pm 22.$	$14. \pm 4.$
π^+	$191 \pm 9. \pm 16.$	$15. \pm 4.$
p	$162 \pm 7. \pm 18.$	$10. \pm 3.$

The fraction of J/ψ 's coming from ψ' decays can then be calculated as:

$$F = \sigma(\psi') \times BR(\psi' \rightarrow \psi + \text{anything}) \tag{7.6}$$

where BR($\psi' \rightarrow J/\psi$+anything) = 0.57 ± 0.04 [9]. Therefore the fraction of J/ψ coming from ψ' decays, F, was found to be:

$$F_\psi = (7.8 \pm 2.2)\% \qquad \text{for pions} \tag{7.7}$$

$$F_{\psi'} = (5.5 \pm 1.6)\% \qquad \text{for protons} \qquad (7.8)$$

Finally, the fraction of J/ψ 's produced directly is given by:

$$F_{direct} = 100 - R - F = (47.1 \pm 4.6)\% \qquad \text{for pions} \qquad (7.9)$$

$$F_{direct} = 100 - R - F = (60.0 \pm 4.8)\% \qquad \text{for protons} \qquad (7.10)$$

Multiplying by the ψ inclusive cross-section, an upper limit for J/ψ direct production cross-section can be estimated:

$$\sigma_{direct}(\psi) = (92 \pm 6. \pm 9.)\ \text{nb/nucleon} \qquad \text{for pions} \qquad (7.11)$$

$$\sigma_{direct}(\psi) = (97 \pm 6. \pm 12.)\ \text{nb/nucleon} \qquad \text{for protons} \qquad (7.12)$$

Although the fraction of J/ψ produced directly has been measured by previous experiments, the measurement of the cross-section has never been very accurate. Since E705 had the capability of measuring the cross-section of several charmonium states, and for different beam types, it was a particular good candidate for measuring the relative contribution of the different processes, given that some of the systematics effects, being common to all the measurements, are canceled. Also, the recent improved measurement of the branching ratio for J/ψ decay in two muons (as published by the Mark III collaboration [57]) decreases the uncertainty in the absolute value of the J/ψ production cross-section. The substantial fraction of J/ψ 's produced directly, indicates that some process other than the simple quark fusion and/or gluon fusion, as predicted by the singlet model, must be involved in hadroproduction of charm.

7.1.3 χ_1 and χ_2 cross-section

The Least-Squares method with a two gaussian function, shown in Equation 7.1, was used to fit the background-subtracted plots for the different beam types. The results of the fit are overlayed to the mass spectra as shown in Figure 7.3 and 7.4. The ratio between the number of observed events for the two χ states, ρ, was derived from the fit and is reported in Table 7.5 for the different beam types. In the same table, the results of the fit for the χ_1-J/ψ mass difference and the χ width are also reported.

Table 7.5: Number of reconstructed χ's for the different beam types

Beam type	N_χ	$M_\chi - M_{J/\psi}$ (MeV/c^2)	σ_χ (MeV/c^2)	ρ
π^-	590 ± 50	413 ± 7	32 ± 3	1.1+0.8 -0.5
π^+	300 ± 35	413 ± 6	32 ± 3	1.1+0.8 -0.5
p	250 ± 35	415 ± 7	30 ± 3	1.4+1.4 -0.7

Table 7.6: χ_1 and χ_2 production cross-sections

	π^-	π^+	p
$\sigma(\chi_1)$ (nb/nucleon)	$140.^{+160.}_{-100.}$	$150.^{+160.}_{-100.}$	$100.^{160.}_{-80}$
$\sigma(\chi_2)$ (nb/nucleon)	$260.^{+100}_{-70.}$	$270.^{+100.}_{-70.}$	$150.^{+90.}_{-50.}$

The χ_1 to χ_2 production cross-sections can be determined using the ratio between the number of observed events for the two χ states, ρ and the χ branching fractions:

$$\rho = \frac{N_{\chi_1}}{N_{\chi_2}} = \frac{\sigma(\chi_1) \cdot \mathrm{BR}(\chi_1 \to \psi\gamma)}{\sigma(\chi_2) \cdot \mathrm{BR}(\chi_2 \to \psi\gamma)} \tag{7.13}$$

The χ_1 and χ_2 cross-section can then be written, as a function of measured parameters:

$$\sigma(\chi_1) = \frac{\rho}{1+\rho} \cdot \frac{R\,\sigma(\psi)}{BR(\chi_1 \to \psi\gamma)} \tag{7.14}$$

$$\sigma(\chi_2) = \frac{1}{1+\rho} \cdot \frac{R\,\sigma(\psi)}{BR(\chi_2 \to \psi\gamma)} \tag{7.15}$$

where R is fraction of ψ coming from χ radiative decays, ρ is the oberved ratio of the χ_1 to χ_2 production, $\sigma(\psi)$ is the ψ inclusive cross-section, and $BR(\chi \to \psi\gamma)$ are the branching ratios for χ radiative decays into J/ψ [9]. Our result for the values of the χ production cross-section are reported in Table 7.6. These results, especially the proton-induced production, cannot be explained in terms of the color singlet model. According to this model, in the absence of valence antiquarks production should be dominated by two-gluon fusion. The color singlet model, therefore, predicts no lowest-order χ_1 production. In contrast, the measured values of the χ production cross-section seem to

favor the color evaporation model, predicting the χ states to be produced according to their statistical weight (χ_1 : χ_2=3:5). These results disagree with previous published data on proton-induced χ hadroproduction [30]. In fact, since no production of χ_1 had been observed (in their statistically-limited χ sample), the authors concluded that χ production was compatible with the color singlet model.

7.2 Conclusions

The production of charmonium states, with particular emphasis on χ states, produced in $\pi^- Li$, $\pi^+ Li$ and $p Li$ collisions at $\sqrt{s} = 23.7$ GeV has been studied.

It was observed that a substantial fraction of J/ψ 's are produced directly. For pions, (47 ± 5)% of the J/ψ 's are produced directly giving a cross-section $\sigma_{direct}(\psi) = 92. \pm 6. \pm 9.$ nb/nucleon ($x_F > 0$). For protons, (60 ± 5)% of the J/ψ 's are produced directly, giving a cross-section $\sigma_{direct} = 97. \pm 6. \pm 12.$ nb/nucleon. As discussed in Chapter 1, the parton model assumes that charmonium production induced by proton beam, since no valence antiquark are available, is dominated by gluon fusion, while the production induced by pion beam can proceed also through quark-antiquark annihilations. As it has been observed[22], [23], [24], that in the framework of the QCD singlet model it is hard to adjust such a high yield of ψ direct production. A very large QCD effective scale (Λ >500 MeV), which is in disagreement with the present measurements of Λ, would be needed to explain the measured cross-section. In contrast, ψ production would seem to be compatible with the color evaporation model.

χ production was studied relatively to ψ production, individual χ_1 and χ_2 cross-sections for protons and pions were determined. For pion beam, the ratio of χ_1 to χ_2 cross-section was found to be $0.54 + 0.40 - 0.25$, both for positive and negative beams, in agreement with previously published results[33]. For proton beam, the ratio of χ_1 to χ_2 cross-sections was found to be $0.69 + 0.70 - .35$ indicating a substantial χ_1 production. This result is in contrast with previously published results by E673[30], although it is not inconsistent given their statistically limited sample. Indication of

substantial χ_1 production induced by proton beam is in contrast with the singlet model predictions since, as seen in Chapter 1, at lowest-order only χ_2 production can proceed through two-gluon fusion. The ratio of the χ_1 to χ_2 cross-sections indicate that color evaporation model, which predicts χ_1 to χ_2 to be produced proportionally to their statistical weights (3:5 for $\chi_1 : \chi_2$), is more consistent with our data. Alternatively, our results should be compared to a less naive, more exhaustive, beyond lowest order, QCD calculation, taking into account the most recent QCD developments. At this wiriting, such a calculation is not available.

In conclusion ψ and χ production cross-sections were determined, both for proton and pion beams. This experiment has measured these quantities for three different beam types. Using the same apparatus and the same analysis procedure has reduced the systematic differences between the different sets of data, making us more sensitive to potential differences among the different production mechanisms. The measured values of χ and ψ cross-sections and relative production yields, favor the color evaporation model over the most basic color singlet model.

Appendix A

Maximum likelihood method and Chi-square fitting

A.1 Background-subtracted mass spectrum

Given the J/ψ -γ plot, the background was estimated by making a chi-square fit to the 9-th degree polynomial shape obtained by mispairing each event in the J/ψ sample with all the photons reconstructed in 25 other events of the sample. The fit was performed in the mass region 0.55–1.0. The χ signal plot was then obtained by subtracting the estimated background. The error attributed to each bin i, as for any background-subtracted distribution, was calculated as:

$$\sigma_i = \sqrt{N^i_{signal} + N^i_{background}} = \sqrt{N^i_{total}}$$

where N^i_{signal} is the number of events in bin i of the background-subtracted distribution, $N^i_{background}$ is the estimated number of background events in bin i, and $N_{total}{}^i$ is the number of entries in the bin i of the measured distribution, before background subtraction. It was assumed that the error in the estimate of the background under the χ signal was negligible when compared to the statistical error of each bin.

The χ mass distribution, after subtracting the background, can be written as the sum of two gaussians, separated by 45.7MeV/c^2[9]. The width, σ_χ, of the two χ peaks, which is presumably dominated by experimental resolution, is assumed to be the same. The probability distribution can be written as:

$$f(M) = \frac{r_{\chi_1} e^{-\frac{(M-M_{\chi_1})^2}{2\sigma_\chi^2}}}{\sqrt{2\pi}\cdot\sigma_\chi} + \frac{r_{\chi_2} e^{-\frac{(M-M_{\chi_1}-45.7)^2}{2\sigma_\chi^2}}}{\sqrt{2\pi}\sigma_\chi}$$

where:

r_{χ_1} it the fraction of χ_1 events contained in the measured distribution.

r_{χ_2} it the fraction of χ_2 events contained in the measured distribution.

M_{χ_1} is the value of the χ_1 mass, as determined by the fit.

σ_χ is the measured width of the χ_1 and the χ_2.

A.2 Maximum Likelihood Method and Least Squares Method

The maximum likelihood function [58] is defined as the product of the probability distribution function calculated for the N events of the sample:

$$\mathcal{L}(M_{\chi_1}, \sigma_\chi, r_{\chi_1}, r_{\chi_2}) = \prod_{i=1}^{N} f(M_i)$$

According to the Maximum Likelihood Principle, the best values of the parameters can be found by maximizing $\mathcal{L}$.

If we assume that the individual measurements M_i are normally distributed around their true, unknown values f_i with variances σ_i^2 then, the likelikehood for observing the series of measurements M_1, M_2, ...M_N is

$$\mathcal{L} = \prod_{i=1}^{N} \frac{e^{-\frac{(M_i - f_i)^2}{2\sigma_i^2}}}{\sqrt{2\pi}\sigma_i}$$

Given that the actual χ_1 mass is known with great accuracy and the detector was carefully calibrated and monitored, the measured value of χ_1 mass, M_{χ_1} is expected to follow a gaussian distribution centered around the "true" value $M_0 = 3510.6\text{MeV/c}^2$with an uncertainty dominated by the photon energy scale error. The uncertainty in the χ mass due to the photon energy scale can be calculated by using the relation:

$$\sigma_M = \frac{M_0^2 - M_\psi^2}{2M_0}\frac{\sigma_E}{E}$$

Therefore the 2% error in the photon energy scale, reported in Chapter 5, implies $\sigma_M = 8$ MeV/c^2.

As seen in Chapter 6, the photon energy resolution is the dominant contribution to the χ width, the Monte Carlo prediction for the χ width being $\sigma_0 = 30\text{MeV/c}^2$.

Its uncertainty was estimated by varying the input parameters to the Monte Carlo, including the photon energy resolution, within reasonable limits, and it was estimated to be $\sigma_\sigma = 3\mathrm{MeV/c^2}$.

This information about the unknown parameters M_{X_1} and σ_X can be added to the maximum likelihood function as multiplicative weighting factors:

$$\mathcal{L}' = \prod_{i=1}^{N} \frac{e^{-\frac{(M_i - f_i)^2}{2\sigma_i^2}}}{\sqrt{2\pi}\sigma_i} \cdot \frac{e^{-\frac{(M_{X_1} - M_0)^2}{2\sigma_M^2}}}{\sqrt{2\pi}\sigma_M} \cdot \frac{e^{-\frac{(\sigma_X - \sigma_0)^2}{2\sigma_\sigma^2}}}{\sqrt{2\pi}\sigma_\sigma}$$

According to the Maximum-Likelihood Principle the most probable values of the unknown f_i's are those which make $\mathcal{L}'$ as large as possible. Evidently $\mathcal{L}'$ has a maximum when the chi-square has a minimum, having defined:

$$\chi^2 = \sum_{i=1}^{N} \frac{(M_i - f_i)^2}{\sigma_i^2} + \frac{(M_{X_1} - M_0)^2}{\sigma_M^2} + \frac{(\sigma_X - \sigma_0)^2}{\sigma_\sigma^2}$$

When the number of observation is large, the data can be grouped into subsets corresponding to the bins of the histogram of the invariant mass distribution. If the N events are grouped into k classes or bins and the number of events in the bin i is n_i, they follow the multinomial distribution law:

- The expectation value for class i is $N\ p_i$
- The variance for class i is $N\ p_i(1 - p_i)$
- The covariance for class i, $j$value is $-N\ p_i\ p_j$

where p_i is the probability for the bin i. This probability can be found by integrating the probabilty distribution function over the bin width ΔM. If the number of bins is large so that the p_i are small, the off-diagonal terms become negligible and σ_i^2=N $p_i \simeq n_i$. therefore:

$$\chi^2 = \sum_{i=1}^{k} \frac{(n_i - f_i)^2}{n_i} + \frac{(M_{X_1} - M_0)^2}{sigma_M^2} + \frac{(M_{\sigma_X} - \sigma_0)^2}{sigma_\sigma^2}$$

The least squares principle asserts that the best values of the parameters are those that minimize the chi-square. The minimization was done in the framework of the MINUIT package [59]. This package provides the minimization through a routine called

MIGRAD, which also gives the parabolic errors for the estimated parameters. A more accurate determination of the errors was obtained by calling the routine MINOS which estimated the true confidence intervals by examining the exact behavior of the chi-square function.

References

[1] T. Nash et al., *Fermilab Conf.* 88/97 (1988)
T. Nash et al., *Fermilab Conf.* 89/58 (1989).

[2] M. Gell-Man, *Phys. Lett.* 8 (1964) 214.

[3] G. Zweig, *Cern Th.* **401** (1964) 412.

[4] M. Han and Y. Nambu, *Phys. Rev.* **139B** (1965) 1006
M. Gell-Man, *Acta Phys. Austriaca Suppl.* 9 (1972) 733.

[5] S.L. Glashow, J. Iliopoulos and L. Maiani, *Phys. Rev.* **D2** (1970) 1285.

[6] J.J. Aubert et al. *Phys. Rev. Lett.* 33 (1974) 1404.

[7] J.E. Augustin et al. *Phys. Rev. Lett.* **33** (1974) 1406.

[8] S.W. Herb et al. *Phys. Rev. Lett.* **39** (1977) 252.

[9] Particle Data Group, *"Review of Particle Properties", Physics Letters*, 239B (1990).

[10] H. Fukuda and Y. Miyamoto, *Prog. Theor. Phys.* 4 (1949) 347
J. Steinberger, *Phys. Rev.* **76** (1949) 1180.

[11] D.J. Gross and F. Wilczeck, *Phys. Rev. Lett.* **30** (1973) 1343
D.J. Gross and F. Wilczeck, *Phys. Rev.* **D8** (1973) 3633
H.D. Politzer, *Phys. Rev. Lett.* **30** (1973) 1346.

[12] T. Appelquist, H. D. Politzer, *Phys. Rev. Lett.* **34** (1975) 43
T. Appelquist, H. D. Politzer, *Phys. Rev.* **D12** (1975) 1404.

[13] E. Eichten et al., *Phys. Rev. Lett.* 34 (1975) 369.

[14] G. Bhanot et al., *Phys. Lett.* **73B** (1978) 119.

[15] J.L. Richardson, *Phys. Lett.* **82B** (1979) 272.

[16] R. McClary and N. Bayers, *Phys. Rev.* **D28** (1983) 1692.

[17] A.B. Henriques et al., *Phys. Lett.* **B64** (1976) 85.

[18] D.W. Duke and J.F. Owens *Phys. Rev.* **30D** (1984) 49.

[19] J. Badier *Phys. Lett.* **89B** (1979) 145.
V. Barger, W.Y. Keung, and R.J.N. Phillips, *Z. Phys. C* **6** (1980) 169.

[20] C.E. Carlson and R. Suaya, *Phys. Rev.* **18D** (1978) 760.

[21] C. N. Yang, *Phys. Rev.* **77** (1950) 242.

[22] C.H. Chang, *Nucl. Phys.* **172B** (1980) 425.
R. Baier and R. Ruckl, *Z. Phys. C* **19** (1983) 251.

[23] L. Clavelli et al., *Phys. Rev.* **32D** (1985) 612.

[24] H. Fritzsch, *Phys. Lett.* **67B** (1977) 217.
V. Barger, W.Y. Keung and R.J.N. Phillips, *Z. Phys. C.* **6** (1980) 169.

[25] J. H. Kuhn, *Phys. Lett.* **89B** (1980) 385.

[26] Y. Afek, C. Leroy and B. Margolis *Nucl. Phys.* **165B** (1980) 339
Y. Afek, C. Leroy and B. Margolis *Phys. Rev.* **22D** (1980) 86.

[27] E.N. Argyres and C.S. Lam, *Nucl. Phys.* **234B** (1984) 26

[28] T. B. W. Kirk et al., *Phys. Rev. Lett.* **42** (1979) 619.

[29] S. R. Hahn et al., *Phys. Rev.* **30D** (1984) 671.

[30] D. A. Bauer et al., *Phys. Rev. Lett.* **54** (1985) 753.

[30] D. A. Bauer et al., *Phys. Rev. Lett.* 54 (1985) 753.

[31] J. Badier et al., *Z. Phys. C* **20** (1983) 100.

[32] C. Kourkoumelis et al., *Phys. Lett.* **81B** (1979) 405
A Cobb et al., *Phys. Lett.* **68B** (1977) 101.

[33] Y. Lemoigne et al., *Phys. Lett.* **113B** (1982) 509
M. A. Abolins et al., *Phys. Lett.* **82B** (1979) 145.

[34] F. Binon et al., *Nucl. Phys.* **239B** (1984) 311

[35] S. Conetti et al., *IEEE Trans. on Nucl. Sci.* **38** (1989) 112.

[36] B. Cox et al., *Nucl. Instr. Meth.* **219** (1984) 487.

[37] D. E. Wagoner et al., *Nucl. Instr. Meth.* **A238** (1985) 315.

[38] S. D. Delchamps et al., *IEEE Trans. on Nucl. Sci.* **38** (1989) 680.

[39] C. M. Jenkins et al., *IEEE Trans. on Nucl. Science* **38** (1989) 117.

[40] L. Spiegel et al., *IEEE Trans. on Nucl. Science* **38** (1989) 86.

[41] S. Conetti et al., *IEEE Trans. on Nucl. Science* **32** (1985) 1326.

[42] G. Zioulas et al., *IEEE Trans. on Nucl. Science* **38** (1989) 375.

[43] H. Areti et al., *Nucl. Inst. and Meth.* **212** (1983) 135.

[44] S. W. Delchamps, E705 Internal Note (1990)

[45] A. Simard, M.S. Thesis, Mc Gill University (1990)

[46] L. Fortney, E705 Internal Note (1990)
Q. Shen, E705 Internal Note (1990)

[47] T. Turkington, Ph.D. Thesis, Duke University (1989)

[48] D.E. Wagoner et al., *Nucl. Instr. and Meth.* **A238** (1985) 315

[49] J.A. Appel et al., *Nucl. Instr. and Meth.* 127 (1975) 495
J.E. Brau et al., *Nucl. Instr. and Meth.* 196 (1982) 403

[50] W. Nelson et al., "The EGS4 Code System", SLAC-Report-265, Dec. 1985.

[51] L. Fortney, E705 Internal Note (1990)

[52] H.-U. Bengtsson, T. Sjostrand, Computer Phys. Comm. 46 (1987) 43.

[53] R. Tesarek, E705 Internal Note (1991)

[54] M. Rosati, in Proceedings of DPF91 Conference, Vancouver, 1991.

[55] T.J. Lecompte, Ph.D. Thesis, Northwestern University (1991)

[56] L. Lyons et al., *Prog. Part. Nucl. Phys.* 7 (1981) 169

[57] D. Coffman et al., SLAC-PUB-5592 (1991)

[58] L. Lyons, *"Statistics for Nuclear and Particle Physicists", Cambridge University Press* (1986).

[59] F. James, M. Roos *"MINUIT Users Manual", CERN Computer Centre Program* (1986).